UZBEKISTAN ACADEMY OF SCIENCES
ASTRONOMICAL INSTITUTE

UDC: 530.12:531.51

TURSUNOV ARMAN ALTAYEVICH

ASTROPHYSICAL PROCESSES IN BLACK HOLE ENVIRONMENT AND HIGH-ENERGY COSMIC RAYS

01.03.01- ASTRONOMY

DISSERTATION OF THE DOCTOR OF SCIENCES (DSc)
IN PHYSICS AND MATHEMATICS

Scientific consultant: Ahmedov Bobomurat Juraevich
doctor of sciences in physics and mathematics,
professor

Tashkent - 2019

Contents

Abbreviations

GR	general relativity
BH	black hole
SMBH	supermassive black hole
NS	Neutron Star
SgrA*	Sagittarius A*
ZAMO	zero angular momentum observer
LNRF	locally non-rotating reference frame
ISCO	innermost stable circular orbit
NEO	negative energy orbit
CMB	cosmic microwave background
UHECRs	ultra-high-energy cosmic rays
EHT	Event Horizon Telescope
VLT	Very Large Telescope
VLBI	very-long-baseline interferometry
AGN	active galactic nucleus
GRB	gamma-ray burst
MPP	magnetic Penrose process
PP	Penrose process
BZ	Blandford-Znajek mechanism
GJ	Goldreich-Julian
GZK	Greisen-Zatsepin-Kuzmin
LL	Landau-Lifshitz
RNdSD	Reissner-Nordström de-Sitter dyon
RIAF	radiatively inefficient accretion flow
NSC	nuclear star cluster

Units and conversions in Gaussian (CGS) and Geometrized systems

Quantity	Symbol	Gaussian	Geometrized	Conv.
Length	r	1 cm	1 cm	1
Time	t, τ	1 s	2.99×10^{10} cm	c
Mass	m, M	1 g	7.42×10^{-29} cm	$\mathrm{G/c^2}$
Energy	E	1 erg	8.26×10^{-50} cm	$\mathrm{G/c^4}$
Force	F	1 dyn	8.26×10^{-50}	$\mathrm{G/c^4}$
Electric current	j	1 statA	9.59×10^{-36}	$\sqrt{\mathrm{G}}/\mathrm{c}^3$
Electric charge	q	1 statC	2.87×10^{-25}cm	$\sqrt{\mathrm{G}}/\mathrm{c}^2$
Charge density	ρ	$1\ \mathrm{statC} \cdot \mathrm{cm}^{-3}$	$2.87 \times 10^{-25}\mathrm{cm}^{-2}$	$\sqrt{\mathrm{G}}/\mathrm{c}^2$
Magnetic field	B	1 Gauss	$8.16 \times 10^{-15}\mathrm{cm}^{-1}$	$\sqrt{\mathrm{G}}/\mathrm{c}$
Ang. momentum	J, L	$1\ \mathrm{g\ cm^2\ s^{-1}}$	$2.47 \times 10^{-39}\ \mathrm{cm}^2$	$\mathrm{G/c^3}$
BH spin	$a = J/(Mc)$	1 cm	1 cm	1

Physical constants & other definitions

Speed of Light	$c = 2.998 \times 10^{10}\ \mathrm{cm\ s^{-1}}$
Gravitational constant	$G = 6.672 \times 10^{-8}\ \mathrm{cm^3\ g^{-1}\ s^{-2}}$
Mass of the Sun	$M_\odot = 1.989 \times 10^{33}$ g
Mass of Sgr A*	$M_* = 4.14 \times 10^6 M_\odot = 8.23 \times 10^{39}$ g
Schwarzschild radius of the Sun	$r_S = 2GM_\odot/c^2 = 2.95 \times 10^5$ cm
Schwarzschild radius of Sgr A*	$R_S = 2GM_*/c^2 = 1.22 \times 10^{12}$ cm

1 parsec = 1 pc = 3.26 ly = 3.08×10^{18} cm

1 eV = 1.6×10^{-19}J = 1.6×10^{-12}erg

1 Gauss = 1 G = 10^{-4} T

Introduction

Topicality and demand of the theme of dissertation. Nowdays there is a great interest to probe the nature of black holes. Black holes are fascinating astrophysical objects with extremely compact sizes and tremendous masses representing the modern physics in its beauty and extremes. Being the darkest cosmic objects, black holes are observed to be the most luminous, powerful and massive objects in the Universe, warping the spacetime and heating surrounding matter to enormous temperatures. Recent progress in development of observational and experimental facilities have enabled to provide both direct and indirect evidences of their presence in nature.

Recently there were the triumphal discoveries, which define the topicality of the subject of the dissertation. In April 2019 the first ever image of a black hole – extragalactic supermassive black hole located at the center of Meisser 87 galaxy, has been revealed by the Event Horizon Telescope (EHT) observing at mm wavelengths. In July 2018 unprecedented discovery of extragalactic high-energy neutrinos by IceCube Neutrino Observatory has been announced which enabled to pinpoint the source to blazar, which is a supermassive black hole (SMBH) at the distance of ~ 1.75Gpc with relativistic jets directed almost exactly towards us. High-energy neutrinos can be produced in the hadronic interactions of primary high-energy cosmic rays with surrounding matter or photons. The origin and production mechanism of ultra-high-energy cosmic rays (UHECRs) still remains unclear. One of the first direct observations of material orbiting very close to a black hole, on the scales of few Schwarzschild radii, has been detected in May-July 2018 by GRAVITY instrument on the Very Large Telescope (VLT) of European Southern Observatory (ESO). New observations, carried out in the near-infrared K-band have shown the hot flares of gas revolving black hole at the center of Milky Way at about 30% of the speed of light, just outside its event horizon. The origin and nature of flares/hot spots around black hole remains under debate. The first successful test of Einstein's general theory of relativity (GR) on the scales of million-solar-mass compact objects has been announced by Gravity Collaboration in mid 2018 based on the observations of the motion of S2-star passing the massive black hole at the center of our Galaxy. The new observations have also enabled to derive the mass of the black hole $M_\bullet$ with the greatest precision, being of 4.14×10^6 of solar masses, which corresponds to the gravitational radius of $R_\mathrm{g} = 2GM_\bullet/c^2 = 1.22 \times 10^{12}\,\mathrm{cm} \sim 10^{12}\,\mathrm{cm}$. Starting 2015, advanced Laser Interferometer Gravitational Wave Observatory have announced the numerous detection of gravitational waves made from the coalescence of black holes and neutron stars in close binary systems. Based on these discoveries one may conclude that predicted by Einstein's general theory of relativity more than a century ago, black holes have risen today from objects mainly of academic interest to realistic cosmic objects, which are responsible for the most energetic astrophysical processes.

In our Republic, great attention is paid to the study of astrophysical processes in the vicinity of black holes. The directions of these fundamental research, which are of great importance for the development of science in our country, are connected with the Strategy for the Further Development of the Republic of Uzbekistan for 2017-2021 years. Over the last 20 years, relativistic astrophysics of compact gravitational objects has been developed in our Republic. In particular, the energetic and optical properties of black holes, wormholes and naked singularities have been studied, the new effects of the general theory of relativity in relativistic astrophysics of neutron stars have been found, relativistic electrodynamics and the plasma magnetosphere of rotating compact objects have investigated, the natures of part-time pulsars and the radioloud magnetars were clarified.

Conformity of the research to the main priorities of science and technology development of the republic. The dissertation research has been carried out in accordance with the priority areas of science and technology in the Republic of Uzbekistan: II. "Power, energy and resource saving".

Review of international scientific researches on dissertation subject. On the study of supermassive black holes and related effects, particles motion and electromagnetic fields around the black hole in external magnetic field it has been obtained a large number of original scientific results by leading scientific institutions and universities, including obtaining and study the properties of rotating black holes shadow in the framework of General Relativity and modified theories of gravity (University of Cologne, Max Planck Institute for Radio Astronomy, Max Planck Institute for Gravitational Physics - Albert Einstein Institute, Frankfurt University, Germany; Inter-University Centre for Astronomy and Astrophysics, Physics Research Laboratory, Tata Institute of Fundamental Research, India; the Centre for Applied Space Technology and Microgravity, Germany; Astronomical Insitute of the Russian Academy of Sciences, Moscow State University, Russia); it has been found the structure of the electromagnetic field around a rotating black hole and studied the equations of motion of charged particles around a rotating black hole in the presence of an external magnetic field (Astronomical Institute, Albert Einstein Center and the Silesian University in Opava, Czech Republic; University of Alberta, Canada; Inter-University Centre for Astronomy and Astrophysics, India; Centre for Applied Space Technology and Microgravity and Oldenburg University, Germany); study of energetic processes in the vicinity of rotating black holes in the framework of General Relativity and alternative theories of gravity, in particular, study of the properties of space-time properties around a black hole in the gravity model of Horava have been carried out (Albert Einstein Center and Silesian University in Opava, Czech Republic; University of Alberta, Canada; Centre for Applied Space Technology and Microgravity, Germany).

The electromagnetic field configurations in the external asymptotically uniform magnetic field, as well as shadows of rotating black holes has been carried out by the world's leading research centers and institutions of higher education, in particular, Astronomical Institute, Albert Einstein Center and the Silesian University in Opava (Czech Republic), the University of Alberta (Canada), the Max Planck Institute for Gravitational Physics - Albert Einstein Institute and the Frankfurt University (Germany), Inter-University Centre of Astronomy and Astrophysics, Research Laboratory of Physics and Tata Institute of Fundamental Research (India), the Centre for Applied Space Technology and Microgravity and the Oldenburg University (Germany), State Astronomical Institute named after Sternberg of Moscow State University, Joint Institute for Nuclear Research in Dubna (Russia), Institute of Nuclear Physics, Astronomical Institute and National University of Uzbekistan (Uzbekistan).

Currently, in order to study energetic processes in the vicinity of compact gravitational objects there have been carried out investigations in the world in a number of priority areas, including: theoretical and experimental studies of ultra-high-energy cosmic rays; origin of extragalactic high-energy neutrinos; efficient energy extraction from rotating black holes; observations of effects occurring around Galactic center black hole; theoretical modelling of electromagnetic fields around black holes and analysis of particle motion around these objects; study of energetic processes in the vicinity of rotating black holes in the presence of an external electromagnetic field.

Degree of study of the problem Properties of matter surrounding astrophysical black hole, as well as the constraints on the black hole parameters has been investigated both theoretically and experimentally in many research centers around the world, for example in Germany (R. Genzel, A. Eckart, A. Zensus, S. Britzen), Spain (R. Schoedel, B. Shahzamanian), Italy (R. Ruffini, C. Cremaschini), Czech Republic (Z. Stuchlik, J. Kolos), Russia (A. Zakharov, D. Gal'tsov), China (C. Bambi, A. Abdikamalov) and others. However, the effect of electromagnetic interaction of matter with black hole on the constraints of black hole parameters or characteristics of accretion flow has not been properly studied.

Among detectors of ultra-high-energy cosmic rays one can highlight two largest cosmic ray observatories, such as the Telescope Array on the northern hemisphere and Pierre Auger Observatory on the southern hemisphere. Apart from the observational study of UHECRs, there are various theoretical and semi-phenomenological models attempting to describe the origin and mechanism of their formation. One can mention the groups in USA (Fly's Eye collaboration), Antarctica (Ice Cube collaboration), Germany (R. Engel, K. Mannheim) among others. However, still the origin and mechanism of the formation of the highest energy cosmic rays are not properly understood. Moreover, the connection of UHECRs with the immediate region of supermassive black holes are not yet discussed.

The properties of the electromagnetic field around rotating Kerr black hole immersed into external homogeneous magnetic field, the investigation of the dynamics of charged particles revolving a rotating black hole in the presence of an external field, particles collisions and decays in the vicinity of a Kerr black hole have been investigated and discussed by many scientists, such as e.g. from the UK (R. Wald et al.), the USA (M. Banados, et al.), Russia (D.V. Gal'tsov, et al.), Canada (V. Frolov, et al.), Turkey (Aliev, N. Ozdemir), Uzbekistan (A. Abdujabbarov, B. Ahmedov), and many others. However, a detailed study of the energy extraction mechanisms in ultra-efficient regime has not been previously mentioned, as this findings was first announced by me and my colleagues. The investigation of these effects leads to explanation of various important phenomena observed in cosmic rays, relativistic jets, quasars, etc.

Shadow of a black holes in both vacuum and plasma cases with the various additional parameters of the central object, sometimes, extraordinary and physically unjustified parameters, have been studied by many scientists, including those from Japan (K. Maeda, K. Hioki), Germany (A. Grenzebach, V. Perlick, C. Laemmerzahl), Uzbekistan (A. Abdujabbarov, B. Ahmedov, F. Atamurotov), Argentina (E. Eiroa, L. Amarilla), Czech Republic (J. Schee, Z. Stuchlik), Russia (G. Bisnovatyi-Kogan, O. Tsupko) and many others. However, all these works being of analytical solutions are oversimplified and should not be applied in realistic observations, have been carried out in the framework of particular choice of solutions of compact objects and it does not exist a formalism describing shadows of black holes independent from the choice of the model of black holes and gravity theories.

Connection of the topic of dissertation with the scientific works of scientific research organizations, where the dissertation was carried out. The dissertation was done in the framework of the scientific projects of the Ulugh Beg Astronomical Institute, Uzbekistan Academy of Sciences: VA-FA-F-2-008 "Astrophysical Processes in Stationary and Dynamic Relativistic Gravitation Objects" (2017-2020); VA-FA-F-2-008a "Relativistic astrophysics of isolated black holes in tight binary systems containing black holes" (2017-2020), YFA-FTECH-2018-8 "Particles and strong gravitational and electromagnetic fields in the vicinity of compact objects in relativistic astrophysics" (2018-2019); Belorussian-Uzbek program MRB-AN-2019-29 "Modelling of compact astrophysical objects and correlation of their observational characteristics with parameters of the telescope RT-70 and russian orbital telescope Gamma-400" (2019-2021).

The aim of the research is the investigation of electromagnetic properties of astrophysical black holes and surrounding matter, as well as the application of results to the description of various observed phonomena, such as ultra-high-energy cosmic rays, relativistic jets, black hole shadow, etc.

The tasks of the research:

to analyse the charged and neutral particles motion, collisions and decays around rotating black holes in the presence of an external magnetic field;

to study the electromagnetic fields in curved spacetimes;

to develop a new model for the ultra-high-energy cosmic rays produced in close vicinity of astrophysical black holes;

to make a comparative analysis of the predictions of the model of UHECRs with observational data;

to determine the influence of an inhomogeneous plasma to the form of rotating black hole shadow;

to discuss the reinterpretation of observational data by taking into account the electromagnetic interactions of black holes and matter in the frame of given model;

to apply theoretical results to particular black hole candidates, including supermassive black hole at the center of the Galaxy.

The objects of the research are rotating black holes immersed into external magnetic fields and such candidates as SgrA*, M87, NGC1052 and similar objects including blazars.

The subjects of the research are the mechanisms of energy extraction from black holes in astrophysical conditions; electromagnetic properties of realistic black holes; electromagnetic radiation of matter in the regime of strong gravity; characteristics of plasma around compact objects and shadow of black hole surrounded by plasma.

The methods of the research. Phenomenological modelling of the properties of various high-energy astrophysical phenomena by means and methods of mathematical apparatus of general relativity combined to electrodynamics and numerical simulations of realistic processes by solving nonlinear differential equations for matter and fields.

The scientific novelty of the research is in the following:

for the first time a small charge associated with the black hole Sgr A* at the center of the Milky Way has been constrained with the uppermost limit of $Q_{\mathrm{SgrA*}} \lesssim 10^{15}\,\mathrm{C}$, which can mimic up to 60% of the maximum spin of a black hole.

for the first time it has been shown that the plasma surrounding Sgr A* is relativistic and magnetized, which leads to the charge separation in a plasma. It has been found that the net charge number density of plasma surrounding Sgr A* is $10^{-5}\mathrm{cm}^{-3}$, while the plasma number density is of order $10^{71}\mathrm{cm}^{-3}$.

it has been shown that it is unlikely to detect a bright star in the innermost $R = 1500$ Schwarzschild radii from Sgr A*, although stellar fly-by at highly-eccentric orbit is possible.

a novel mechanism for the production of ultra-high-energy cosmic rays (UHECRs) by extracting the energy from supermassive black holes has been suggested. It has been shown that proton's energy can naturally exceed 10^{20}eV for supermassive black hole of $10^9 M_\odot$ and magnetic field of 10^4G.

it has been shown for the first time that the energy of escaping proton in the most efficient regime of energy extraction from the Galactic center Sgr A* black hole is of order $10^{15.5}$eV, which coincides with the knee of the cosmic ray energy spectra, where the flux of particles shows significant decrease.

new analytical expressions for the shadow sizes of the RNdSD black holes has been obtained.

gravitational deflection in a plasma surrounding rotating gravitational objects and Faraday rotation of polarization plane has been studied for the first time and the expression for the lensing angle in the case of a strongly non-uniform plasma surrounding rotating compact object has been derived.

Practical results of the research are as follows:

novel mechanism which suggests supermassive black holes as sources of ultra-high-energy cosmic rays (UHECRs) provides verifiable constraints on the mass, distance and magnetic field of the UHECR source.

novel observational test proposed for determination of the black hole charge will be possible to perform in the near future by the new generation of X-ray telescopes.

it has been shown that unscreened charge of a black hole can effectively mimic the spin parameter of the black hole up to 60% of its maximal value, which is reflected in considerable shift of the innermost stable circular orbits for charged particles.

new expressions for the gravitational lensing in a plasma and the shadow of black holes may be used to constrain parameters of two black hole candidates, M87 and Sgr A* and surrounding plasma based on the data from the Event Horizon Telescope.

Reliability of the research results is provided by the following: is provided by the following: use of methods of general theory of relativity (GR) and the-oretical physics, highly efficient numerical methods and codes; most of the figures were plotted on Wolfram Mathematica software. Careful tests of a consistence of the obtained theoretical results with available observational data and results from other scientists are performed; conclusions are well consistent with the main provisions of the field theory of gravitational compact objects.

Scientific and practical significance of the research results. The scientific significance of the research results is determined by the ability of the developed formalism in the dissertation to analyse the electromagentic fields of astrophysical black holes, energy extraction mechanisms from astrophysical black holes and determination of black holes shadow obtained by a new generation of radiotelescopes in the near future, and get an information on the various parameters and properties of the supermassive black holes at the centers of galaxies. In addition, future X-ray observations at the galactic center of the bremsstrahlung surface brightness could provide tight constraints on the presence of electric charge of the black hole, whih plays crucial role in acceleration mechanisms around supermassivel black holes, related to AGNs, quasars etc.

The practical significance of the results of research lies in the fact that they can be used to obtain estimates of black holes of different parameters such as mass, spin, orientation, charge and magnetic field. Results can also be useful for the analysis of the nature and dynamics of the gravitational field, in the development of observational experiments and criteria for the detection and identification of compact black hole alternatives.

Application of the research results Based on the study of astrophysical phenomena and processes in the vicinity of black holes and high-energy cosmic rays:

results of the parameters of SMBH Sgr A* in the center of our galaxy and plasma dynamics in its vicinity have been used in the SFB-956 project of the German Science Foundation and programs funded from the structural funds of the European Union and the Polish Science Center to test the theory of gravity in a strong field regime (letter from Center for Theoretical Physics of the Polish Academy of Sciences dated July 8, 2019). The results were used to obtain restrictions on the electric charge of Sgr A*;

the results on the study of the electromagnetic properties of supermassive black hole in the center of our galaxy were used by foreign researchers (cited in refereed scientific journals Physical Review D, 2018, 2019; International Journal of Modern Physics D, 2019; Journal of Cosmology and Astroparticle Physics, 2019) to study the interaction of interstellar space and the neighborhood of a black hole in the center of the Galaxy, as well as to test the predictions of the theory of gravity of Hordesky in the case of a black hole with electric charge;

study on the energy properties of black holes, realistic methods of electromagnetic extraction of the rotational energy of black holes, and high-energy processes were used to carry out projects of the Indian Inter-University Grant Committee (letter from Indian Inter-University Grant Committee dated June 15, 2019), as well as foreign researchers (cited in refereed scientific journals Physics of the Dark Universe, 2019; The European Physical Journal C, 2019; Physical Review D, 2019; Monthly Notices of the Royal Astronomical Society, 2019). The results were generalized for the case of extracting the energy of black holes in brane by colliding particles in the ergosphere. In addition, the results were used to obtain the limiting values of the parameters of astrophysical compact candidates;

the motion of charged particles around a magnetized black hole, as well as the corresponding quasi-periodic oscillations were used in the work of foreign colleagues (cited in scientific journals Physical Review D, 2019; International Journal of Modern Physics D, 2019; The European Physical Journal C, 2019; Physics of The Dark Universe, 2019; The Astrophysical Journal, 2018) for determining the mass, spin and magnetic fields of some microquasars and stellar-mass black holes;

studies on the optical properties of black holes in plasma were used to carry out projects funded from the State budget of the Czech Republic, in particular, registered under number SGS/12/2019, as well as by foreign researchers (cited in foreign scientific journals Physical Review D, 2018, 2019; Astrophysics and Space, 2016; The European Physical Journal C, 2018, 2019; International Journal of Modern Physics D, 2018; Modern Physics Letters A, 2018; Monthly Notices of the Royal Astronomical Society, 2016) for obtaining many new results, such as effects of gravitational lensing in plasma, shadows of black holes in plasma, in Einstein's theory of gravity, and in alternative theories of gravity.

Approbation of the research results. The research results were reported in the form of reports and tested at 9 international and local scientific conferences, 8 scientific seminars and 3 summer schools.

Publication of the research results. On the dissertation theme there were published 22 scientific works, including 12 scientific papers in international scientific journals recommended by the Supreme Attestation Commission of the Republic of Uzbekistan for publishing basic scientific results of doctoral theses.

Volume and structure of the dissertation. The dissertation consists of an introduction, four chapters, conclusion and a bibliography. The size of the dissertation is 216 pages.

List of published papers [1, 2, 3, 4, 5, 6, 7, 8, 9, 10, 11, 12, 13] .

Part I.

1. Tursunov A., Kološ M., Stuchlík Z., Gal'tsov D.V. Radiation Reaction of Charged Particles Orbiting a Magnetized Schwarzschild Black Hole // Astrophysical Journal. - The American Astronomical Society (USA), 2018. - Vol. 861. - pp. 2-18. (No.1. Web of Science: IF=5.551).

2. Dadhich N., Tursunov A., Ahmedov B., Stuchlík Z. The distinguishing signature of magnetic Penrose process // Monthly Notices of the Royal Astronomical Society Letters. - Oxford University Press (Great Britain), 2018. - Vol. 478. - pp. 89-94. (No.1. Web of Science: IF=5.194).

3. Zajaček M., Tursunov A., Eckart A., Britzen S. On the charge of the Galactic

centre black hole // Monthly Notices of the Royal Astronomical Society. - Oxford University Press (Great Britain), 2018. - Vol. 480. - pp. 4408-4423. (No.1. Web of Science: IF=5.194).

4. Tursunov A., Kološ M., Stuchlík Z. Orbital widening due to radiation reaction around a magnetized black hole // Astronomische Nachrichten. - Wiley Online Library (Germany), 2018. - Vol. 339. - no. 5 - pp. 341-346. (No.1. Web of Science: IF=1.322).

5. Tursunov A., Kološ M. Constraints on Mass, Spin and Magnetic Field of Microquasar H 1743-322 from Observations of QPOs // Physics of Atomic Nuclei - Pleiades Publishing (Russia), 2018. - Vol. 81, - pp. 279-282. (No.1. Web of Science: IF=0.524).

6. Zajaček M., Tursunov A. A stellar fly-by close to the Galactic center: Can we detect stars on highly relativistic orbits? // Astronomische Nachrichten. - Wiley Online Library (Germany), 2018. - Vol. 339. - pp. 324-330. (No.1. Web of Science: IF=1.322).

7. Kološ M., Tursunov A., Stuchlík Z. Some astrophysical processes around magnetized black hole // Contributions of the Astronomical Observatory Skalnate Pleso. - SAS (Slovakia), 2018. - Vol. 48. - pp. 282-283. (No.1. Web of Science: IF=0.733).

8. Zajaček M., Tursunov A. Electric charge of black holes: Is it really always negligible? // Observatory. - Oxford (Great Britain), 2019. - Vol. 149. - pp. 215-222. (No.1. Web of Science; IF=0.130).

9. Eckart A., Tursunov A., Zajaček M., Parsa M., Hosseini E., Subroweit M., Peissker F., Straubmeier C., Horrobin M., Karas V. Mass, Distance, Spin, Charge, and Orientation of the super massive black hole SgrA // Proceedings of Science. - SISSA (Italy), 2019 - Vol. 342. - pp.48-59, 11p. (No.3. Scopus; IF=0.3)

10. Zajaček M., Tursunov A., Eckart A., Britzen S., Hackmann E., Karas

V., Stuchlík Z., Czerny B., Zensus J.A. Constraining the charge of the Galactic centre black hole, //Journal of Physics Conference Series - IOP Publishing (Great Britain), 2019, 17pp. (No.40. ResearchGate: IF = 0.69)

11. Eckart A., Zajaček M., Valencia-S M., Parsa M., Hosseini E., Straubmeier C., Horrobin M., Subroweit M., Tursunov A. The central light-year of the Milky Way: How stars and gas live in a relativistic environment of a super-massive black hole, // Journal of Physics Conference Series. - IOP Publishing (Great Britain), 2019. - 14pp. (No.40. ResearchGate: IF = 0.69)

12. Tursunov A., Dadhich N. Fifty years of energy extraction from rotating black hole: revisiting magnetic Penrose process // Universe - MDPI (China), Invited Review for the special issue on Accretion Disks, Jets, GRBs and related Gravitational Waves, 2019. - Vol. 5. - pp. 125-150. (No.1. Web of Science; IF=2.165)

Part II.

13. Abdujabbarov A., Hakimov A., Turimov B., Tursunov A. Effect of geometric optics in conformal Weyl gravity // Arabian Journal of Mathematics. - Springer (Germany), 2019. - Vol.8. - pp. 1-9.

14. Tursunov A. Synchrotron radiation reaction of charged particles around astrophysical black holes // 42nd COSPAR Scientific Assembly on 14-22 July, 2018. - Pasadena, California, 2018. - Vol. 42 .- pp. E1.4-80-18.

15. Tursunov A. Production of ultra-high-energy particles in the vicinity of supermassive black holes //42nd COSPAR Scientific Assembly on 14-22 July, 2018. - Pasadena, California, 2018. - Vol. 42 .- pp. E1.5-82-18.

16. Zakharov A., Stuchlík Z., Jaluvkova P., Tursunov A., Shadow sizes around black holes as possible signatures of Horndeski gravity // 42nd COSPAR Scientific Assembly on 14-22 July, 2018. - Pasadena, California, 2018. - Vol. 42 .- pp. H0.1-12-18.

17. Zakharov A., Stuchlík Z., Jaluvkova P., Tursunov A. Shadows around supermassive black holes as a tool to test GR and alternative theories of gravity // 42nd COSPAR Scientific Assembly on 14-22 July, 2018. - Pasadena, California, 2018. - Vol. 42 .- pp. E1.8-25-18.

18. Tursunov A., Kološ M., Stuchlík Z., Zamora-Saa J., Alvarez-Castillo D., Supermassive black hole as a source of ultra-high-energy cosmic rays // Fifteenth Marcel Grossmann Meeting - MG15, July 1 to 7, 2018. - Rome (Italy), 2018. - HE6, N8.

19. Zakharov A., Stuchlík Z., Jaluvkova P., Tursunov A. Shadows for Reissner-Nordstrom - de-Sitter dyon black holes // Fifteenth Marcel Grossmann Meeting - MG15, July 1 to 7, 2018. - Rome (Italy), 2018. - PT2, N5.

20. Tursunov A. Ultra-high-energy cosmic rays from supermassive black holes // Ultra High Energy Cosmic Rays, 8-12 October, 2018. - Paris (France), 2018. - P196.

21. Tursunov A. Motion of radiating charged particle in curved spacetime // Invited Talk at the International School "Advanced Methods of Modern Theoretical Physics: Integrable and Stochastic Systems", 2018, dubnaschool.cz/2018

22. Tursunov A. Brief tutorial on energy mining from rotating black holes // Invited Talk at the International School "Advanced Methods of Modern Theoretical Physics: Integrable and Stochastic Systems", 2019, dubnaschool.cz/2019

Chapter I

Electrodynamics of black hole magnetospheres

1.1 Kerr black hole hypothesis: astrophysical perspective

Among the experimental tests successfully passed by Einstein's general theory of relativity are the tests of precession of Mercury's perihelion, deflection of photons by Sun's gravity, measurement of gravitational redshift, orbital decay of binary pulsars [14], direct detection of gravitational waves [15], investigation of properties of the Galactic center supermassive black hole [16], and others. So far, all experimental tests of general relativity at various scales and regimes bear no convincing evidence of any deviation of black holes from the rotating Kerr black hole hypothesis, which pronounces that an astrophysical black hole can be well characterized solely by two parameters, namely its mass M and spin a.

The mass is the most fundamental parameter of a black hole, which in many cases can be measured with relatively high precision through observations of dynamics of nearby objects. For example, the most recent estimates of the mass of order $4.14 \times 10^6 M_\odot$ of the currently best known black hole candidate SgrA* located at the center of our Galaxy have been achieved by near infrared observations of S2 star revolving around central black hole [17]. In order to measure spin of a black hole one needs to probe effects occurring in strong gravity regime, as its gravitational contribution has no Newtonian analogue and hence it is very small and hard to measure. Acceleration of interstellar matter floating towards a black hole gets heated up, resulting in X-ray emission from accretion disk or hot spots. Some progress on the spin determination methods has been achieved with observations and modeling of X-ray spectra from both stellar mass and supermassive black holes [18]. In addition, potential detection of gravitational waves from extreme mass ratio inspirals (EMRIs) by future space-based Laser Interferometer Space Antenna (LISA) [19] seems to be a promising avenue for determination of spin of astrophysical black holes. However, since method of observation is model dependent and it cannot be directly measured, the estimated spin values in various models may differ dramatically.

According to the no-hair theorem, there can exist the third black hole parameter, electric charge arising from Einstein-Maxwell equations for rotating charged mass. The charge parameter of a black hole is usually set explicitly equal to zero, which is justified by quick discharge of any net charge of a black hole due to selective accretion of a plasma matter surrounding any astrophysical black hole. However, as black holes are usually embedded into external magnetic field arising due to plasma dynamics, and more specifically twisting of magnetic field lines due to the frame dragging of effect in the vicinity of a rotating black hole induces electric field in both vacuum and plasma cases [20, 21]. It posits a net quadrupole charge on the black hole [22, 4]. This charge is weak in the same sense as magnetic field, i.e. its stress-energy tensor does not alter spacetime metric. Thus the assumption of the Kerr hypothesis is well founded. However, it would turn out as we will show later that black hole charge would play crucial role in making energy extraction process ultra-efficient, so much so that efficiency could range over 10^{10}. In the next section we shall describe the black hole charging mechanisms in astrophysical context and discuss its possible screening by surrounding plasma.

Spacetime around an astrophysical black hole is described by the Kerr metric in the standard form given in the Boyer-Lindquist coordinates,

$$ds^2 = -\left(1 - \frac{2Mr}{\Sigma}\right) dt^2 - \frac{4Mra\sin^2\theta}{\Sigma} dt d\phi + \frac{\Sigma}{\Delta} dr^2 \\ +\Sigma\, d\theta^2 + \left(r^2 + a^2 + \frac{2Mra^2}{\Sigma}\sin^2\theta\right)\sin^2\theta\, d\phi^2, \tag{1.1}$$

where $\Sigma = r^2 + a^2\cos^2\theta$ and $\Delta = r^2 - 2Mr + a^2$. Physical singularity occurs at the ring $r = 0$, $\theta = \pi/2$. The roots of $\Delta = 0$ define outer and inner horizons located at

$$r_\pm = M \pm (M^2 - a^2)^{1/2}. \tag{1.2}$$

It is the outer horizon which is referred as the event horizon $r_+ \equiv r_H$. The geometry is characterized by existence of the two Killing vectors, timelike, $\delta/\delta t$ and spacelike, $\delta/\delta\phi$, indicating the corresponding conserved quantities, energy E and angular momentum L. One can introduce an observer with timelike four-velocity and zero angular momentum $L = u_\phi = 0$, which is infalling into the black hole from rest at infinity. This corresponds to the locally non-rotating frame of reference (LNRF) of the zero angular momentum observers (ZAMO) with the four-velocity given by

$$n^\alpha = (n^t, 0, 0, n^\phi), \quad (n^t)^2 = \frac{g_{\phi\phi}}{g_{t\phi}^2 - g_{tt}g_{\phi\phi}}, \quad n^\phi = -\frac{g_{t\phi}}{g_{\phi\phi}}\, n^t. \tag{1.3}$$

Computing the angular velocity of LNRF/ZAMO we get

$$\Omega_{\rm LNRF} = -\frac{g_{t\phi}}{g_{\phi\phi}} = \frac{2Mar}{(r^2 + a^2)^2 - a^2\Delta\sin^2\theta}. \tag{1.4}$$

Since $\Omega/(2Ma)$ is always positive, ZAMO co-rotates with the black hole being dragged.

1.2 Electromagnetized black holes

1.2.1 Magnetization of black holes

Black holes are indeed embedded into external magnetic fields which can arise due to dynamics of surrounding plasma, e.g. electric currents inside accretion disks, intergalactic or interstellar plasma dynamics. Magnetic field could also be generated in early phases of expansion of the Universe. Strength of magnetic field can vary for each particular black hole candidate, usually being in the range 10 - 10^8G, highly dependent on properties of surrounding plasma. For example, the best known black hole candidate Sgr A*, which is located at the Galactic center is surrounded by highly oriented magnetic field measured at distance of few Schwarzschild radii from the center has field of order $10 - 100\,\mathrm{G}$ [23, 24]. Recent detection of orbiting hot-spots around the object [25] indicates presence of strong poloidal magnetic field at the ISCO scale.

It is important to note that any astrophysical magnetic field is weak in a sense that its energy-momentum tensor does not modify the background Kerr metric. It is easy to see by comparing magnetic field energy in a given volume with that of black hole's mass energy. This condition for stellar mass black holes [26] is given by

$$B \ll B_{\mathrm{G}} = \frac{c^4}{G^{3/2} M_\odot} \left(\frac{M_\odot}{M} \right) \sim 10^{18} \frac{10 M_\odot}{M} \mathrm{G}\,. \tag{1.5}$$

Observations of various black hole candidates and astrophysical phenomena occurring in their vicinity indicate that inequality (1.5) is perfectly satisfied. This implies that an astrophysical black hole is weakly magnetized, hence its effect on neutral test particle dynamics is negligible. On the other hand its effect for motion of charged particles is non-ignorable – rather immense, as ratio of Lorentz to gravitational force would be very large due to large value of charge to mass ratio. Since matter surrounding black hole is usually moving with relativistic velocities and highly ionized, one can characterize relative influence of Lorentz to gravitational force by dimensionless parameter $\mathcal{B} = |q|BM/(mc^4)$. For electrons close to event horizon of the Galactic center black hole [16], the estimate of this parameter is

$$\mathcal{B}_{\mathrm{SgrA}^*} \approx 2 \times 10^9 \left(\frac{q}{e}\right)\left(\frac{m}{m_{\mathrm{e}}}\right)^{-1}\left(\frac{B}{10\,\mathrm{G}}\right)\left(\frac{M}{4 \times 10^6\,M_{\odot}}\right). \tag{1.6}$$

For protons this ratio is ~ 2000 times lower. Stellar mass black holes, e.g. in binary systems can attribute magnetic fields of order 10^8G [27], for which $\mathcal{B}$ is of similar order of magnitude as (1.6). This implies that the effect of magnetic field on dynamics of charged particles is very dominant in realistic astrophysical conditions.

In the Kerr geometry, it is natural to assume that external magnetic field would also share symmetries of stationarity and axial symmetry. Using the Killing equation $\xi_{\alpha;\beta} + \xi_{\beta;\alpha} = 0$ one finds solution for electromagnetic field in the form [28]

$$A^{\mu} = C_1 \xi^{\mu}_{(t)} + C_2 \xi^{\mu}_{(\phi)}. \tag{1.7}$$

First solution of Maxwell equations in background rotating black hole spacetime corresponding to black hole embedded in homogeneous magnetic field aligned with the spin axis was obtained by R. Wald in [20], while for magnetic field inclined to the axis of rotation was due to J. Bičák and V. Janiš [29]. Magnetic field of current loop around rotating black hole corresponding to dipole magnetic field configurations was solved by J. Petterson in [30]. In case of external uniform magnetic field, the solution of Maxwell equations for corresponding four-vector potential in rotating black hole spacetime can be written in the following form [20]

$$A_t = \frac{B}{2}\left(g_{t\phi} + 2a g_{tt}\right), \quad A_{\phi} = \frac{B}{2}\left(g_{\phi\phi} + 2a g_{t\phi}\right). \tag{1.8}$$

Inserting metric coefficients we rewrite (1.8) in explicit form

$$A_t = aB\left(\frac{Mr}{\Sigma}\left(1+\cos^2\theta\right)-1\right), \tag{1.9}$$

$$A_\phi = \frac{B}{2}\left(r^2+a^2-\frac{2Mra^2}{\Sigma}\left(1+\cos^2\theta\right)\right)\sin^2\theta. \tag{1.10}$$

One can notice that rotation of black hole generates quadrupole electric field given by A_t which is the result of twisting of magnetic field lines – the frame-dragging effect. Electric field due to this induced charge is for arbitrary magnetic field configuration in the vicinity of axially symmetric black hole. This induced quadrupolar charge may be referred as black hole charge [4, 31] and it is this which is responsible for providing necessary negative energy to particle in the ergosphere. By this way, the inconvenient and unsurmountable condition on relative velocity for the original mechanical PP could be easily overcome. One should note that above is true until the extremality of black hole spin is reached, where the gravitational analogue of Meissner effect comes into play. Extremally rotating black hole expels fields out acting thus like a superconductor [20, 32], which happens exactly at $a/M = 1$. On the other hand, it is generally assumed that the maximum plausible spin of astrophysical black holes is $a/M = 0.998$ [33] marking equipartition of magnetic and gravitational energy. Thus, the further study and discussion is well in order and well motivated.

1.2.2 Electrification of black holes

Assumption of electrical neutrality of a black hole in many cases is justified by the presence of a plasma around black hole which can quickly discharge any charge excess. Indeed, one can estimate the discharge timescale of maximally charged black hole using the following arguments. Maximal theoretical value of the charge of a black hole of mass M is given by $Q = 2G^{1/2}M$, written in Gaussian units.

For spinning black hole it's of order [4]

$$Q_{\max} \approx 3.42 \times 10^{20} \left(\frac{M}{M_{\odot}} \right) \mathrm{C}. \tag{1.11}$$

If such a charge is carried by protons and electrons, this corresponds to the mass $M_Q = m_{p,e} Q/e$, where p and e denote proton and electron, respectively. Luminosity of black hole surrounded by plasma or accretion disk can be derived from infalling matter as $L = \epsilon \dot{M} c^2$, where $\dot{M}$ accretion rate and ϵ is the fraction of the rest mass energy radiated away. On the other hand, from the balance of gravitational force and radiation pressure in the vicinity of a black hole one can derive the Eddington luminosity for fully ionized hydrogen plasma surrounding a black hole in the form

$$L_{\mathrm{Edd}} = \frac{4\pi G M m_p c}{\sigma_{\mathrm{T}}} \approx 1.26 \times 10^{38} \left(\frac{M}{M_{\odot}} \right) \mathrm{erg/s}. \tag{1.12}$$

Defining charged matter accretion rate as the fraction of total accretion rate, $\dot{M}_Q = \delta \cdot \dot{M}$, we get the neutralization timescale of the maximally charged black hole as

$$t_{Q,\mathrm{acc.}} = \frac{4}{3} \frac{e^3 \, \epsilon \, m_{p,e}}{G^{1/2} \, c^3 \, \delta \, m_p m_e^2} \approx 2.5 \times 10^{-2} \left(\frac{m_{p,e}}{m_p} \right) \left(\frac{\epsilon}{\delta} \right) \mathrm{s}, \tag{1.13}$$

which is estimated for positive black hole charge. In case of negative charge, the timescale is $\approx$ 1835 times lower. Both ϵ and δ have values in the range $(0\,,\,1)$ and in many cases are of similar order of magnitude. This implies that in all astrophysically relevant settings any net charge on black hole would be neutralized relatively quickly unless there is a mechanism preventing the black hole from neutralization.

For a spinning black hole immersed into external stationary magnetic field it is easy to see from (1.7) and (1.9), that any local observer within the ergosphere can measure nonzero electric field component if magnetic field has nonvanishing poloidal component [20, 34, 35]. Black hole spin contributes to the Faraday induction generating the electrostatic potential A_t, which can be associated with induced electric field. The charging process is similar to the classical Faraday's homopolar generator. In case of the uniform external magnetic field, there exists the potential difference between event horizon and infinity taking the form

$$\Delta\phi = \phi_{\rm H} - \phi_{\infty} = \frac{Q - 2aMB}{2M},$$

which leads to the selective accretion into black hole until the potential difference vanishes. In that case the black hole acquires net charge $Q = 2aMB$. The process of charging of a black hole due to spin-induced effect in magnetic field takes place in any magnetic field configuration which shares the symmetry of background Kerr metric spacetime. On the other hand, chosen form of the field configuration may put restrictions on the dynamical timescales of the process of selective accretion due to following charge separation in a plasma. In general, the energy of charged test particle is given by $E = -P_\mu \xi^\mu_{(t)} = -(mu_\mu - qA_\mu)\xi^\mu_{(t)}$. Difference between electrostatic energy of a charged particle at the event horizon and at infinity is given by $E_H - E_\infty = qA_{t|r\to r_H} - qA_{t|r\to\infty} \equiv \delta$. For positive δ, more favourable is the accretion of particles with the sign of charge of q, while for negative δ, it is more likely to accrete particles with $-q$ sign of charge. In both cases this leads to the formation of the net black hole charge with a sign which depends on the orientation of magnetic field with respect to the rotational axis of a black hole [36]. For a magnetic field generated by the dynamics of co-rotating surrounding plasma matter the black hole's charge is more likely to be positive. In [4] it was shown that in realistic cases applied to the Galactic center black hole even a small charge of the black hole can have non-negligible effects on the observed bremsstrahlung emission profile. We would like to emphasize that the black hole charge plays a key role in the black hole energy extraction processes, such as Blandford-Znajek mechanism and magnetic Penrose process [3]. Discharge of induced electric field by oppositely charged accreting matter drives the rotational energy away from the black hole in both of the processes. We will discuss the prospects of charging in case of astrophysical candidates as well as the mechanisms of energy extraction associated with the black hole charge in Chapters 2 and 3, respectively.

However, in order to tap the gravitationally induced electrostatic energy from black hole and support particle acceleration, this electric field should not be screened as usually occurs in the presence of a plasma. In the past the problem has been widely discussed [37, 38] resulting with the Komissarov's theorem [39] which states that induced electric field of rotating black hole in magnetic field is not screened at least within ergosphere. Indeed, total screening of black hole's charge may occur only when the following two conditions are satisfied simultaneously

$$\vec{B} \cdot \vec{D} = 0, \quad B^2 - D^2 > 0, \tag{1.14}$$

where B and D are magnetic and electric field measured LNRO or ZAMO. It is easy to show that the relation $B^2 - D^2$ which is positive far away from black hole, is negative everywhere inside the ergosphere [1] [39]. Moreover the sign of this relation is independent of the strength of magnetic field being only dependent on the location. In other words, electric field is stronger for stronger magnetic field and within the ergosphere it cannot be screened off.

Black hole charge associated with gravitationally induced electric field has been estimated in [4] for the Galactic center supermassive black hole Sgr A*, with an upper limit of 10^{15}C. On the other hand, classical estimates of charge, based on the difference between thermal velocities and masses of electrons and protons in the fully ionized plasma around Sgr A*, imply the presence of equilibrium charge of the central body of order 10^{8}C. It therefore follows that black holes posses an electric charge in the range $10^{2} - 10^{12}$C per solar mass. This charge is gravitationally weak in a sense that its influence to the spacetime metric can be

[1] As for energy E, sign of $B^2 - D^2$ would dependent upon the location of observer whether inside or outside ergosphere. There could exist no static observer in ergosphere, it could at best be stationary with non-zero frame dragging angular velocity.

neglected. For it to be gravitationally significant would require charge of order $\sim 10^{20}$C per solar mass, and therefore, Kerr black hole hypothesis stands firm and valid. It is important to note that such a charge cannot be measured by imaging of black holes, based on the observations of their shadows. However, even such a small charge associated with the black hole has significant effects on the processes occurring in its neighbourhood, such as acceleration of charged particles to ultra-high energy.

1.3 Electromagnetic radiation reaction in curved spacetime

1.3.1 General approach

In many astrophysically relevant scenarios one cannot neglect the effects of radiation reaction due to the synchrotron radiation of charges in the vicinity of black holes, which are believed to be immersed into an external magnetic field. It is important to identify the conditions of stability of circular orbits in such regime. Detailed studies of charged particle dynamics around Schwarzschild and Kerr black holes in magnetic field neglecting radiation reaction were done by several authors, see, e.g. [40, 41, 36]. Qualitative and quantitative studies of synchrotron radiation reaction problem in curved background can be found e.g. in [42, 43] and in more recent papers [44, 2]. Equation of motion for a point charge in its most general form is usually referred as the DeWitt-Brehme equation [45, 46]. Resulting equation of motion of a charged particle in a curved spacetime reads [47]

$$\begin{aligned} \frac{Du^\mu}{d\tau} &= \frac{q}{m} F^\mu{}_\nu u^\nu + \frac{2q^2}{3m}\left(\frac{D^2u^\mu}{d\tau^2} + u^\mu u_\nu \frac{D^2u^\nu}{d\tau^2}\right) \\ &+ \frac{q^2}{3m}\left(R^\mu{}_\lambda u^\lambda + R^\nu{}_\lambda u_\nu u^\lambda u^\mu\right) + \frac{2q^2}{m}\, f^{\mu\nu}_{\text{tail}}\, u_\nu, \end{aligned} \tag{1.15}$$

where in the last term of Eq.(1.15) the tail integral is given by

$$f^{\mu\nu}_{\text{tail}} = \int_{-\infty}^{\tau-0^+} D^{[\mu} G^{\nu]}_{+\lambda'}\big(z(\tau), z(\tau')\big) u^{\lambda'} \, d\tau'. \tag{1.16}$$

Here u^μ is the four-velocity of the particle with charge q and mass m. The tensor of electromagnetic field is $F_{\mu\nu} = A_{\nu,\mu} - A_{\mu,\nu}$, where A_μ is the four-vector potential of external electromagnetic field. $R^\mu_{\ \nu}$ is the Ricci tensor, $G^\mu_{+\lambda'}$ is the retarded Green's function, and the integration is taken along the worldline of the particle z, i.e., $u^\mu(\tau) = dz^\mu(\tau)/d\tau$. The tail integral is calculated over the history of the charged particle, where primes indicate its prior positions. Other quantities in (1.15) are evaluated at the given position of the particle $z(\tau)$. The Ricci term is irrelevant, as it vanishes in the vacuum metrics, while the tail term can be neglected for elementary particles, as shown in [2] and references therein. In particular, for electrons the ratio of the "tail" force and the "gravitational" force at the horizon of a black hole of 10 solar masses is of the order of 10^{-19}. Since there are no any convincing evidences of the deviations of metrics of astrophysical black holes from vacuum Kerr solution, the motion of electrons and protons in the vicinity of astrophysical black holes can be well described by the covariant form of the Lorentz-Dirac equation. The Lorentz-Dirac equation contains the Schott term – the third order derivative of coordinate, which leads to the appearance of pre-accelerating solutions in the absence of external forces. However, one can effectively reduce the order of the equation by substituting the third order terms by derivatives of the external force. This is identical to imposing Dirac's asymptotic condition $\frac{Du^\mu}{d\tau}|_{\tau\to\infty} = 0$ [48]. Then, the resulting equation of motion reads

$$\frac{Du^\mu}{d\tau} = \frac{q}{m} F^\mu_{\ \nu} u^\nu + \frac{2q^2}{3m}\left(F^\alpha_{\ \beta;\mu} u^\beta u^\mu + \frac{q}{m}\left(F^\alpha_{\ \beta} F^\beta_{\ \mu} + F_{\mu\nu} F^\nu_{\ \sigma} u^\sigma u^\alpha\right) u^\mu\right),$$

where semicolon denotes the covariant coordinate derivative, given by

$$\frac{DF^\alpha_{\ \beta}}{dx^\mu} = \frac{\partial F^\alpha_{\ \beta}}{\partial x^\mu} + \Gamma^\alpha_{\mu\nu} F^\nu_{\ \beta} - \Gamma^\nu_{\beta\mu} F^\alpha_{\ \nu}. \tag{1.17}$$

The equation (1.17), which is usually called as Landau-Lifshitz equation [49], is a habitual second order differential equation which satisfies the principle of inertia and does not contain runaway solutions. Below we use this form of equation for the description of the motion of charged particles in magnetized black hole vicinity.

More details on the problem of electromagnetic radiation of point charged particles and related self-force can be found in e.g. [50, 42, 51, 52, 47, 53, 54, 55].

1.3.2 Synchrotron radiation around magnetized black hole

Computational ways of integration of dynamical equation (1.17) and corresponding analyses of trajectories were presented in [2]. In particular it was shown that for equatorial motion of a charged particle depending on the orientation of external Lorentz force, the final fate of the particle is either collapse to the black hole or stable circular orbit, i.e., the radiation reaction force leads to decay of any oscillations around equilibrium radius. Let us consider a purely circular motion of a charged particle revolving around black hole at the equatorial plane, in the presence of a uniform, or a dipole magnetic field. We will specify the components of the fields later.

If the radiation-reaction force is neglected, two components of generalized four-momentum $P_\alpha = mu_\alpha + qA_\alpha$ are conserved, namely energy and angular momentum of a particle. They can be associated with the Killing vectors in the form

$$-\mathcal{E} = \xi^\mu_{(t)} \frac{P_\mu}{m} = g_{tt}\frac{dt}{d\tau} + g_{t\phi}\frac{d\phi}{d\tau} + \frac{q}{m}A_t, \tag{1.18}$$

$$\mathcal{L} = \xi^\mu_{(\phi)} \frac{P_\mu}{m} = g_{\phi\phi}\frac{d\phi}{d\tau} + g_{t\phi}\frac{dt}{d\tau} + \frac{q}{m}A_\phi. \tag{1.19}$$

In this case the standard approach can be used (see, e.g. [36] and references therein).

The motion of charged particle in magnetic field is always bounded, which can be described by introducing the effective potential. In the equatorial motion it takes the form

$$V_{\text{eff}} = -\frac{q}{m}A_t - \frac{g_{t\phi}}{g_{\phi\phi}}(\mathcal{L} - \frac{q}{m}A_\phi) + \left[(-g_{tt} - \omega g_{t\phi})\left(\frac{(\mathcal{L} - \frac{q}{m}A_\phi)^2}{g_{\phi\phi}} + 1\right)\right]^{1/2}, \quad (1.20)$$

One sees that V_{eff} can attain both positive and negative values depending on the angular momentum, charge and location of the particle. Occurrence of negative energy orbits (NEOs) in the ergosphere is critical requirement for extraction of energy from rotating black holes. Presence of the term $-qA_t$ in the effective potential extends the region of existence of NEOs far beyond the ergosphere, while the last two terms in V_{eff} can be negative only within the ergosphere. In fact, the region with possible NEOs and thus, the energy extraction zone for charged test particles extends to infinity [56, 57]. Ergosphere is maximal in the equatorial plane, therefore we consider decay of a particle falling onto black hole in the equatorial plane.

In addition to energy and angular momentum and their conservation due to the Killing symmetries, the normalization condition $u^\alpha u_\alpha = -k$ must be satisfied for both charged and uncharged particles, where $k = 1$ for massive particle and $k = 0$ for massless particle. In the equatorial motion with the four-velocity $u^\alpha = u^t(1, v, 0, \Omega)$, where $v = dr/dt$ and $\Omega = d\phi/dt$ we get the angular velocity of a test particle with respect to the asymptotic observer at rest in the form

$$\begin{aligned}
\Omega &= \frac{1}{B}\left(-Cg_{t\phi} \pm \sqrt{u_t^2\left(Cg^2 - Ag_{rr}v^2\right)}\right), && (1.21)\\
B &= kg_{t\phi} + u_t^2 g_{\phi\phi}, \quad C = kg_{tt} + u_t^2, && (1.22)\\
g^2 &= g_{t\phi}^2 - g_{\phi\phi}g_{tt}, \quad u_t = -\left(\mathcal{E} + q/mA_t\right). && (1.23)
\end{aligned}$$

where the sign defines the co or counter rotation with respect to LNRO. The limit of u^α tending to a null vector gives the restrictions to the angular velocity of a particle (both charged and uncharged) surrounding black hole in the form [58]

$$\Omega_- \leq \Omega \leq \Omega_+, \quad \Omega_\pm = \frac{1}{g_{\phi\phi}}\left(-g_{t\phi} \pm \sqrt{g_{t\phi}^2 - g_{tt}g_{\phi\phi}}\right). \quad (1.24)$$

The evolutions of specific energy $\mathcal{E}$ and specific angular momentum $\mathcal{L}$ of charged particle in Schwarzschild black hole spacetime in the case of uniform magnetic field take the following form

$$\begin{aligned}
\frac{d\mathcal{E}}{d\tau} &= -4k\mathcal{B}^2\mathcal{E}^3 + 2k\mathcal{B}\mathcal{E}\left(2\mathcal{B}f + \frac{u^\phi}{r}\right), && (1.25)\\
\frac{d\mathcal{L}}{d\tau} &= 4\mathcal{B}^2 k u^\phi \left(f^2(u^t)^2 - f\right) - 2u^r u^\phi \left(r - 4\mathcal{B}^2 k^2\right) + 2r\mathcal{B}u^r, && (1.26)\\
\mathcal{B} &= \frac{qGBM}{mc^4}, && (1.27)
\end{aligned}$$

where $f = 1 - 2M/r$ and $k = 2q^2/(3m)$, and q, m are mass and charge of test particle. For ultrarelativistic charged particle ($\mathcal{E} \gg 1$, or $\mathcal{B} \gg 1$). the leading contribution for energy loss is the first term on the right hand side of Eq.(1.25). Inserting all constants, the cooling timescale of charged particle is given by

$$\tau_{\rm cooling} \approx \left(1 - \frac{2\,GM}{r\,c^2}\right)^{-1} \frac{3\,m^3c^5}{2\,q^4B^2}. \quad (1.28)$$

In this case the Lorentz force is dominant over gravitational "force" which happens in realistic settings as discussed above Eq.(1.6). Closer to black hole the cooling timescale increases. In Tab.1.1 we give typical cooling timescales of electrons, proton and fully ionized iron nuclei for various values of magnetic field. Due to cubic dependence on mass, electrons cool 10^{10} times faster than protons. One can compare the cooling timescale with an orbital timescales of particles at ISCO $\tau_{\rm orb} \approx 4\pi r_{\rm isco}/c$, which is of order of $\sim 10^{-3}$s for non-rotating stellar mass black holes or $\sim 10^5$s for supermassive black holes. Thus, the energy loss can be quite relevant especially in case of lighter particles, such as electrons.

Oscillatory motion of charged particles and related circular orbits in magnetized Schwarzschild black hole spacetime were studied by [40, 41], in magnetized Kerr spacetime by [59, 36, 60], in magnetized "Ernst" metric by [61], as well as in other papers, e.g. [62, 63, 64, 65, 66]. Resonant phenomena were extensively discussed in [67]. It is well known that small perturbations of circular orbits from

B (Gauss)	τ_e (s)	τ_p (s)	$\tau_{\rm Fe}$ (s)
10^{12}	10^{-16}	10^{-6}	10^{-5}
10^{8}	10^{-8}	10^{2}	10^{3}
10^{4}	1	10^{10}	10^{11}
1	10^{8}	10^{18}	10^{19}
10^{-4}	10^{16}	10^{26}	10^{27}

Table 1.1: Typical cooling times of electrons τ_e, protons τ_p and fully ionized iron nucleus $\tau_{\rm Fe}$ for various values of magnetic field strength B.

equilibrium positions lead to the appearance of quasi-harmonic oscillations. However such oscillations will decay in relatively short timescales due to synchrotron radiation [44, 2]. This implies that particle's energy at the circular orbit under influence of the radiation reaction force is always located at the minimum of the effective potential. The radiation reaction force in the locally geodesic frame of reference is aligned against the direction of the motion of the charged particle, concentrating along the motion at a narrow cone. This statement implies that the radiation reaction in fact reduces the velocity of a particle and corresponding kinetic energy. On the other hand, if the motion is stable due to balance of the gravitational and Lorentz forces, reducing the angular velocity of the particle causes the widening of its circular orbit. Such widening leads to increase of particle's energy and angular momentum measured by observer at rest at infinity, while the energy of the particle in the particle's frame always decreases. Below we examine the orbital widening effect for magnetic fields of uniform and dipole configurations.

1.3.3 Effect of orbital widening

Orbital widening in uniform magnetic field

Radiation reaction acting on a charged particle moving at a stable circular orbit of a magnetized black hole can lead to the shift of the orbital radius outwards from the black hole. The effect causes increase of the energy and angular momentum of the particle measured by an observer at rest at infinity. In this note we show that "widening" of such orbits is independent of the field configuration, however, it appears only in the cases with the external Lorentz force acting outwards from the black hole. This condition corresponds to $qLB > 0$, where q and L are the charge and angular momentum of the particle and B is intensity of the external magnetic field. As examples of the orbital widening we consider two scenarios with an external homogeneous magnetic field and a magnetic dipole field generated by a current loop around a Schwarzschild black hole. We show that the orbital widening is accompanied by quasi-harmonic oscillations of the particle which are considerably large in the magnetic dipole fields. We also estimate the timescales of orbital widening from which it follows that the effect can be relevant in the vicinity of stellar mass black holes.

It has been pointed out in [2] that one of the consequences of the synchrotron self-force in the vicinity of a black hole, and in presence of an external magnetic field, is the evolution of the circular orbits of charged particles during the radiation process and shifting of the radius of the circular orbits outwards from the black hole. This can be realized for repulsive Lorentz force only, while in attractive case, the particle spirals down to the black hole and no closed circular orbits can be formed. In this section we investigate the effect of widening of the stable circular orbit of charged particle undergoing radiation reaction force around a Schwarzschild black hole immersed in a uniform, or a dipole, magnetic field. The effect is considerable, if the radiation reaction cannot be neglected and appears, as we show, due to the diversity in the dependencies of the kinetic and potential energies of a charged particle on the radius of its orbit. Although the kinetic energy of the particle decreases due to the synchrotron radiation, its potential energy increases faster, due to the widening of the orbit. In fact, the self-force decreases the components of four-velocity of the particle with a rate proportional to the derivative of the field. If the stability of the orbit is guaranteed by the location of the particle at the minimum of the effective potential, the energy of the particle measured at infinity can start to increase.

Moreover, the orbital widening leads to appearance of quasi-harmonic oscillations of charged particles with amplitudes increasing with increasing energy of the particle.

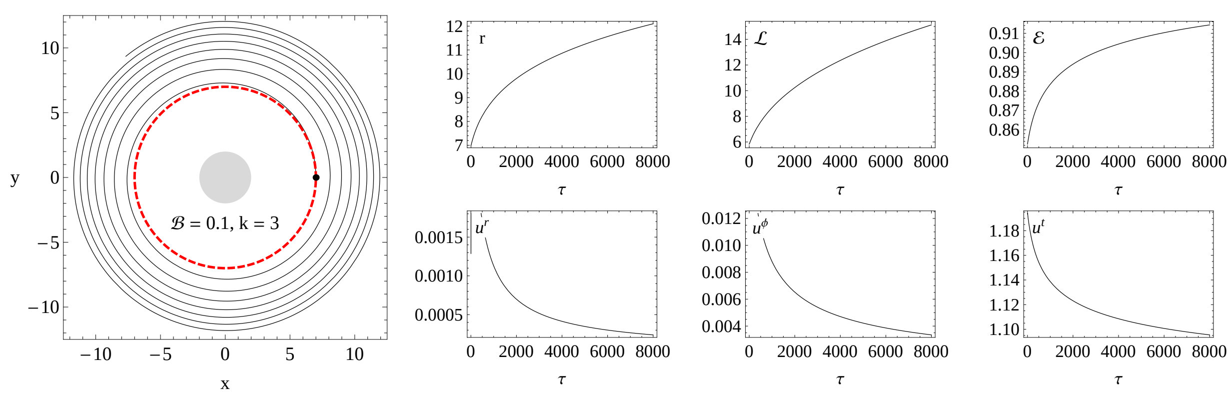

Figure 1.1: Radiative widening of circular orbit of a charged particle around black hole in uniform magnetic field and corresponding evolutions of orbital radius, angular momentum, energy and different components of velocity of the particle. Starting point on the trajectory is indicated by black dot. The trajectory without radiation is shown by dashed red circle.

Let the black hole is immersed into an asymptotically homogeneous magnetic field which has the strength B at spatial infinity. The field is aligned perpendicularly to the equatorial plane coinciding with the plane of the motion of the charged particles. The corresponding solution of Maxwell's equations in the Schwarzschild spacetime implies the existence of only nonzero covariant component of four-vector

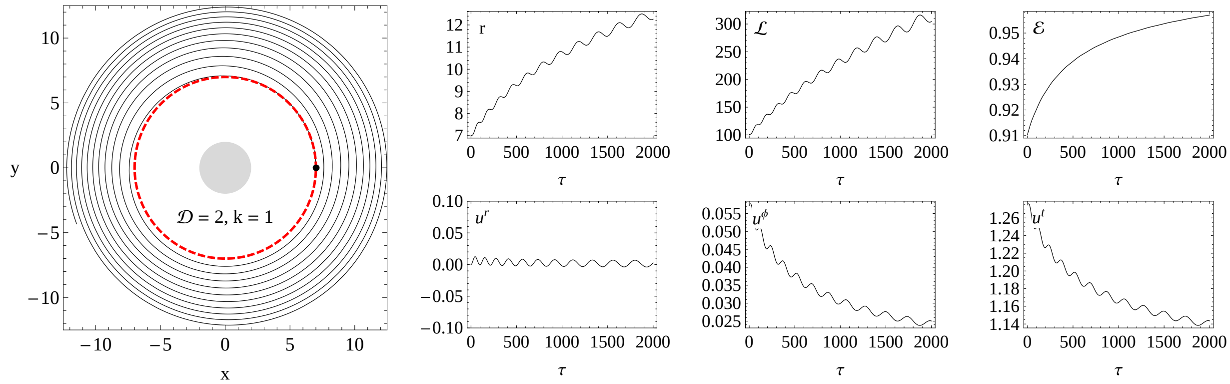

Figure 1.2: Same as in Fig.1.1 for magnetic dipole field case.

potential A^μ [20]

$$A_\phi^{\mathrm{U}} = \frac{B}{2} r^2 \sin^2\theta. \tag{1.29}$$

Dynamics and corresponding oscillatory motion of charged particles in the absence of radiation reaction force in the magnetized Schwarzschild spacetime can be found in [41] and magnetized Kerr spacetime in [68, 60]. Let us introduce two dimensionless parameters characterizing the influences of magnetic field and radiation reaction force in the black hole vicinity as follows

$$\mathcal{B} = \frac{qBM}{2m}, \quad k = \frac{2\,q^2}{3mM}, \tag{1.30}$$

where q and m are charge and mass of a test particle and M is the black hole mass.

The rate of the energy loss of a charged particle can be calculated directly from the time component of the equation of motion (1.17). Skipping over details, one can write [2]

$$\frac{d\mathcal{E}}{d\tau} = -\mathcal{K}_1\mathcal{E}^3 + \mathcal{K}_2\mathcal{E}x(\tau), \tag{1.31}$$

where $\mathcal{K}_1 = 4k\mathcal{B}^2$ and $\mathcal{K}_2 = 2k\mathcal{B}$ are constants and $x(\tau) = 2k\mathcal{B}f(\tau) + u^\phi(\tau)/r(\tau)$. The analytical solution of equation (1.31) can be found in the form

$$\mathcal{E}(\tau) = \frac{\mathcal{E}_i e^{\mathcal{K}_2 X(\tau)}}{\left(1 + 2\mathcal{K}_1\mathcal{E}_i^2 \int_0^\tau e^{2\mathcal{K}_2 X(\tau')} d\tau'\right)^{\frac{1}{2}}}, \tag{1.32}$$

where $X(\tau) = \int_0^\tau x(\tau) d\tau$.We solve the equation (1.31) numerically and illustrate the results in representative plots for the particular set of initial conditions.

When the orbital radius r increases faster than the deceleration of velocities u^t and u^ϕ, the energy $\mathcal{E}$ and angular momentum $\mathcal{L}$ of the charged particle increase accordingly. Example of the orbital widening of radiating charged particle around Schwarzschild black hole in uniform magnetic field is illustrated in Fig.1.1. Corresponding changes of the orbital radii in time are given in the $r - \tau$ plot. If the external Lorentz force is attractive, which corresponds to $(\mathcal{L} \cdot \mathcal{B} < 0)$, the charged particle collapses to the black hole. In the opposite case, the particle slows down due to radiation reaction while keeping the circular character of the motion. Decrease of particle's velocity u^ϕ in stable motion shifts the particle outwards from the black hole. The $\mathcal{E} - \tau$ plot shows the corresponding increase of particle's energy measured by an observer at rest at infinity, which is in fact the potential energy of the particle, while kinetic energy given by $m\gamma = mu^t$ decreases as the particle slows down due to radiation, as represented in the $u^t - \tau$ plot. The energy of the particle asymptotically tends to its rest energy $\mathcal{E}_{|\tau\to\infty} = 1$. If the radiation reaction can be neglected, the trajectory of a particle is circular as indicated by the red dashed circle. Note that the orbital widening can be observed when the energy of a charged particle $\mathcal{E} < 1$, i.e. when the motion of the particle is bounded in the vicinity of a black hole. For ultrarelativistic particles with $\mathcal{E} \gg 1$ the leading contribution to the evolution of energy is given by the first term on the right hand side of Eq.(1.31), leading to the loss of particle's energy.

Orbital widening in a magnetic dipole field

Dipole magnetic field can be generated by circular current loop with radius $R \geq 2M$, located on the surface of a compact object in the equatorial plane. Outer solution for the electromagnetic 4-vector potential A^μ in the Schwarzschild metric is given by only nonzero covariant component [30]

$$A_\phi^{\rm D} = -\frac{3}{8}\frac{\mu r^2 \sin^2\theta}{M^3}\left[\ln\left(1-\frac{2M}{r}\right) + \frac{2M}{r}\left(1+\frac{M}{r}\right)\right], \tag{1.33}$$

where $\mu = \pi R^2 (1-2M/R)^{1/2} I$ is the magnetic dipole moment and I is electric current of the loop. The term in square brackets is negative for $r > 2M$. One can parametrize the dynamical equations of charged particles by introducing the relative influence of the dipole magnetic field and the gravitational force as follows

$$\mathcal{D} = \frac{3|q|\mu G}{8mM^2c^4}. \tag{1.34}$$

As in the case of the uniform field, for the motion at the equatorial plane one can distinguish two different situations depending on the orientation of the Lorentz force. The widening of the circular orbit occurs only when the Lorentz force is repulsive, i.e. for chosen parametrization, the condition reads $\mathcal{L}\cdot\mathcal{D} > 0$, thus the angular momentum and the magnetic dipole parameters have the same sign. The representative example of orbital widening in the magnetic dipole field is plotted in Fig.1.2. In the absence of radiation reaction the orbit is purely circular, as in case of uniform magnetic field. The distinguishing signature of orbital widening in magnetic dipole case is the presence of radial oscillations due to radiation reaction. Anisotropy of the field lines increases the non-linearity of dynamical equations which in the magnetic dipole case can lead to the appearance of quasi-harmonic oscillations of charged particles. The radiation reaction in this case plays a role of small perturbation to the orbit and appearance of a perihelion shift.

1.4 Conclusions

In this chapter we have discussed the prospects for "electromagnetization" of astrophysical black holes and discussed the fundamental property of black hole candidates – the Kerr black hole hypothesis. Based on the recent achievements of modern observational techniques, any black hole candidate can be considered as a Kerr black hole immersed into external magnetic field with induced electric charge. This leads to several new consequences, which are the subjects of current dissertation.

We have shown that the radiation reaction force can shift the circular orbits of charged particles outwards from the black hole. This effect occurs only in the case with repulsive Lorentz force, while for opposite orientation the particle spirals down to the black hole. If the stability of the circular orbit is conserved, the radiation reaction acting opposite to the motion of the particle decreases its linear velocity. This in turn leads to the orbital widening which we demonstrated in plots. Actual escape of the charged particle from the black hole in the equatorial plane fixed by magnetic field implies that the potential energy of the charged particle increases while the kinetic energy always decreases. Let us estimate the formal maximal efficiency of the gain of potential energy due to orbital widening for the shift of the circular orbit from ISCO to infinity. Defined as the ratio between gained energy to the final energy at infinity ($E_\infty = mc^2$), the efficiency depends on the position of ISCO, which is a function of the magnetic field strength for the charged particles [41]. Since the ISCO of a charged particle can be located very close to the event horizon, the maximal efficiency can reach the values up to 100%. However, 100% efficiency is unreachable, since it would require the ISCO to be located at the black hole horizon and $\mathcal{B}, \mathcal{D} \to \infty$. In the absence of magnetic fields, the formal efficiency of the inverse mechanical process of shifting the particle orbit from infinity to the ISCO is 5.7%. One needs to note that in realistic scenarios the effect of radiative widening of orbits is many orders of magnitude slower than the orbital timescales. However, in some astrophysical scenarios with large magnetic fields this effect can be potentially relevant.

Orbital widening accompanied by the increase of the potential energy of charged particle is governed by the second term on the right hand side of Eq.(1.31), in the case of uniform magnetic field, while the first term governs the decay of the particle's oscillations around stable circular orbit. When the decay of oscillations is irrelevant, i.e., when the particle is located at the stable circular orbit, one can find the timescale of the orbital widening in the form

$$\tau_{\mathrm{W}} \approx \frac{1}{2k\mathcal{B}} \ln \left| \frac{E}{E_0} \right| , \tag{1.35}$$

where E_0 and E are the initial and final energies of the charged particle. Note that all quantities in Eq.(1.35) are dimensionless. Inserting back the physical constants we get

$$\tau_{\mathrm{W}} = \frac{3m^2MGc}{4q^3B} \ln \left| \frac{E}{E_0} \right| , \tag{1.36}$$

where all quantities are given in Gaussian units. For an electron orbiting a stellar mass black hole one can estimate the widening timescale as follows

$$\tau_{\mathrm{W}} \approx 10^3 \left(\frac{q}{e}\right)^{-3} \left(\frac{m}{m_e}\right)^2 \left(\frac{M}{10M_\odot}\right) \left(\frac{B}{10^8\mathrm{G}}\right)^{-1} \mathrm{s}. \tag{1.37}$$

Here we assumed $\ln|E/E_0| \sim 1$, which is well justified by previous studies, see, e.g. [41]. One can conclude that the effect of the orbital widening can be relevant in stellar mass black holes and relatively weak in supermassive black holes. More precise calculation of widening timescales can be done by numerical integration of the equations of motion for a particular set of initial conditions.

Another interesting consequence of the orbital widening caused by the radiation reaction force is the appearance of the quasi-harmonic oscillations of charged particle which is a special signature of the presence of a dipole magnetic field. One of the important extensions of our work could be comparison of the frequencies of such oscillations in both radial and vertical modes with mysterious frequencies of the quasi-periodic oscillations observed in many miqroquasars containing black holes or neutron stars.

Chapter II

Supermassive black hole at the center of the Milky Way

2.1 Relativistic environment of the Galactic center

The central region of our Milky Way is extremely active. It harbours the closest galactic nucleus that is accessible to us allowing us to study it in fine detail. Most recent results obtained with state of the art instruments provide sensitive measurements at their highest angular resolution. The central star cluster harbours a small cusp of high velocity mostly young and dusty stars that are in orbit around the 4 million solar mass super massive black hole (SMBH) Sagittarius A* (Sgr A*). Molecular and atomic gas is streaming towards this region in the form of a spiral connecting it to the Circum Nuclear Ring. Using the Large Atacama Millimeter Array (ALMA) the kinematics and composition of this material have been investigated in detail, highlighting signatures of star formation and the interaction with a wind emerging form the direction of SgrA*. Using results from the Very Large Telescope (VLT) we will highlight the dynamics of the ultra-fast stars, hot-spots and present theories on their origin with an account on importance of electromagnetic interactions. The interaction of plasma with Sgr A* reveals that matter is orbiting and is being accreted onto the SMBH to produce powerful flares. These are detectable all across the electromagnetic spectrum and help us to understand the region close to the event horizon of Sgr A* which is currently under investigation using the Event Horizon Telescope (EHT).

Sgr A* at the center of the Milky Way is the supermassive black hole that is most suited for a determination of its fundamental properties. The most recent results on it's mass and distance are the following: $R_{\rm SgrA*} = 8.12 \pm 0.03$kpc and $M_{\rm SgrA*} = 4.11 \pm 0.03 \times 10^6 M_\odot$, corresponding to relative uncertainties in these quantities of about 0.4% and 0.7%. Spin values of above $0.5M$ are suggested but the model dependent determination is not yet very conclusive. Models suggest that the spin vector is orientated towards the East and inclined towards the observer at an appreciable angle. Below we derive constraints on the charge of a Sgr A* from both theoretical and observational prospects.

The observations of the Galactic centre across the electromagnetic spectrum, ranging from radio to gamma wavelengths, revealed the complex structure of the Nuclear Star Cluster (NSC) as well as that of the gaseous-dusty medium of the central parsec [69, 70]. The presence of the concentrated, dark mass at the dynamical centre of the NSC was revealed by the near-infrared observations of stars using adaptive optics. The first proof for the compact dark single object in the Galactic centre came with the detection and the analysis of the first proper motion of stars orbiting Sgr A* inside $1'' \sim 0.04\,$pc, so-called S stars [71, 72]. Based on these and follow-up observations [73, 74, 75, 17], the large mass of the dark object has been confirmed and a more precise value has been determined, $M \sim (4.11 \pm 0.03) \times 10^6\, M_\odot$ [74]. If we associate this dark mass with a non-rotating black hole for simplicity, this yields a Schwarzschild radius of $R_{\rm Schw} = 1.2 \times 10^{12}\,{\rm cm}(M_\bullet/4 \times 10^6\, M_\odot)$ and the expected mean density is,

$$\rho_\bullet = 1.7 \times 10^{25} \left(\frac{M_\bullet}{4 \times 10^6\, M_\odot}\right) \left(\frac{R_{\rm Schw}}{3.9 \times 10^{-7}\,{\rm pc}}\right)^{-3} M_\odot {\rm pc}^{-3}\,. \tag{2.1}$$

In case of stellar orbits, the tightest constraint for the density of the dark mass comes from the monitoring of B-type star S2 with the pericentre distance of $r_{\rm P} \simeq 5.8 \times 10^{-4}\,{\rm pc}$ [74, 75, 17]

$$\rho_{\rm S2} = 5.2 \times 10^{15} \left(\frac{M_\bullet}{4.3 \times 10^6\,M_\odot}\right)\left(\frac{r_{\rm P}}{5.8 \times 10^{-4}\,{\rm pc}}\right)^{-3} M_\odot {\rm pc}^{-3}\,. \tag{2.2}$$

The most stringent density constraint was given by 3σ VLBI source size of $\sim 37\mu$as [76]. When combined with the lower limit on the mass $M_{\rm SgrA*} \gtrsim 4\times10^5\,M_\odot$ based on the proper motion measurements [77], VLBI yields the lower limit of $\rho_{\rm SgrA*} \geq 9.3 \times 10^{22}\,M_\odot{\rm pc}^{-3}$. This is about two orders of magnitude less than the density expected for a black hole of $\sim 4 \times 10^6\,M_\odot$, see Eq. (2.1). The most plausible stable configuration that can explain such a large concentration of mass emerges within the framework of general relativity: a singularity surrounded by an event horizon – a black hole, ruling out most of the alternatives [70].

According to the uniqueness or the general relativistic “no-hair" theorem, any stationary black hole is fully characterized by only three classical and externally observable quantities: mass $M_\bullet$, angular momentum $J_\bullet$ (often the quantity $a_\bullet = J_\bullet/M_\bullet c$ is used which has a dimension of length), and the electric charge $Q_\bullet$[1]. Thanks to the high-precision observations of stars in the Nuclear Star Cluster, including the innermost S cluster, the current value for the SMBH mass is $M_\bullet = (4.3 \pm 0.3) \times 10^6\,M_\odot$ [70], which is based on different methods, primarily the orbits of S stars [74], the Jeans modelling of the properties of the NSC [78], and the general relativistic fits to the double-peaked X-ray flares that show signs of gravitational lensing [79]. The constraints for the spin $J_\bullet$ were inferred indirectly based on the variable total and polarized NIR emission [80]. The spin can be determined based on the modelling of spin-dependent quantities, mainly the light curves of a hot spot or a jet base. In this way, [81] obtained constraints for the

[1] In case a magnetic monopole could exist, it could be the forth parameter.

spin, which are rather weak and the spin parameter is $a_\bullet \gtrsim 0.4$, as well as the inclination, which is inferred based on the stable polarization angle of the flares and tends to be rather large $i \gtrsim 35°$. The value of the spin parameter determined based on quasi-periodic oscillations for Sgr A* reaches a unique value of ≈ 0.44 [82], which is consistent with the value inferred from the fitting of the NIR flares.

2.2 Constraining the charge of the Galactic centre black hole

In general, the charge of the black hole $Q_\bullet$ is often set equal to zero due to the presence of plasma around astrophysical black holes. However, a black hole can acquire primordial charge because it was formed by a collapse of a charged (compact) star [83]. It is not clear on which timescales such a charged black hole discharges or alternatively, can increase its charge. Also, from an astrophysical point of view, it is of a general interest if a charged black hole can be observationally distinguished from a non-charged case, clearly depending on the value of the charge.

In addition, electric charge can be loaded or induced by black hole due to its rotation in external magnetic field within the mechanism similar to the Faraday unipolar generator. Such a mechanism is more relevant for supermassive black holes in the local Universe, since the primordial charge information is expected to be lost. The induction mechanism works in such a way that the rotation of a black hole generates electric potential between horizon and infinity which leads to the process of selective accretion of charged particles of plasma surrounding the black hole. In particular, a rotating black hole embedded in a uniform, aligned magnetic field will acquire an electric charge until an equilibrium value is reached $Q_{\bullet,W} = 2B_0 J_\bullet$, a so-called Wald charge [20], where B_0 is an asymptotic magnetic field strength. There is an evidence that significant and highly aligned magnetic field must be present in the Galactic center with equipartition strength of 10 G in the vicinity of the event horizon of the SMBH [84, 85, 23].

The twisting of magnetic field lines threading the horizon of rotating black hole produces an electric field which accelerates the charged particles along the magnetic field lines. Moreover, magnetic field plays the role of a catalyzing element that allows the extraction of rotational energy from rotating black hole through interaction of charged particles with an induced electric field in such processes as the Blandford-Znajek mechanism [86] and the magnetic Penrose process [87]. Both of these processes that allow the energy extraction from rotating black holes require the presence of an induced electric field [3].

Even a small charge associated with the black hole can have considerable effects on the electromagnetic processes in its vicinity, such as the bremsstrahlung emission and the motion of charged particles as we will show. The value of this small electric charge for black holes embedded in plasma will be necessarily temporary and fluctuating, mainly due to the attraction of oppositely charged particles and/or the variability of the magnetic field in which the black hole is immersed. Even for an extreme case of a charged black hole in vacuum, a spontaneous loss of charge would occur due to pair production with an exponential time-dependency [88].

In this section, we revisit the question of a charge, mainly of an electric origin, associated with the Galactic centre SMBH. Previously, several theoretical studies have focused on the spacetime structure of charged black holes [89, 90]. Here we are aiming at the connection between the current theoretical knowledge with a real astrophysical case – Sgr A* supermassive black hole, for which we gathered most constraints on its nearby plasma environment [70] – in order to put realistic constraints on electric charge of our nearest supermassive black hole.

2.2.1 Prospects for charging SgrA* and charge limits

Based on the analysis of surface brightness profiles in soft X-ray bands, there is an evidence for hot extended plasma, which surrounds the compact radio source Sgr A* [91, 92, 93]. In addition, observations of polarized emission show that a relatively strong magnetic field is present in the Central Molecular Zone, which exhibits a highly ordered configuration [23]. The large-scale ordered magnetic field as well as the ionized, extended gas surrounding Sgr A* in the central region can be used to put constraints on the charge of the SMBH at the Galactic Centre, which has not been done properly before for any black hole candidate. The decreasing surface brightness profile is satisfactorily fitted by thermal bremsstrahlung [93]. The plasma is dynamically modelled in the framework of hot accretion flows, obtaining the temperature of $k_{\mathrm{B}}T_{\mathrm{e}} = 1$, 2, and 3.5 keV ($T_{\mathrm{e}} = (11.6{-}40.6)\times 10^{6}\,\mathrm{K}$) at the outer radius of the flow, using either the radiatively inefficient accretion flow (RIAF) model [92], outflows of stars [91], or the classical Bondi accetion flow [93], respectively. Although several models are consistent with the observed surface brightness of plasma, both the RIAF and the Bondi accretion, which occur within the Nuclear Star Cluster, are expected to have a stagnation radius R_{stag} which divides the matter flowing in towards the SMBH and the outflowing gas [94]. In Fig. 2.1, we illustrate the basic set-up, including the inflow, outflow region, and the stagnation radius.

Magnetic field properties

There is an observational evidence for the highly ordered structure of the magnetic field in the central regions of the Galaxy [23]. Two configurations were inferred from the observations of the polarized emission: a toroidal magnetic field associated with denser molecular clouds that is parallel with the Galactic plane and a poloidal field in the diluted intercloud region approximately perpendicular

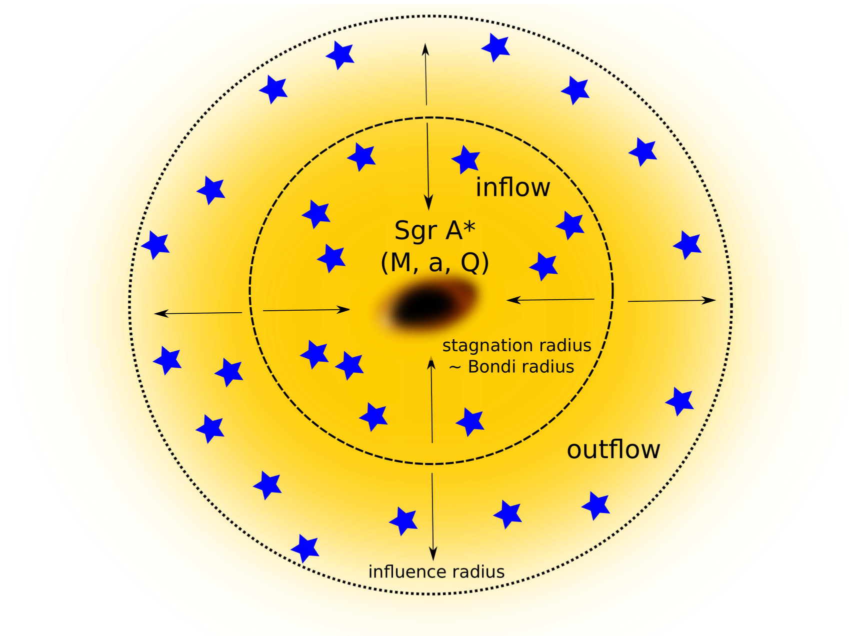

Figure 2.1: Illustration of the basic set-up at the Galactic centre: a supermassive black hole characterized by mass $M_\bullet$, spin $a_\bullet$, and an electric charge $Q_\bullet$ surrounded by a Nuclear star cluster and hot plasma emitting thermal bremsstrahlung. The dark area at the centre illustrates the shadow the black hole casts, which can be non-spherical due to the black hole rotation and the viewing angle. The inner circle denotes the stagnation radius, which is approximately equal to the Bondi radius, inside which the gas inflow towards the black hole takes place. The outer circle represents the sphere of gravitational influence of the supermassive black hole, inside which its potential prevails over the stellar cluster potential.

to the Galactic plane, which is also manifested by non-thermal radio filaments. The poloidal field in the intercloud region has magnitudes of $\sim 10\,\mu$G (close to the equipartition value with cosmic rays), and it reaches $\sim 1\,$mG in thin non-thermal filaments. The magnetic field in dense clouds has a toroidal geometry and it reaches the value of $\sim 1\,$mG [95].

Closer to Sgr A*, [85] inferred the lower limit of magnetic field strength along the line of sight, $B \gtrsim 8\,$mG, based on the Faraday rotation of the polarized emission of magnetar PSR J1745-2900, which is located at the deprojected distance of $r \gtrsim 0.12\,$pc. In addition, they confirmed an ordered configuration of the magnetic field threading the hot plasma. Inside the stagnation radius, hot and magnetized plasma descends towards Sgr A* and in this direction, an increase in the plasma density as well as in the magnetic field intensity is necessary. To explain the synchrotron emission of flares on the event-horizon scales, a magnetic field of the order of ~ 10–$100\,\mathrm{G}$ is required [96, 97, 98, 84]. A simple scaling $B \propto r^{-1}$ is generally consistent with the increase from the Bondi-radius scales up to the event horizon.

Plasma properties

The inflow of plasma effectively takes place inside the Bondi radius, which gives the range of influence of the SMBH on the hot plasma,

$$R_{\mathrm{B}} \approx 0.125 \left(\frac{M_{\bullet}}{4\times 10^{6}\,M_{\odot}}\right)\left(\frac{T_{\mathrm{e}}}{10^{7}\,\mathrm{K}}\right)^{-1}\left(\frac{\mu_{\mathrm{HII}}}{0.5}\right)\,\mathrm{pc}\,, \tag{2.3}$$

where we assumed a fully ionized hydrogen plasma with the mean molecular weight of $\mu_{\mathrm{HII}} = 0.5$ [99]. This assumption is supported by the observation of hot, ionized gas in the central arcsecond [93]. In addition, at the inferred temperature of several keV and the number density of the order of $10\,\mathrm{cm}^{-3}$ at the Bondi radius [100], the ionization fraction of hydrogen atoms is basically unity according to the Saha equation, $(1-\chi)/\chi^2 \simeq 4.14\times 10^{-16} n_{\mathrm{tot}} T_{\mathrm{g}}^{-3/2} \exp\left(1.58\times 10^{3}\,\mathrm{K}/T_{\mathrm{g}}\right)$, where $\chi \equiv n_{\mathrm{i}}/n_{\mathrm{tot}}$ is the ionization fraction of the gas with the total gas number density of n_{tot} and temperature of T_{g}. However, during the past high-luminosity states of Sgr A* thermal instability could have operated in the inner parsec, creating the multi-phase environment where hot and cold phases could coexist [101]. In addition, observations at millimeter wavelengths show the presence of both ionized and neutral/molecular medium in this region [102] (the denser and colder region is referred to as the minispiral). In the following, we will focus on the hot ionized phase, which is expected to dominate inside the Bondi radius.

Plasma in the Galactic centre region is so hot inside the Bondi radius that it may be considered weakly coupled. This is easily shown by the coupling ratio R_{c}

of the mean potential energy of particles and their kinetic energy,

$$R_{\rm c} = \frac{E_{\rm p}}{E_{\rm k}} \sim \frac{e^2 (L_{\rm i} 4\pi\epsilon_0)^{-1}}{k_{\rm B} T_{\rm e}} = \frac{e^2 n_{\rm p}^{1/3} (4\pi\epsilon_0)^{-1}}{k_{\rm B} T_{\rm e}}\,, \tag{2.4}$$

where $L_{\rm i}$ is the mean interparticle distance, $L_{\rm i} = n_{\rm p}^{-1/3}$, where $n_{\rm p}$ is the particle density. For the typical (electron) particle density at the Bondi radius $n_{\rm p} \approx n_{\rm e} \approx 10\,{\rm cm}^{-3}$ and the electron temperature of $k_{\rm B} T_{\rm e} \sim 1\,{\rm keV}$ [100, 92] as inferred from Chandra observations, we get $R_{\rm c} \approx 3 \times 10^{-10}$, i.e. the Galactic centre plasma is very weakly-coupled.

The Bondi radius of the accretion flow in the Galactic centre is thus well inside the sphere of influence of the SMBH, which represents the length-scale on which the potential of the SMBH prevails over the stellar cluster potential. For the Galactic centre SMBH and the averaged one-dimensional stellar velocity dispersion of $\sigma_\star \approx 100\,{\rm km\,s^{-1}}$, we get [103],

$$R_{\rm inf} \simeq GM_\bullet/\sigma_\star^2 = 1.7 \left(\frac{M_\bullet}{4\times 10^6\,M_\odot}\right) \left(\frac{\sigma_\star}{100\,{\rm km\,s^{-1}}}\right)^{-2} {\rm pc}\,. \tag{2.5}$$

When considering a one-dimensional steady-state inflow-outflow structure of the gas in the vicinity of a galactic nucleus, a characteristic feature is the existence of the stagnation radius $R_{\rm stag}$, where the radial velocity passes through zero [103]. Stellar winds inside the stagnation radius flow towards the black hole and a fraction of the matter is accreted, while the matter outside it forms an outflow, which is illustrated in Fig. 2.1. For the case when the heating rate due to fast outflows $v_{\rm w}$ is larger than the stellar velocity dispersion $\sigma_\star$, $v_{\rm w} \gg \sigma_\star$, the stagnation radius can be approximately expressed as [103],

$$\begin{aligned} R_{\rm stag} &\approx \left(\frac{13+8\Gamma}{4+2\Gamma} - \frac{3\nu}{2+\Gamma}\right) \frac{GM_\bullet}{\nu v_{\rm w}^2} \\ &\approx \begin{cases} 0.30\,\left(\frac{M_\bullet}{4\times10^6\,M_\odot}\right)\left(\frac{v_{\rm w}}{500\,{\rm km\,s^{-1}}}\right)^{-2}\,{\rm pc} & ,\,{\rm core}\ \ (\Gamma = 0.1)\,, \\ 0.16\,\left(\frac{M_\bullet}{4\times10^6\,M_\odot}\right)\left(\frac{v_{\rm w}}{500\,{\rm km\,s^{-1}}}\right)^{-2}\,{\rm pc} & ,\,{\rm cusp}\ \ (\Gamma = 0.8)\,, \end{cases} \end{aligned} \tag{2.6}$$

where Γ is the inner power-law slope of the stellar brightness profile, where we consider two limiting cases, the core profile with $\Gamma = 0.1$ and the cusp profile with $\Gamma = 0.8$. The quantity $\nu = -\mathrm{d}\rho/\mathrm{d}r|_{\mathrm{R_{stag}}}$ is the gas density power-law slope at R_{Stag}, which according to the numerical analysis of [103] is $\nu \approx 1/6[(4\Gamma + 3)]$. According to the estimates in Eq. (2.6), the stagnation radius is expected to be nearly coincident with the Bondi radius with an offset given by the factor [103]

$$\frac{R_{\mathrm{Stag}}}{R_{\mathrm{B}}} \approx \frac{13 + 8\Gamma}{(2 + \Gamma)(3 + 4\Gamma)}\,, \tag{2.7}$$

which is of the order of unity.

In the further analysis and estimates, we consider the dynamical model of [93], who fitted the thermal bremsstrahlung emission of the hot plasma with the classical Bondi solution. They found that the Bondi solution can reproduce well the surface brightness profile up to the outer radius of $r_{\mathrm{out}} \sim 3'' \approx R_{\mathrm{B}}$ (where $1'' \approx 0.04\,\mathrm{pc}$), which is consistent with the Bondi radius expressed in Eq. (2.3).

Considering the surface brightness profile of the hot flow inferred from 134 ks Chandra ACIS-I observations, the best fitted model of the spherical Bondi flow gives the asymptotic values of the electron density of $n_{\mathrm{e}}^{\mathrm{out}} = 18.3 \pm 0.1\,\mathrm{cm^{-3}}$, the electron temperature of $T_{\mathrm{e}}^{\mathrm{out}} = 3.5 \pm 0.3\,\mathrm{keV}$, and the sound speed of $c_{\mathrm{s}}^{\mathrm{out}} = 7.4 \times 10^{7}\,\mathrm{cm\,s^{-1}}$. The steady spherical Bondi solution gives power-law profiles for the electron density and the electron temperature inside the Bondi radius,

$$\begin{aligned} n_{\mathrm{e}} &\approx n_{\mathrm{e},0}\left(\frac{r}{r_0}\right)^{-3/2}\,, \\ T_{\mathrm{e}} &\approx T_{\mathrm{e},0}\left(\frac{r}{r_0}\right)^{-1}\,, \end{aligned} \tag{2.8}$$

where $n_{\mathrm{e},0} = 70\,\mathrm{cm^{-3}}$ and $T_{\mathrm{e},0} = 9\,\mathrm{keV}$ at $r_0 = 0.4''$ [93]. The temperature has a virial profile for the adiabatic index of $\gamma_{\mathrm{ad}} = 5/3$.

The importance of collisional processes between plasma constituents – mainly protons and electrons – can be evaluated by comparing the collisional timescales of electron-electron and electron-proton interactions with the typical dynamical timescale (free-fall timescale) and the viscous timescale. The electron-electron collisional frequency approximately is $\nu_{\rm ee} \simeq 3.75 n_{\rm e} T_{\rm e}^{-3/2} \log\Lambda_{\rm ee}\,{\rm Hz}$, where $\log\Lambda_{\rm ee}$ is the Coulomb logarithm, while the frequency of electrons colliding with protons may be estimated as $\nu_{\rm ep} \simeq 5.26 n_{\rm i} T_{\rm e}^{-3/2} \log\Lambda_{\rm ei}\,{\rm Hz}$. Assuming that the electron and proton number densities are approximately the same, $n_{\rm i} \approx n_{\rm e}$, the corresponding collisional timescales of electrons with themselves and protons are approximately constant with radius, given the Bondi profiles in Eqs. (2.8). The electron-electron collisional timescale is $\tau_{\rm ee} \approx (\nu_{\rm ee})^{-1} \approx 13\,{\rm yr}$ for $\log\Lambda_{\rm ee} = 10$. In a similar way, the electron-proton collisional timescale is $\tau_{\rm ep} \approx 9\,{\rm yr}$. The free-fall (dynamical) timescale evaluated for the initial infall distance of $r_0 = 1000 r_{\rm S}$ is,

$$t_{\rm dyn} \approx t_{\rm ff} \simeq 0.062\,\left(\frac{r_0}{1000\,r_{\rm S}}\right)^{3/2}\left(\frac{M_\bullet}{4\times10^6\,M_\odot}\right)^{-1/2}. \tag{2.9}$$

The viscous timescale $t_{\rm vis}$ may be in general expressed as [104],

$$t_{\rm vis} \approx \alpha^{-1}(H/r_0)^{-2} t_{\rm dyn} \tag{2.10}$$

where the ratio of the thickness of the accretion flow to the radial length-scale is expected to be of the order of unity since the accretion flow around Sgr A* is generally considered to be optically thin and geometrically thick as for hot accretion flows in general [105]. When the viscosity parameter α is of the order of 0.1 [106, 104], the viscous timescale is $t_{\rm vis} \approx 10 t_{\rm dyn}$.

When compared to the free-fall and viscous timescales, see Fig. 2.2, the electron-electron and electron-proton interactions take place on longer timescales than the dynamical and accretion processes inside the inner 1000 Schwarzschild radii. This implies that particle collisions are irrelevant for the dynamical processes in the immediate vicinity of Sgr A*.

On the other hand, the ordered plasma oscillations with the characteristic plasma frequency $\nu_{\rm p}$ are relevant on all spatial scales. The presence of plasma close to the SMBH at the Galactic centre means that the immediate vicinity of Sgr A* cannot be observed at frequencies smaller than the plasma frequency, $\nu < \nu_{\rm p}$, because of charge oscillations in the plasma. The Bondi-flow model of [93] predicts the number densities of electrons at the scale of $r = 10\,r_{\rm S}$ to be $n_{\rm e} \approx 10^7\,{\rm cm^{-3}}$ and that yields the plasma frequency of,

$$\nu_{\rm p} = 28.4 \left(\frac{n_{\rm e}}{10^7\,{\rm cm^{-3}}}\right)^{1/2} {\rm MHz}\,, \tag{2.11}$$

which would effectively block electromagnetic radiation with wavelengths longer than $\lambda_{\rm p} \simeq 11\,{\rm m}$ from the innermost region. By coincidence, the plasma frequency close to the Galactic centre expressed by Eq. (2.11), which depends on the electron density, is close to the cyclotron frequency for electrons gyrating in the magnetic field with the intensity of $B \sim 10\,{\rm G}$,

$$\nu_{\rm cyc} = \frac{B}{2\pi\gamma_{\rm L}}\frac{e}{m_{\rm e}} \simeq 28 \left(\frac{B}{10\,{\rm G}}\right) \gamma_{\rm L}^{-1}\,{\rm MHz}\,, \tag{2.12}$$

where $\gamma_{\rm L}$ is a Lorentz factor. The approximate profile of the cyclotron timescale can be evaluated using the assumption that the magnetic field pressure is a fraction of the gas pressure, $P_{\rm gas} = n_{\rm e} k_{\rm B} T_{\rm e}$. Then the magnetic field is $B = \sqrt{8\pi P_{\rm gas}/\beta}$, where we take $\beta = 100$ to reproduce the magnetic field strengths as determined based on the magnetar observations at larger distances and the flare observations on the ISCO scales [84, 85]. The Lorentz factor is taken in the range $\gamma_{\rm L} = 10^3 - 10^5$ as inferred from the flare observations in the X-ray and infrared domains [84]. Based on Fig. 2.2, both the plasma timescale and the cyclotron timescales for electrons are shorter than the dynamical, viscous, and collisional timescales in the whole considered region.

Although particle collisions can be neglected for dynamical processes in the vicinity of Sgr A*, this does not apply to radiative processes in the same region, namely for the detected thermal X-ray bremsstrahlung [100, 107]. By definition, the bremsstrahlung requires the Coulomb interaction of particles, with the dom-

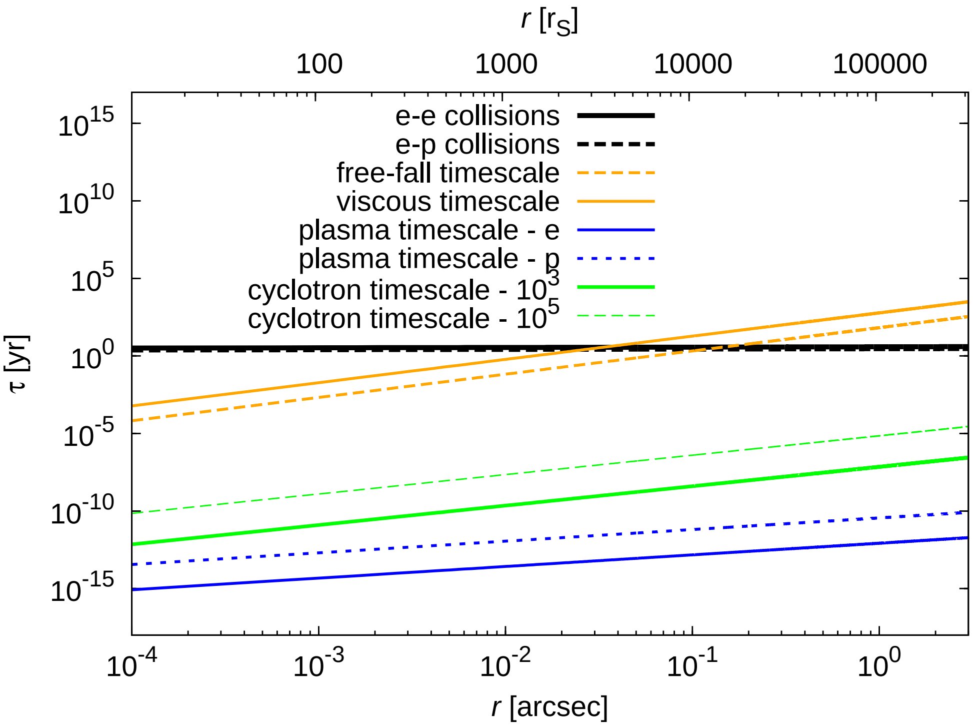

Figure 2.2: Radial profiles of electron-electron and electron-proton collisional timescales estimated based on density and temperature radial profiles expressed by Eqs. 2.8. Inside the innermost 1000 Schwarzschild radii, the electron-electron and electron-proton collisions occur on longer timescales than the dynamical and accretion processes governed by Sgr A*. On the other hand, the density and velocity plasma oscillations take place on significantly shorter scales throughout the GC region. The same applies to the range of cyclotron timescales.

inant contribution of unlike particles, electrons and protons. This is not in contradiction with the low estimated rate of collisions in the central region, since the interactions over the whole region contribute to the observed surface brightness.

The average electron and proton (ion) density can be estimated from the emissivity of thermal bremsstrahlung and the quiescent X-ray luminosity of Sgr A*. In principle, the thermal bremsstrahlung can experience losses due to Thomson scattering. The optical depth along the line of sight may be estimated as $\tau_{\rm T} = \int_0^{R_{\rm B}} \sigma_{\rm T} n_{\rm e}(l) {\rm d}l$, where l is the line-of-sight coordinate. Given the cross-section of Thomson scattering, $\sigma_{\rm T} = 6.65 \times 10^{-25}\,{\rm cm}^2$, the electron density profile given by Eq. (2.8), and the typical length-scale given by the Bondi radius, $R_{\rm B}$, the optical depth is given by

$$\tau_{\rm Brems}=\int_0^{R_{\rm B}}\sigma_{\rm T}n_{\rm e}(l){\rm d}l=\frac{\sigma_{\rm T}n_{\rm e,0}r_0^{3/2}}{R_{\rm B}^{1/2}}\approx 2\times 10^{-7}\,, \tag{2.13}$$

and hence the losses due to Thomson scattering are negligible. Given the average quiescent X-ray luminosity of Sgr A* in the range of 2–10 keV, $L_{2-10}=2\times 10^{33}\,{\rm erg\,s^{-1}}$ [108], one can estimate the electron density from the thermal bremsstrahlung luminosity,

$$\begin{aligned}L_{\rm brems}\approx&6.8\times 10^{-38}Z^2 n_{\rm i}n_{\rm e}T_{\rm g}^{-1/2}V(R_{\rm B})g_{\rm ff}(\nu,T_{\rm g})\times\\&\times\int_{\nu_1}^{\nu_2}\exp\left(-h\nu/kT_{\rm g}\right){\rm d}\nu\,{\rm erg\,s^{-1}}\,,\end{aligned} \tag{2.14}$$

where $n_{\rm i}$ is the ion number density, Z is the proton number of participating ions, $T_{\rm g}$ is the temperature of the gas, $V(R_{\rm B})\approx 4/3\pi R_{\rm B}^3$ is the volume inside the Bondi radius, $g_{\rm ff}(\nu,T_{\rm g})$ is a Gaunt factor used for the quantum corrections to classical formulas, which we set to $g_{\rm ff}=1.5$ in the given temperature range of $(10^7,10^8)\,{\rm K}$ and the frequency range of $(2,10)\,{\rm keV}=(\nu_1,\nu_2)=(0.5,2.4)\times 10^{18}\,{\rm Hz}$. The integral in Eq. (2.14) can be approximated as $\int_{\nu_1}^{\nu_2}\exp\left(-h\nu/kT_{\rm g}\right){\rm d}\nu\sim 0.98\times 10^{10}\,T_{\rm g}$. For fully ionized hydrogen and helium plasma, the term $Z^2n_{\rm i}n_{\rm e}$ becomes $1.55n_{\rm e}^2$. Putting the numerical factors all together into Eq. (2.14) yields,

$$L_{\rm brems}\approx 3.725\times 10^{30}\overline{n}_{\rm e}^2\left(\frac{T_{\rm g}}{10^8\,{\rm K}}\right)^{1/2}\left(\frac{R_{\rm B}}{0.125\,{\rm pc}}\right)^3\,{\rm erg\,s^{-1}}\,. \tag{2.15}$$

Given the measured X-ray luminosity of $L_{2-10}\approx 2\times 10^{33}\,{\rm erg\,s^{-1}}$, the mean electron density using Eq. (2.15) is $\overline{n}_{\rm e}\approx 23\,{\rm cm^{-3}}$, which is very close to the asymptotic value of $n_{\rm e}^{\rm out}=18.3\pm 0.1\,{\rm cm^{-3}}$ derived by [93] from the Bondi solution.

Classical estimates of charging

The fundamental mechanism, which can lead to charging of the black hole, are different thermal speeds for electrons and protons in the fully ionized plasma, $v_{\rm th,e}=(k_{\rm B}T_{\rm e}/m_{\rm e})^{1/2}$ and $v_{\rm th,p}=(k_{\rm B}T_{\rm p}/m_{\rm p})^{1/2}$, following from the fact that the Galactic centre plasma is collisionless. Given a considerable mass difference between electrons and protons, $m_{\rm p} = 1837 m_{\rm e}$, it is expected that the ratio of thermal speeds is,

$$\frac{v_{\rm th,e}}{v_{\rm th,p}} = \left(\frac{T_{\rm e}}{T_{\rm p}}\frac{m_{\rm p}}{m_{\rm e}}\right)^{1/2} \approx 43\,, \tag{2.16}$$

under the assumption that $T_{\rm e} \approx T_{\rm p}$. This leads to the ratio of the corresponding Bondi radii for protons and electrons,

$$\frac{R_{\rm B,p}}{R_{\rm B,e}} = \frac{T_{\rm e}}{T_{\rm p}}\frac{m_{\rm p}}{m_{\rm e}}\,. \tag{2.17}$$

Next, we can estimate the total charge by integrating across the corresponding Bondi radius. In the spherical symmetry, the total charge inside the Bondi radius can be calculated as $|Q| = \int_0^{R_{\rm B}} \rho_Q 4\pi r^2 {\rm d}r$, where ρ_Q is the charge density. Under the assumption of a power-law density profile for both electrons and protons, $n_{\rm e,p} = n_0 (r/r_0)^{-\gamma_{\rm n}}$ ($\gamma_{\rm n} = 3/2$ for the spherical Bondi flow), the ratio of positive and negative charge in the range of influence of the SMBH can be calculated as follows,

$$\begin{aligned}\left|\frac{Q_+}{Q_-}\right| &= \frac{\int_0^{R_{\rm B,p}} e n_{\rm p} 4\pi r^2 {\rm d}r}{\int_0^{R_{\rm B,e}} e n_{\rm e} 4\pi r^2 {\rm d}r}\\ &= \left(\frac{R_{\rm B,p}}{R_{\rm R_{B,e}}}\right)^{3-\gamma_{\rm n}} = \left(\frac{T_{\rm e}}{T_{\rm p}}\frac{m_{\rm p}}{m_{\rm e}}\right)^{3-\gamma_{\rm n}} \approx 8\times 10^4\,.\end{aligned} \tag{2.18}$$

where the last estimate is valid for $T_{\rm e} \approx T_{\rm p}$, which, however, does not have to be quite valid in the hot accretion flows that surround quiescent black holes, such as Sgr A* or M87, where a two-temperature flow is expected to exist [105]. At large distances from the black hole, close to the stagnation radius, the electron and proton temperatures are expected to be almost the same. Closer to the black hole, in the free-fall regime of the Bondi flow, the electron and the proton (ion) temperatures differ, the proton temperature is larger than the electron temperature by about a factor of $\simeq 1-5$, $T_{\rm e}/T_{\rm p} \geq 1/5$ [97, 98], which gives the lower limit to the excess of the positive charge in the range of influence of the SMBH, $\left|\frac{Q_+}{Q_-}\right| \gtrsim 7000$.

A similar analysis as above was discussed and performed for stationary plasma atmospheres of stars [109] and in general, for gravitationally bound systems of plasma [110]. In the hot atmosphere, where the plasma may be considered collisionless, lighter electrons tend to separate from heavier protons. The separation is stopped by an induced electrostatic field $\psi = (1/4\pi\epsilon_0)Q_{\rm eq}/r$. In the gravitational field of an approximately spherical mass of $M_\bullet$, $\phi = GM_\bullet/r$, the potential energy of protons can be expressed as $E_{\rm p} = -m_{\rm p}\phi + e\psi$, and for electrons with negative charge in a similar way, $E_{\rm e} = -m_{\rm e}\phi - e\psi$. Given the assumption of the stationary equilibrium plasma densities, the number densities of protons and electrons are proportional to $\exp\left(-E_{\rm p}/k_{\rm B}T_{\rm p}\right)$ and $\exp\left(-E_{\rm e}/k_{\rm B}T_{\rm p}\right)$, respectively. Given the quasineutrality of plasma around stars and Sgr A*, the difference between the densities of protons and electrons is expected to be small, which implies $E_{\rm p} \approx E_{\rm e}$. The induced equilibrium charge of the central body surrounded by plasma then is,

$$Q_{\rm eq} = \frac{2\pi\epsilon_0 G(m_{\rm p} - m_{\rm e})}{e} M_\bullet \approx 3.1 \times 10^8 \left(\frac{M_\bullet}{4 \times 10^6\, M_\odot}\right) C\,. \tag{2.19}$$

Eq. (2.19) was derived under the assumption of spherical stationary plasma around a point mass, which is certainly not met in the environment of dynamical plasma around Sgr A*. The real charge of Sgr A* will therefore deviate from the stationary value of $Q_{\rm eq}$. The mechanism of charging will, however, still tend to operate and a rough approximation of charge expressed by Eq. (2.19) is still more precise than the assumption of a neutral black hole. The equilibrium value $Q_{\rm eq}$ also expresses the upper limit of an electric charge associated with Sgr A*, for which the stationary number densities of protons and electrons in plasma remain approximately constant. For charges $Q \gg Q_{\rm eq}$, a significant difference in the number densities is expected that would decrease with the distance, unless the charge of the black hole would be Debye-shielded, as we will discuss later in this section.

Given the simple calculations above, it is expected that the black hole at the Galactic centre can acquire a small positive charge, given the fact that more positive charge is in the range of its gravitational influence than negative charge. In the following, we will look at more realistic scenarios of how the black hole charge could be induced in the accretion flow, given the fact that black holes are expected to have a non-zero spin and should be immersed in a magnetic field.

Maximum theoretical values of the charge of Sgr A*

The uppermost limit on the charge of Sgr A* may be derived using the the space-time of the black hole that is characterized by its mass $M_\bullet$, electric charge $Q_\bullet$, and rotation parameter $a_\bullet$. In the most general case, the Kerr-Newman (KN) solution [111] fully describes such a black hole in vacuum. The KN metric can be expressed in Boyer-Lindquist coordinates in the following way [112],

$$\begin{aligned} ds^2 = &- \left(\frac{dr^2}{\Delta} + d\theta^2\right)\rho^2 + \left(cdt - a_\bullet \sin^2\theta d\Phi\right)^2 \frac{\Delta}{\rho^2} - \\ &- [(r^2 + a_\bullet^2)d\Phi - a_\bullet cdt]^2 \frac{\sin^2\theta}{\rho^2}\,, \end{aligned} \tag{2.20}$$

where $\rho^2 = r^2 + a_\bullet^2 \cos^2\theta$ and $\Delta = r^2 - r_S r + a_\bullet^2 + r_Q^2$. The length-scales r_S and r_Q^2 correspond to the Schwarzschild radius $r_S = 2GM_\bullet/c^2 = 1.2 \times 10^{12}(M_\bullet/4 \times 10^6\,M_\odot)\,\mathrm{cm}$ and $r_Q^2 = GQ_\bullet^2/(4\pi\epsilon_0 c^4)$, respectively. The position of the event horizons is obtained with the condition $\Delta = 0$, which leads to the quadratic equation, $r^2 - r_S r + a_\bullet^2 + r_Q^2 = 0$, with two possible horizons $r_{1,2} = 1/2(r_S \pm \sqrt{r_S^2 - 4(a_\bullet^2 + r_Q^2)})$ for $r_S > 2\sqrt{a_\bullet^2 + r_Q^2}$. For $r_S < 2\sqrt{a_\bullet^2 + r_Q^2}$, no horizons exist, so the object is a naked singularity. The condition $r_S = 2\sqrt{a_\bullet^2 + r_Q^2}$ leads to a single event horizon located at $r = 1/2 r_S$, which represents an extremal black hole, and it also gives an upper limit for an electric charge of the SMBH at the

Galactic centre,

$$Q_{\max}^{\mathrm{rot}} = 2c^2\sqrt{\frac{\pi\epsilon_0}{G}\left(\frac{G^2M_\bullet^2}{c^4} - a_\bullet^2\right)} \tag{2.21}$$

which can be rewritten using a dimensionless parameter $a_\bullet = \tilde{a}_\bullet GM_\bullet/c^2$ into the form,

$$Q_{\max}^{\mathrm{rot}} = 2M_\bullet\sqrt{\pi\epsilon_0 G(1-\tilde{a}_\bullet^2)}\,. \tag{2.22}$$

Relation (2.21) represents a theoretical limit for the maximum charge of a rotating black hole. Above this limit, the massive object at the Galactic centre would be not a black hole anymore, but a naked singularity, which can be ruled out based on observational and causal arguments [70]. In addition, a direct transition between a non-extremal black hole and an extremal one due to the accretion of charged matter (test particles or shells) is not possible as was shown in [113].

For a non-rotating black hole ($a_\bullet = 0$), the maximum charge is proportional to the black hole mass. Evaluating for Sgr A* gives,

$$Q_{\max}^{\mathrm{norot}} = 2\sqrt{\pi\epsilon_0 G}M_\bullet = 6.86\times 10^{26}\left(\frac{M_\bullet}{4\times 10^6\,M_\odot}\right)C\,. \tag{2.23}$$

In Fig. 2.3, we plot the effect of the rotation of the black hole on its maximum electric charge. Close to the maximum rotation, the maximum charge is close to zero.

In the following, we discuss limits on the electric charge of the Galactic centre black hole based on induced electric field of a rotating black hole immersed in the circumnuclear magnetic field.

Charge induced by rotating SMBH

There are indications that a considerable magnetic field must be present in the vicinity of SMBH at the Galactic centre [84, 85, 93], which suggests the value of 10 G in the vicinity of the even horizon. The exact solution for the electromagnetic fields in the vicinity of Sgr A* is far from being properly defined, however

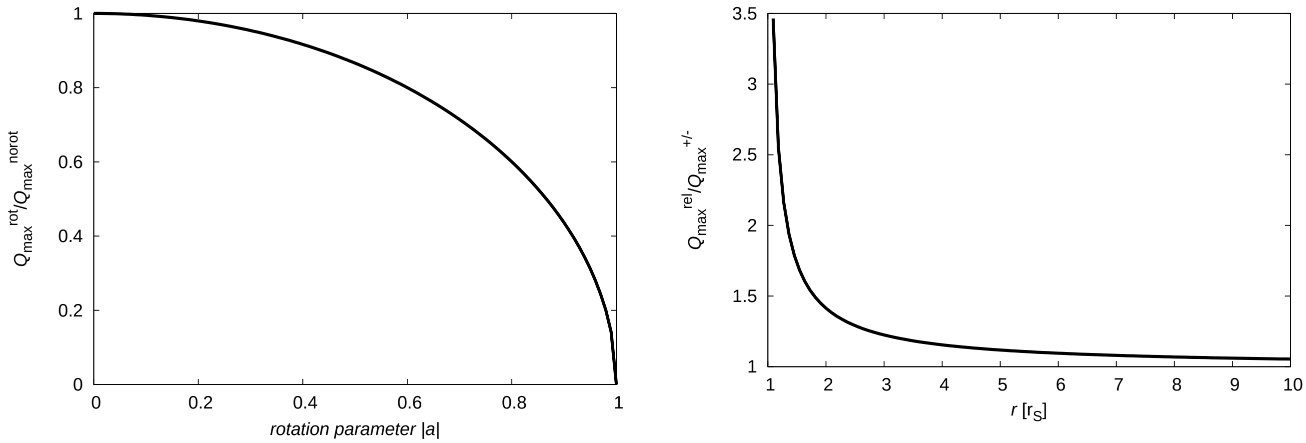

Figure 2.3: **Left:** Effect of the rotation of the black hole on its maximum electric charge. **Right:** The dependence of the relativistic correction to both the maximum positive and negative charge of the supermassive black hole. In the relativistic regime, the electrostatic force increases towards the event horizon, which becomes apparent inside the innermost stable orbit.

it is natural to assume that the magnetic field shares the symmetries of the background spacetime metric, such as the axial symmetry and stationarity. The central SMBH is assumed to be a standard Kerr black hole whose gravitational potential dominates the system. Moreover, the small density of the plasma around Sgr A* implies that the magnetospere of SMBH can be described within the test field approximation. For estimation purposes, one can assume that the magnetic field is homogeneous and aligned along the axis of rotation of black hole with the strength B. The rotation of a black hole gives the contribution to the Faraday induction which generates the electric potential A_t and thus produces an induced electric field, just in the same manner as if the field would be induced in magnetic field by a rotating ring. The potential difference leads to the process of selective accretion, which implies that a rotating black hole in external homogeneous magnetic field can obtain maximum net electric charge $Q = 2aMB$.

The statement of selective accretion by rotating black hole in the presence of magnetic field is quite general and independent of the exact shape of the field and the type of accreting charged matter. If one assumes that the magnetic field is created by the dynamics of the surrounding conducting plasma which co-rotates with the black hole, then the sign of induced charge is more likely positive. If magnetic field is oriented along the rotation axis of a black hole, the black hole induces electric charge given by $Q_{\bullet\text{ind}} = 2aM_{\bullet}B_{\text{ext}}$. Given an upper boundary for the spin parameter $a_{\bullet} \leq M_{\bullet}$ one can estimate the upper boundary for the induced charge as follows

$$Q_{\bullet\text{ind}}^{\max} = 2.32 \times 10^{15} \left(\frac{M_{\bullet}}{4 \times 10^{6} M_{\odot}}\right)^{2} \left(\frac{B_{\text{ext}}}{10\text{G}}\right) \text{ C}, \tag{2.24}$$

where the external magnetic field is expressed in units of 10 Gauss, which is the estimated magnetic field strength associated with the flaring activity of Sgr A* [84]. Independently from the precise configuration of magnetic field in the Galactic center, the order of magnitude of estimated induced charge is about $10^{15\pm1}$C, if the assumptions of the axial symmetry and stationarity is preserved. In the case of Sgr A*, there is a convincing evidence that the magnetic field in the Galactic center is indeed highly oriented and ordered [23], which supports our assumptions.

We would like to stress that two leading processes by which the rotational energy can be extracted out are the Blandford-Znajek mechanism [86] and the magnetic version of Penrose process [114, 87], both of which use the existence of negative energy states of particles with respect to observer at infinity. In both of these processes, the rotation of a black hole in magnetic field generates quadrupole electric field by twisting of magnetic field lines [3]. An infall of oppositely charged particles (relative to the sign of induced charge) leads to the discharge of the induced field and therefore the extraction of rotational energy of a black hole. In Blandford-Znajek mechanisms the presence of induced field completes current circuit for in-falling oppositely charged negative energy flux. This field is responsible for acceleration of charged particles which can be launched as black hole jets. Similarly, e.g. in the case of a uniform magnetic field considered above, the discharge of induced electric field $Q_{\bullet\text{ind}} = 2aM_{\bullet}B$ would lead to the decrease of black hole spin a and resulting extraction of rotational energy of a black hole, while B is constant by its definition.

Multiple numerical simulations of two processes for general relativistic magnetohydrodynamic flow showing the efficient extraction of energy from rotating black holes imply that the induced electric field are not screened at least in the close vicinity of black holes. The problem of screening of induced electric field by surrounding plasma for Sgr A* is discussed in Sections 1.2.2 and 2.2.2.

The value of $Q_{\bullet \mathrm{ind}}^{\max}$ is small in comparison with $Q_{\max}$ implying that its effect on the spacetime geometry can be neglected. The upper boundary for the charge-to-mass ratio for the Galactic centre SMBH [115] is

$$\begin{aligned} \frac{Q_{\bullet \mathrm{ind}}}{M_{\bullet}} &= 2B_0 \frac{J_{\bullet}}{M_{\bullet}} \leq 2B_0 M_{\bullet} = \\ &= 8 \times 10^{-13} \left(\frac{B_0}{10\,\mathrm{G}}\right) \left(\frac{M_{\bullet}}{4 \times 10^6\, M_{\odot}}\right) \ll 1\,. \end{aligned} \tag{2.25}$$

Relation (2.25) implies that the induced black hole charge is weak in a sense that its effect on the dynamics of neutral matter can be neglected and Kerr metric approximation can be used. However, induced charge can have considerable effect on the dynamics of charged matter and consequently on some of the observables of Sgr A*, which we specifically discuss in Section 2.2.2.

Charge fluctuation due to accretion

The electric charge of $Q_{\max}^{\mathrm{norot}}$ is a theoretical upper limit. In reality, the accretion of positively charged particles (protons) will stop to proceed when the Coulomb force between the SMBH and the proton is of the same value and opposite orientation as the gravitational force, giving the condition for the maximum positive charge in a non-relativistic case,

$$Q_{\max}^{+} = 4\pi\epsilon_0 G M_{\bullet} \left(\frac{m_{\mathrm{p}}}{e}\right) = 6.16 \times 10^8 \left(\frac{M_{\bullet}}{4 \times 10^6\, M_{\odot}}\right) C\,, \tag{2.26}$$

which is much smaller than the maximum charge, $Q_{\max}^{+}/Q_{\max} = 2\sqrt{\pi\epsilon_0 G}\, m_{\mathrm{p}}/e \approx 9 \times 10^{-19}$.

In a similar way, the maximum negative charge derived for accreting electrons is,

$$Q^{-}_{\rm max} = 4\pi\epsilon_0 G M_\bullet \left(\frac{m_{\rm e}}{e}\right) = 3.36 \times 10^5 \left(\frac{M_\bullet}{4\times 10^6\, M_\odot}\right) C\,, \tag{2.27}$$

which leads to an even smaller ratio $Q^{-}_{\rm max}/Q_{\rm max} = 2\sqrt{\pi\epsilon_0 G} m_{\rm e}/e \approx 4.9 \times 10^{-22}$. The ratios of maximum positive and negative charges to the maximum charge allowed for the SMBH imply that the space-time metric is not affected by an electric charge in a significant way.

Eqs. (2.26) and (2.27) are applicable only far from the black hole. In the relativistic regime, the motion of charged particles in the simplest regime without rotation can be studied within the Reissner-Nordström solution, which can be acquired from the Kerr-Newman metric by setting $a_\bullet = 0$ in Eq. (2.20). The line element in the geometrized units with $c = 1 = G$ can be written as

$$ds^2 = -f(r)dt^2 + f(r)^{-1}dr^2 + r^2 d\theta^2 + r^2 \sin^2\theta d\phi^2, \tag{2.28}$$

where the lapse function is defined as

$$f(r) = 1 - \frac{r_S}{r} + \frac{r_Q^2}{r^2}. \tag{2.29}$$

The four-vector potential A_α of electromagnetic field generated by the charge $Q_\bullet$ of the Reissner-Nordström black hole takes the form

$$A_\mu = \frac{Q_\bullet}{r}\delta^{(t)}_\mu. \tag{2.30}$$

The dynamics of charged particle in curved spacetime in presence of electromagnetic fields is governed by the equation

$$\frac{du^\mu}{d\tau} + \Gamma^\mu_{\alpha\beta}u^\alpha u^\beta = \frac{q}{m}F^\mu{}_\nu u^\nu, \tag{2.31}$$

where $u^\mu = dx^\mu/d\tau$ is the four-velocity of the particle with mass m and charge q, normalized by the condition $u^\mu u_\mu = -1$, τ is the proper time of the particle, $F_{\mu\nu} = A_{\nu,\mu} - A_{\mu,\nu}$ is an antisymmetric tensor of the electromagnetic field and components of $\Gamma^\mu_{\alpha\beta}$ are the Christoffel symbols.

One of the interesting features of the motion of charged particles in the vicinity of Reissner-Nordström black hole is the existence of trapped equilibrium state of a particle where the electrostatic forces between two charges compensate the gravitational attraction of a black hole. The four velocity of a particle at this state is $u^\alpha = (1/\sqrt{-g_{tt}}, 0, 0, 0)$. Thus, the time component of equation (2.31) takes the form

$$r_S - 2\frac{r_Q^2}{r} + 2\frac{Qq}{m}\left(1 - \frac{r_S}{r} - \frac{r_Q^2}{r^2}\right)^{1/2} = 0 \tag{2.32}$$

Since the gravitational effect of the charge $Q_\bullet$ is small in comparison with those of the mass of the black hole (corresponding to $r_Q \ll r_S$) one can neglect the higher order terms in $Q_\bullet$ equation (2.32). Thus, for the charge Q we get

$$Q_\bullet = \frac{m r_S}{2q}\left(1 - \frac{r_S}{r}\right)^{-1/2}. \tag{2.33}$$

The charge (2.33) can be interpreted as the maximum net charge that can be accreted into the black hole from the given position r before the electrostatic force will prevail and the accretion of same-charge particles stops. Restoring the constant in (2.33) we get charge in SI units as

$$Q_{\rm max}^{\rm rel} = 4\pi\epsilon_0 G M_\bullet \frac{m_{\rm par}}{q_{\rm par}}\left(1 - \frac{r_S}{r}\right)^{-1/2}. \tag{2.34}$$

The factor $\left(1 - \frac{r_S}{r}\right)^{-1/2}$ is the general relativistic correction to the corresponding Newtonian equation. This implies that the electrostatic force increases while approaching black hole. Close to the horizon, the divergence of (2.34) means that the black hole requires infinite charge in order to keep the equilibrium position of the particle. We plot the ratio $Q_{\rm max}^{\rm rel}/Q_{\rm max}^{+/-}$, i.e. the relativistic correction in Fig. 2.3.

Charge and dynamical timescales

The electric charge of the SMBH is expected to fluctuate due to discharging by particles of an opposite charge. This is especially efficient when the free-fall timescale of particles with the opposite charge is significantly shorter than the free-fall timescale of the particles with the same charge as that of the black hole. The free-fall timescale for a charged black hole is modified due to the presence of an additional Coulomb term in the equation of the motion for a radial infall (neglecting the gas pressure),

$$\frac{\mathrm{d}v}{\mathrm{d}t} = -\frac{GM_{\bullet}}{r^2} + \frac{1}{4\pi\epsilon_0}\frac{Q_{\bullet}}{r^2}\frac{q_{\rm par}}{m_{\rm par}}\,, \tag{2.35}$$

where $q_{\rm par}$ and $m_{\rm par}$ are the charge and the mass of the particle, respectively. The signs in the equation are the following: for the positive charge of the black hole $Q_{\bullet} = +Q^+$, the particle charge is $q_{\rm par} = +e$ for the proton ($m_{\rm par} = m_{\rm p}$) and $q_{\rm par} = -e$ for the electron ($m_{\rm par} = m_{\rm e}$). For the negative charge of the black hole $Q_{\bullet} = -Q^-$, the signs of particle charges are kept as before.

The Newtonian free-fall timescale derived from Eq. 2.35 for a particle falling in from the initial distance of r_0 is

$$t_{\rm ff,Q} = \frac{\pi r_0^{3/2}}{\sqrt{8(GM_{\bullet} - \frac{1}{4\pi\epsilon_0}Q_{\bullet}\frac{q_{\rm par}}{m_{\rm par}})}}\,, \tag{2.36}$$

which becomes $t_{\rm ff}(Q_{\bullet} = 0) = \pi r_0^{3/2}/\sqrt{8GM_{\bullet}}$ for zero charge of the SMBH. The direct outcome of Eq. (2.36) is the difference of free-fall timescales for protons and electrons for a given charge of the SMBH.

In Fig. 2.4, we plot the free-fall timescales for protons and electrons for a positive charge of the SMBH (left panel) and for its negative charge (right panel). The timescales are comparable up to $Q^+ \lesssim 10^{-5}\,Q^+_{\rm max}$ for the positively charged black hole and up to $Q^- \lesssim 10^{-2}\,Q^-_{\rm max}$, which further limits a charge of the SMBH since for larger charges the infall of opposite charges is progressively faster than the infall of the same charges. For the maximum positive charge of Sgr A*, the free-fall timescale for electrons is $t_{\rm ff,Q^+_{max}} = 8.5\,\mathrm{yr}$ for an initial distance at the Bondi radius. This is a much shorter timescale than the free-fall timescale of protons

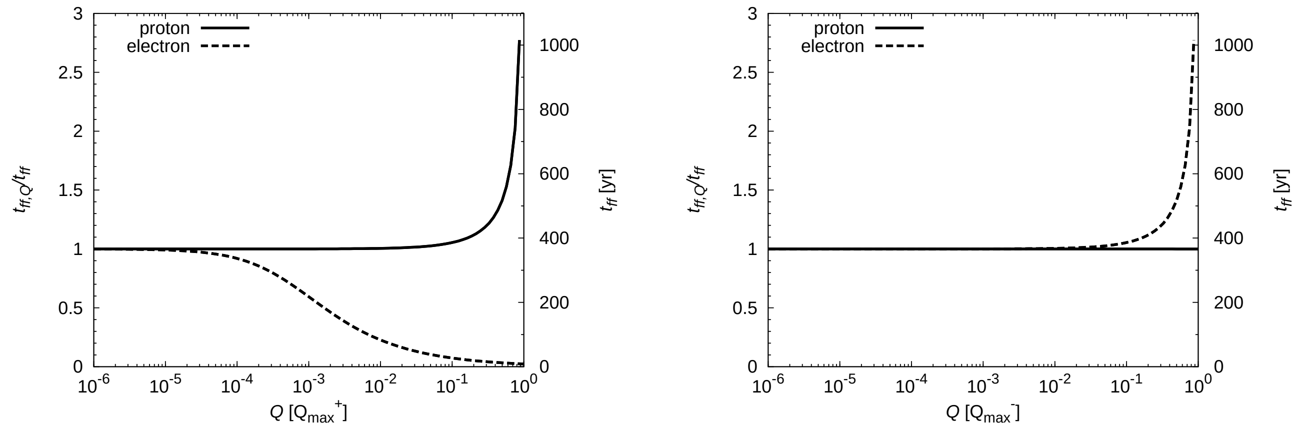

Figure 2.4: **Left panel:** The free-fall timescales for protons and electrons calculated for a positive charge of the supermassive black hole at the Galactic centre expressed in units of the maximum positive charge ($Q^+_{\rm max}$, see Eq. 2.26). The scale on the left vertical axis expresses the ratio $t_{\rm ff,Q}/t_{\rm ff}$ whereas the scale along the right vertical axis is the free-fall timescale for an initial distance equal to Bondi radius (Eq. (2.3)) expressed in years. **Right panel:** The same as in the left panel, calculated for a negative charge of the SMBH expressed in units of the maximum negative charge ($Q^-_{\rm max}$, see Eq. 2.27).

for the maximum negative charge, which is close to the free-fall timescale for a non-charged black hole with an initial distance at the Bondi radius, $t_{\rm ff} = 366\,{\rm yr}$.

The free-fall time-scale from the Bondi radius is the basic dynamical timescale in the accretion flow. Any disturbance in the accretion flow develops on the viscous timescale given by Eq. (2.10), which for the assumption of the thick flow $H \approx r_0$ and $\alpha \approx 0.1$ is approximately $t_{\rm vis} \approx 10 t_{\rm ff}(r_0, Q_\bullet)$.

In the following, we define a specific charge of accreted matter ϵ, which relates the accretion rate of the charged matter to the total accretion rate as $\dot{M}_{\rm acc}^{\rm charge} = \epsilon \dot{M}_{\rm acc}$. From this relation, the charging rate of the black hole, $\dot{Q}_\bullet$, may be expressed as,

$$\dot{Q}_\bullet = \epsilon \frac{q_{\rm par}}{m_{\rm par}} \dot{M}_{\rm acc}\,, \tag{2.37}$$

where $\dot{M}_{\rm acc}$ is the total accretion rate. The total accretion rate was inferred from the observations via the Faraday rotation by [116], who obtain $\dot{M}_{\rm acc} = 2 \times 10^{-9}\,{\rm M}_\odot\,{\rm yr}^{-1}$ up to $2 \times 10^{-7}{\rm M}_\odot\,{\rm yr}^{-1}$, depending on the configuration of the magnetic field. For the induced positive charge $Q_{\rm ind}^{+}$, the charging (induction) time-scale follows from Eq. (2.37),

$$\tau_{\rm charge}^{+} = \frac{m_{\rm p} Q_{\rm ind}^{+}}{e\epsilon_{\rm pos}\dot{M}_{\rm acc}}\,, \tag{2.38}$$

while for the induced negative charge we get,

$$\tau_{\rm charge}^{-} = \frac{m_{\rm e} Q_{\rm ind}^{-}}{e\epsilon_{\rm neg}\dot{M}_{\rm acc}}\,. \tag{2.39}$$

To charge the black hole positively, mainly by the induction process described in Section 2.2.1, the charging timescale expressed by Eq. (2.38) needs to be smaller than the discharge timescale, which can be estimated by the viscous timescale of electrons on the scale of the gravitational radius. On the other hand, the charging timescale must be larger than the timescale given by the plasma frequency for protons, $\tau_{\rm p} = 2\pi(\epsilon_0 m_{\rm e}/(n_{\rm e}e^2))^{1/2}$, which expresses the charged density fluctuations on scales larger than the Debye length. For the exemplary values of $Q_{\rm ind} = Q_{\bullet,10} 10^{10}\,C$ and $\dot{M}_{\rm acc} = \dot{M}_{-8} = 10^{-8}\,M_{\odot}{\rm yr}^{-1}$, we obtain the limits

$$1.3\times 10^{-13} Q_{\bullet,10}\dot{M}_{-8}^{-1} \lesssim \epsilon_{\rm pos} \lesssim 1.4\times 10^{-6} Q_{\bullet,10}\dot{M}_{-8}^{-1}\,. \tag{2.40}$$

In an analogous way, the negative charged fraction of the accretion rate is

$$1.7\times 10^{-18} Q_{\bullet,10}\dot{M}_{-8}^{-1} \lesssim \epsilon_{\rm neg} \lesssim 3.3\times 10^{-8} Q_{\bullet,10}\dot{M}_{-8}^{-1}\,, \tag{2.41}$$

as inferred by comparing (2.39) to the viscous timescale of protons (upper timescale limit for discharging) and to the timescale of electron plasma oscillations (both evaluated at the ISCO scale of $r_{\rm ISCO} \approx GM_{\bullet}/c^2$).

The charging of Sgr A* can thus effectively proceed when a rather small fraction of accreted matter ($\epsilon_{\rm pos}$ or $\epsilon_{\rm neg}$) is charged. The charging process of the accreted fluid may proceed at a larger distance from the SMBH horizon plausibly due to strong irradiation or the external (Galactic) magnetic field [90].

The process of the black hole charging can proceed efficiently when the gravitational and electrostatic forces acting on a particle are greater than the thermal

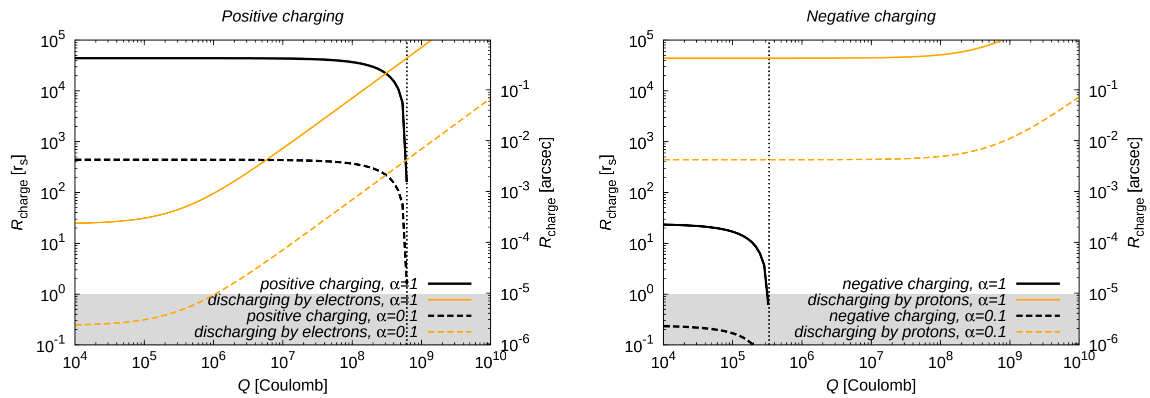

Figure 2.5: The dependence of the radius of the sphere, where the basic condition for the charging or the discharging, $t_{\rm vis,Q} < t_{\rm th}$, is met for both the positive charging (left panel) and the negative charging (right panel). The solid lines mark the charging/discharging length-scale for the purely free-fall accretion while the dashed lines represent the viscous infall for $\alpha = 0.1$. The charging can effectively proceed when the charging length-scale $R_{\rm charge}$ is larger than the discharging length-scale. The shaded region marks the region below the event horizon.

pressure forces inside a region of radius $R_{\rm charge}$, which is equivalent to the condition that the viscous time-scale of the inward motion must be smaller than the thermal time-scale, $t_{\rm vis,Q} < t_{\rm th}$ inside $R_{\rm charge}$. The thermal time-scale is simply, $t_{\rm th} = R_{\rm charge}/v_{\rm th}$, where the thermal speed $v_{\rm th}$ is related to either electrons or protons. The condition of the smaller viscous time-scale is met inside the sphere of radius $R_{\rm charge}$, whose radius progressively gets smaller and it reaches zero at either the maximum positive or negative charge, see Eqs. (2.26) and (2.27). Under the assumption that the accretion flow is thick in a sense $(H/r_0) \approx 1$, it can be simply derived that,

$$R_{\rm charge} \lesssim (\alpha/\pi)^2 \frac{m_{\rm par}}{k_{\rm B} T_{\rm g}} (8GM_\bullet - \frac{2}{\pi \epsilon_0} Q_\bullet \frac{q_{\rm par}}{m_{\rm par}})\,, \tag{2.42}$$

with the sign convention as in Eq. (2.36). For the zero charge of the black hole, the relation (2.42) is similar to the definition of the Bondi radius, Eq. (2.3), $R_{\rm charge} \lesssim 8(\alpha/\pi)^2 GM_\bullet/v_{\rm th}^2$.

In Fig, 2.5, we plot Eq. (2.42) for both positive charging (protons falling into the positively charged black hole; see left panel) and negative charging (electrons falling into negatively charged black hole; right panel). Inside the radius $R_{\rm charge}$ basic condition for charging is met – particles with the same sign of the charge are not prevented from descending towards the black hole by thermal pressure. However, the particles of the opposite charge also fall in progressively faster inside the discharging sphere with the radius of $R_{\rm discharge}$ defined analogously to Eq. (2.42), which effectively limits the realistic values of the electrostatic charge of the black hole.

The necessary condition for an increasing charge of the SMBH is that $R_{\rm charge} \gtrsim R_{\rm discharge}$, which is only met for the positive charging, see the left panel of Fig. 2.5. For negative charging, the discharging length-scale of protons is always larger than the charging length-scale of electrons purely because of the mass difference. Therefore, the negative charging of black holes is rather inefficient.

Hence, the Galactic centre black hole and black holes in general are prone to have a small positive charge. This is also supported by the analysis in Section 2.2.1, where it is shown that black holes whose spin is oriented parallel to the magnetic field intensity preferentially accrete positively charged particles, while those with anti-parallel spin are being negatively charged. Since we expect a certain degree of alignment in a relaxed system of a black hole and its associated accretion flow, the induced charge is expected to be positive.

For the positive charging in Fig. 2.5 (left panel), the charging length-scale for protons is larger than the discharging radius of electrons up to a certain charge $Q_{\rm eq}$, which for the general case of different electron and proton temperatures is,

$$Q_{\rm eq} = \frac{4\pi\epsilon_0 G M_\bullet}{e} \frac{[(T_{\rm e}/T_{\rm p})m_{\rm p} - m_{\rm e}]}{1 + T_{\rm e}/T_{\rm p}}\,. \tag{2.43}$$

For the case of the same temperature $T_{\rm e} \approx T_{\rm p}$, Eq. (2.43) becomes identical to the equilibrium charge in Eq. (2.19), $Q_{\rm eq} = 3.1 \times 10^8 \left(M_\bullet/4 \times 10^6\,M_\odot\right)\,C$. This charge is associated with the charging/discharging length-scale of $R_{\rm charge} = 0.2''$ for the free-fall accretion and $R_{\rm charge} = 2.1\,$mas for the accretion with the viscosity parameter of $\alpha = 0.1$, which is one and three orders of magnitude smaller than the Bondi radius, respectively.

2.2.2 Observable effects associated with a charged black hole

Although the simple analysis based on the first principles showed that the charge associated with the Galactic centre black hole is at least ten orders of magnitude smaller than the charge corresponding to an extremal black hole, it is useful to list observational signatures that a charged black hole could have. The electric charge, if present, most likely does not reach values significant for the spacetime metric. However, despite its expected small value, it is useful to design observational tests of its presence. It is therefore of astrophysical interest to name several potential observables that can be employed to test the presence of the charged SMBH at the Galactic centre.

Effect on the black hole shadow

For shorter wavelengths in the radio domain than $\lambda_{\rm p}$, plasma does not block the emission, however it causes significant scatter broadening of any structure up 1.4 mm [117]. At wavelengths $\lambda < 1.4$ mm, it is possible to resolve the structure using the VLBI, since the size of Sgr A* starts to be source-dominated [118, 76]. Of a particular interest is a well-defined curve on the sky plane which divides the region where photon geodesics intersect the even horizon from the region where photons can escape to the observer – the so-called black hole shadow [119].

It was previously claimed by [120] that the charge associated with the Galactic centre black hole could be detected via the VLBI imaging of Sgr A*, based on the detection of the shadow. They report that a Reissner-NordstrΓųm black with a significant charge close to $Q_\bullet = Q_{\rm max}^{\rm norot}$ is more consistent with the VLBI detection of Sgr A* by [76] with the core diameter of $37^{+16}_{-10}\,\mu$as. This argument is based on

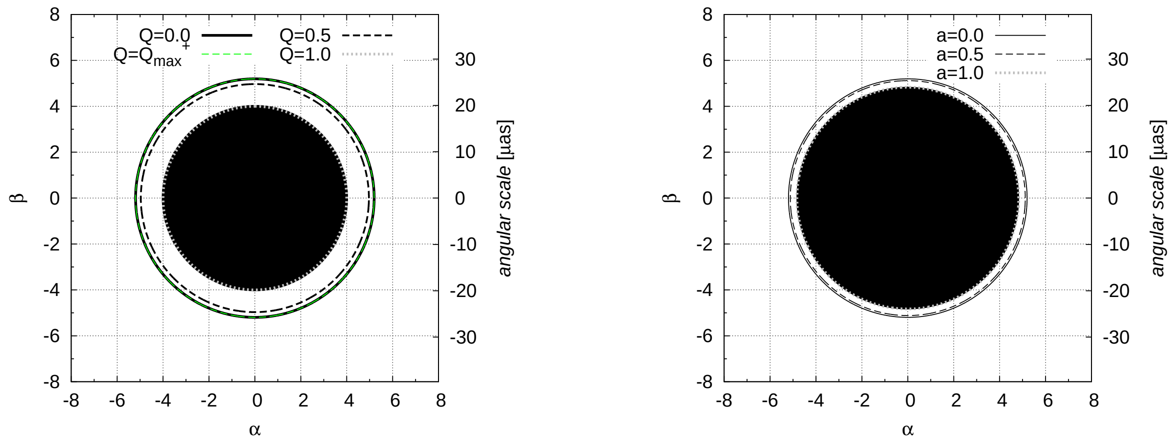

Figure 2.6: **Left:** The black hole shadow size in gravitational units for a non-rotating, Reissner-NordstrΓųm black hole for an increasing value of the charge according to the legend. The right vertical axis is expressed in microarcseconds for the distance of the Galactic centre – 8 kpc. **Right:** The same as the left figure but for the rotating black hole (Kerr). The calculations are performed for the top view, in the direction of the spin axis, for increasing values of the spin parameter according to the legend.

the theoretical calculations of the shadow diameter, namely the shadow diameter for the Schwarzschild black hole is $6\sqrt{3}GM_{\bullet}/c^2$, which is $\sim 51.2\,\mu$as at the distance of 8 kpc at the Galactic centre. For an extremal Reissner-Nordströmblack hole, one gets the shadow diameter $4GM_{\bullet}/c^2$, i.e. by about 38% smaller than for the Schwarzschild black hole, which corresponds to $\sim 39.4\,\mu$as. The shadow diameter for the nearly extremal charged black hole is thus closer to the core size found by [76] ([76]).

However, the core size found by [76] does not correspond in a straightforward way to the black hole shadow size. It can be either a Doppler beamed accretion flow or the footpoint of the jet [76, 121, 70] and in these cases it is difficult to make a connection to the charge of the black hole. In general, the black hole shadow is not a clean observable. Not only does the charge influence its size, but also the spin, see Fig. 2.6 for comparison. In addition, the charge starts significantly influencing the size of the shadow for fractions of the maximum charge, $Q_{\bullet} \gtrsim 0.1\,Q_{\rm max}^{\rm norot}$. For the maximum positive charge value of $Q_{\rm max}^{+} \approx 6 \times 10^8\,C$, see

Eq. (2.26), there is practically no difference in the size of the shadow.

Below we show that the bremsstrahlung surface brightness profile on the scales of $100\,r_{\rm S}$ up to $1000\,r_{\rm S}$ can be used to test the presence of a much smaller charge associated with Sgr A* than by using the shadow size.

Testing the presence of a Black Hole Debye shield – does a charged black hole have an impact on the bremsstrahlung profile?

The charge associated with Sgr A* can have a considerable impact on the motion and the distribution of charged particles, electrons, protons, and ions, in its vicinity. However, this only applies to the charged black hole that is not shielded. In the classical plasma theory, any charged body immersed in stationary plasma with the electron density $n_{\rm e}$ and temperature $T_{\rm e}$ is shielded beyond the characteristic Debye length-scale, $\lambda_{\rm D} = \sqrt{\epsilon_0 k_{\rm B} T_{\rm e}/(n_{\rm e} e^2)}$, which results in the exponential potential decrease, $\phi = \phi_0 \exp\left(-r/\lambda_{\rm D}\right)$, where ϕ_0 is the potential of a point charge in vacuum.

The plasma around Sgr A* is, however, certainly not stationary but rather dynamic, given the large velocity of accretion flow in the potential of Sgr A* and turbulence. Therefore, the standard Debye theory is not applicable to this environment.

Even if the Debye shield around Sgr A* were created, it would have such a small length-scale that it would completely lie inside the ISCO, where it would be dynamically sheared and it would be therefore highly unstable. When evaluated on the scale of the ISCO, using the extrapolated density and temperature profiles in Eqs. 2.8, the Debye length is,

$$\lambda_{\rm ISCO} = 5 \left(\frac{T_{\rm e}}{8.7\times 10^{12}\,{\rm K}}\right)^{1/2} \left(\frac{n_{\rm e}}{1.7\times 10^{9}\,{\rm cm}^3}\right)^{-1/2} {\rm m}\,, \tag{2.44}$$

while at the Bondi radius it would be only one order of magnitude larger, $\lambda_{\rm Bondi} \approx 141\,{\rm m}$.

Moreover, using the classical estimates, the Debye sphere would not be formed based purely on viscous timescales if the charged fraction of accreted matter is large enough. If we imagine that the positively charged black hole is surrounded by a negatively charged Debye shell, its mass can be estimated simple as $M_{\rm Debye} \approx (Q^{+}_{\rm ind}/e)m_{\rm e}$, where $Q^{+}_{\rm ind}$ is the induced positive black hole charge. Since the Debye shell lies inside the ISCO, it is being depleted as well as refilled all the time. If the depletion rate of electrons $\dot{M}^{-}_{\rm acc} = \epsilon_{\rm neg}\dot{M}_{\rm acc}$ is larger than the filling rate $\dot{M}_{\rm Debye}$, then the Debye shell is highly transient and does not screen out the charge of the black hole. The filling rate of the Debye shell is assumed to take place on the viscous timescale of electrons, taking into account the positive charge of the black hole, $t^{-}_{\rm vis} = \alpha^{-1}(H/r_{\rm ISCO})^{-2}t_{\rm ff}(r_{\rm ISCO}, Q^{+}_{\rm ind})$. Then the Debye filling rate can be expressed as,

$$\dot{M}_{\rm Debye} \sim \frac{Q^{+}_{\rm ind} m_{\rm e}}{e t^{-}_{\rm vis}} \,. \tag{2.45}$$

The Debye shell will not form if $\dot{M}^{-}_{\rm acc} > \dot{M}_{\rm Debye}$, which puts the lower limit on the negatively charged fraction of the accreted matter, $\epsilon_{\rm neg} > Q^{+}_{\rm ind} m_{\rm e}/(e\dot{M}_{\rm acc}t^{-}_{\rm vis}) \approx 7 \times 10^{-17}$. It implies that if the accreted matter contains a negatively charged fraction of the order of $\epsilon_{\rm neg}$, then the Debye shell is expected not to form at all. Even if the Debye shell forms temporarily, it would be strongly perturbed by the turbulence and outflows. In addition, a more general analysis done by [110] showed that all self-gravitating systems with length-scales L larger than the Debye-length, $L \gg \lambda_{\rm D}$, are positively charged in order to hold in the electron gas, i.e. these objects are not Debye-screened.

An unshielded charged black hole would lead to the charge separation that directly influences the emissivity of the thermal bremsstrahlung, since the emission efficiency drops significantly for like particles, proton-proton and electron-electron interactions, since there is no dipole component in the collisions. The bremsstrahlung is dominantly produced by radiating electrons that move in the

Coulomb field of protons (or positively charged ions) and the corresponding emissivity is given by Eq. (2.14), $\epsilon_{\rm Brems} \propto Z^2 n_{\rm i} n_{\rm e}$. Therefore, inside the sphere of the electrostatic influence of the black hole, the drop in bremsstrahlung emissivity is expected, creating a drop or "hole" in the surface density of the thermal bremsstrahlung, which is centred at Sgr A*.

Let us assume that Sgr A* is positively charged with the charge of $Q_\bullet$. The electrostatic potential further from the unscreened charged black hole is $\phi \approx Q_\bullet/(4\pi\epsilon_0 r)$. Under the assumption of the equilibrium Maxwell-Boltzmann distribution, it would yield to the charge separation and the corresponding charge particle density would vary as $n_{\rm q} \propto \exp\left(-q\phi/k_{\rm B}T_{\rm p}\right)$ on top of the power-law (Bondi) dependency $n_{\rm q} \propto r^{-3/2}$. In Fig. 2.7 (left panel), several number density profiles are plotted for electrons (solid lines) and protons (dashed lines) for increasing positive charge of the black hole, $Q_\bullet = 10^7 - 10^9\,{\rm C}$, including the zero charge.

To simulate the effect of an unscreened supermassive black hole with the positive charge of $Q_\bullet$, we use the Abel integral to obtain the projected luminosity profile $J(R_{\rm proj})$ from the deprojected one $L_{\rm brems}(r)$, see Eq. (2.14),

$$J(R_{\rm proj}) = 2\int_{R_{\rm proj}}^{R_{\rm t}} \frac{L_{\rm brems}(r) r\,{\rm d}r}{\sqrt{r^2 - R_{\rm proj}^2}}\,, \tag{2.46}$$

where the truncation radius $R_{\rm t}$ represents the length-scale where the thermal bremsstrahlung in the Galactic centre becomes negligible. We set the truncation radius to the Bondi radius (or approximately the stagnation radius), $R_{\rm t} \approx R_{\rm B} \approx R_{\rm stag}$, see also Eqs. (2.3) and (2.7).

The projected luminosity profile calculated using Eq. (2.46) is plotted in Fig. 2.7 (right panel). The solid line represents the case of the non-charged black hole, or a completely Debye-shielded black hole, and the dashed lines depict the cases of the supermassive black hole with the positive charge of $Q_\bullet = 10^7 - 10^9\,{\rm C}$,

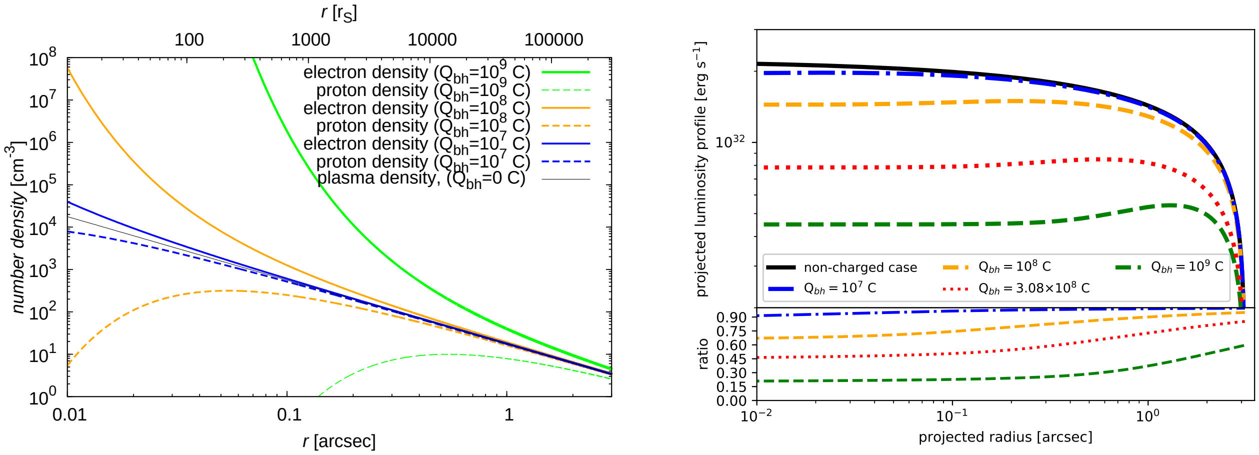

Figure 2.7: **Left:** Density profiles of electrons and protons in the Galactic centre as affected by a potential charged supermassive black hole. The black solid line represents the non-charged power-law. The coloured lines (blue, orange, green) manifest the changed profiles due to the presence of a positive point charge at the centre: the blue solid and dashed lines represent the case for $Q_\bullet = 10^7\,\mathrm{C}$, the orange lines stand for $Q_\bullet = 10^8\,\mathrm{C}$, and blue lines represent $Q_\bullet = 10^9\,\mathrm{C}$. **Right:** The *bremsstrahlung* surface brightness profile for the case of a non-charged black hole (solid black line) and for the case of a charged black hole in the Galactic centre with the charge of $10^7\,\mathrm{C}$, $10^8\,\mathrm{C}$, and $10^9\,\mathrm{C}$, represented by dashed blue, orange, and green lines, respectively. The drops in the brightness profile with respect to the non-charged case are depicted by a sub-plot that shows the ratio of the brightness profile for the charged case with respect to the non-charged case.

which have progressively smaller luminosity profile than the non-charged case. A special case is the equilibrium charge $Q_{\rm eq}$, see Eq. 2.19, up to which the electron and proton number densities are comparable within a factor of a few, $n_{\rm e} \approx n_{\rm p}$, see also Fig. 2.7 (left panel) for $Q_\bullet = 10^7 - 10^8\,C$. For larger black hole charges, the drop in the bremsstrahlung profile is more prominent, specifically reaching $\sim 37\%$ of the luminosity for non-charged case at the projected radius of $R \sim 1\,\mathrm{arcsec}$ for $Q_\bullet = +10^9\,\mathrm{C}$. In general, the difference in the electron and proton number densities by factor $f_{\rm n}$, $n_{\rm e} = f_{\rm n} n_{\rm p}$, corresponds to the black-hole charge of,

$$Q_\bullet(f_{\rm n}) = \frac{2\pi\epsilon_0 G(m_{\rm p} - m_{\rm e})}{e} M_\bullet + \frac{2\pi\epsilon_0 k_{\rm B} T_{\rm e,0} r_0}{e} \log f_{\rm n}\,, \tag{2.47}$$

where $T_{\rm e,0}$ is the electron ($\sim$ proton) temperature at radius r_0. Relation (2.47) holds under the assumption of the equilibrium Maxwell-Boltzmann distribution of electrons and protons.

The calculated surface brightness in Fig. 2.7 corresponds to the quiescent state of Sgr A*, i.e. this profile is expected if one can remove the nonthermal variable source at the very centre. In order to satisfactorily do that, the angular resolution of X-ray instruments should be better than ~ 0.1 arcsec. The effect of the bremsstrahlung flattening or drop is just at (or rather beyond) the limit of what can be measured right now. Therefore this experiment and the analysis speaks for next generation X-ray telescopes that have a half and the full order of magnitude better resolving powers compared to the current situation.

[93] construct a projected bremsstrahlung profile in their Fig. 6. At the 1σ level, the profile shows a decrease in the brightness at radii $\lesssim 0.4''$. This is, however, still consistent within uncertainties with the flat and the slightly rising profile at the 3σ level. Flat to slightly decreasing luminosity profile allows us to put the upper limit on the black hole charge if we assume that the charge is not screened. The projected profile inferred from Chandra observations by [93] is consistent within the uncertainty with all profiles up to the equilibrium value of $Q \lesssim Q_{\rm eq} \approx 3.1 \times 10^8\,{\rm C}$, see Fig. 2.7 (right panel). For larger charge values, the projected profile is expected to decrease below $R = 2''$, see the green dashed curve in Fig. 2.7, which corresponds to $Q_\bullet = 10^9\,{\rm C}$. The equilibrium value of the black hole charge $Q_{\rm eq} \approx 3.1 \times 10^8\,{\rm C}$, which was derived based on the classical mass segregation arguments, see Eq. (2.19), corresponds to the charging/discharging length-scale of $R_{\rm charge} \approx 0.21''$ according to Eq. (2.42), assuming the free-fall flow. This scale is comparable to the projected radius, where the observed bremsstralung profile is consistent with the flat to decreasing flux density [93].

Within uncertainties, this is consistent with the constraints given by induction mechanism presented in section 2.2.1, which gives an upper limit of the order of 10^{15} C. In the future, if the angular resolution of X-ray instruments is one half to one order of magnitude better, one can distinguish the unresolved central component from the surroundings and it will be possible to model it away without assuming intrinsic physics. One could, in particular, take multiple images of the flares and model a variable point source and an extended quiescent component. Hence, this procedure should yield a well-constrained background with a more precise brightness profile, based on which the decrease could be confirmed or excluded.

In case the drop in the bremsstrahlung profile is confirmed on sub-arcsecond scales from Sgr A*, one should naturally consider also other possibilities for the decrease, in particular the lower temperature due to plasma cooling and/or the decrease in the ambient gas density. However, the presence of small electric charge associated with Sgr A* remains as an interesting possibility for both explaining the bremsstrahlung flattening as well as for testing the presence of the Debye-shell effect around supermassive black holes immersed in plasma.

Effect of charge on the innermost stable circular orbit of Sgr A*

One of the important characteristics of black holes in accretion theory playing crucial role in observational constraints of black hole parameters is the location of the innermost stable circular orbit (ISCO). For a non-rotating neutral black hole, the ISCO is located at $r = 3r_S$. Rotation of black hole shifts the position of ISCO of co-rotating particles towards the horizon matching with it in the extremely rotating case $a_\bullet = J_\bullet/M_\bullet = 1$. The presence of the black hole charge acts in a similar way to the ISCO, shifting it towards the horizon for both neutral and charged particles [89]. Motion of charged particle with mass $m_{\rm par}$ and charge $q_{\rm par}$ moving around non-rotating black hole with charge $Q_\bullet$ is restricted by the energy boundary function or the effective potential

$$\frac{E_{\rm par}}{m_{\rm par}c^2} = \frac{k_1 q_{\rm par}\ Q_\bullet}{r} + \left[\left(1 - \frac{1}{r} + \frac{k_2 Q_\bullet^2}{r^2}\right)\left(1 + \frac{L_{\rm par}^2}{m_{\rm par}c^2 r^2}\right)\right]^{1/2}, \tag{2.48}$$

where $E_{\rm par}$ and $L_{\rm par}$ are the energy and angular momentum of charged particle and r is the radius given in the units of gravitational radius r_S. At infinity or in the absence of the fields $E_{\rm par}/(m_{\rm par}c^2) = 1$. For neutral particles at ISCO of neutral black hole $E_{\rm par}/(m_{\rm par}c^2) = \sqrt{8/9}$. The constants k_1 and k_2 are the coupling constants responsible for the interaction between charges and the gravity. For an electron around Sgr A*, the constants can be estimated as

$$k_1 = \frac{1}{m_e c^2 r_S^*} \approx 1.03 \times 10^{-6} \frac{\rm s^2}{\rm g\ cm^3}, \tag{2.49}$$

$$k_2 = \frac{G}{c^4 r_S^{2*}} \approx 5.92 \times 10^{-74} \frac{\rm s^2}{\rm g\ cm^3}. \tag{2.50}$$

Smallness of the constant k_2 representing the gravitational effect of the black hole charge imply that the effect of the black hole charge on the spacetime curvature can be neglected in most of the physically relevant cases. Indeed, the possible charge of SMBH at the Galactic centre restricted by the upper limits (see Section 2.2.1) is not able to provide sufficient curvature of the background black hole geometry, and thus, does not influence the motion of neutral particles. However, for the motion of charged particles the effect of even small black hole charge can sufficiently shift the location of orbits, due to large values of the charge to mass ratio for elementary particles.

The location of the ISCO of charged particles around Sgr A* as a function of the black hole charge $Q_\bullet$ is plotted in Fig. 2.8 (right). As one can see from Fig. 2.8, the position of the ISCO for electrons shifts from $r = 3r_S$ (corresponding to the ISCO of neutral particles) towards or outwards from black hole starting already from relatively small charges of the order of 10^3 - 10^5C. Thus, even a small black hole charge which does not affect the background geometry can sufficiently shift the ISCO of free electrons and protons orbiting around Sgr A*. In case of like-charges (e^-, $Q_\bullet < 0$ or p^+, $Q_\bullet > 0$) the ISCO can be shifted from the distance $r = 3r_S$ up to $r = 1.83\ r_S$, which can mimic the black hole spin with the value of $a_\bullet = 0.64$. This should be taken into account in the spin determination of Sgr A*, since previous estimates are close to this value, in general above ~ 0.4 [82, 122, 123].

Particles at the ISCO can have ultrarelativistic velocities, which leads to the emision of electromagnetic radiation from the inner parts of the accretion flow. The shift of the ISCO towards the event horizon increases the gamma-factor of charges and the gravitational redshift $z = (\lambda_0 - \lambda)/\lambda_0$ of emitted photons, where λ and λ_0 are the wavelengths of a photon measured by local and detached observers. The shift of the ISCO radius from $r = 3r_S$ (neutral) to $r = 1.83\ r_S$ (charged) increases the gravitational redshift of emitted electromagnetic radiation from $z = 0.225$ to $z = 0.485$.

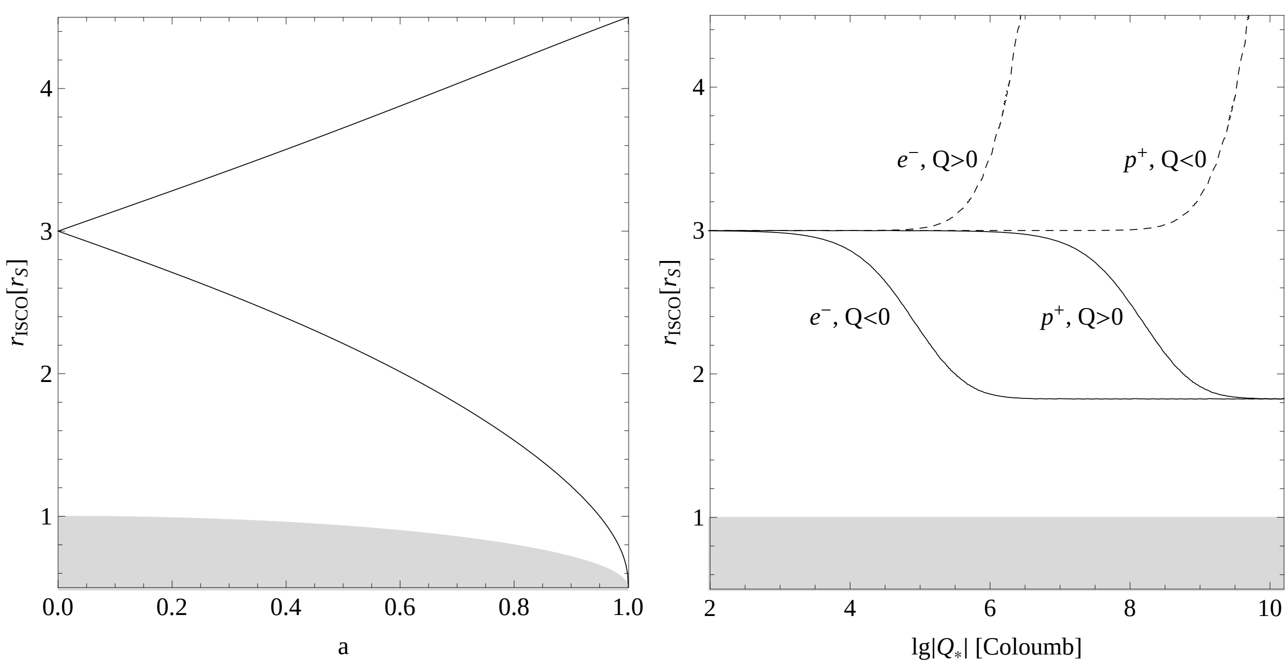

Figure 2.8: **Left panel:** The position of the ISCO as a function of the black hole spin: the upper line represents the retrograde spin, the lower line the prograde one. **Right panel:** The ISCO position for charged particles – electrons (e^-) and protons (p^+) – that orbit the SMBH (Sgr A*) that has either positive ($Q_\bullet > 0$) or negative electric charge ($Q_\bullet < 0$).

Table 2.1: Summary of the constraints on the electric charge of the SMBH at the Galactic centre presented in Section 2.2.1.

Process	Limit	Notes
Mass difference between p and e	$Q_{\rm eq} = 3.1 \times 10^{8} \left(\frac{M_{\bullet}}{4\times10^{6}\,M_{\odot}}\right) \mathrm{C}$	stable charge
Accretion of protons	$Q^{+}_{\rm max} = 6.16 \times 10^{8} \left(\frac{M_{\bullet}}{4\times10^{6}\,M_{\odot}}\right) \mathrm{C}$	unstable charge
Accretion of electrons	$Q^{-}_{\rm max} = 3.36 \times 10^{5} \left(\frac{M_{\bullet}}{4\times10^{6}\,M_{\odot}}\right) \mathrm{C}$	unstable charge
Magnetic field & SMBH rotation	$Q^{\rm max}_{\bullet\rm ind} \lesssim 10^{15} \left(\frac{M_{\bullet}}{4\times10^{6}M_{\odot}}\right)^{2} \left(\frac{B_{\rm ext}}{10\mathrm{G}}\right) \mathrm{C}$	stable charge
Extremal SMBH	$Q_{\rm max} = 6.86 \times 10^{26} \left(\frac{M_{\bullet}}{4\times10^{6}\,M_{\odot}}\right) \sqrt{1-\tilde{a}_{\bullet}^{2}}\,\mathrm{C}$	uppermost limit

2.2.3 Summary on the black hole charge

In this section, we summarize the constraints on the electric charge of the Galactic centre black hole. Subsequently, we look at the potential effects of the rotation on the maximum electric charge. In addition, we discuss potential non-electric origins of the black hole charge.

Charge values associated with the Galactic centre black hole

In Section 2.2.1, we studied limits on the electric charge of Sgr A* based on different mechanisms, namely the accretion of charged constituents of plasma and the induction mechanism based on a rotating SMBH in the external magnetic field. We summarize these constraints in Table 2.1. The charging based on accretion of protons or electrons is not stable and leads to the discharging on the discharging time-scale. However, the rotation of the SMBH within the external magnetic field is a plausible process that can result in a stable charge of the SMBH not only in the Galactic centre but in galactic nuclei in general.

All the upper limits on the electric charge in Table 2.1 are at least ten orders of magnitude below the maximum charge (see Eq. 2.23) and hence the space-time metric is not affected. However, the dynamics of charged particles is significantly affected by even these small values and can be observationally tested via the change in the bremsstrahlung brightness profile.

Effect of rotation

As was already indicated by Eq. (2.22), the rotation of the SMBH does effect the value of the maximum allowed charge for a black hole. For the maximum rotation, $\tilde{a}_\bullet = 1$, the maximum charge vanishes completely. However, the dependence of $Q_{\rm max}^{\rm rot}$ on $a_\bullet$ is only prominent for large spins, see also the left panel of Fig. 2.3. In astrophysical relevant systems, the maximum rotation parameter is $a_\bullet^{\rm max} = 0.998$ [124], which results in $Q_{\rm max}^{\rm rot} \approx 0.06\, Q_{\rm max}^{\rm norot} = 4.3 \times 10^{25}\, C$. This is still about ten orders of magnitude larger than the constraints analysed in Section 2.2.1. For Sgr A*, the spin is estimated to be even smaller, $a_\bullet \sim 0.5$ [123, 122]. Therefore, the previous analysis is valid also for the case when Sgr A* has a significant spin.

Non-electric origin of the black hole charge

The black-hole charge can also be of a non-electric origin [120], namely a tidal charge induced by an extra dimension in the Randall-Sundrum (RS) braneworld solutions or 5D warped geometry theory [125, 126, 127], in which the observable Universe is a $(3+1)$-brane (domain wall) that includes the standard matter fields and the gravity field propagates further to higher dimensions. The RS solution yields the 4D Einstein gravity in the low energy regime. However, in the high energy regime deviations from the Einstein solution appear, in particular in the early universe and the vicinity of compact objects [128]. Both the high-energy (local) and the bulk stress (non-local) affects the matching problem on the brane in comparison with Einstein solutions. In particular, the matching does not result in the exterior Schwarzschild metric for spherical bodies in general [129].

A class of the RS brane black-hole solutions is obtained by solving the effective gravitational field equations given the spherically symmetric metric on the $(3+1)$-brane [130]. These black holes are characterized by Reissner-NordstrΓ¶m-like static metric which has the non-electric charge b instead of the standard Q^2. This charge characterizes the stresses induced by the Weyl curvature tensor of the bulk space, i.e. 5D graviton stresses that effectively act like tides. Thus, the parameter b is often referred to as the tidal charge and can be both negative and positive. Detailed studies of the optical phenomena associated with brany black holes, in particular quasiperiodic oscillations (QPOs) that are of an astrophysical relevance, were performed in several studies [131, 128].

As pointed by [120], the tidal charge could be tested by detecting the black hole shadow. While the electric charge causes the shadow to shrink, which is only noticeable for nearly extremal charges (see Section 2.2.2), the tidal charge could act in the opposite sense – enlarging the shadow size. Thus, if a noticeable change in the shadow size is detected, it would most likely be caused by non-electric tidal charge since the electric charge is expected to have negligible effects on the metric as we showed in Section 2.2.1 and summarized in Section 2.2.3.

Comparison with previous studies

[120] uses an argument that the measured core size of Sgr A* of $\sim 40\,\mu$as [76, 132] is more consistent with the Reissner-Nordstrom black hole with the charge close to the extremal value of $Q_{\rm max}^{\rm norot}$ than with the Schwarzschild black hole whose shadow is expected to be $\sim 53\,\mu$as. However, one needs to stress that the core size does not directly express the shadow size at all since it does not have to be centered at the black hole – it can, for instance, be caused by a Doppler-boosted accretion flow or the jet-launching site [121, 70]. Hence, the charge constraint given by [120] is uncertain at this point and should be further tested when the analysis of the observations by the Event Horizon Telescope[2] is available.

[133] gives the following estimate on the charge of Sgr A* based on the geodesic

[2] http://eventhorizontelescope.org/

trajectories of the orbital motion [134], in particular using S2 star orbit, $Q_{\bullet} \lesssim 3.6 \times 10^{27}\,$C, leaving space for the charge larger than an extremal value.

In comparison with [133] and [120], we take into account the presence of plasma and the magnetic field in the vicinity of Sgr A*, which leads to tighter constraints and significantly smaller values, see Table 2.1. Moreover, our suggested test based on the bremsstrahlung brightness profile, see Subsec. 2.2.2, is significantly more sensitive to smaller charge than the shadow size or stellar trajectories.

2.3 Flaring hot-spot orbiting Galactic center black hole

Recently, near-infrared GRAVIY@ESO observations at $2.2\,\mu$m have announced detection of three bright "flares" in the vicinity of the Galactic center black hole that exhibited orbital motion at the radius about $6 - 11$ gravitational radii of $4.14 \times 10^6\,M_{\odot}$ black hole. There are strong indications of the presence of highly aligned magnetic field at the Galactic center. Relativistic motion of a plasma in magnetic field leads to the charge separation in a plasma and non-negligible net charge density. Therefore, we investigate the effect of electromagnetic interaction on the properties and dynamics of flare components around Sgr A*. In particular we give constraints on the charge of the flare components being $< 10^{13-16}$C. This corresponds to the net charge number density of order 10^{-5}cm^{-3}, while the plasma number density is of order 10^{6-8}cm^{-3}. The electromagnetic effects on the hot-spot dynamics were previously not taken into account. In particular, we address how the electromagnetic field can affect the measuring of the spin of Sgr A*.

2.3.1 Detection of orbital motion around SgrA*

Compact radio source Sgr A* associated with the supermassive black hole and the dynamical centre of our Galaxy is a highly-variable source across all wavelengths [69, 135]. The source structure of Sgr A* was resolved out on event-horizon scales by the Very Long Baseline Interferometry (VLBI) technique at 1.3 mm [76, 132, 136], which showed that the bulk of emission of Sgr A* may not be centered at the black hole itself. The VLBI study by [136] inferred from the linearly polarized emission that partially ordered magnetic field is present on the scale of 6 Schwarzschild radii. They also detected an intro-hour variability time-scale associated with this field. These findings are consistent with the recent GRAVITY@ESO[3] discovery of continuous positional and polarization offsets of emission centroids during high states of Sgr A* activity, so-called "flares", in the near-infrared K_s-band ($2.2\,\mu$m) continuum emission [25]. The linear polarization angle turns around continuously with the period comparable to the orbital motion of the emission centroid or hereafter called *hot spot*, $P_{\rm HS} = 45(\pm 15)\,$min, which implies the ordered poloidal magnetic field, i.e. perpendicular to the orbital plane, while for the toroidal geometry one expects two polarization loops per orbital period [137, 138]. The presence of dynamically significant magnetic field in the accretion zone close to the innermost stable circular orbit is also consistent with the magnetic field strength of $B \geq 50\,\mu$G at the projected distance of $R \sim 0.1\,$pc as inferred from the Faraday rotation measurements of the magnetar J1745-2900 [85].

The present activity of Sgr A* is very low and in comparison with active galactic nuclei (AGN), it can be generally characterized as extremely low-luminous [135, 70], which stems from the comparison of its theoretical Eddington limit,

$$L_{\rm Edd} = 5.2 \times 10^{44} \left(\frac{M_\bullet}{4.14 \times 10^6\, M_\odot}\right) {\rm erg\,s^{-1}}\,, \tag{2.51}$$

and its eight orders-of-magnitude smaller bolometric luminosity of $\sim 10^{36}\,{\rm erg\,s^{-1}}$ inferred from observations and explained by radiatively inefficient accretion flow models (RIAFs) [139, 140]. The mass of Sgr A* in Eq. (2.51) is scaled to the value

[3] A near-infrared, beam-combining interferometry instrument operating in K_s-band continuum, which is capable of high-resolution imaging (resolution of 3 mas) and astrometry (resolution $\sim 20 - 70\,\mu as$).

derived from the most recent S2-star observations by [17], see also for comparison [73, 74, 75], which corresponds to the gravitational radius of $R_{\rm g} = GM_{\bullet}/c^2 = 6.106 \times 10^{11}\,{\rm cm} \sim 10^{12}\,{\rm cm}$ that we apply in the further analysis.

Sgr A* is surrounded by ~ 200 massive HeI emission-line stars and it is thought to capture their wind material with the estimated rate of $\dot{M}_{\rm B} \approx 10^{-5}\,M_{\odot}\,{\rm yr}^{-1}$ at the Bondi radius of $r_{\rm B} = 4''(T_{\rm a}/10^7\,{\rm K}) \approx 0.16\,{\rm pc} = 8.1 \times 10^5\,R_{\rm g}$ [100, 91, 141], where the gravitational pull of the SMBH prevails over that of the thermal gas pressure with the temperature of $T_{\rm a}$. From the submm Faraday rotation measurements within the inner $r \lesssim 200\,R_{\rm g}$ it was inferred that Sgr A* accretes at least two orders of magnitude less than the Bondi rate, $\dot{M}_{\rm acc} \approx 2 \times 10^{-7} - 2 \times 10^{-9}\,M_{\odot}\,{\rm yr}^{-1}$ [116], hence most of the material captured at the Bondi radius is expelled and leaves the system in an outflow, which is also consistent with the RIAF solutions with the flat density profile $n(r) \propto r^{-3/2+p}$ with $p = 1$ [92]. The inflow-outflow RIAF models (disc-jet/wind or advection-dominated accretion flow and jet – jet-ADAF) can inhibit the accretion rate on smaller spatial scales by the transport of energy released during accretion to larger radii [142, 91, 143, 144, 145], which reduces the accretion rate to $\lesssim 1\%$ of the Bondi rate and the jet-ADAF models can generally capture the main features of the Sgr A* broadband spectrum. The extremely low-luminosity of Sgr A* is thus best explained by the combination of a low accretion rate $\dot{M}_{\rm acc}$ and very low radiative efficiency of the accretion flow $\eta \approx 5 \times 10^{-6}$ [146], which is four orders of magnitude below the standard 10% efficiency applicable to luminous AGN with significantly higher accretion rates.

In the radio/mm domain, the flux density generally increases with frequency with the rising spectral index from $\alpha = 0.1 - 0.4$ to $\alpha = 0.76$ at 2-3 mm[4], and with the clear peak or bump close to 1 mm, which is referred to as submm-bump [147, 98, 148]. Below 1 mm the medium gets optically thin and the flux density

[4]Using the notation $S_\nu \propto \nu^\alpha$

gradually drops all the way X-ray wavelengths, where the quiescent counterpart of Sgr A* was detected with the unabsorbed luminosity of $L_{\rm x} \approx 4 \times 10^{32}\,{\rm erg\,s^{-1}}$ [100, 91], with no detected quiescent counterpart in the infared domain. See, however, the upper limits on the FIR flux density based on the detected variability by [149]. While in the radio/mm domain, Sgr A* is mildly variable, it exhibits order-of-magnitude high states or flares in the infrared and X-ray domain a few times per day on the timescale of ~ 1 hour [150, 151, 152, 80, 84, 79, 153, 25], with infrared flares being linearly polarized with the polarization degree of $20\% \pm 15\%$ and a rather stable polarization angle of $13^{\circ} \pm 15^{\circ}$[154], which plausibly reflects the overall stability of the disc-jet system of Sgr A*.

The $K_{\rm s}$-band observations by GRAVITY@ESO [25] brought the first direct evidence that flares are associated with hot spots. The GRAVITY observations of hot spots close to the innermost stable circular orbit (ISCO) of Sgr A* have enabled to fit their orbital periods as well as orbital radii with the equatorial circular orbits of neutral test particles around rotating Kerr black hole of mass 4.14 million solar masses.

The origin and nature of flares/hot spots still remains unclear. Despite many speculations, including their connection to the tidal disruption of asteroids [155], they are most likely connected to dynamical changes in the hot, magnetized accretion flow. As transient phenomena, they could originate from magnetohydrodynamic instabilities or magnetic reconnection events as is the case of X-ray flares on the Sun [156]. The model of ejected plasmoids during reconnection events is supported by their statistical properties, namely the count rate can be fitted with the power-law in the X-ray-, infrared-, submm- and radio- domain, ${\rm d}N/{\rm d}E \propto E^{-\alpha}{\rm d}E$, which is consistent with the self-organized criticality phenomena of spatial dimension $S = 3$ [157, 158, 159, 153].

On the other hand, the relativistic motion of a plasma in the presence of magnetic field leads to the charge separation in a plasma and consequent grow of its net charge density. This charge rises in a compensation of an electric field in the co-moving frame induced by the motion of a plasma in external magnetic field. In case when the rotating plasma is a star threaded onto magnetic field, arising charge density is known as the Goldreich-Julian charge density [160]. Partially ordered magnetic field in the vicinity of Sgr A* has been estimated with the strength of $10 - 100$G. Observations of horizontal polarization loops with the timescales comparable to the orbital periods of the recently observed bright flares imply the direction of magnetic field lines perpendicular to flares' orbital plane. This implies that the hot spots associated with flares orbiting at the relativistic orbits can possess net electric charge due to charge separation in a plasma.

In this section we focus on the possible interplay between gravitational and electromagnetic fields in the interpretation of the observational features of flares. Orthogonal orbital orientation with respect to the magnetic field lines of three most recent hot-spots and possible charge separation in a plasma may lead to the appearance of an external Lorentz force arising from interactions of the flare components with magnetic field. Taking into account the error bars of the measurement arising mainly due to astrometric errors and incomplete orbital coverage we put constraints on the strength of the Lorentz force, electric charges of hot spots and net charge densities.

Similar situation may occur if the black hole possess small non-vanishing electric charge, which can be induced due so-called Wald mechanism – twisting of magnetic field lines due to black hole rotation [20]. Such an induced charge of Sgr A* has an upper limit of $< 10^{15}$C [4]. In that case the black hole may act as a pulsar, leading to the charge separation in a magnetosphere of a black hole [31]. Further this leads to the inclusion of additional "electrostatic" interaction between black hole and the flare components leading to certain charge constraints for hot spots.

Electromagnetic interactions of flare components with external electromagnetic fields leads to uncertainty in the determination of the black hole spin. Depending on the orientation of the Lorentz force and the electrostatic interaction between hot-spot and black hole, orbital period and radius of the hot-spot can be shifted in both ways which in certain level can mimic the effect of the black hole's spin.

Below we consider hot spot models with various charging mechanisms combined with observational data. It is worth noting that all obtained constraints on the charge values of hot spots have comparable orders of magnitude.

2.3.2 Charge separation in a plasma surrounding Sgr A*

It is usually assumed that a plasma in most cases including surroundings of astrophysical black holes is electrically neutral due to neutralization of charged plasma in relatively short timescales. Any oscillation of net charge density in a plasma is supposed to decay very quickly due to induction of large electric field caused by charge imbalance. However, in the presence of external magnetic field and when the plasma is moving at relativistic speeds, one can observe the charge separation effect in a plasma and consequently measure the net charge density. Applied to rotating neutron stars in magnetic field, this, special relativistic effect of plasma charging is known as the Goldreich-Julian (GJ) charge density [160]. In fact, the motion of a plasma induces an electric field, which in the co-moving frame of a plasma should be neutralized, which leads to the appearance of the net charge in the rest frame. GJ charge density is usually referred to puslar magnetosphere, although is aplicable in more general case as we should below

Neglecting for now the general-relativistic effects Maxwell's equations read

$$\nabla \cdot \mathbf{E} = 4\pi\rho, \qquad \nabla \cdot \mathbf{B} = 0, \tag{2.52}$$

$$\nabla \times \mathbf{E} = -\frac{\partial \mathbf{B}}{\partial t}, \qquad \nabla \times \mathbf{B} = 4\pi\mathbf{j} + \frac{\partial \mathbf{E}}{\partial t}. \tag{2.53}$$

where ρ and $\mathbf{j}$ is the charge and current densities. For a frame moving with a system with the velocity v with respect to the rest frame the Lorentz transformations lead to

$$\mathbf{E}' = \gamma(\mathbf{E} + \mathbf{v} \times \mathbf{B}) - \frac{\gamma^2}{\gamma + 1}\mathbf{v}(\mathbf{v} \cdot \mathbf{E}), \tag{2.54}$$

$$\mathbf{B}' = \gamma(\mathbf{B} + \mathbf{v} \times \mathbf{E}) - \frac{\gamma^2}{\gamma + 1}\mathbf{v}(\mathbf{v} \cdot \mathbf{B}), \tag{2.55}$$

where "primes" denote the quantities measured with respect to the inertial frame moving at the given moment together with the system and $\gamma = (1 - v^2)^{-1/2}$. In a co-moving frame of the system the current density is connected with the electric field by the Ohm's law $\mathbf{j}' = \sigma \mathbf{E}'$, where σ is the conductivity of the medium. For an observer at rest one gets the Ohm's law in the form

$$\mathbf{j} = \gamma\sigma \left(\mathbf{E} + \mathbf{v} \times \mathbf{B} - \mathbf{v} \cdot (\mathbf{v} \cdot \mathbf{E})\right) + \rho\mathbf{v}. \tag{2.56}$$

Let us now assume that the matter containing plasma is perfect electrical conductor. This implies that the following relation holds

$$\mathbf{E} = -\mathbf{v} \times \mathbf{B}, \tag{2.57}$$

From this it follows that an external observer measures the induced electric field which arises in order to compensate the electric field in the co-moving frame of the system.

One can express velocity in terms of orbital angular velocity of the hot-spot moving around black hole in equatorial plane, $\mathbf{v} = \mathbf{\Omega} \times \mathbf{R}$. Substituting (2.57) into the first equation of (2.52) in terms of angular velocity we get the net charge density in the form

$$\rho = -\frac{1}{4\pi}\Omega B. \tag{2.58}$$

2.3.3 Constraints on the hot-spot parameters

For the mean orbital period of 45min at ISCO of Sgr A* immersed into magnetic field with equipartition strength of 10G and the axis orthogonal to the orbital

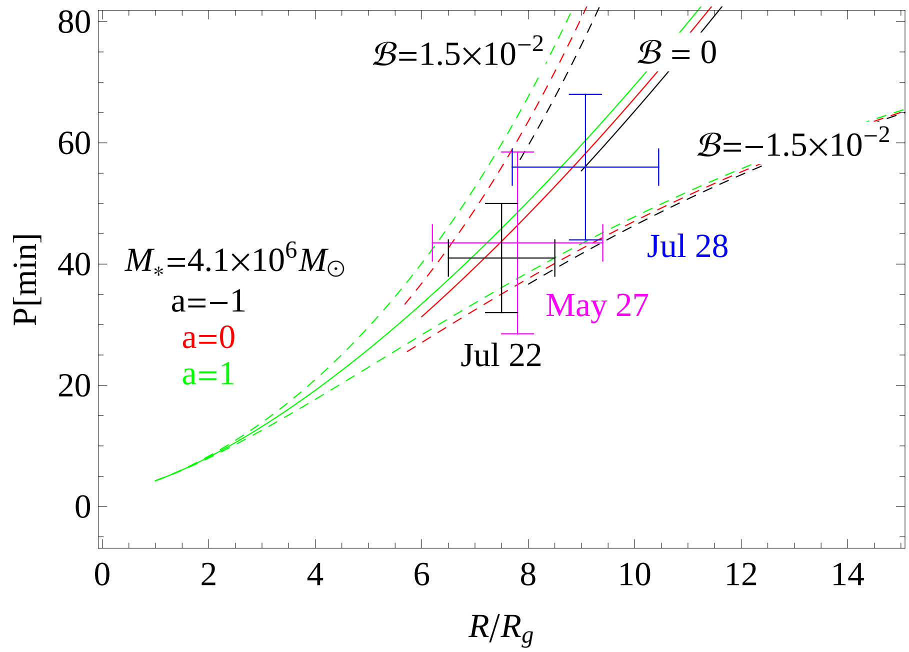

Figure 2.9: Orbital period - radius relations of three flares observed by GRAVITY on July 22 (black), May 27 (pink) and July 28 (blue) fitted with the charged hot-spot orbiting around Kerr black hole of mass $4.14 \times 10^6 M_\odot$ immersed into external magnetic field oriented perpendicular to the orbital plane. Case $\mathcal{B} = 0$ (solid lines) corresponds to the pure Kerr blak hole case, while $\mathcal{B} = \pm 1.5 \times 10^{-2}$ denotes the ratio of the Lorentz force to the gravitational force. The mid value of all three flares correspond to the value of parameter $\mathcal{B} = -3 \times 10^{-3}$.

plane, we get the number density of net charge particles ρ_q of order

$$\rho_q \approx 2 \times 10^{-5} \left(\frac{B}{10\text{G}} \right) \left(\frac{v}{v_{\text{isco}}} \right) \text{cm}^{-3}. \tag{2.59}$$

Assuming a spherical volume of the radius $R \sim R_s \approx 10^{12}$cm we get the net charge excess of the order

$$|q| \approx 3 \times 10^{12} \left(\frac{B}{10\text{G}} \right) \left(\frac{v}{v_{\text{isco}}} \right) \left(\frac{R}{R_s} \right)^3 \text{C}. \tag{2.60}$$

If the hot-spot possesses the charge of such an order, this can imply that the motion of the hot-spot can be considerably affected by the magnetic field due to the action of the Lorentz force on the dynamics.

Magnetic field influence on the motion of hot spot

Relative influence of magnetic and gravitational fields on the motion of hot spot can be described by dimensionless parameter $\mathcal{B} = q\, G\, B\, M_*/(m_{\rm hs} c^4)$, where B is the strength of magnetic field, M_* is the black hole mass, q and $m_{\rm hs}$ are the charge and the mass of the hot spot and G and c are constants. Hereafter we call $\mathcal{B}$ as magnetic parameter. Given the period-radius relations of three flares observed in 2018 July 22, May 27 and July 28, we put constraints on the magnetic parameter $\mathcal{B}$ in Figure 2.9 for the orbits of charged hot spot in external magnetic field oriented in perpendicular direction to the orbital plane. One can see that the spin parameter of the black hole does not play crucial role in the period-radius relation of circular orbits, while magnetic parameter shifts the orbits and periods significantly. Depending on the orientation of the Lorentz force the shift of the orbital frequency can occur in both direction for given value of the orbital radii [36].

Various measurements and estimates of magnetic field strength in the vicinity of Sgr A* suggest the equipartition magnetic field of order of $B \sim 10$G [70]. This gives constraints on the specific charge (charge to mass ratio) following Figure 2.9, of order $q/m_{\rm hs} \approx \pm 7 \times 10^{-4}$C/g. For comparison, this ratio for electrons is of order $\sim -10^{8}$C/g and for protons is $\sim 10^{5}$C/g. This implies that the observed flares can be considered as quasi-neutral, with the charge concentration of 1 charged particle to at least 10^8 neutral particles.

Observed flares have strengths 0.4 of S2 star in K-band, which corresponds to 5.2mJy. Other parameters of the flares can be estimates using the results of previous flare studies from Sgr A* observed in millimeter, near-infrared and to X-ray parts of spectra, summarized in [84]. From the adiabatic expansion of the emitting sources observed at speeds $\sim 0.01c$ [161], light travel arguments give constraints on the flare diameter $\sim GM_*/c^2 \approx 10^{12}$cm. Number densities of flares are found to be of order of $\sim 10^6 - 10^8 \mathrm{cm}^{-3}$ derived either from the synchrotron model or radio Faraday rotation of the polarization planes [84, 162]. This gives us the estimates of the masses of flares with an upper limit $\sim 10^{17} - 10^{20}$g depending on whether the radiation comes from electrons or protons. This implies that the upper limit of flare charges vary in the range $q_{\rm hs}^{\rm min} < q < q_{\rm hs}^{\rm max}$, where

$$
\begin{aligned}
q_{\rm hs}^{\rm min} &\approx -10^{13} \left(\frac{B}{10\mathrm{G}}\right) \left(\frac{m_{\rm hs}}{10^{17}\mathrm{g}}\right)^{-1} \left(\frac{M_{\rm SgrA^*}}{4\times 10^6 M_\odot}\right)^{-1} \mathrm{C}\,, \\
q_{\rm hs}^{\rm max} &\approx 10^{16} \left(\frac{B}{10\mathrm{G}}\right) \left(\frac{m_{\rm hs}}{10^{20}\mathrm{g}}\right)^{-1} \left(\frac{M_{\rm SgrA^*}}{4\times 10^6 M_\odot}\right)^{-1} \mathrm{C}\,,
\end{aligned}
$$

for the magnetic parameter $-1.5\times 10^2 < \mathcal{B} < 1.5\times 10^2$ constrained in Figure 2.9.

Synchrotron radiation from charged hot spot

Emission of flares observed at X-ray wavelengths gives the flare luminosity of order 10^{33}erg s^{-1} [162]. This can be compared with the luminosity of a hot spot as a single charge emitting synchrotron radiation in magnetic field. Intensity of radiation in all directions of the hot spot orbiting black hole in magnetic field in fully relativistic approach is given by [43, 44]

$$
L = \frac{2}{3}\frac{q^4 B^2 v^2 \gamma^2}{m^2 c^3} \left(1 - \frac{2R_g}{R_0}\right)^3 \mathrm{erg\ s^{-1}}, \tag{2.61}
$$

where v is the velocity of the hot spot in units of the speed of light, R_0 is the orbital radius. Equalizing (2.61) to 10^{33}erg s^{-1} for the hot spot at ISCO of nonrotating black hole we get another limit for the charge of the hot spot as $q_{\rm hs}^{\rm min} < q < q_{\rm hs}^{\rm max}$, where

$$
q_{\rm hs}^{\rm min} \approx -10^{14} \left(\frac{B}{10\mathrm{G}}\right)^{-\frac{1}{2}} \left(\frac{m}{10^{17}\mathrm{g}}\right)^{\frac{1}{2}} \left(\frac{L}{10^{33}\mathrm{erg\,s^{-1}}}\right)^{\frac{1}{4}} \mathrm{C}, \tag{2.62}
$$

$$
q_{\rm hs}^{\rm max} \approx 10^{16} \left(\frac{B}{10\mathrm{G}}\right)^{-\frac{1}{2}} \left(\frac{m}{10^{20}\mathrm{g}}\right)^{\frac{1}{2}} \left(\frac{L}{10^{33}\mathrm{erg\,s^{-1}}}\right)^{\frac{1}{4}} \mathrm{C}. \tag{2.63}
$$

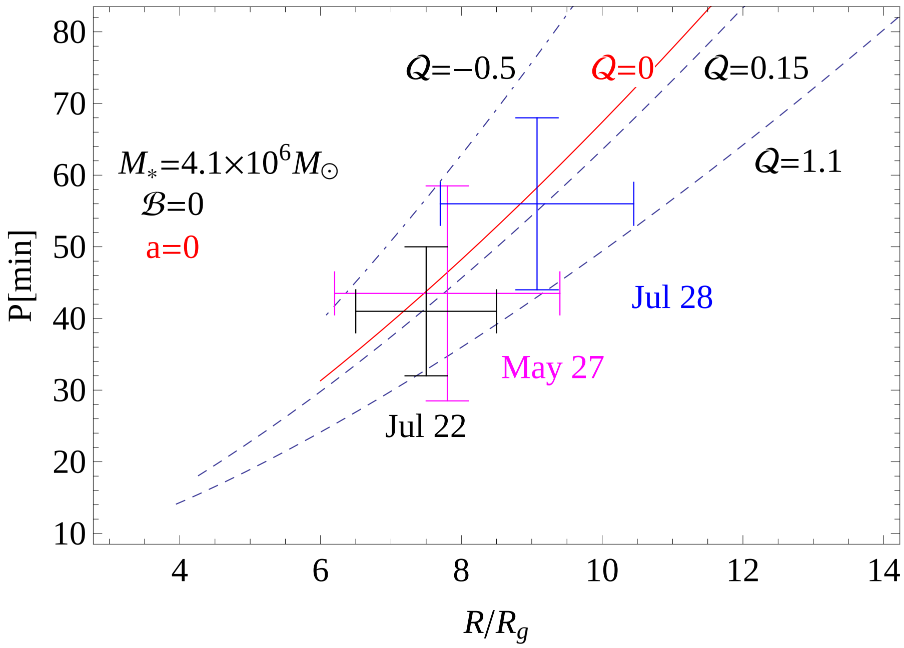

Figure 2.10: Same as Fig.2.9 constraints for weakly charged black hole

Effect of the black hole charge

Given that the hot spot carries small electric charge one can also consider the possible influence on its motion of unscreened charge of the black hole, which has been recently estimated with an upper limit of $\sim 10^{15}$C [4]. Results are summarized in Figure 2.10. Given that the black hole possess Wald charge $Q_{\rm W} = 2G^2aMB/c^4 \approx G^2M^2B/(2c^4)$ we get the limits for the charge of hot spot as follows

$$q_{\rm hs}^{\rm min} \approx -10^{15}\left(\frac{Q}{Q_{\rm W}(\sim 10^{15}C)}\right)\left(\frac{m}{10^{17}{\rm g}}\right){\rm C}, \tag{2.64}$$

$$q_{\rm hs}^{\rm max} \approx 10^{18}\left(\frac{Q}{Q_{\rm W}(\sim 10^{15}{\rm C})}\right)\left(\frac{m}{10^{20}{\rm g}}\right){\rm C}. \tag{2.65}$$

One can conclude that combining various methods of estimates of the charge of the flare component we get the charge of order from 10^{12}C up to 10^{16}C.

2.4 Stellar fly-by close to the Galactic centre black hole

The Galactic centre Nuclear Star Cluster is one of the densest stellar clusters in the Galaxy. The stars in its inner portions orbit the supermassive black hole associated with compact radio source Sgr A* at the orbital speeds of several thousand km/s. The B-type star S2 is currently the best case to test the general relativity as well as other theories of gravity based on its stellar orbit. Yet its orbital period of $\sim 16\,\mathrm{yr}$ and the eccentricity of ~ 0.88 yields the relativistic pericentre shift of $\sim 11'$, which is observationally still difficult to reliably measure due to possible Newtonian perturbations as well as reference-frame uncertainties. A naive way to solve this problem is to find stars with smaller pericentre distances, $r_{\rm p} \lesssim 1529$ Schwarzschild radii (120 AU), and thus more prominent relativistic effects. In this contribution, we show that to detect stars on relativistic orbits is progressively less likely given the volume shrinkage and the expected stellar density distributions. Finally, one arrives to a sparse region, where the total number of bright stars is expected to fall below one. One can, however, still potentially detect stars crossing this region. In this contribution, we provide a simple formula for the detection probability of a star crossing a sparse region. We also examine an approximate time-scale on which the star reappears in the sparse region, i.e. a "waiting" time-scale for observers.

2.4.1 Galactic centre Nuclear Star Cluster

The Galactic centre Nuclear Star Cluster (NSC) is considered as a laboratory for studying stellar dynamics in the dense stellar environment [163]. It is the only galactic nucleus, in which we can study the proper motion and radial velocities of individual stars inside the gravitational influence radius of Sgr A* associated with the supermassive black hole (SMBH),

$$
\begin{aligned}
r_{\rm h} &= GM_{\bullet}/\sigma_{\star}^2\,,\\
&\approx 1.72\left(\frac{M_{\bullet}}{4\times 10^6\,M_{\odot}}\right)\left(\frac{\sigma_{\star}}{100\,{\rm km\,s^{-1}}}\right)^{-2}\,{\rm pc}\,,
\end{aligned}
\tag{2.66}
$$

which is derived by setting the characteristic circular velocity of stars bound to the black hole, $v_{\rm K}=\sqrt{GM_{\bullet}/r}$, equal to the one-dimensional, often line-of-sight, stellar velocity dispersion in the NSC, $\sigma_{\star}$. For $r\lesssim r_{\rm h}$, the gravitational potential of the SMBH prevails over the one of the NSC and the Keplerian rise in orbital velocities can be detected, $v_{\rm K}\propto r^{-1/2}$. At the Galactic centre distance of $\sim 8\,{\rm kpc}$, the angular scale of the influence radius is $\theta_{\rm h}\simeq 43''$, which can be resolved out to the angular scales of $\theta_{\rm min}\approx 63\,(\lambda/2\,\mu{\rm m})$ mas for diffraction-limited observations in the NIR $K_{\rm s}$-band with eight-meter class telescopes [69]. An even larger angular resolution is nowadays achieved with the Very Large Telescope Interferometer (VLTI), in particular GRAVITY@ESO instrument [164], which performs precision narrow-angle astrometry of the order of $10\,\mu$as as well as the phase-referenced interferometric imaging with the angular resolution of 4 mas.

Based on the stellar counts in the central $\lesssim 2\,{\rm pc}$, the stellar mass and number density of late-type stars can be in general fitted by a broken power-law [165],

$$
\rho_{\star}=\rho_0\left(\frac{r}{r_{\rm b}}\right)^{-\gamma}\left[1+\left(\frac{r}{r_{\rm b}}\right)^{\delta}\right]^{(\gamma-\gamma_0)/\delta}\,,
\tag{2.67}
$$

where γ is the slope of the inner distribution, γ_0 of the outer one, δ is the sharpness of the transition. The normalization constant ρ_0 is set according to the measured total enclosed mass of the NSC at a certain distance. [163] determined that the enclosed mass in the inner parsec is in the range $M_{\star}(<1\,{\rm pc})=0.5-1.0\times 10^6\,M_{\odot}$. The observed stellar distribution is consistent with the power-law model for $\rho_0=5.2\times 10^{-5}\,M_{\odot}\,{\rm pc}^{-3}$, $r_0\approx 0.5\,{\rm pc}$, $\gamma=0.5$, $\gamma_0=1.8$, and $\delta=2$. This describes the fact that the late-type stars exhibit a flat core in the inner $r_{\rm b}\approx 0.5\,{\rm pc}$. The density of early-type stars, on the other hand, increases towards the compact radio source Sgr A*, forming a cusp [165]. The illustration of the distribution is in Fig. 2.11, which shows different stellar populations – late-type stars with a core and early-type stars with a cusp as well as stellar remnants. Moreover, denser gaseous-dusty structures are located in the same region as the NSC and they orbit around the Galactic centre in a quasi-Keplerian way. The inner edge of the neutral and molecular Circum-Nuclear Disc (CND) coincides with the radius of the SMBH sphere of influence, $r_{\rm inner}^{\rm CND} \sim 1.7\,{\rm pc}$ [166], inside which the ionized hot plasma is located that emits thermal X-ray bremsstrahlung [107]. Three ionized denser streamers of Sgr A West or the Minispiral are thought to have dynamically originated in the CND via the loss of the angular momentum due to mutual collisions of CND clumps or the interaction with fast stellar winds of massive OB stars [167, 168].

Of a particular interest is the inner cluster within the projected radius of $\sim 1'' \simeq 0.04\,{\rm pc}$ that consists of ~ 30 mostly B-type bright stars – so-called S cluster [71, 75, 169]. These stars have nearly isotropic distribution of elliptical orbits with considerable eccentricities and pericentre distances of ~ 1500 Schwarzschild radii and orbital velocities at the periapse of several $1000\,{\rm km\,s^{-1}}$. One of the brightest stars S2 has the orbital period of ~ 16 years and it was possible to take measurements of its proper motions and radial velocities along its whole orbit. Thanks to the long-term monitoring of S2 and other two stars (S38 and S55/S0-102), it was possible to put the first weak constraints on the periastron shift of S2, which so far agrees with the relativistic prediction [74]. It should be noted that the first-order post-Newtonian effects can also be revealed in the orbital radial velocities, when the near-infrared spectroscopic data is available. For the S2 star, the general relativistic radial-velocity shift per orbit is $<\Delta V^{\rm GE}>= -11.6\,{\rm km\,s^{-1}}$ [170].

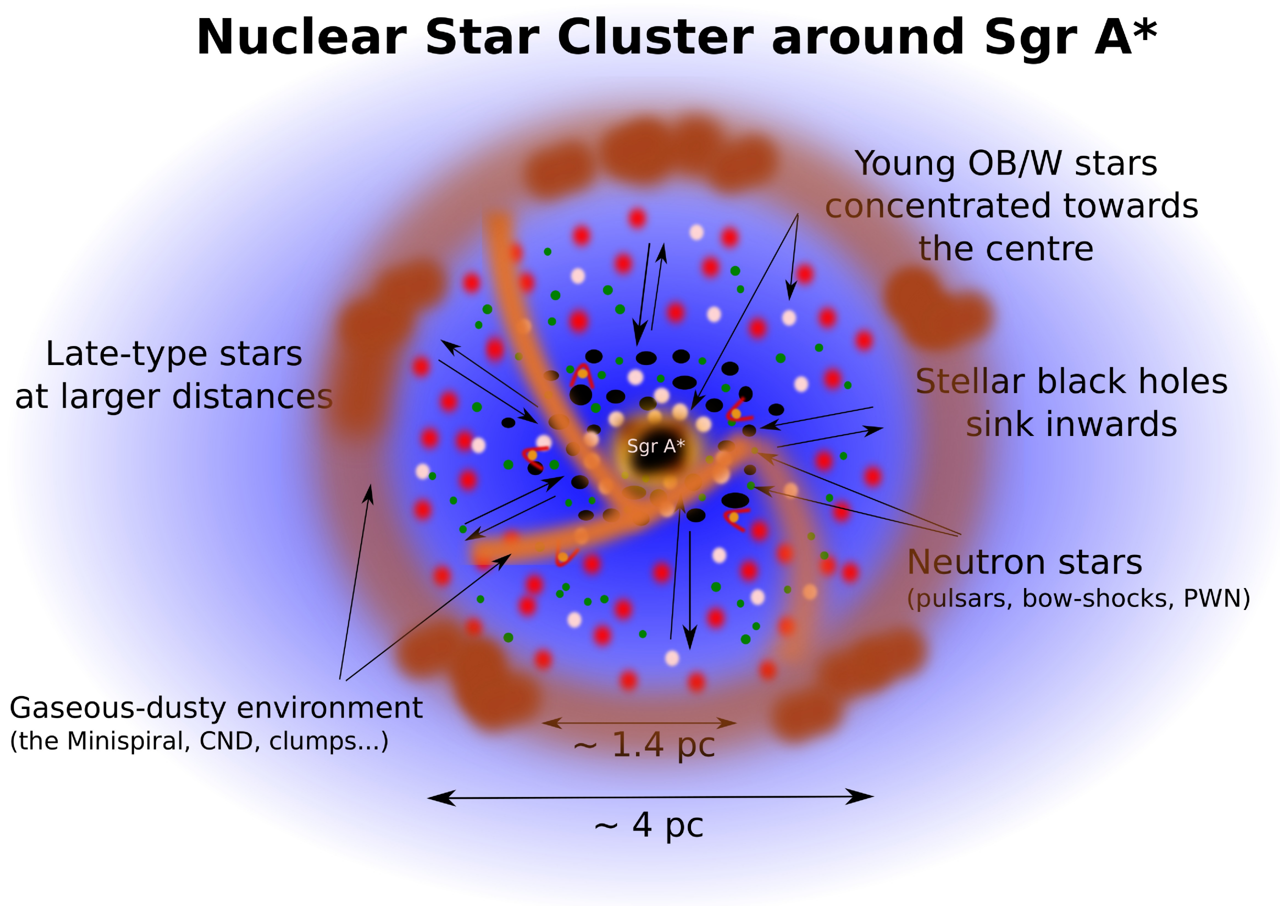

Figure 2.11: Illustration of different components of the NSC: old, late-type stars decrease towards the centre, forming a flatter core, while young OB stars seem to increase in numbers in the same direction, forming a cusp. In the central $\sim 2\,\mathrm{pc}$, prominent gaseous-dusty structures are located, mainly the nuclear and molecular CND as well as ionized streamers of the Minispiral.

Although the number density of stars is in general assumed to increase as $n_\star(r) \approx n_0(r/r_0)^{-\gamma}$, where $\gamma \geq 0$, the total number of stars inside radius r, $N_\star(<r)$, will decrease for $0 \leq \gamma < 3$. The maximum value of γ as inferred from the infrared observations typically reaches $\gamma_{\mathrm{max}} \approx 2$ [163], hence the total number of stars within the sphere of radius r must necessarily decrease, just because the total volume scales with r^3.

The number of stars inside the given radius r can then be calculated as follows,

$$N_\star(<r) = \int_0^r n(r')4\pi r'^2 \mathrm{d}r = \frac{4\pi n_0}{r_0^{-\gamma}(3-\gamma)} r^{3-\gamma}\,. \tag{2.68}$$

For the number of stars inside the influence radius $N_\star(<r_\mathrm{h}) = N_\mathrm{h}$, we obtain

the analogical expression to Eq. (2.68). Hence, the general expression can be normalized with respect to the influence radius $r_{\rm h}$ in the following way,

$$N_{\star}(<r) = N_{\rm h}\left(\frac{r}{r_{\rm h}}\right)^{(3-\gamma)}\,, \tag{2.69}$$

which can be inverted to obtain the radius, within which there is a total number of $N_{\star}$ stars,

$$r_{N_{\star}} = r_{\rm h}\left(\frac{N_{\rm h}}{N_{\star}(<r)}\right)^{-\frac{1}{3-\gamma}}\,. \tag{2.70}$$

In this section, we define the sparse region (hereafter SR) around Sgr A* with radius $r_{\rm sparse} \lesssim r_1$, which is expected to contain less than one star, where r_1 directly follows from Eq. (2.70), by setting $N_{\star}(<r) = 1$,

$$r_1 = r_{\rm h} N_{\rm h}^{-\frac{1}{3-\gamma}}\,. \tag{2.71}$$

Equation (2.71) implies that the radius of the SR depends strongly on the number of objects of particular type (late-type stars, early-type stars, compact objects) as well as their power-law slopes. In Fig. 2.12, we calculate r_1 for different numbers of objects inside $r_{\rm h}$, $N_{\rm h} = [10^3, 10^4, 10^5, 10^6]$, and expected power-law slopes in the range $\gamma = (0, 2)$.

It is useful to compare r_1 with characteristic length-scales in the inner parts of the NSC, where relativistic effects may become important. If we assume that Sgr A* is a black hole, its Schwarzschild radius is (for a non-rotating case) $r_{\rm s} = 2GM_{\bullet}/c^2 \simeq 1.18 \times 10^{12}\left(M_{\bullet}/4\times10^6\,M_{\odot}\right)$ cm. The tidal disruption of stars close to the black hole is expected at the tidal radius,

$$\begin{aligned} r_{\rm t} &= R_{\star}\left(\frac{3M_{\bullet}}{M_{\star}}\right)^{1/3} \\ &\approx 13\left(\frac{R_{\star}}{R_{\odot}}\right)\left(\frac{M_{\star}}{M_{\odot}}\right)^{-1/3} r_{\rm s}\,. \end{aligned} \tag{2.72}$$

The observationally important length-scale is the periapse distance of the brightest star S2. With the semimajor axis of $a = 0.126''$ and the eccentricity of $e = 0.884$

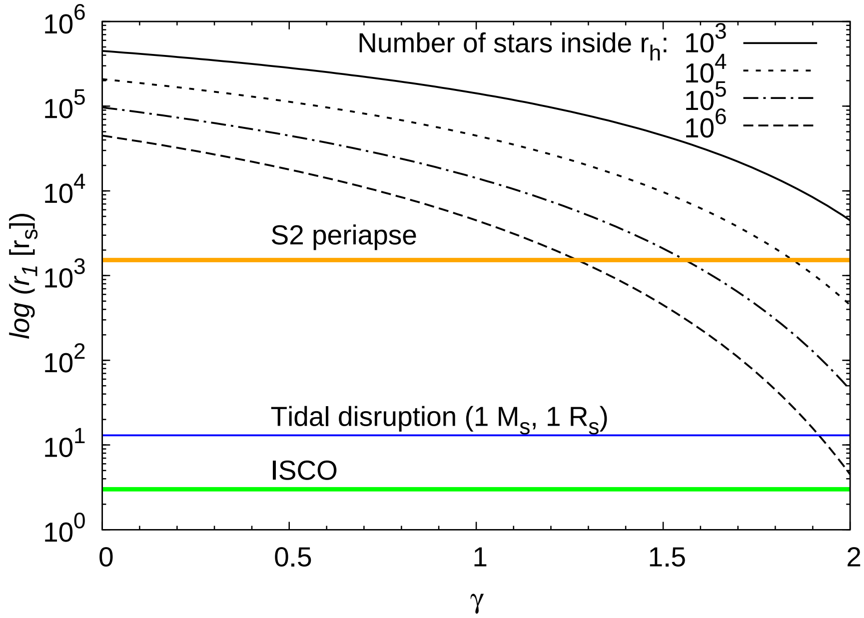

Figure 2.12: The radius of the sparse region r_1, see Eq. (2.71), inside which the number of stars is expected to be less or equal to one. The power-law slope of the stellar population is varied continuously in the range $\gamma = (0, 2)$ and the number of objects inside the influence radius is increased in discrete steps by an order of magnitude, $N_{\rm h} = [10^3, 10^4, 10^5, 10^6]$.

[74], the periapse distance is $r_{\rm p} = a(1-e) \approx 1529\, r_{\rm s} = 120.6\,{\rm AU}$. These length-scales are plotted in Fig. 2.12 alongside different profiles of r_1 as a function of the power-law slope γ. We see that only for steeper stellar density profiles, $\gamma > 1$, the radius r_1 reaches the S2 periapse distance, which implies that inside S2 periapse distance the number of stars can be of the order of unity, as we will discuss in more detail in the following section.

2.4.2 Analysis of a detection probability in a sparse region

Even though the density of stars and stellar remnants in the Galactic centre is one of the largest in the Galaxy, the total number of stars falls below one at a certain distance from Sgr A* due to the finite number of stars. [171] calculated the inner radius where the stellar cusp ends for different stellar components or types of objects (general notation T): main-sequence stars (MS), white dwarfs (WD), neutron stars (NS), and black holes (BH). Their general relation is merely

Population T	C_T	γ_T	$r_{1,T}$ [pc]	$r_{1,T}$ [r_s]
MS	1	1.4	2×10^{-4}	523
WD	10^{-1}	1.4	7×10^{-4}	1831
NS	10^{-2}	1.5	2×10^{-3}	5231
BH	10^{-3}	2	6×10^{-4}	1569

Table 2.2: The inner radii of the stellar cusp for different stellar populations T calculated according to Eq. 2.73.

an adjustment of our Equation (2.71) to specific stellar types,

$$r_{1,T} = (C_T N_h)^{-1/(3-\gamma_{\mathrm{T}})} r_{\mathrm{h}}\,, \tag{2.73}$$

where N_{h} is the total number of MS stars, $C_T N_h$ is the total number of stars of type T within the radius of influence of the black hole r_{h}, and γ_T is the power-law exponent for stellar type T. According to [171] the total number of MS stars within the radius of the gravitational influence $r_h = 1.7\,\mathrm{pc}$ is $N_h = 3.4 \times 10^6$. Table 2.2 summarizes the inner radii of different stellar populations of the NSC.

In these sparse regions of the Galactic centre which have a general radius R with respect to the Galactic centre black hole, we may always detect with a certain probability a star whose orbital elements meet specific criteria given by the radius R. These criteria may be expressed in terms of the orbital elements of the star, see Fig. 2.13.

In order to detect a star inside the sphere of radius R, the orbit must be intersected by a sphere at two points with the distance $r = R$ from the focus – black hole. In general, the distance of the star from the black hole along the elliptical orbit is given by $r = a(1 - e\cos E)$, where a is the semi-major axis, e is the eccentricity and E is the eccentric anomaly. Since $|\cos E| < 1$, we obtain general conditions on the orbital elements of the star (a, e) and the probability of its detection inside the regions of a given radius R.

The probability of detection P_{D} is non-zero, i.e. $0 < P_{\mathrm{D}} < 1$, if $r_{\mathrm{p}} = a(1-e) <$

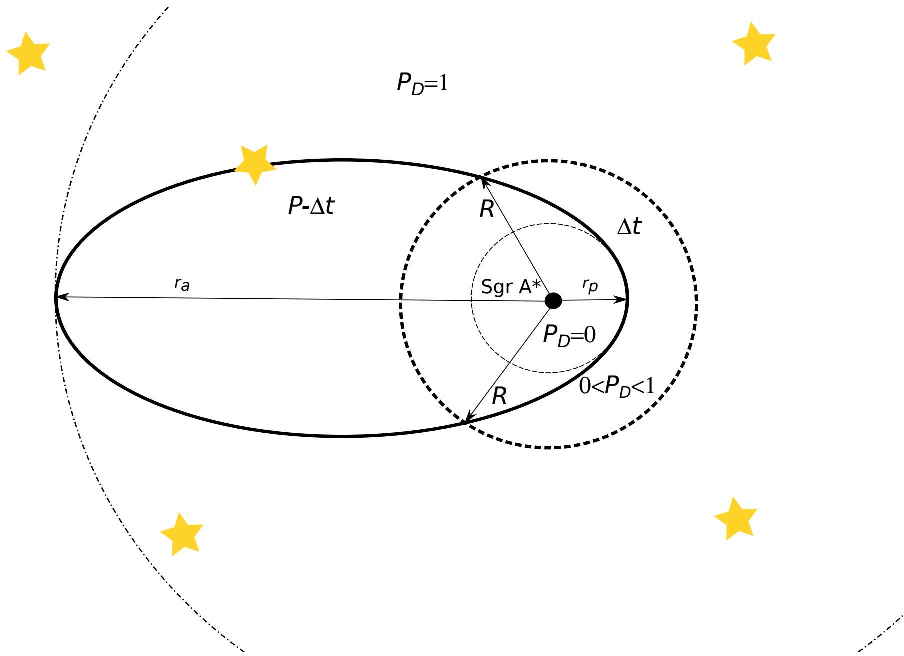

Figure 2.13: Basic geometry of a stellar fly-by close to Sgr A*. The ratio of the time interval Δt which expresses the time the star spends inside the radius R and its orbital period P gives the probability of detecting a star in sparse regions close to the Galactic centre.

$P_{\mathrm{D}} \to 0$	$0 < P_{\mathrm{D}} < 1$	$P_{\mathrm{D}} \to 1$
$a(1-e) \to R$	$a(1-e) < R < a(1+e)$	$a(1+e) \to R$

Table 2.3: General conditions for the detection probability P_{D} of a star with the semi-major axis a and the eccentricity e inside the sphere of a given radius R.

R and simultaneously $r_{\mathrm{a}} = a(1+e) > R$, where r_{p} and r_{a} are apparently the pericentre and apocentre distances of the star from the black hole. If r_{p} approaches R, the probability of detection goes to zero, since the star never intersects the region of radius R except for one point. On the other hand, if r_{a} approaches R, the probability of detection goes to one since the star is always located inside the region of radius R. The conditions are summarized in Table 2.3.

A non-trivial case is when a star passes through a region of radius R for a certain time Δt. Under the assumption that we have an ideal detector (with infinite sensitivity), the probability of detecting a star at any point is given by the ratio of the time Δt, during which the star is inside R, and the orbital period

P_{orb} of the star,

$$P_{\mathrm{D}} = \frac{\Delta t}{P_{\mathrm{orb}}}\,. \tag{2.74}$$

The interval Δt is equal to twice the time when the star is located at the distance R after the peribothron passage at time T_0, $\Delta t = 2(t(R) - T_0)$. A useful formula for the detection probability is then obtained using the Kepler equation, $M = 2\pi(t(R) - T_0)/P_{\mathrm{orb}} = E(R) - e\sin E(R)$, where M is the mean anomaly at the distance of R. Finally, using Eq. 2.74 we get,

$$P_{\mathrm{D}} = \frac{\Delta t}{P_{\mathrm{orb}}} = \frac{1}{\pi}[E(R) - e\sin E(R)] \tag{2.75}$$

where the eccentric anomaly $E(R)$ at distance R can be obtained in a straightforward way from $E(R) = \arccos\left[\frac{1}{e}\left(1 - \frac{R}{a}\right)\right]$.

For practical purposes, the eccentric anomaly expressed at the distance R (when the star crosses the sphere of radius R), may be expressed as,

$$\cos E(R, e, \Upsilon) = \frac{1}{e}\left[1 - \left(\frac{R}{r_{\mathrm{s}}}\right)\Upsilon^{-1}(1-e)\right]\,, \tag{2.76}$$

where we expressed the radius of the field of view in Schwarzschild radii and introduced the relativistic parameter $\Upsilon = r_{\mathrm{p}}/r_{\mathrm{s}}$ [74], which basically represents the term, on which the post-Newtonian corrections depend. In particular, the smaller the parameter Υ is, the larger the periastron shift is. Using the eccentric anomaly as expressed in Eq. (2.76), the detection probability depends on three parameters, $P_{\mathrm{D}} = P_{\mathrm{D}}(R, e, \Upsilon)$.

Even more concise representation can be obtained by introducing the parameter $\Lambda = r_{\mathrm{p}}/R$ as the ratio of the pericentre distance of a star to the field-of-view radius R. Then the eccentric anomaly is,

$$\cos E(\Lambda, e) = \frac{1}{e}\left[1 - \Lambda^{-1}(1-e)\right]\,, \tag{2.77}$$

which leads to the overall dependency of the detection probability $P_{\mathrm{D}} = P_{\mathrm{D}}(\Lambda, e)$. In Fig. 2.14, we plot the detection probability as a function of the eccentricity in the range $e = [10^{-3}, 0.999]$ and the parameter $\Lambda = [10^{-3}, 1]$. For $\Lambda > 1$, the star does not enter the region, hence the detection probability is zero. Another limiting line in the parameter space (e, Λ) is $r_{\rm a} = R$, below which the detection probability is not properly defined by Eq. (2.75), but is identically equal to one, $P_{\rm D} = 1$ since the whole stellar orbit for these orbital constraints lies inside the region of radius R.

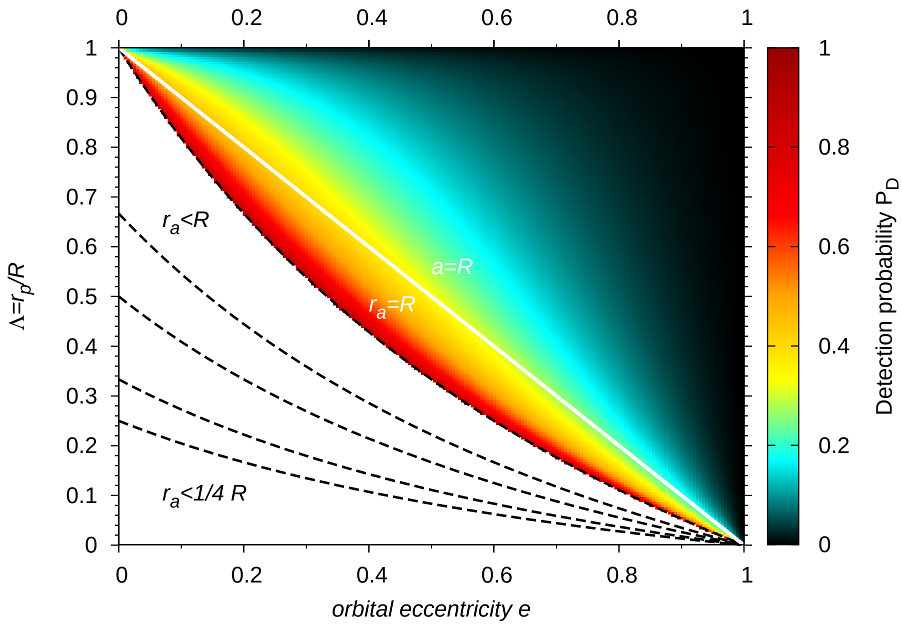

Figure 2.14: A colour-coded plot of the detection probability $P_{\rm D}$ of a star inside the sphere of radius R (which can be understood as a circular field of view) as a function of both the orbital eccentricity e and the parameter Λ, which represents the ratio of the pericentre distance $r_{\rm p}$ to R.

The procedure for the detection probability estimate will be illustrated for a case when for a given field of view with the length-scale of R, we would like to know the probability of detecting a star with semi-major axis that is comparable to R, $a \approx R$, and the orbital period near the black hole then is $P_{\rm orb} = (4\pi^2 R^3/GM_\bullet)^{1/2}$. This particular case is represented in Fig. 2.14 by a solid white line. For the eccentric anomaly we get $E = \arccos 0 = \pi/2$, which then leads to the very simple relation for the detection probability $P_{\rm D} = 1/2 - e/\pi$ that depends linearly on the eccentricity e. The dependence of $P_{\rm D}$ on the orbital eccentricity for the case

$R/a = 1$ is plotted in Fig. 2.16, with the values along the left axis.

We also define and calculate an observationally interesting quantity $\tau_{\rm max}$ – maximum time to spot a star with $a = R$ or a maximum "waiting time" if the star is not spotted within the field of view of radius R with a given near-infrared instrument. It is simply given by $\tau_{\rm max} = P_{\rm orb} - \Delta t = P_{\rm orb}(1 - P_{\rm D})$.

As an instructive case, we consider the field of view that is equal to the pericentra distance of S2 star: $R = r_{\rm p}^{\rm S2} \approx 0.6\,{\rm mpc} = 0.024\,{\rm mas}$. This field of view is chosen not quite arbitrarily since it corresponds to the radial scale with respect to the SMBH, on which relativistic effects are important. In addition, we can show that it is expected to be practically devoid of bright stars. From Eq. (2.69), we get the total number of main-sequence stars within the periapse of S2 of the order of $N_{\star}(< r_{\rm p}^{\rm S2}) = 3.4 \times 10^6\,(r/r_{\rm h})^{1.6} = 9.8$. However, to obtain a number of stars bright enough to be detected, we have to multiply the total number by a fraction that follows from an IMF, ${\rm d}N \propto m^{-\alpha}{\rm d}m$, or in an integrated form,

$$N_{\rm MS,det} = N_{\rm MS}\frac{m_2^{1-\alpha} - m_1^{1-\alpha}}{m_{\rm max}^{1-\alpha} - m_{\rm min}^{1-\alpha}}\,, \tag{2.78}$$

where α is the slope of the IMF, which we consider standard ($\alpha = 2.35$) [172], $(m_{\rm min}, m_{\rm max}) = (0.1, 100)\,M_{\odot}$ are the minimum and the maximum masses of main-sequence stars, and (m_1, m_2) are the mass limits of the subset of stars of our interest. The faintest main-sequence stars in the central parsec that are detectable with current instruments have the mass of $\sim 2\,M_{\odot}$ and therefore we set $m_1 = 2\,M_{\odot}$ and $m_2 = 100\,M_{\odot}$. The number of detectable MS stars below S2 periapse falls then below one, $N_{\star,det}(< r_{\rm p}^{\rm S2}) = 3.4 \times 10^6 \times 0.017\,(r/r_{\rm h})^{1.6} = 0.17$. Therefore, the formula (2.75) for the detection of one star crossing a sparse region applies to the sphere of radius $R = r_{\rm p}^{S2}$.

Using Eq. (2.77), we calculate the time $\tau_{\rm max}$ as a function of the ratio $\Lambda = r_{\rm p}/R$ and the eccentricity e. For a specific evaluation, we consider the crossing radius of $R = r_{\rm p}^{S2}$, i.e. the pericentre distance of S2. For a large span of ratios Λ and

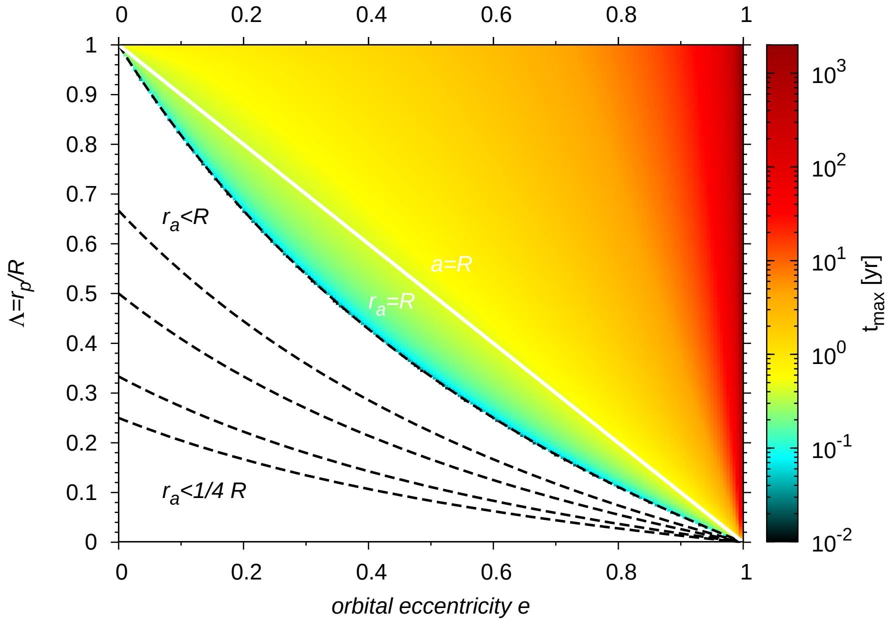

Figure 2.15: A colour-coded plot of the maximum time $\tau_{\max}$ to detect a star inside the sphere of radius R, which is devoid of stars, as a function of both the orbital eccentricity e and the parameter Λ, which represents the ratio of the pericentre distance $r_{\rm p}$ to R.

eccentricities e, the maximum time to detect a star in a sparse region is less than or of the order of one year. Only for highly-eccentric orbits and larger ratios Λ (when the pericentre distance is close to the radius R), it reaches hundreds to thousands of years.

For the specific case $a \approx R$, we show the basic trend in Fig. 2.16 – the detection probability $P_{\rm D}$ decreases linearly for increasing eccentricities as expected, whereas the maximum time $\tau_{\max}$ increases in the same direction. The orbit of a star, whose semi-major axis is comparable to the pericentre distance of S2, $a \approx R \approx 1529\,r_{\rm s}$, has the orbital period of $P_{\rm orb} = (4\pi^2 R^3/GM_\bullet)^{1/2} \simeq 0.687\,{\rm yr}$, which is short enough to spot a few orbits within several years. For very small eccentricities, the detection probability is close to $1/2$ and the maximum time to detect a star in the given field of view is close to the half of the orbital period as expected, $\tau_{\max} \approx 0.344\,{\rm yr}$. For increasing eccentricities, the detection probability and $\tau_{\max}$ behave simply linearly, as shown in Fig. 2.16. In case of highly-eccentric orbits with $e \approx 0.999$, the probability is $P_{\rm D} = 0.182$ and the maximum "waiting" time

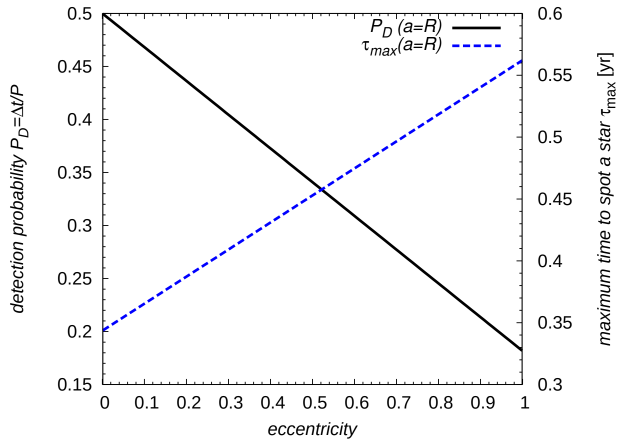

Figure 2.16: The relation between the detection probability (left y-axis) and the orbital eccentricity for the case $R/a = 1$. The right y-axis depicts the maximum time to a spot a star $\tau_{\rm max} = P_{\rm orb}(1 - P_{\rm D})$ as function of the eccentricity. The field-of-view is taken to be equal to the pericentre distance of S2 star $R = 0.6\,{\rm mpc} = 0.024\,{\rm mas}$, and the semi-major axis of a star is equal to R, whereas its pericentre distance is $r_{\rm p} = a(1-e)$.

is $\tau_{\rm max} = 0.562\,{\rm yr}$.

Under the assumption that within a certain volume around the Galactic centre the distribution of orbital eccentricities of stars is approximately thermalized, $n(e){\rm d}e \simeq 2e{\rm d}e$, with which the eccentricity distribution of monitored S stars is marginally consistent [173, 174, 135], the mean eccentricity is expected to be $\overline{e} \simeq 0.67$. If we adopt this value, the pericentre distance of the star crossing the sphere with radius $R = r_{\rm p}^{\rm S2}$ is $r_{\rm p} \simeq 505\,r_{\rm s}$. Post-Newtonian effects for such a star would be easier to measure, especially the relativistic periastron advance,

$$\Delta\phi(\overline{e} = 0.67) = \frac{6\pi G M_{\bullet}}{c^2 a(1-e^2)} \simeq 38'\,, \tag{2.79}$$

i.e. it would be more than half a degree, whereas for S2 star it is expected to be about one third of this value, $\Delta\phi_{\rm S2} \simeq 11.3'$.

2.4.3 Results

The derived probability $P_{\rm D}$ to detect a star in a sparse region of radius R is an upper limit, i.e. we assumed that the detector has an infinite sensitivity to detect an object of a given type (a main-sequence star or a pulsar). For real detectors, in particular near-infrared telescopes or radiotelescopes, the detection threshold needs to be considered, below which the probability of detecting faint stars is naturally zero. However, for stellar flux densities above the threshold, we showed that the innermost regions close to the Galactic centre are expected to be rather sparse, with the number of bright stars, i.e. with magnitudes $< 19^m$ in infrared K-band, being less than unity below the periapse distance of S2. In case no star is detected within the field of view equal to the periapse distance of S2,$R = 0.6\,\mathrm{mpc}$, the maximum time to spot a star is $\sim 0.3\,\mathrm{yr}$ for eccentricities close to zero and $\sim 0.6\,\mathrm{yr}$ for highly-eccentric orbits, under the assumption that the semi-major axis of a star is comparable to the radius of the field-of-view, $a \approx R$.

A small analysis presented here shows that a number of stellar objects (bright main-sequence stars or pulsars) ideal for doing precise tests of general relativity close to Sgr A* is rather limited. Basically, below 100 Schwarzschild radii the total number of MS stars is $N_\star(< 100\,r_\mathrm{s}) \approx 0.1$ according to Eq. (2.68). Naturally, the expected number of bright enough stars to be detected and the number of compact remnants (pulsars) is even smaller than that. In addition, the existence of main-sequence stars is dynamically limited by the tidal disruption radius, which is $\sim 13\,r_\mathrm{s}$ for Solar-type stars.

Therefore, the probability to detect any stellar objects on orbits at or close to ISCO, which would be important for distinguishing the black hole nature of Sgr A* from other compact scenarios, such as, boson stars, macroquantumness [70], is negligible or a matter of a coincidence. In this context, a more promising way for testing strong-gravity effects on the scale of $\sim 10\,\mathrm{r_s}$ is the analysis of light curves of detected bright X-ray flares, some of which contain a substructure with the main peak and a "shoulder" [79]. Their axisymmetric shapes can be explained to result from a flash on the length-scale of $\sim 10-20$ Schwarzschild radii. As the spot temporarily orbits around the SMBH, relativistic effects – Doppler boosting, gravitational redshift, light focusing, and light-travel time delays– modulate the observed signal. The mass of the central object (Sgr A*) inferred from X-ray light curves agrees well with the mass determined from stellar orbits that are more distant by two orders of magnitude. Hence, flares and stars can complement each other on different scales.

In this contribution, we neglected the effect of the orbital inclination, which by itself does not effect the detection probability $P_{\rm D}$ and the maximum timescale $\tau_{\rm max}$ if we consider a spherical region of radius R. It can, however, affect the measurement of the pericentre shift $\Delta\phi$, Eq. (2.79), which is most difficult to be reliably measured for nearly edge-on orbits. On the other hand, the gravitational redshift $z_{\rm g}$ for the observer at infinity depends only on the distance from the black hole $r_{\rm e}$, where photons were emitted,

$$z_{\rm g}(\infty, S2) = \frac{1}{\sqrt{1 - r_{\rm s}/r_{\rm e}}} - 1 \approx 3.3 \times 10^{-4}\,, \tag{2.80}$$

which is evaluated for the pericentre distance of S2, $r_{\rm e} = a_{\rm S2}(1 - e_{\rm S2}) \simeq 1529\, r_{\rm s}$ and leads to the radial velocity contribution to the shift of spectral lines, $v_{\rm g} = z_{\rm g} c \simeq 99\,{\rm km\,s^{-1}}$.

The other effect that was neglected were Newtonian perturbations from other stars and the stellar cluster as a whole, which, however, should be negligible in the sparse region where the number of stars is of the order of unity. In a similar way, the occurrence of blend or false stars due to the superposition of faint stars that are at the confusion limit of telescopes [175] is expected to be rather small in the sparse region, although sources along the line of sight can still cause a certain degree of confusion. These intervening stars in the foreground can, however, be excluded based on the kinematics.

2.5 Conclusions

We derived the probability to detect a star very close to the Galactic centre (inside the pericentre distance of S2 star), where the time-averaged number of bright stars is less than one. Considering the region of a general length-scale R, trivial cases for determining the detection probability $P_{\rm D}$ are when the pericentre of the stellar orbit approaches R, when $P_{\rm D}$ does to zero. On the other hand, the detection probability goes to one as the apocentre distance approaches R.

The non-trivial case is for $r_{\rm p} < R < r_{\rm a}$, when the probability is given by $P_{\rm D} = \pi^{-1}(E - e\sin E)$, where is E is the eccentric anomaly of a quasi-Keplerian stellar orbit. For stellar orbits with the semi-major axis comparable to the radius of the sparse region , $a \simeq R$, the detection probability is $P_{\rm D} = 1/2 - e/\pi$, i.e. it is decreasing for an increasing eccentricity. The maximum time to spot a star can then be calculated simply as $\tau_{\rm max} = P_{\rm orb}(1 - P_{\rm D})$, i.e. it is larger for an increasing orbital eccentricity. For a particular and observational interesting case, when the field of view is equal to the pericentre distance of S2 star, $\tau_{\rm max}$ reaches $\sim 0.3\,{\rm yr}$ for nearly circular and $\sim 0.6\,{\rm yr}$ for highly-eccentric orbits.

To sum up, we showed that it is unlikely to detect a bright star in the inner-most $R = 1500$ Schwarzschild radii from Sgr A*, where relativistic effects are prominent. However, a regular monitoring with current and future near-infrared facilities with the separation of at least $\sim 0.1\,{\rm yr}$ can yield the detection of a stellar fly-by that can be utilized as a probe of strong-gravity effects.

Chapter III

Black holes as sources of ultra-high-energy cosmic rays

Recent neutrino and multimessenger observations strongly established the existence of ultra-high-energy cosmic rays (UHECRs) of energy $> 10^{20}$eV, as well as they also indicate their source being an extragalactic supermassive black hole (SMBH) [176, 177, 178, 179]. However, production and acceleration mechanisms of UHECRs remain unclear. Energy range of UHECRs beyond the GZK-cutoff [180, 181] points to exotic nature of the phenomena. We demonstrate that extraction of rotational energy of a black hole by novel, ultra-efficient regime of the magnetic Penrose process (MPP) could indeed foot the bill. We envision ionization of neutral particles, such as neutron beta-decay, skirting close to the black hole horizon that energizes protons to over 10^{20}eV for supermassive black hole (SMBH) of mass $10^9 M_\odot$ and magnetic field of strength 10^4G. The driving engine of the process is in the presence of a stable charge of a black hole induced by the black hole rotation, being plausible in both vacuum and plasma settings. It is remarkable that the process neither requires extended acceleration zone, nor fine-tuning of accreting matter parameters. Further, we provide certain verifiable constraints on SMBH's mass and magnetic field strength as UHECRs sources. Applied to the Galactic center SMBH we have proton energy of order

$\approx 10^{15.5}$eV that coincides with the knee of the cosmic ray spectra. We model the results numerically and discuss the energy loses of primary cosmic rays along the propagation distance.

3.1 Black hole energetics

One of the most interesting properties of the Kerr black hole geometry is the existence of direct analogy between event horizon area A_H of a black hole with thermodynamical entropy S_H (see, e.g. [182, 183, 184]), which implies that a black hole of mass M and spin a has irreducible energy,

$$E_{\rm irr} = \sqrt{\frac{S_H \hbar c^5}{4\pi G k_{\rm B}}} \equiv \sqrt{\frac{A_H}{16\pi G^2}} c^4 = \frac{Mc^2}{\sqrt{2}} \left[1 + \sqrt{1 - \left(\frac{a}{M}\right)^2} \right]^{\frac{1}{2}} . \qquad (3.1)$$

For extremally rotating black hole this is 71% of its total energy [185, 186], while the rest of 29% is the rotational energy and is thus available for extraction. For stellar mass black holes this energy is of order 10^{63}eV, while for supermassive black holes of mass $M = 10^9 M_\odot$ it is of order 10^{74}eV making them the largest energy reservoirs in the Universe. It is therefore most pertinent to tap this enormous source most effectively and ultra efficiently. In this study we shall entirely address to classical black holes and their physics and astrophysics without any reference to quantum effects, such as the Hawking radiation etc.

First attempt to tap energy from black hole was made by Roger Penrose in 1969 [187] who pointed out existence of negative energy states of particles orbiting black hole with respect to observer at infinity. Negative energy orbits for neutral particles can exist inside the ergosphere. Static observer with timelike trajectory, having spatial velocity $\mathbf{v} = \mathbf{0}$, needs to satisfy the inequality $g_{tt} u^t u^t < 0$ implying $g_{tt} < 0$. This means static observers cannot exist when g_{tt} turns positive; i.e. they can only exist for $r > r_{\rm stat}(\theta) \equiv M + (M^2 - a^2 \cos^2\theta)^{1/2}$. The ergosphere is the region bounded by event horizon, r_H and static surface $r_{\rm stat}(\theta)$, so that $r_{\rm stat}(\theta) \geq$

r_H. Energy of a particle with momentum p_α measured by an observer of velocity $u^\alpha_{(obs)}$ is $E = -p_\alpha u^\alpha_{(obs)}$. Since no observer can remain static below $r_{\rm stat}(\theta)$, i.e. u^α turns spacelike, energy E relative to an observer at infinity can turn negative for some suitable particle parameters. However local energy would now be defined relative to stationary observer – locally non-rotating or zero angular momentum observer, that has radial velocity zero but angular velocity is necessarily non-zero, $\omega = -g_{t\phi}/g_{\phi\phi}$, the frame dragging velocity. Thus energy relative to LNRO/ZAMO is conserved and would however be always positive while it could be negative relative to observer at infinity. Thus in ergosphere where $g_{tt} > 0$, there exist particle orbits of negative energy states relative to infinity. This is the key property that drives Penrose process of energy extraction from a rotating black hole.

Following the original idea of Penrose let us consider the equatorial motion of a freely falling particle 1 which decays inside the ergosphere into two fragments one of which (particle 2) attains negative energy relative to infinity, while the other one (particle 3) escapes to infinity with energy grater than that of incident particle. The efficiency of the process, defined as ratio of extracted to infalling energy, and is given by the relation

$$\eta_{\rm PP} = \frac{E_3 - E_1}{E_1} = \frac{1}{2}\left(\sqrt{\frac{2M}{r}} - 1\right). \tag{3.2}$$

For split occurring close to horizon, it is then given by

$$\eta_{\rm PP} = \frac{M}{2a}\left(\sqrt{2}\sqrt{1 - \sqrt{1 - \frac{a^2}{M^2}}} - \frac{a}{M}\right). \tag{3.3}$$

It is maximal for extremally rotating black hole ($a = M$), being $\eta_{\rm PP} = 0.207$, or $\approx 21\%$. While for moderate spins, e.g. $a = 0.5M$, PP efficiency is $< 2\%$. In addition to low efficiency, PP is inoperable in realistic conditions because threshold relative velocity between two fragments after split required to be greater than half of the speed of light [188, 189]. This is the condition for a particle to ride on a negative energy orbit relative to an observer at infinity. There exists no conceivable astrophysical process that could almost instantaneously accelerate neutral particle to such high velocities. Nor there exists any observational evidence to support such a happening. Thus PP though very novel and purely relativistic in nature cannot be astrophysically viable.

In the mid 1980s, PP was revived astrophysically by inclusion of interaction of matter with electromagnetic field surrounding black hole [190, 191, 58], nicely reviewed in [192]. This was magnetic version of Penrose process (MPP), where the inconvenient relative velocity threshold between two fragments after split could be easily overcome in presence of an external magnetic field in which black hole is immersed. In other words, energy required for a particle to get onto negative energy orbit could now come from particle's interaction with electromagnetic field leaving mechanical velocity completely free. It was then shown that the process turned very efficient and its efficiency could even exceed 100%. For example for electrons around stellar mass black hole, efficiency is greater than 100%, for as low a field as milliGauss [3]. Although energy extraction efficiency 100% was first shown in 1985 [190] for discrete particle accretion and idealized magnetosphere, it is highly gratifying to see that recent fully general relativistic magnetohydrodynamic (GRMHD) simulations [193, 194] have wonderfully borne out this most important and interesting feature of the process.

Another similar process of energy extraction from rotating black hole is the Blandford-Znajek mechanism (BZ) [21]. BZ operates on the principle of unipolar generator, similar to classical Faraday disc. Here the role of disc is played by a black hole rotating in magnetic field. As in the case of MPP, black hole's rotation generates electric currents along the horizon surface which convert mechanical spin energy of a black hole into electromagnetic energy to be extracted. In addition, both BZ and MPP act due to existence of quadrupole electric field, being produced by twisting of magnetic field lines. However, BZ requires force-free magnetosphere which can be formed e.g. by a cascade of electron-positron pairs [195]. This requires the threshold magnetic field of order 10^4G. In addition BZ cannot provide ultra high efficiency, which is the distinguishing feature of MPP [3]. Below we will show that MPP is a general process which includes and approximates to BZ for high magnetic field regime. As mentioned before, MPP operates in three regimes of efficiency: low, moderate and ultra high. BZ is included in the middle – moderate efficiency regime. MPP has thus become one of the leading processes for powering the central engine of high energy astrophysical objects like quasars and AGNs involving black holes.

Following the work of Roger Penrose, several other modifications and variants of the original PP were proposed. these included collisional Penrose process (CPP) [196, 197] and its various variants [198, 199] based on multiple collisions of particles within the ergosphere, whose energy in the center-of mass could grow arbitrarily high for extremally rotating black hole (see, recent review [200] and references therein). It was however agreed that CPP was unlikely to be relevant in realistic high-energy phenomena, since the efficiency of the process in astrophysical situations (i.e. non-extremal black hole, collision occurring not exactly on horizon, incident particle falls from infinity) was severely constrained with maximum $\eta_{\mathrm{CPP}} < 15$ [201]. In [202], energy extraction from boosted black holes, i.e. black holes moving at relativistic speeds, has been studied. Among similar high-energy processes which have drawn attention in the literature is also the so-called BSW mechanism [203], which can provide arbitrarily high center-of-mass energy for collision again occurring at the horizon of extremally spinning black hole. It has also been generalized to include magnetic field [204] and to many other cases of modified gravity (see, e.g. [205, 206, 207]).

3.2 Efficiency of energy extraction

3.2.1 Split of infalling particle

Let us now consider decay of a particle 1, which is not necessarily neutral, into two charged fragments 2 and 3 close to horizon in the equatorial plane. According to conservation of energy and angular momentum after decay, we write

$$E_1 = E_2 + E_3, \quad (3.4)$$

$$L_1 = L_2 + L_3, \quad (3.5)$$

$$q_1 = q_2 + q_3, \quad (3.6)$$

$$m_1 \dot{r}_1 = m_2 \dot{r}_2 + m_3 \dot{r}_3, \quad (3.7)$$

$$0 = m_2 \dot{\theta}_2 + m_3 \dot{\theta}_3, \quad (3.8)$$

$$m_1 \geq m_2 + m_3, \quad (3.9)$$

where a dot indicates derivative relative to particle's proper time. If energy of particle 2 is negative relative to infinity, then particle 3 attains energy $E_3 = E_1 - E_2 > E_1$ greater than that of incident particle 1. Infalling negative energy into the black hole results in extraction of its rotational energy. Using the conservation laws, one can show that the local angular velocities of particles at the point of split satisfy the relation

$$m_1 u_1^{\phi} = m_2 u_2^{\phi} + m_3 u_3^{\phi}. \quad (3.10)$$

Reminding that $u^{\phi} = \Omega\ u^{t} = -\Omega\ e/X$, where $e = (E + qA_t)/m$ and $X = g_{tt} + \Omega\ g_{t\phi}$, Eq.(3.10) can be rewritten in the form

$$\Omega_1 m_1 e_1 \frac{X_2 X_3}{X_1} = \Omega_2 m_2 e_2 X_3 + \Omega_3 m_3 e_3 X_2. \quad (3.11)$$

After several algebraic manipulations we get the energy of escaping particle in the form

$$
\begin{aligned}
E_3 &= \chi(E_1 + q_1 A_t) - q_3 A_t, && (3.12)\\
\chi &= \frac{\Omega_1 - \Omega_2}{\Omega_3 - \Omega_2}\frac{X_3}{X_1}, \quad X_i = g_{tt} + \Omega_i g_{t\phi}. && (3.13)
\end{aligned}
$$

where $\Omega_i = d\phi/d\tau$ is the angular velocity of i-th particle, which is given by Eq.(1.21) and restricted by the limiting values (1.24). If the parameters are chosen in such a way that at the point of split $q_3 A_t < 0$, then this term plays the dominant role in the energy extraction from black hole. If $q_3 > 0$, and B and a are positive, it is easy to see that the condition $q_3 A_t < 0$ is perfectly satisfied.

3.2.2 Three regimes of energy extraction

MPP can operate in three regimes providing low, moderate and ultra high efficiency for the energy extraction from black hole, depending essentially on strength of magnetic field. As in the neutral case, Eq. (3.2), we define the energy extraction efficiency as the ratio between gain and input energies, i.e. in our notation

$$
\eta = \frac{E_3 - E_1}{E_1} = \frac{-E_2}{E_1}. \tag{3.14}
$$

Using Eqs. (3.12) and (3.13) at the point of split the general expression for the efficiency reads

$$
\eta_{\mathrm{MPP}} = \chi - 1 + \frac{\chi\, q_1 A_t - q_3 A_t}{E_1}, \tag{3.15}
$$

where A_t is calculated at the point of split. Setting Ω_1 to Ω given by Eq.(1.21) and $\Omega_2 = \Omega_-$, $\Omega_3 = \Omega_+$, which maximizes the efficiency, and reminding that the velocity component u_t is related to energy E as $m u_t = -(E + qA_t)$, we get

$$
\chi = \frac{1}{2}\left(1 + \sqrt{1 + \frac{k}{u_t^2}\, g_{tt}}\right), \tag{3.16}
$$

which for freely falling massive particle ($k = 1$) reduces to $\chi = (1 + \sqrt{1 + g_{tt}})/2$. For massless infalling particle ($k = 0$), $\chi = 1$, the expression (3.15) can also be rewritten as

$$\eta_{\rm MPP} = \eta_{\rm PP} + \frac{q_3 A_t - q_1 A_t(\eta_{\rm PP}+1)}{m_1 u_{t1} + q_1 A_t}, \tag{3.17}$$

where $\eta_{\rm PP}$ is the efficiency of original Penrose process given by Eq.(3.2). In the absence of magnetic field, MPP turns to original Penrose process giving its lower limit with the maximum efficiency $\eta_{\rm MPP}^{\rm low} \equiv \eta_{\rm PP} = (\sqrt{2}-1)/2 \approx 0.207$ or 20.7%, corresponding to extremally rotating black hole.

If all particles are charged the efficiency is given by its full form (3.17). However, as we have shown before in the presence of magnetic field for elementary particles the electromagnetic forces are dominating in the system, implying that $|\frac{q}{m}A_t| \gg |u_t|$. Relating this to (3.17) one can simplify the expression to the form

$$\eta_{\rm MPP}^{\rm mod.} \approx \frac{q_3}{q_1} - 1. \tag{3.18}$$

This is the moderate regime of MPP, which can operate, as we see, when $q_3 > q_1$, thus neutralizing gravitationally induced electric field of black hole. MPP in moderate regime has direct analogy with another famous process, namely Blandford-Znajek mechanism (BZ). In both cases the driving engine is a quadrupole electric field of a black hole which arises due to twisting of magnetic field lines by the frame-dragging effect. It is important to note, that the efficiency of BZ and moderate regime of MPP cannot grow ultra-large due to natural restrictions of global plasma neutrality surrounding black hole. In moderate regime MPP approximates to BZ and that explains why ultra-high efficiency has not been observed in numerical simulations of the process.

There could as well exist the third and the most efficient regime of MPP, which requires special attention leading to several important predictions. If the particle 1 is neutral $q_1 = 0$ splitting into two charged fragments, it is easy to see, that dominant contribution in (3.15) is due to

$$\eta_{\rm MPP}^{\rm ultra} \approx \frac{q_3}{m_1} A_t. \tag{3.19}$$

For elementary particles, such as electrons and protons, ratio q/m is very large, which makes the efficiency to grow to enormous values. This causes MPP to turn ultrahigh-efficient regime imparting ultra-high energy to escaping particle. In Fig.3.1 we plot the efficiency in ultra-regime for a proton around stellar mass black hole against magnetic field strength and different values of black hole spin. One can see that efficiency exceeds 100% already for magnetic field of order of Gauss. In case of electrons, same happens already for milliGauss fields.

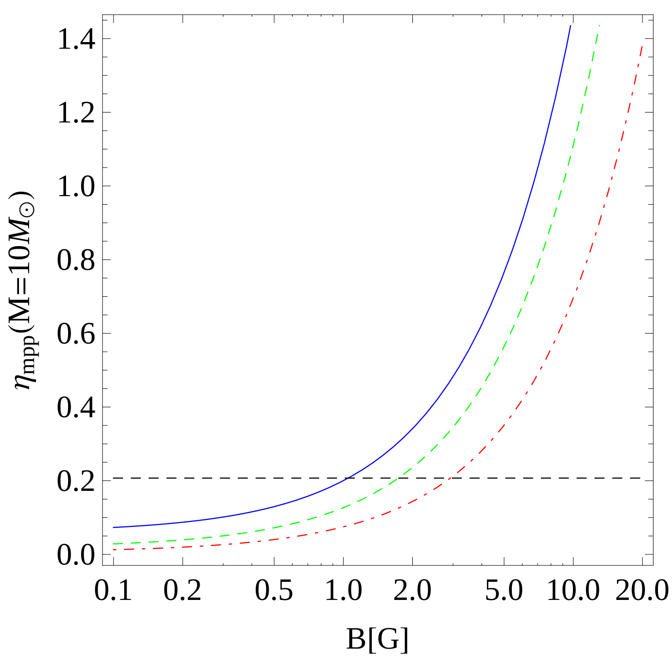

Figure 3.1: Efficiency of energy extraction in ultra-high regime from rotating stellar mass black hole of mass $10M_{\odot}$. Dashed horizontal line on the plot correspond to the efficiency of original "neutral" Penrose process for black hole with extremal spin. Colored curves correspond to various spins: $a = 0.8$ (solid blue), $a = 0.5$ (dashed green) and $a = 0.3$ (dot-dashed red).

Note, that all expressions for efficiency in three regimes are quite general and independent of magnetic field configuration. We also do not specify splitting point at this stage. Essentially axial symmetry of spacetime and electromagnetic field is what is required for MPP to operate in three regimes of efficiency depending upon the two parameters, magnetic field strength and charge to mass ratio of particles involved in the process of energy extraction. The other factor that matters is split point should be as close to horizon as possible which means infalling particle is neutral so that it can reach closer to horizon without any hindrance and then it splits or decays into charged fragments of opposite charge. So the ultra-high regime is characterized by magnetic field, particles involved are electron or protons, and it is neutral particle that decays closest to horizon.

The field configuration however matters for direction of escape and final fate of escaping particle, which is expected to move along the magnetic field lines. For example, in case of uniform magnetic field the collimation of escaping particles is maximal, while in case of hypothetical magnetic monopole the particles escape isotropically. In case of closed magnetic field lines such as for dipole magnetic field generated by current loops in the accretion disk of black hole, the escaping zone is concentrated on the polar caps collimating bipolar outflow of matter similar to relativistic jets. On the other hand, if energy of escaping particle is ultra-high powered by ultra-high efficient MPP, particle can get across the field lines and escape in arbitrary direction.

3.3 Ultra high energy cosmic rays

One of the fascinating applications of MPP is the explanation of the origin and production mechanism of ultra-high-energy cosmic rays (UHECR). These are the most energetic among particles detected on Earth, with energy $E > 10^{18}$eV unreachable by current most powerful particle accelerators as LHC with maximum energy $< 10^{13}$eV per beam. There are extragalactic charged particles with mixed composition [208, 209], although previous cosmic ray fluorescence measurements have demonstrated proton dominated flux [210, 211]. For Galactic cosmic rays one should observe anisotropy in arrival direction dominantly on the Galactic plane. As observed by both Pierre Auger Observatory[179] in the southern hemisphere and Telescope Array in the northern hemisphere[212], UHECRs with energy $>$

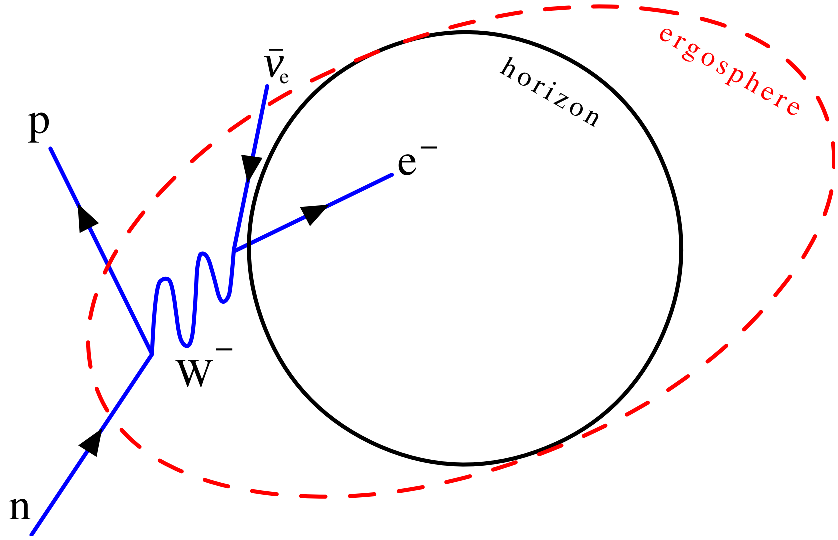

Figure 3.2: Schematic illustration of neutron beta-decay (Feynman diagram) in ergosphere of rotating black hole in the presence of external magnetic field. The escaping particle after beta-decay is a proton due to presence of positive electric charge of black hole produced by twisting of magnetic field lines. Similar regimes of energy extraction are possible for different radioactive decay modes. Conditions for ultra-efficient energy extraction are described below.

10^{18}eV are extragalactic with very high confidence level. Spectrum of cosmic rays demonstrate the presence of so-called knees and ankle. The cosmic rays with energy up to $\sim 10^{15.5}$eV (knee) are generally believed to be produced in Galactic supernova explosions, while significant lowering of flux between knee and $10^{18.5}$eV (ankle) suggests change of source of such particles. Though several studies suggested extragalactic origin of cosmic rays with energy exceeding $10^{15.5}$eV, the origin of cosmic rays with energies between knee and ankle is still under debate.

Recent unprecedented discovery of extragalactic high-energy neutrinos have enabled to pinpoint their source to blazar [177, 178], which is a supermassive black hole (SMBH) at the distance of ~ 1.75Gpc with relativistic jets directed almost exactly towards us. High-energy neutrinos can be produced in the hadronic interactions of primary cosmic rays with surrounding matter or photons resulting in production of secondary particles. In case of recent flare observations from blazar TXS $0506 + 056$ the energy of primary cosmic rays in the source region could reach $10^{14} - 10^{18}$eV [213].

The flux of cosmic rays with energies $> 5 \times 10^{19}$eV is extremely low, which causes the main difficulty in unveiling their source and its physics. In order to explain the highest-energy cosmic rays several exotic scenarios have been proposed including extra dimensions, violation of Lorentz invariance[214, 215], existence of new exotic particles [216] etc. Among the astrophysical acceleration mechanisms for UHECRs, the relativistic shocks in a plasma of relativistic jets has been previously considered as the most plausible[217]. The recent results and estimates indicate[218] that shock acceleration is not able to account for protons with energies above 10^{20}eV. E.g., the maximum energy of protons in mildly relativistic shocks of GRBs reach $< 10^{19.5}$eV. In addition, in realistic situations unavoidable interaction looses of UHECRs with matter and light reduce the energies of primaries significantly. Therefore, the production and acceleration mechanisms of UHECRs remain unclear.

3.3.1 Efficiency in various radioactive decay modes

In order to compare different regimes of MPP we choose the external magnetic field to be asymptotically homogeneous [20] with the strength B. Thus the four-vector potential A^μ around black hole is given by relations (1.9) and (1.10). We start from the expression for efficiency of MPP in ultra-high regime, given by

$$\eta_{\rm MPP}^{\rm ultra} = \frac{1}{2}\left(\sqrt{\frac{r_S}{r_{\rm split}}} - 1\right) + \frac{q_3 GBM\, a}{m_1 c^4}\left(1 - \frac{r_S}{2r_{\rm split}}\right), \tag{3.20}$$

where B is the strength of uniform magnetic field, $r_S = 2GM/c^2$, and $r_{\rm split}$ is the splitting point. The first term on the right hand side is positive only if the splitting point $r_H \leq r_{\rm split} < r_S$ with maximum at $r_{\rm split} = r_H$. This, purely geometrical term is due to the original Penrose process and it varies in the range $(0\,;\,0.21)$. The second term gives the contribution due to electromagnetic interaction, which can exceed 1 for electrons with a few milliGauss field and stellar mass black

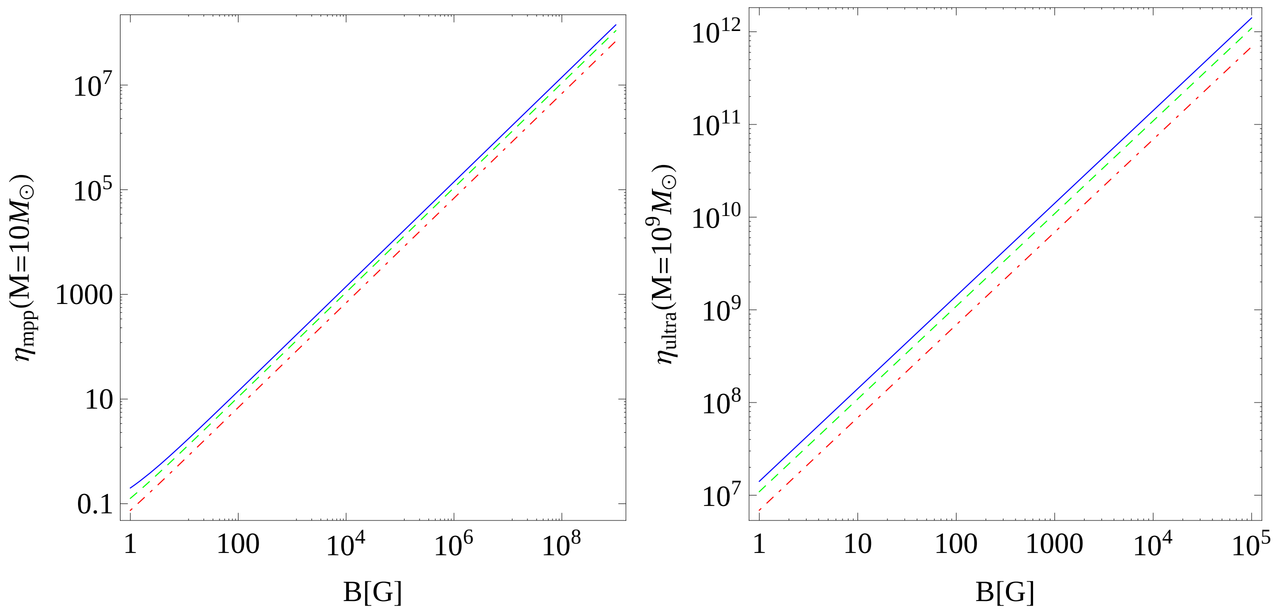

Figure 3.3: Efficiency of MPP in ultra-high regime. Left: stellar mass black hole of mass $10M_\odot$, right: supermassive black hole of mass $10^9 M_\odot$. Dashed horizontal line on the left plot correspond to the efficiency of original Penrose process for black hole with extremal spin. Colored curves correspond to various spins: $a = 0.8$ - solid blue, $a = 0.5$ - dashed green and $a = 0.3$ - dot-dashed red.

hole [3]. The important point to be noted is that electromagnetic interaction effectively expands ergosphere beyond the geometric bound, $r = 2M$. That is negative energy orbits are available in much enlarged region which goes on to enhance efficiency and overall working of the process.

Efficiency of MPP for escaping proton in ultra-high regime after decay of freely falling neutron above horizon is plotted against magnetic field in Fig.3.3 for different values of black hole mass and spin. The interesting and important that emerges from this is that MPP does not require rapid rotation of black hole and can as well operate for low spins.

In Table 3.1 we compare efficiency of energy extraction in different regimes for some typical radioactive decay modes occurring above horizon of a black hole with mass $10M_\odot$, spin $a = 0.8M$ and magnetic field of strength $10^4 G$. Magnetic field is taken to be asymptotically uniform.

Decay mode	Generic equation	Esc. p.	Efficiency $\eta_{\max}$	Regime of MPP
α decay	${}^{A}_{Z}\mathrm{X}^{0} \rightarrow {}^{A-4}_{Z-2}\mathrm{Y}^{2-} + {}^{4}_{2}\alpha^{2+}$	Y	< 0	-
		α	$2824/A$	ultra
	${}^{A}_{Z}\mathrm{X}^{+} \rightarrow {}^{A-4}_{Z-2}\mathrm{Y}^{-} + {}^{4}_{2}\alpha^{2+}$	Y	< 0	–
		α	~ 1	moderate
	${}^{A}_{Z}\mathrm{X}^{-} \rightarrow {}^{A-4}_{Z-2}\mathrm{Y}^{3-} + {}^{4}_{2}\alpha^{2+}$	Y	~ 2	moderate
		α	< 0	-
β^{-} decay	${}^{A}_{Z}\mathrm{X}^{0} \rightarrow {}_{Z+1}{}^{A}\mathrm{Y}^{+} + e^{-} + \bar{\nu}$	Y	$1412/A$	ultra
		e^{-}	< 0	–
		$\bar{\nu}$	0.06	low
β^{+} decay	${}^{A}_{Z}\mathrm{X}^{+} \rightarrow {}_{Z-1}{}^{A}\mathrm{Y}^{0} + e^{+} + \nu$	Y	< 0	–
		e^{+}	~ 0	low/–
		ν	< 0	–
γ emission	${}^{A}_{Z}\mathrm{X}^{0} \rightarrow {}^{A}_{Z}\mathrm{X'}^{0} + {}^{0}_{0}\gamma^{0}$	X'	0.06	low
		γ	0.06	low
Pair production	$\gamma^{0} \rightarrow e^{-} + e^{+}$	e^{-}	< 0	–
		e^{+}	2.6×10^{6}	ultra

Table 3.1: Maximum efficiency of magnetic Penrose process and corresponding energy extraction regime for some typical radioactive decay modes in the vicinity of a black hole of mass $10M_{\odot}$ with the spin parameter $a = 0.8M$. Magnetic field is aligned along the rotation axis and has the strength 10^{4}G. Initial energy of decaying particle is taken to be of order of its rest mass, $m_X c^2$. In case of the pair production the energy of photon is taken to be $E_{\gamma} = 2m_e c^2$ with recoil term neglected for simplicity.

3.3.2 Maximum energy of proton

Neutral particle can reach arbitrarily close to horizon without being influenced by the electromagnetic field, hence split could occur very close to horizon and thereby infalling particle in addition to gravitational/geometric negative energy would have very strong Coloumbic contribution tremendously enhancing quantum of energy being extracted. It is this that turns the process "ultra" efficient with efficiency exceeding $\eta = 10^{12}$. For plasma or any other environment (containing charged matter) as obtaining for BZ, the point of split cannot occur very close to horizon and hence cannot have advantage of tremendous gain of Coloumbic contribution. This is the reason why BZ efficiency remains in the moderate range of order of few[219] and hence could not reach ultra high range.

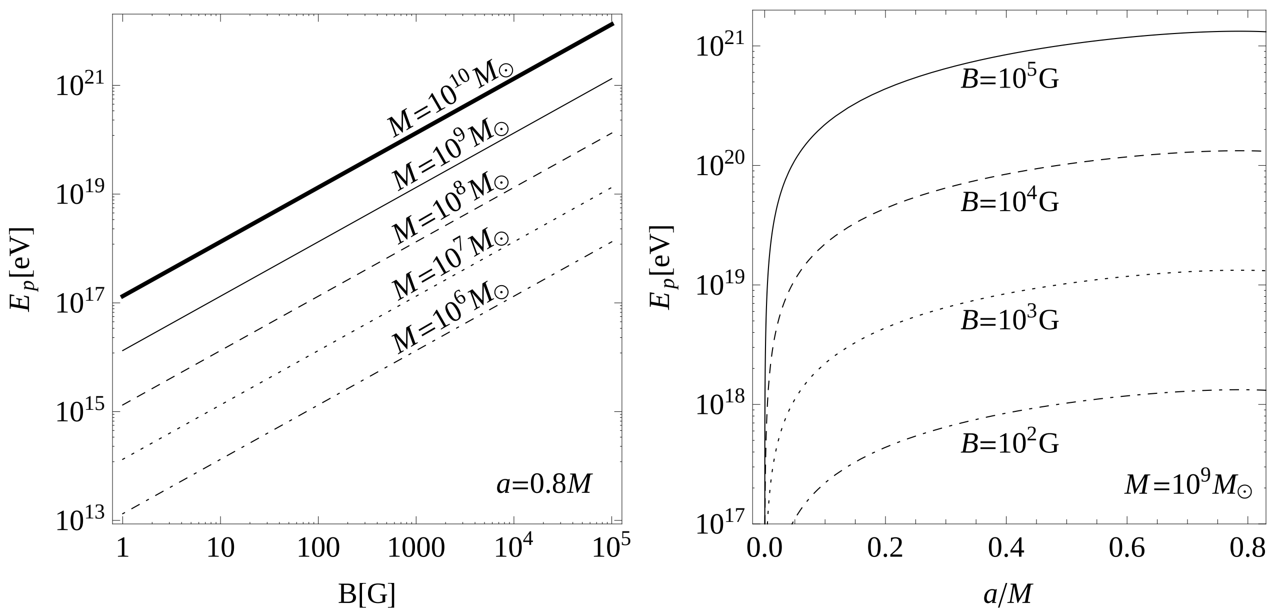

Figure 3.4: Energy of a proton after neutron beta-decay in dependence on magnetic field (left) and spin (middle) for various values of the SMBH's mass and the magnetic field, respectively. Right plot represents the constraints on the black hole's mass and magnetic field to accelerate protons with various energies: 10^{20}eV (dashed), GZK-cutoff $10^{19.7}$eV (solid), ankle $10^{18.5}$eV (dotted) and knee $10^{15.5}$eV. Blue vertical bars correspond to SMBH candidates, such as SgrA*, M87 and NGC 1052 with the constraints obtained from observations[220, 84, 221, 222]. The source marked as BZ corresponds to SMBH with mass $10^9 M_\odot$ and magnetic field $10^3 - 10^4$G, consistent with Blandford-Znajek model of relativistic jets[21].

Straightforward calculation of efficiency respecting energy conservation gives $\eta \sim qA_t/E_n$, where q is charge of escaping particle after decay, E_n is energy of incident neutral particle and A_t is a time component of four-vector potential of electromagnetic field induced by black hole's spin (see, Eq.(3.19)). In general, magnetic field has complicated structure in vicinity of black hole horizon, however in a small fraction of a space where split occurs one can always consider field to be approximately uniform. In this case (when the Wald solution [20] can be used) the expression for efficiency takes the form $\eta = qBMG/(m_n c^4)$, where M is black hole mass, q is charge of escaping particle and m_n is mass of an incident neutral particle. Applying this to the neutron beta-decay processes in vicinity of a SMBH having mass M and magnetic field of strength B, we get energy of the escaping protons after the neutron decays determined by the relation

$$E_{\rm p} = 1.33 \times 10^{20}{\rm eV} \left(\frac{q}{e}\right) \left(\frac{m}{m_{p^+}}\right)^{-1} \left(\frac{B}{10^4{\rm G}}\right) \left(\frac{M}{10^9 M_\odot}\right), \tag{3.21}$$

predicting energy of escaping proton $E_{\rm p}$ exceeding 10^{20} eV for $M \sim 10^9 M_\odot$ and $B \sim 10^4 G$. A schematic view of the process of neutron beta-decay in a magnetic field in vicinity of rotating black hole is illustrated in Figure 3.2. The dependence of energy of escaping proton on magnetic field for different black hole masses is given in Figure 3.4 (left). Proton energy against black hole spin is shown in Figure 3.4 (right) for different values of magnetic fields. One can see that the process does not require extreme or rapid rotation of the black hole, in spite of the fact that the black hole rotation is of essential and crucial requirement of the model.

3.3.3 Numerical modeling

In Figures 3.5 and 3.6 we depict the result of numerical modeling of process of ionization of neutral particle skirting in inner edge of Keplerian accretion disk [223]. In order to demonstrate the operation of the process, we have modeled the split of neutral particle into two charged fragments in the ergosphere of rotating black hole with particular representative initial conditions and dimensionless parameters. Without loss of generality we set the black hole mass to be equal to unity. Results of numerical calculations are demonstrated in Fig.3.6.

Neutral particle spirals down to the black hole in the equatorial plane from the innermost stable circular orbit (first column). In the ergosphere, at $r = 1.95$, neutral particle (1) with mass $m_1 = 1.01$ splits into two charged fragments (2)

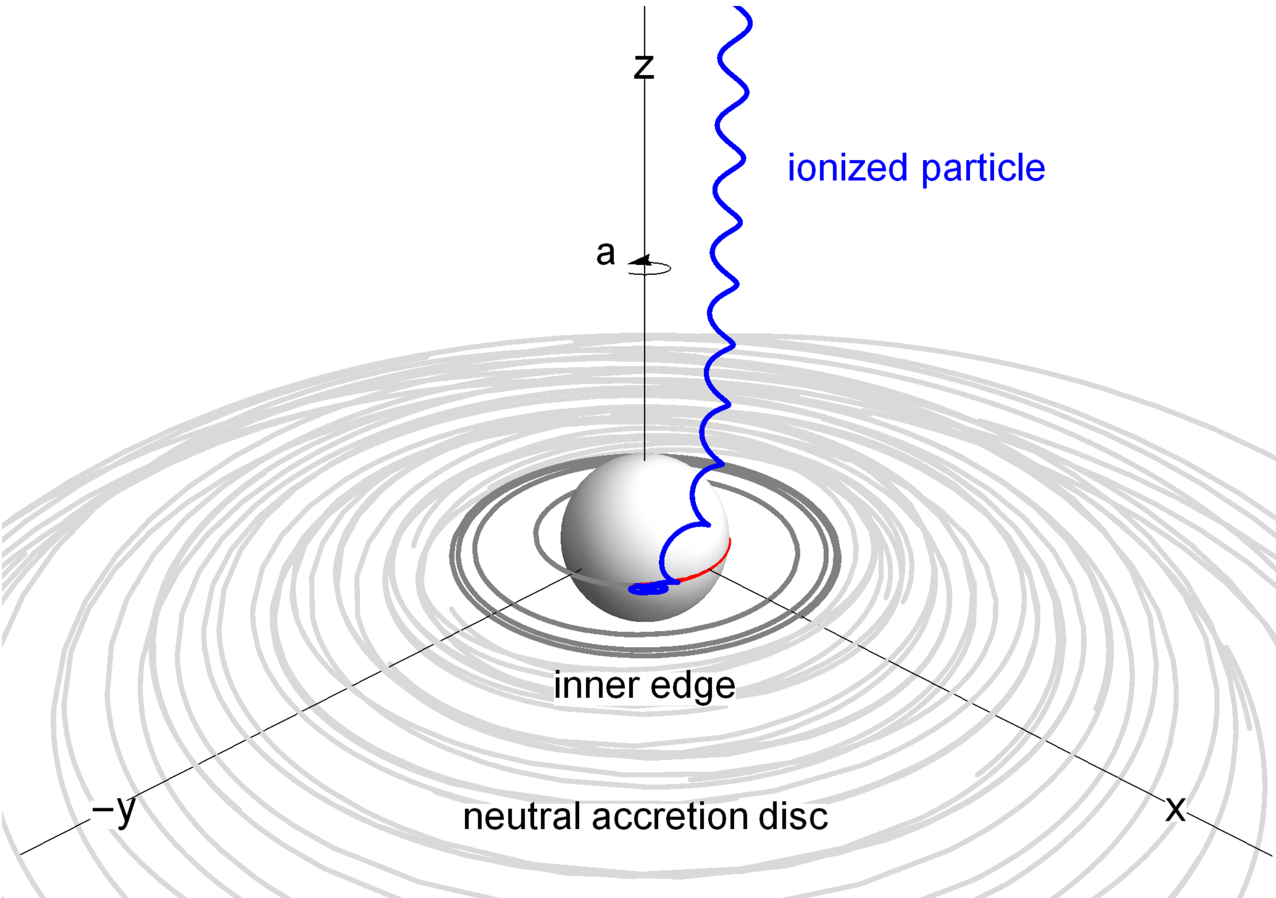

Figure 3.5: Numerical modeling of decay of neutral particle (thick gray curve) falling from the inner edge of Keplerian accretion disk onto the rotating black hole and resulting escape of positively charged particle (blue curve). Negative fragment of decay (red curve) collapses into black hole. More detailed numerical analysis of the process is given in Fig.3.6.

and (3) with masses $m_2 = 1$ and $m_3 = 0.01$ and charges $q_2 = 1$ and $q_3 = -1$. Binding energy is neglected in order to avoid additional energy gain and, therefore, highlight acceleration caused purely by MPP. Magnetic field is taken to be homogeneous far away from the black hole[20], where it has the strength $B = 100$. This allows us to introduce dimensionless parameter $\mathcal{B} = qB/m$, which is $\mathcal{B} = 10^2$ for particle (2) and $\mathcal{B} = -10^4$ for particle (3). Rotation of black hole causes twist of magnetic field lines which induces electric field – if the spin and magnetic field are co-aligned black hole will obtain positive charge. This causes more heavier positively charged particle escape the black hole (second column), while lighter negatively charged particle collapses onto horizon (third column).

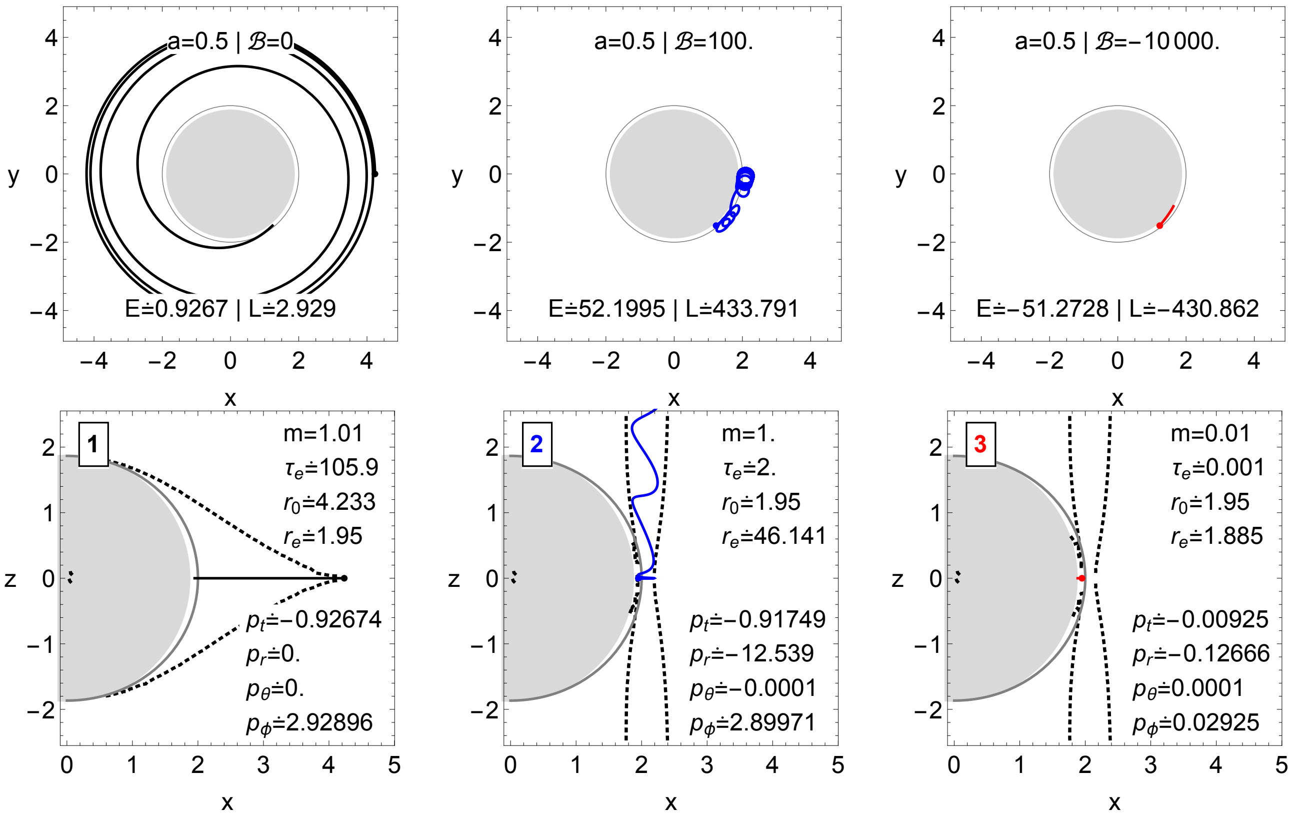

Figure 3.6: Modeling of split of neutral particle (black thick curve) into two charged particles (blue and red curves) in the ergosphere of rotating black hole (space between grey disk and circle) immersed into external magnetic field. Dashed lines represent particle energetic boundary.

Values of energy, angular momenta and components of kinetic momenta are given inside the plots.

Acceleration mechanism caused by the ionization of neutral particle can be examined using 2D effective potential for particle motion [223]. Particle ionization modifies the effective potential and creates the potential minimum at infinity, which becomes greatly deeper while energy E increases. The angular momentum L plays minor role in the acceleration process, determining only the exact location of the extrema of effective potential. After the ionization, particle's position in equatorial plane becomes unstable and charged particle (2) starts to roll down towards the minimum of effective potential located at infinity. This transforms particle's potential energy into velocity causing escape of charged particle from the black hole along magnetic field lines. For the second ionized fragment (3), whose charge is opposite to the charge of black hole, the effective potential changes in such a way that it creates outer barrier for the particle motion and hence the particle (3) collapsed onto black hole.

The presented effect of production of particles with ultra-high energy due to neutral particle ionization is independent from the configuration of magnetic field. More important is the existence of A_t component of electromagnetic field, which naturally arises due to black hole rotation in arbitrary magnetic field. Although the configurations with open field lines could seem more promising for particle's escape, once the particle is accelerated to ultra relativistic velocities it may cross the field lines and escape from black hole with corresponding deflections. Testing MPP for various magnetic field configurations (uniform, dipole and split monopole[21]) one can conclude that the total energy of escaping particle is nearly same for any field configuration, while the direction of escape varies. For uniform magnetic field all escaping particles (with slightly different initial conditions) are collimated maximally, while for radial magnetic fields of monopole character the charged particles (in various numerical setups) escape black hole isotropically. In addition one can note that initial energy and angular momentum of incident neutral particle do not play significant role in the acceleration of its charged fragments.

In realistic situations the numerical results presented in Fig.3.6 should be much more exaggerated, since for SMBH of mass $10^9 M_\odot$ and $B = 10^4$G introduced dimensionless parameter $|\mathcal{B}|$ is of order $\sim 10^{11}$ for protons and $\sim 10^{14}$ for electrons.

3.3.4 Constraints on potential UHECR sources

Source candidates of the highest-energy cosmic rays should be located within $\sim$ 100Mpc distance from Earth to avoid significant energy drop due to GZK

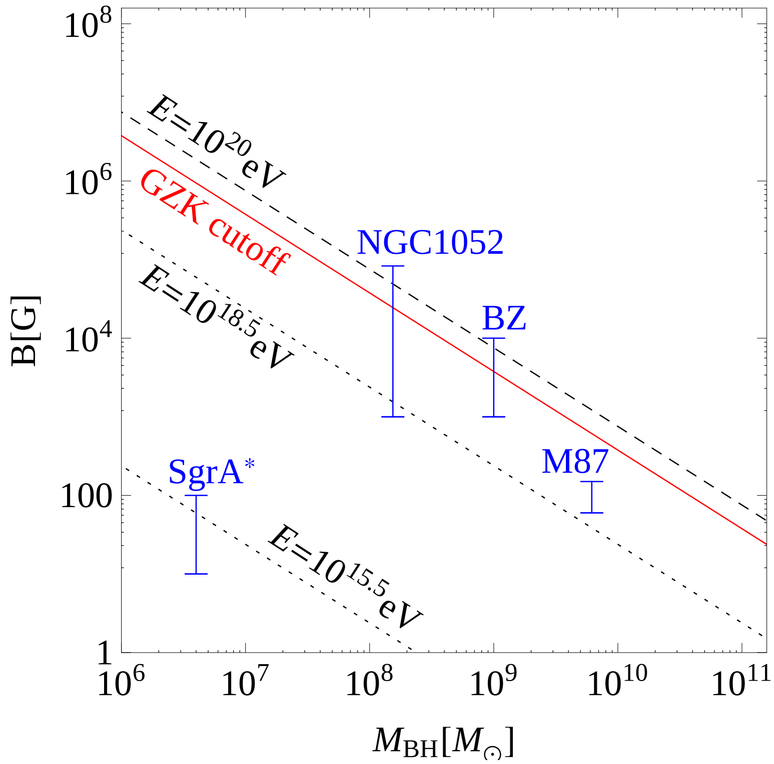

Figure 3.7: Constraints on the black hole's mass and magnetic field to accelerate protons with various energies: 10^{20}eV (dashed), GZK-cutoff $10^{19.7}$eV (solid), ankle $10^{18.5}$eV (dotted) and knee $10^{15.5}$eV by extracting its rotational energy after neutron beta-decay. Blue vertical bars correspond to SMBH candidates, such as SgrA*, M87 and NGC 1052 with the constraints obtained from observations[220, 84, 221, 222]. The source marked as BZ corresponds to SMBH with mass $10^9 M_\odot$ and magnetic field $10^3 - 10^4$G, consistent with Blandford-Znajek model of relativistic jets[21].

suppression and synchrotron radiation losses. Constraints on SMBH's mass and magnetic field to produce high-energy protons are given in Figure 3.7, where several representative SMBH candidates are pointed out. The main difficulty in the identification of all possible sources predicted by the model is the lack of measurements of magnetic field strengths in the inner regions of SMBH candidates. There are only few sources for which the horizon scale magnetic fields are estimated with confidential models and precision [220, 84, 221, 222]. Magnetic fields of sources given in Figure 3.7 have been obtained by spectroscopic and polarimetric modeling. For SgrA* at the Galactic center[221] and SMBH of AGN NGC 1052[220] magnetic fields are estimated for the distances of $\sim 1R_S$ from the horizon and for M87[222] for the distance of $\gtrsim 2R_S$. Due to amplification of magnetic fields in a plasma, the strength of magnetic field close to the horizon can be sufficiently larger[224].

The proposed model gives relatively precise prediction for the maximum energy of protons produced by SMBH in the center of our Galaxy. The central region of the Galaxy attributes highly-ordered magnetic field[23] which reaches 10–100G on the event-horizon scales[24] of Sgr A*. The mass of SMBH is estimated to be $\approx 4 \times 10^6 M_\odot$ [74, 84]. Thus the maximum energy of a proton in the described mechanism reaches $\approx 5 \times 10^{15}$eV. This energy approximately coincides with the knee of cosmic ray energy spectra, above which flux of particles suppresses.

Applied MPP to M87 SMBH we get the proton's energy in the range $10^{18.6} - 10^{19}$eV. For comparison the maximum energy achievable by protons inside the jet of M87 is $< 10^{16}$eV[225]. The source indicated as BZ corresponds to the requirements of Blandford-Znajek model to power relativistic jets. This implies that despite lack of direct measurements of horizon scale magnetic fields of SMBH candidates it is quite plausible that SMBHs of mass $10^8 - 10^9 M_\odot$ having relativistic jets and located in the local Universe are capable to produce protons of energies exceeding $> 10^{18}$eV. The logical extension of this conclusion could be the search of correlations in the observational data of UHECRs with predictions of our model.

3.3.5 Energy losses: GZK-cutoff and synchtrotron radiation

Depending on particle's type and energy the primary UHECR lose a large part of its energy in the interactions with photons of cosmic microwave background (CMB) while propagating over distances comparable to size of local cosmological structures. These interactions mainly appear as photo-pion production and force protons with energies above 5×10^{19}eV to lose major part of their energy. Conse-

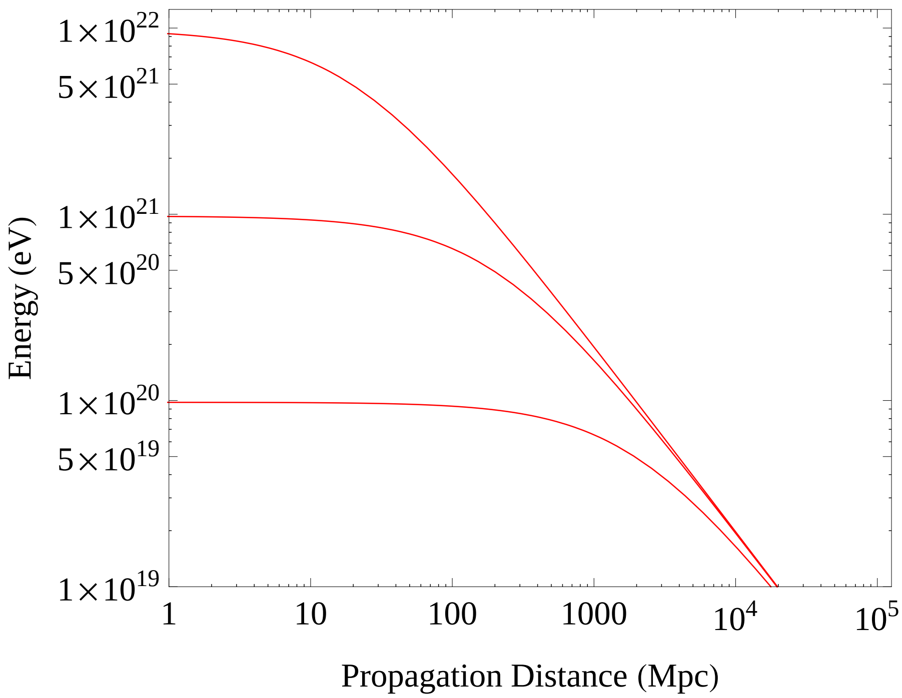

Figure 3.8: Mean energy of a proton undergoing synchrotron radiation reaction in a magnetic field of 10^{-5}G as a function of the propagation distance.

quently, spectrum of protons shows suppression of flux at these energies, which is known as the GZK cut-off [180, 181]. Detection of UHECRs with energies beyond GZK-cutoff imply location of sources within a distance of $\sim$ 100Mpc if primary particle is a proton.

On the other hand, presence of magnetic field along trajectory of primary cosmic rays can lead to synchrotron radiation reaction and correspoding energy loss. Although suppression of energy of UHECRs in a Galactic and intergalactic magnetic fields is small in comparison with losses caused by GZK phenomenon, high-energy charged particles can loose the major part of their energies in the source regions where magnetic fields can be considerably large. If we assume that UHECRs are originated in the dynamical environment of SMBHs attributing relatively strong magnetic fields, UHECRs may undergo the synchrotron radiation reaction, consequently affecting the spectrum of UHECRs considerably. The dependence of the energy of UHECR proton on the propagation distance in a magnetic field of 10^{-5}G is given in Figure 3.8. In the Methods we derive table 1.1 with typical decay timescales of electron, protons and fully ionized iron nuclei for different values of magnetic field strengths. This in particular shows that electrons loose their energies 10^{10} times faster than protons. Therefore, for typical SMBH with magnetic field of 10^4G order the primary cosmic rays are more plausibly protons or ions, while the decay timescales of electrons are extremely short to be able to escape from the vicinity of SMBH. On the other hand, in the case of neutron star (sometimes suggested as UHECRs source), whose magnetic field is typically above 10^{12}G, the timescale of synchrotron energy loss is extremely short even for protons and ions, so cosmic rays are not able to escape sufficiently far from neutron star preserving energy ultra-high.

In addition to GZK-cutoff and synchrotron emission the UHECRs may loose major parts of their energies in interactions with astrophysical background matter, which is especially dense in the SMBH environments. In this case various scenarios could be involved. Kinematics of the process shows that the UHECR produced in MPP escapes along the magnetic field lines due to chaotic scattering at the corresponding effective potential. However, field lines can be broken due to magnetic reconnection events occurring in a strong gravity regime, which can lead the direction of escape of primary cosmic rays out of the dense accretion disk and jet dominated regions. On the other hand, UHECRs resulting the ultra-efficient MPP can be part of jets and combined effects of accelerations by MPP and relativistic shocks in jets could be applied. MPP in this case can play a role of supporting engine in the various models of UHECRs acceleration by relativistic shocks in a plasma jets. UHECRs produced in MPP can also be tracers of secondary cosmogenic messengers, such as high-energy neutrinos and gamma rays [226].

3.4 Acceleration of particles in relativistic jets

Relativistic, collimated ejections of matter named jets have been observed in variety of objects, such as AGNs, X-ray binaries, quasars, etc. It is generally believed that the mechanism of production of jets is strongly connected with accretion processes in combined strong gravitational and electromagnetic fields. Being one of the fundamental problems of the modern relativistic astrophysics, the relativistic jets are under intensive considerations. Large interest is connected with attempts to understand how the energy from accreting matter is converted into the kinetic energy of escaping matter in a narrow cone, so that the jets acquire very large gamma-factors. Here we describe a simple model of jet-like motion of particles due to the ionization of neutral Keplerian accretion disc in the equatorial plane of weakly magnetized rotating black hole. As we have already seen above, the ionization of neutral particles in the vicinity of black hole can provide ultra-high-energy to one of its charged fragments after the split, so the fragment has enough energy to escape from the black hole. However, the motion of charged matter in the presence of magnetic field is always bounded in the equatorial plane (see, e.g. [36] and refs therein). Therefore the escape of particles from black hole is possible only along the magnetic field lines, which we assume to be aligned with the rotation axis of the black hole. This assumption is well justified due to the fact that any field configuration in the vicinity of black hole generally shares the symmetries of the background spacetime metric. Transition from equatorial motion of charged particles to the linear motion along the rotation axis occurs due to chaotic scattering of high-energy particles in the effective potential. This causes the interchange between the oscillatory and transnational modes of energy $E_0 \rightarrow E_z$ of charged particles. The mathematical technique and numerical modelling of the chaotic scattering of charged particles by black hole is given in [223].

3.4.1 Chaotic scattering of ionized particles

Motion of test particle is limited by the effective potential, so that $E = V_{\rm eff}$. While bounded in equatorial plane in the presence of magnetic field, the boundaries of motion can be open for escape to infinity along perpendicular direction to the equatorial plane. A particle is able to escape to infinity if its energy is grater than asymptotic value, which in terms of the specific energy ($\mathcal{E} = E/m$) is given by

$$\mathcal{E}_{\rm min} = \begin{cases} 2a\mathcal{B} + 1 & \text{for} \quad \mathcal{B} \geq 0, \\ 2a\mathcal{B} + \sqrt{1 - 4\mathcal{B}\mathcal{L}} & \text{for} \quad \mathcal{B} < 0, \end{cases} \tag{3.22}$$

where $\mathcal{B}$ is defined by (1.27). One can derive that

$$\mathcal{E}_{\infty}^2 = \mathcal{E}_{\rm z}^2 + \mathcal{E}_0^2, \tag{3.23}$$

$$\mathcal{E}_0^2 = \dot{r}^2 + g_{\phi\phi}\omega^2 = \dot{r}^2 + (\mathcal{L}/r - \mathcal{B}r)^2 + 1, \tag{3.24}$$

$$\mathcal{E}_{\rm z}^2 = \dot{z}^2, \tag{3.25}$$

where $\mathcal{E}_{\infty}$ is the energy of a particle measured at infinity. Thus the total energy of a particle measured at infinity is composed from the longitudinal $\mathcal{E}_{\rm z}$ and transverse $\mathcal{E}_0$ parts. It appears that near the black hole two components of energy $\mathcal{E}_{\rm z}$ and $\mathcal{E}_0$ are interchangable [223], while in Minkowski spacetime the energies given by (3.23) - (3.25) are integrals of motion and therefore cannot be transferred between two energy modes. In Kerr spacetime metric the conserved quantity is the total covariant time component of momentum i.e., $\mathcal{E}_{\infty}$. Interchange in two energy modes imply the change of the velocity of charged particles along the magnetic field line, which can increase to extremely large values due to combination of MPP with chaotic scattering effect.

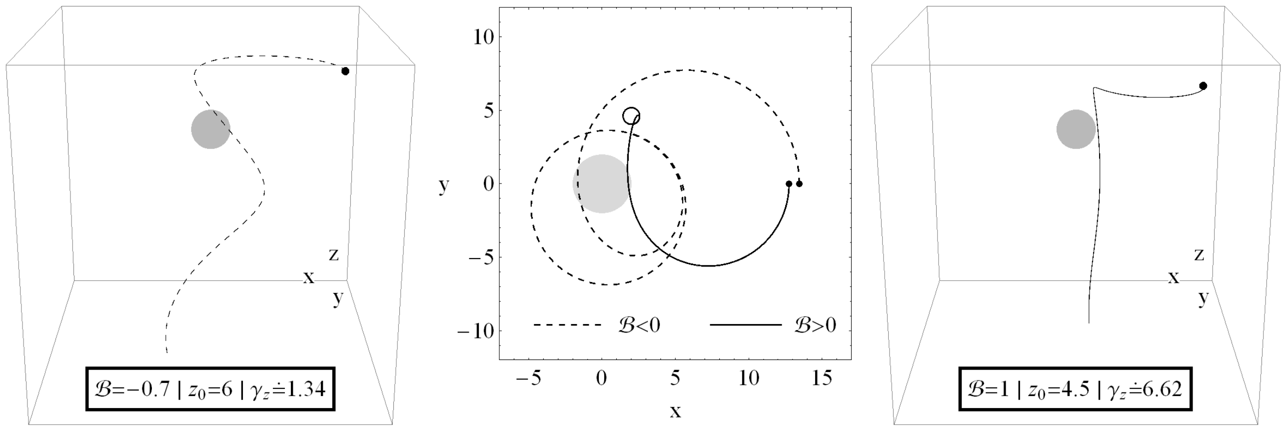

Figure 3.9: Trajectories of charged particles with negative (left) and positive (right) magnetic parameter $\mathcal{B} = qBGM/(mc^4)$ escaping black hole along z axis. Numerical values of corresponding Lorentz factors are given inside the plots. The plot in the middle shows the projections of both trajectories in the $x - y$ plane. The figure is reproduced from [223].

3.4.2 Escape velocity

Asymptotic value of Lorentz gamma factor is related to the energy at infinity in the following form

$$\gamma = u^t = \frac{dt}{d\tau} = \mathcal{E} + \frac{q}{m}A_t = \mathcal{E} - 2a\mathcal{B} = \mathcal{E}_\infty. \tag{3.26}$$

Escape velocity $u^z = dz/(d\tau)$ or $v^z = dz/(dt)$ and the Lorentz gamma in z-direction γ_z can be expressed in terms of relation (3.23) as follows

$$u_z = \mathcal{E}_z, \quad v_z = \frac{\mathcal{E}_z}{\mathcal{E}_\infty}, \quad \gamma_z = \frac{1}{\sqrt{1 - v_z^2}} = \frac{\mathcal{E}_\infty}{\mathcal{E}_0}. \tag{3.27}$$

The Lorentz factor is maximal when $\mathcal{E}_0$ is minimal, i.e.

$$\mathcal{B} > 0 \ : \ \gamma_{z(\max)} = \frac{\mathcal{E}_\infty}{\mathcal{E}_{0(\min)}} = \mathcal{E}_\infty, \tag{3.28}$$

$$\mathcal{B} < 0 \ : \ \gamma_{z(\max)} = \frac{\mathcal{E}_\infty}{\sqrt{1 - 4\mathcal{B}\mathcal{L}}}. \tag{3.29}$$

In case of maximal acceleration with positive $\mathcal{B}$, the orbital velocity of particle around black hole vanishes and all energy in equatorial plans tranfers into kinetic energy in z direction, so that $u^\phi = 0$, for $\mathcal{B} > 0$. In case $\mathcal{B} < 0$, for maximal acceleration the orbital velocity tends to the limit $u^\phi = 2\mathcal{B}\mathcal{L}$.

Comparison of trajectories in two cases with negative (left) and positive (rights) magnetic parameter $\mathcal{B}$ is represented in Fig. 3.9, which is reproduced from [223]. The trajectories are found in [223] by numerical integration of the full set of equations of motion. Acceleration is larger in case of positive $\mathcal{B}$. The Fig. 3.9 represents the cases with relatively low magnetic parameters $|\mathcal{B}| \sim 1$. For elementary particles around astrophysical black holes the magnetic parameter $\mathcal{B}$ is usually very large (see, e.g. (1.6) for electron around Sgr A* black hole). Therefore, the Lorentz factor of escaping particles after decay following MPP can be extremely large. Energy of charged particles produced in MPP is mainly concentrated in $\mathcal{E}_0$ mode due to considered formalism of decay in equatorial plane. The motion in that case is quasi-circular. Due to chaotic scattering all energy in $\mathcal{E}_0$ mode can be transformed to longitudinal kinetic energy $\mathcal{E}_\mathrm{z}$ in the black hole vicinity. Notable feature of the "transmutation" effect is that it does not require black hole's rotation and can operate also in Schwarzschild spacetime immersed into external magnetic field. However, in order to produce high-energy particles the black hole rotation plays crucial role as it generates electric potential A_t providing ultra-high acceleration to the charged particles. Thus, the combination of MPP with chaotic scattering effect for the acceleration of charged particles can serve as a simple model of relativistic jets as the model provides extremely large Lorentz factors ($\gamma_z \gg 1$) and strong collimation of escaping charged particles along the symmetry axis.

3.5 Conclusions

The high energy phenomena like quasars, AGNs, GRBs, FRBs, UHECRs and so on ask for two things: one, a very large reservior of energy and two, it has to be harnessed very-very efficiently to give enormous power output. A rotating black hole has 29% its mass in rotational energy which could be mined out. It therefore becomes the natural candidate for the huge reservior we are looking for. Now the question is of very efficient tapping of this rotational energy.

In 1969 Roger Penrose proposed a very novel and purely geometric process [187] of energy extraction from a rotating black hole. The key property driving the process was the existence of negative energy orbits relative to an observer at infinity in the vicinity of black hole horizon, the region called ergosphere. At the root of all this is the property of frame-dragging by which black hole shares its rotation with surrounding space. That is, space around a rotating black hole has inherent rotation so as to give angular velocity even to particle having zero angular momentum. The crucial point is that this property of existence of negative energy orbits in ergosphere is at the root of all processes involved in extracting energy from black hole.

The question then boils down to find the most efficient process. In the original Penrose process, the maximum possible efficiency was 20.7%. More important was the question that energy required to push a particle on NEOs is non-trivial – relative velocity between fragments to be greater $1/2c$ [188, 189]. This requirement was astrophysically unsurrountable because there can be no astrophysical mechanism that could accelerate particles to such relativistic velocity almost instantaneously. Thus Penrose process was very ingenious and interesting but it was astrophysically not viable to power high energy sources. Then various variants of the process were considered [196, 197, 198, 199, 200, 201, 203, 204, 202] but not of much any consequence or avail.

In 1977 came the BZ [21] which is set with black hole sitting in a magnetic field whose field lines are twisted due to frame dragging producing quadrupolar electric potential difference between pole and equator. The discharge of which drives out energy and angular momentum from black hole. It was astrophysically very exciting and interesting process. However NEOs also play the critical role in working of the process. Further the process requires polarization of vacuum in ergosphere which would require threshold magnetic field of order 10^4G. Here rotational energy of black hole is extracted electromagnetically – magnetic field plays the role of a catalytic agent.

In 1985 an electromagnetic version of Penrose process – MPP [190, 191, 58, 192] was considered and it was shown that the limit on threshold relative velocity could be easily overcome by particle's interaction with electromagnetic field; i.e. energy required for particle to ride on NEO could now come from $-qA_t$ leaving particle's velocity completely free. This was a wonderful revival of the process for astrophysical applications. Not only that it was shown that the process is highly efficient, so much so efficiency could exceed 100% for as low field as milli Gauss. This was for the first demonstration of efficiency exceeding 100%.

Clearly BZ and MPP share the same setting of black hole immersed in magnetic field, and so are the two the same? True, in moderately high magnetic fild range, the two seem to be similar. Recently it has been argued [3] that MPP is a general process which works in all magnetic field range while BZ requires the threshold magnetic field, and for that range the former approximates to the latter. That is BZ is contained in MPP in high field range.

All this was of course in the linear test particle accretion regime which is admittedly an idealized situation. More realistic setting could not be taken up due to lack of computing power at that time. Since around 2010, fully relativistic magnetohydrodynamic flow simulation models have been studied [193, 194], it is remarkable that the process continues to remain highly efficient, efficiency ranging to 300%. It turns out that MPP/BZ is the most plausible and important powering mechanism for high energy sources like quasars etc. It is remarkable and very gratifying for one of us that the mid 1980s prediction of efficiency exceeding 100% has been beautifully borne out. Thus MPP is perhaps the key process of mining rotational energy of black hole and powering the high energy sources.

Among astrophysical phenomena which can be directly related to MPP are the ultra-high-energy cosmic rays and relativistic jets. In case of UHECRs, MPP is able to produce protons with energy exceeding 10^{20}eV employing neutron beta-decay in the ergosphere of supermassive black hole of mass $10^9 M_\odot$ and magnetic field of 10^4G. Heavier cosmic ray constituents of similar energy range can also be achieved depending on the decay mode of infalling neutral matter. We summarized some of the potential radioactive decay modes with ultra efficient energy extraction in Table 3.1. Depending on the energy range and constituents of primary UHECRs, this can provide constraints on the black hole's mass, magnetic field and the distance to the source candidate. Remarkably, the knee energy of the cosmic ray spectrum at $\sim 10^{15.5}$eV coincides with the maximum proton energy obtained by MPP applied to the Galactic center black hole Sgr A*. Correlations of detected cosmic rays with nearby SMBHs of mass and magnetic field predicted by MPP needs to be explored.

Similarly, MPP can provide jet-like behaviour of charged particles, namely the large Lorentz gamma factor and strong collimation of ejected matter. This can be related to the ionization of accretion disk either by decay of infalling neutral particle into charged fragments or due to charge separation in a relativistic plasma of accretion disk. In the latter scenario black hole may behave like a pulsar [31] with net stable charge of both black hole and surrounding magnetosphere with respect to observer at rest at infinity. Ejection of ionized particles to infinity takes place along magnetic field lines, which can be open to infinity at the polar caps of black holes. Then, charged particles escape to infinity due to chaotic scattering effect caused by the interchange between the oscillatory and translational modes of the total energy of escaping particles $E_0 \to E_z$ [223]. Thus the combination of MPP with chaotic scattering effect leads to the high Lorentz factors and alignment of trajectories of escaping particles along the rotation axis of a black hole. This is quite promising and exciting that MPP may find further astrophysical applications in the near future, such as to be relevant for the operation of many other high-energy astrophysical phenomena, such as e.g. GRBs, FRBs among others.

Finally, we have come long way down from 1969 – good half a century, and it is remarkable to see what was proposed as a thought experiment had come to stay firmly and beautifully as one of the prime movers in high energy astrophysical phenomena. It is an excellent example of purely geometry driven process aided by magnetic field could wonderfully serve as powering engine for such complex astrophysical systems like quasars, AGNs, UHECR, and so on. In this review we have attempted to recount the historical evolution of the process, and it is fair to say that it has more borne out the promise it held.

We propose a mechanism which suggests supermassive black holes as sources of ultra-high-energy cosmic rays. We list the main advantages of the model as follows:

– clearly predicts SMBHs as the source of highest-energy cosmic rays

– provides verifiable constraints on the mass and magnetic field of the SMBH candidate to produce UHECRs

– operates in viable astrophysical conditions for SMBH with moderate spin and typical magnetic field strength in its vicinity.

– does not require extended acceleration zone for particle to reach ultra-high energy

– maximum energy of a proton in the process occurring at the Galactic center SMBH ($10^{15.5}$eV) coincides with the knee of the cosmic ray energy spectra, where the flux of particles shows significant decrease.

The driving engine of the process is in the presence of a non-screening gravitationally induced black hole charge which arises from the magnetic field twist due to black hole rotation in both vacuum and plasma surroundings.

We supported our results numerically by modeling the process in case of vacuum magnetic fields. Production of particles with ultra-high energy due to neutral particle ionization is independent from the configuration of magnetic field. Acceleration of UHECRs in the fully relativistic magnetohydrodynamic simulations should be tested and we give clear prediction of similar results. Motion of relativistic two component plasma fluids demonstrate instabilities causing a separation of charges inside the innermost stable circular orbit (ISCO) of rotating black holes[227]. The effect of neutral plasma separation into two charged fluids in the black hole ergosphere is the next interesting step to test MPP in ultra regime.

We have shown that synchrotron radiation loss of relativistic electrons is of $\sim 10^{10}$ times faster than for protons. Therefore, heavier constituents of UHECRs seem more plausible. Giving an alternative acceleration mechanism for production of charged particles with ultra-high-energy we do not contradict the present standard models based on the shock acceleration in a plasma of relativistic jets. Moreover, both could be combined leading tighter constraints on the parameters of possible sources.

It is usually expected that the spectrum of UHECRs has to be harder in the direction of nearby structures and softer further away from the source. However, it is not necessarily so, if the SMBH source is confirmed. The fit of candidate SMBHs with proposed model requires also the estimates of magnetic fields on the event horizon scale. Nowadays, the number of such precise estimates is very few and model dependent, although should increase by future global VLBI observations.

We believe that the proposed model of SMBH as power engine of UHECRs can open up new vista for understanding of this remarkable high energy phenomena as well as of its applications in other similar high energy settings.

Chapter IV

Optical properties and shadow of black holes

4.1 State of the art

Different models (including exotic ones) have been proposed for the Galactic Center, such as a dense cluster of stars [228], fermion balls [229], boson stars [230, 231], neutrino balls [232]. Some of these models have been ruled out, or the range of parameters of these models is significantly restricted due to observations [228]. However, as it was demonstrated in computer simulations, differences for different models may be very tiny, as shown in [233] where the authors discussed a shadow formation for the boson star and the black hole models (see also discussion in [234, 235]).

Now it is accepted that there is a super-massive black hole at the Galactic Center (see, e.g., recent reviews [16, 236, 237]). To evaluate a gravitational potential, one can analyse trajectories of test particles moving in the potential, and as a result one could constrain the parameters of the black hole. To prove the hypothesis, one could use bright stars or photons as test bodies to evaluate a gravitational potential at the Galactic Center. Indeed, the observations of the motion of S-stars in the Galactic Center demonstrate the shift of the pericenters of orbits of these stars which fit with the predictions of the weak-field post-Newtonian (PN) approximation [74]. One could use such an approach to evaluate gravitational potentials for the black holes located at the centres of galaxies. For example, the M87 galaxy looks very perspective to check predictions of the black hole model at the center of the galaxy – since the corresponding distance towards the galaxy is around 16 Mpc, and the black hole mass is $M_{M87} = 6 \times 10^9 M_\odot$, one can investigate structure of the black hole shadow for the galaxy center, as will be described below.

To create an adequate theoretical model for the Galactic Center, astronomers measure trajectories of bright stars (or clouds of hot gas) using the largest telescopes, such as VLT and Keck [238, 239, 152, 240, 241, 242, 243]. Due to the results of these observations, one could evaluate parameters of black hole, stellar cluster and dark matter cloud around the Galactic Center, because if there is an extended mass distribution inside a bright star orbit, in addition to the central black hole, the extended mass distribution causes an apocenter shift in direction which is opposite to the relativistic one [244, 245].

One could also check predictions of general relativity or alternative theories of gravity. For instance, one could evaluate constraints on the parameters of the R^n theory, Yukawa gravity, and graviton masses, using the trajectories of bright stars at the Galactic Center, because in the case of alternative theories of gravity a weak gravitational field limit differs from the Newtonian one. Therefore, the trajectories of bright stars then differ from the elliptical ones, and analysing observational data with theoretical fits obtained in the framework of alternative theories of gravity, one constrains parameters of such theories.

Another option is to use photons as test particles and one can analyse the images or the shadow of the Galactic Center black hole in mm band. We remind papers where the authors discussed issues which were connected with the subject. In 1973 Bardeen considered the apparent shape of a Kerr black hole located between a luminous screen and a distant observer [246]. The apparent shape of a black hole could be obtained from the region of critical photon orbits, with a reflection in respect to the rotation axis. In paper [247] a silhouette of a Schwarzschild black hole, and images of thin accretion disks around a spherical symmetric black hole, have been reproduced, earlier, visible shapes of circular orbits around Schwarzschild and Kerr black holes had been shown (beautiful pictures of accretion disks around a Kerr black hole had been reproduced recently for the *Interstellar* movie [248]).

Photon geodesics in a Kerr metric are characterized with two parameters (integrals of motion), called ξ and η. One could introduce a function $\eta_{cr}(\xi)$ of critical values of ξ and η which correspond to unstable spherical photon orbits with $r = const$ (r is the radial Boyer – Lindquist coordinate). One can use the parametric representation of the functions $\eta_{cr}(r)$ and $\xi(r)$, which is however not very convenient. This function separates scatter and plunge photon orbits, namely, photons are plunging only if $\eta < 0$ or $(\xi, \eta) \in S$, where

$$S = \{(\xi, \eta) | 0 \leq \eta < \eta_{cr}(\xi) \quad \& \quad \xi_1 \leq \xi \leq \xi_2\}, \tag{4.1}$$

and ξ_1 and ξ_2 are the critical impact parameters of the retrograde and direct unstable photon circular equatorial orbits, respectively; all length quantities are expressed in M units, while η is expressed in M^2 units

$$\xi_1 = -6 \cos\left(\frac{\arccos a}{3} + \frac{2}{3}\pi\right) - a \tag{4.2}$$

and

$$\xi_2 = 6 \cos\frac{\arccos(-a)}{3} - a. \tag{4.3}$$

Pairs $(\xi, \eta) \in S$ correspond to double roots of the polynomial $R(r)$ governing the radial motion of photons. The maximal value of the function $\eta_{cr}(\xi)$ is 27 and

$\eta_{cr}(-2a) = 27$; the radial Boyer – Lindquist coordinate value for this orbit reads $r(-2a) = 3$.

A model with a luminous screen behind a black hole, studied in [246], was not considered realistic, because in astronomy there is no luminous screen behind a black hole, and the sizes of a silhouette (shadow) are too small to be detectable in seventies and eighties of the last century for masses and distances of known black holes – for example the super-massive black hole at the Galactic Center has the angular size of the shadow, as observed from the Earth, around 50 μas. But currently this assumed shadow size is rather sufficient, as the resolution in the mm-band was significantly improved, and secondary faint images of the astronomical sources are located near the shadows.

In paper [244] the authors have studied the properties of the $\eta_{cr}(\xi)$ function and considered different types of the shadow shapes for the Kerr black holes, and different position angles of a distant observer. Moreover, in paper [244] it was shown that for an equatorial plane position of a distant observer, maximal impact parameter $|\beta_{\max}|$ in the z-direction (which coincides with the black hole rotation-axis direction) is $\sqrt{27}$ (in GM/c^2 units), and $\beta_{\max} = \sqrt{27}$ for $\alpha = 2a$, or $|\beta(2a)| = \sqrt{27}$, if we consider the function $\beta(\alpha)$ for the critical impact parameters separating plunge and scatter regions of photons ($\beta(\alpha)$ is expressed through function $\eta_{cr}(\xi)$ and a position angle of a distant observer). It means that for an observer in the equatorial plane, $|\beta_{\max}|$ remains the same, the shadow is deformed in the direction which is parallel to equatorial plane, and such a deformation depends on the black hole spin a. This theoretical property of the black hole shadow is widely used to evaluate the black hole spin from observations.

Some time ago Falcke, Melia and Agol [119] simulated the shadows for super-massive black holes and showed that the black hole silhouette could be formed in a rather natural way. The authors used a toy model for their analysis, and they concluded that the strong gravitational field bends trajectories of photons emitted by accreting particles, and in principle an observer can see a dark spot (shadow) around a black hole position. For the black hole at the Galactic Center the size of the shadow is around $3\sqrt{3}R_S$ (where $R_S \approx 10\ \mu$), as is the angular size of the Schwarzschild radius. Based on results of simulations, Falcke, Melia and Agol [119] concluded that the shadow may be detectable at mm and sub-mm wavelengths, however, scattering may be very significant at cm wavelengths, so there are very small chances to observe the shadows at the cm band. Importantly, the results obtained in [119] are rather general, in spite of their specific model. Strictly speaking, it is impossible to see darkness (shadows) in astronomical observations and people try to investigate structures of bright spots near shadows since shadows are formed by envelopes of bright images – analysing structures of images one could reconstruct shadows. Further simulations and observations are basically confirming the claims.

There is a tremendous progress in evaluation of minimal size of a spot detectable by recent observational techniques near the Sgr A^*. For example, Doeleman et al. [76] evaluated a bright spot size as small as $37^{+16}_{-10}\ \mu as$ for the VLBI technique in mm-band, but a boundary of a dark spot (shadow) has to be bright, and the related size of the bright boundary has been evaluated (therefore, a theoretical estimate of the shadow size and the bright spot size obtained from the observations should have similar values). These activities, including design and construction of new facilities, observations, and data analysis, are important steps to create the so-called Event Horizon Telescope [249], see also for a more recent information http://eventhorizontelescope.org/. The idea is to build a world-wide VLBI network to observe pictures of the supermassive black hole at the Galactic Center and in the galaxy M87 center. As the authors of the project say, they create Earth size telescope because lengths of arms are comparable with the Earth diameter. Initially, it was expected to analyse accretion structures near the black hole horizon at the Galactic Center, but consequent observations and estimates showed that the shortest wavelength of Radioastron is around 1.3 cm, and it is too long to observe a shadow at the Galactic Center.

Recently, the first image of the shadow of a black hole at the center of M87 galaxy has been released [250, 251, 252] by the Even Horizon Telescope collaboration. The obtained shape of an image leaves, however, a space for the existence of alternative theories of gravity. As it was noted, a turbulence is an important issue and it could spoil images of the bright spots near the shadows, but we do not consider the issue, because our aim is to obtain the simple theoretical model for shadows, ignoring the scatter effects.

4.2 Gravitational lensing by rotating black hole in a plasma

We study gravitational lensing in the vicinity of a slowly rotating massive object surrounded by a plasma. We have studied two effects i) the influence of the frame dragging on the deflection angle of the light ray in the presence of plasma ii) Faraday rotation of the polarization plane of the light. We derive the expression for the lensing angle in a non-diagonal space-time in the weak field regime in the presence of plasma and discuss it for the spacetime metric of the slowly rotating object. The obtained deflection angle depends on i) the frequency of the electromagnetic wave, due to the dispersion properties of the plasma; ii) the gravitational mass M; and iii) the angular momentum J of the gravitational lens. We studied the influence of rotation of the gravitational lens on the magnification of brightness of the source star in the case of microlensing and have shown that it is negligibly small. For the completeness of our study the effect of the Faraday rotation of the polarization plane is considered.

4.2.1 Light propagation in non-diagonal space-time

We start from the metric of space-time

$$ds^2 = g_{\alpha\beta} dx^\alpha dx^\beta \ , \tag{4.4}$$

and assume that the gravitational field is week and the space-time is asymptotically flat, what mathematically means

$$\begin{gathered} g_{\alpha\beta} = \eta_{\alpha\beta} + h_{\alpha\beta} \ , \quad \eta_{\alpha\beta} = (-1, 1, 1, 1) \ , \\ h_{\alpha\beta} \ll 1 \ , \quad h_{\alpha\beta} \to 0 \quad \text{under} \quad x^i \to \infty \ , \end{gathered} \tag{4.5}$$

and

$$g^{\alpha\beta} = \eta^{\alpha\beta} - h^{\alpha\beta} \ , \quad h^{\alpha\beta} = h_{\alpha\beta} \ . \tag{4.6}$$

Note, however, that we don't require the space-time to be static, but require it to be stationary. In particular, we assume the existence of non-zero time independent g_{0i} components of the metric, responsible for the rotation of the gravitating object. Henceforth below we use the realistic assumption that the metric of the space-time is fixed and the influence of the propagating light on the gravitational background is neglected.

Following the preceding works on the topic we will base our calculation on the description of the geometrical optics in an arbitrary medium in the presence of gravity, given by [253]. In their work Synge reformulated the Fermat's least-time principle for the light ray propagation in the case when the dispresive medium is present. Using this principle Synge developed the Hamiltonian approach for the description of the geometrical optics. In particular, Synge has shown that the variational principle

$$\delta \left(\int p_\alpha dx^\alpha \right) = 0 \tag{4.7}$$

together with the restriction condition

$$W(x^\alpha, p_\alpha) = \frac{1}{2} \left[g^{\alpha\beta} p_\alpha p_\beta - (n^2 - 1) \left(p_\alpha V^\alpha \right)^2 \right] = 0 \ , \tag{4.8}$$

where p^α is the photon momentum, V^α is the 4-velocity of the observer and n is the refractive index of the medium, give the following system of differential equations governing the trajectory of the photon

$$\frac{dx^\alpha}{d\lambda} = \frac{\partial W}{\partial p_\alpha} \,, \qquad\qquad \frac{dp_\alpha}{d\lambda} = -\frac{\partial W}{\partial x^\alpha} \,, \tag{4.9}$$

where λ is the affine parameter along the photon's trajectory. More information on the relativistic geometrical optics in dispersive media may be found in the book of [254].

Taking into account that (see [253])

$$p_\alpha V^\alpha = -\frac{\hbar\omega(x^i)}{c} \,, \tag{4.10}$$

where $\hbar$ is the Planck constant, $\omega(x^i)$ is the photon frequency, which depends on the spatial coordinates x^i due to the presence of the gravitational field, and c is the speed of light, the scalar function $W(x^\alpha, p_\alpha)$ may be rewritten in the form

$$\begin{aligned} W(x^\alpha, p_\alpha) = \frac{1}{2}\big[& g^{00}p_0p_0 + 2g^{0k}p_0p_k + g^{ik}p_ip_k \\ & - (n^2-1)\frac{\hbar^2\omega^2(x^i)}{c^2})\big] \,. \end{aligned} \tag{4.11}$$

Refractive index of a stationary inhomogeneous plasma n depends on x^i and $\omega(x^i)$ as

$$n^2 = 1 - \frac{\omega_e^2}{\omega^2(x^i)} \,, \qquad \omega_e^2 = \frac{4\pi e^2 N}{m} \equiv K_e N \,, \tag{4.12}$$

where $N = N(x^i)$ is the electron concentration in plasma, e and m are the electron charge and mass correspondingly. Henceforth we will adopt the notations for the values at infinity as $\omega(\infty) = \omega$, $\omega_e(\infty) = \omega_0$, $n(\infty) = \sqrt{1-\omega_0^2/\omega^2} = n_0$.

Using (4.11) and (4.12) the equations (4.9) for the trajectory of the photon may be rewritten as

$$\begin{aligned} \frac{dx^i}{d\lambda} &= g^{ik}p_k + g^{i0}p_0 = p^i \\ \frac{dp_i}{d\lambda} &= -\frac{1}{2}g^{lm}_{,i}p_lp_m - \frac{1}{2}g^{00}_{,i}p_0^2 - g^{0k}_{,i}p_0p_k - \frac{1}{2}\frac{\hbar^2 K_e N_{,i}}{c^2} \,. \end{aligned} \tag{4.13}$$

Solution for the photon's trajectory in flat space-time in vacuum is a straight line. The components of the 4-momentum of photon moving along the straight line along the z-axis are

$$p^\alpha = \left(\frac{\hbar\omega}{c}, 0, 0, \frac{n_0\hbar\omega}{c}\right), \; p_\alpha = \left(-\frac{\hbar\omega}{c}, 0, 0, \frac{n_0\hbar\omega}{c}\right) \; . \tag{4.14}$$

In the case of small plasma inhomogeneity and weak gravitational field, we may consider the components (4.14) as null approximation for the trajectory of the photon. Inserting them into the right-hand side of the equations (4.13) one gets in the left-hand side the first order deviation of the trajectory from a straight line as

$$\frac{dp_i}{dz} = \frac{1}{2}\frac{n_0\hbar\omega}{c}\left(h_{33,i} + \frac{1}{n_0^2}h_{00,i} + \frac{1}{n_0}h_{03,i} - \frac{K_e N_{,i}}{n_0^2\omega^2}\right) \; . \tag{4.15}$$

with

$$\frac{dz}{d\lambda} = \frac{n_0\hbar\omega}{c} \tag{4.16}$$

The deflection angle of the light ray in the plane perpendicular to the z-axis is equal to

$$\begin{aligned} \hat{\alpha}_k &= [p_k(\infty) - p_k(-\infty)]/p \; , \\ p &= \sqrt{p_1^2 + p_2^2 + p_3^2} = |p_3| = \frac{n_0\hbar\omega}{c} \; , k = 1, 2 \; , \end{aligned} \tag{4.17}$$

and from the equation (4.15) one can get

$$\hat{\alpha}_k = \frac{1}{2}\int_{-\infty}^{\infty} \frac{\partial}{\partial x^k}\left(h_{33} + \frac{h_{00}\omega^2}{\omega^2 - \omega_0^2} + \frac{1}{n_0}h_{03} - \frac{K_e N}{\omega^2 - \omega_0^2}\right) dz \; . \tag{4.18}$$

4.2.2 Deflection of light by lensing object in a plasma

Using expression (4.18) one can calculate the deflection angle of light propagating in the vicinity of a slowly rotating massive object surrounded by homogeneous plasma. In a general case the nondiagonal components of the metric tensor $\vec{h} \equiv (h_{01}, h_{02}, h_{03})$ in the vicinity of the slowly rotating object with the total angular momentum J are given by

$$\vec{h}(\vec{r}) \cong -\frac{2G}{c^3}\frac{\vec{J} \times \vec{r}}{|\vec{r}|^3} \; , \tag{4.19}$$

where G is the Newton's gravitation constant. When the angular momentum is directed along the z-axis expression (4.19) gives in spherical coordinates $h_{0\phi} \cong -2GJ\sin^2\theta/c^3 r$, as in the more familiar form of the metric for the slowly rotating massive object

$$\begin{aligned} ds^2 &= -\left(1-\frac{2GM}{c^2 r}\right)dt^2 + \left(1-\frac{2GM}{c^2 r}\right)^{-1} dr^2 \\ &+ r^2(d\theta^2 + \sin^2\theta d\phi^2) - 2\omega_{_{LT}} r^2 \sin^2\theta dt d\phi \ , \end{aligned} \tag{4.20}$$

where M is the total mass of the object, $\omega_{_{LT}} = 2GMa/c^2 r^3 = 2GJ/c^3 r^3$ is the Lense-Thirring angular velocity of the dragging of inertial frames, $a = J/cM$ is the specific angular momentum of the object.

From the expression (4.19) one can see that in Cartesian coordinates the component $h_{03} \sim J_x y - J_y x$ vanishes if one assumes the angular momentum J to be parallel to the z-axis. The effect of the dragging of inertial frames contributes to the deflection angle (4.18) only by means of the projection J_r of the angular momentum on the xy-plane. Introducing polar coordinates (b, χ) of the intersection point of the light ray with the xy-plane, where $\chi = \angle(\vec{J_r}\vec{b})$, one obtains

$$h_{03} = -2\frac{GJ_r \sin\chi}{c^3}\frac{b}{(b^2+z^2)^{3/2}} \ . \tag{4.21}$$

The deflection angle of light (4.18) will contain the following contributions due to the derivatives of h_{03} with respect to b and χ (the integrals are taken from 0 to ∞ because the functions under integration are symmetric with respect to z)

$$\begin{aligned} \hat{\alpha}_b &= \frac{1}{n_0}\int_0^\infty \frac{\partial h_{03}}{\partial b} dz \\ &= -2\frac{GJ_r \sin\chi}{c^3 n_0}\int_0^\infty \left[\frac{1}{(b^2+z^2)^{3/2}} - \frac{3b^2}{(b^2+z^2)^{5/2}}\right] dz \\ &= -2\frac{GJ_r \sin\chi}{c^3 n_0}\left(\frac{z^3}{b^2(b^2+z^2)^{3/2}} - \frac{2z}{b^2\sqrt{b^2+z^2}}\right)\Bigg|_0^\infty \\ &= \frac{2GJ_r \sin\chi}{c^3 b^2 n_0} \end{aligned} \tag{4.22}$$

and

$$\begin{aligned}\hat{\alpha}_\chi &= \frac{1}{n_0}\int_0^\infty \frac{1}{b}\frac{\partial h_{03}}{\partial \chi}dz \\ &= -2\frac{GJ_r\cos\chi}{c^3 n_0}\int_0^\infty \frac{1}{(b^2+z^2)^{3/2}}dz \\ &= -2\frac{GJ_r\cos\chi}{c^3 b^2 n_0}\frac{z}{\sqrt{b^2+z^2}}\bigg|_0^\infty = -\frac{2GJ_r\cos\chi}{c^3 b^2 n_0}\end{aligned} \tag{4.23}$$

Combining this with the previous result on the deflection angle of light in the case of Schwarzschild space-time one gets the final expression for the deflection angle by the slowly rotating gravitational source surrounded by homogeneous plasma as

$$\begin{aligned}\hat{\alpha}_b &= \frac{2GM}{c^2 b}\left(1+\frac{1}{1-\frac{\omega_0^2}{\omega^2}}\right)+\frac{1}{\sqrt{1-\frac{\omega_0^2}{\omega^2}}}\frac{2GJ_r\sin\chi}{c^3 b^2}\ , \\ \hat{\alpha}_\chi &= -\frac{1}{\sqrt{1-\frac{\omega_0^2}{\omega^2}}}\frac{2GJ_r\cos\chi}{c^3 b^2}\ .\end{aligned} \tag{4.24}$$

For the clarity of importance of our research we compare the second term in the right hand side of the equation (4.24) for $\hat{\alpha}_b$ with the first term by the order of magnitude. In the case $\omega_0 << \omega$ the ratio of these terms is equal to

$$\frac{J_r\sin\chi}{2bcM}\sim\frac{\Omega R}{c}\frac{R}{b}\ . \tag{4.25}$$

which can be of the order of 10^{-1} for the millisecond neutron star with the radius $R = 10$km and period of rotation $P = 10^{-3}$s. Observational data for the innermost stable circular orbits (ISCO) radius of rotating black holes show that the black holes are almost extremely rotating and the effect of dragging of inertial frames on the deflection angle may become very significant.

4.3 Amplification of brightness and Faraday effect in a plasma

4.3.1 Amplification of brightness of the image source

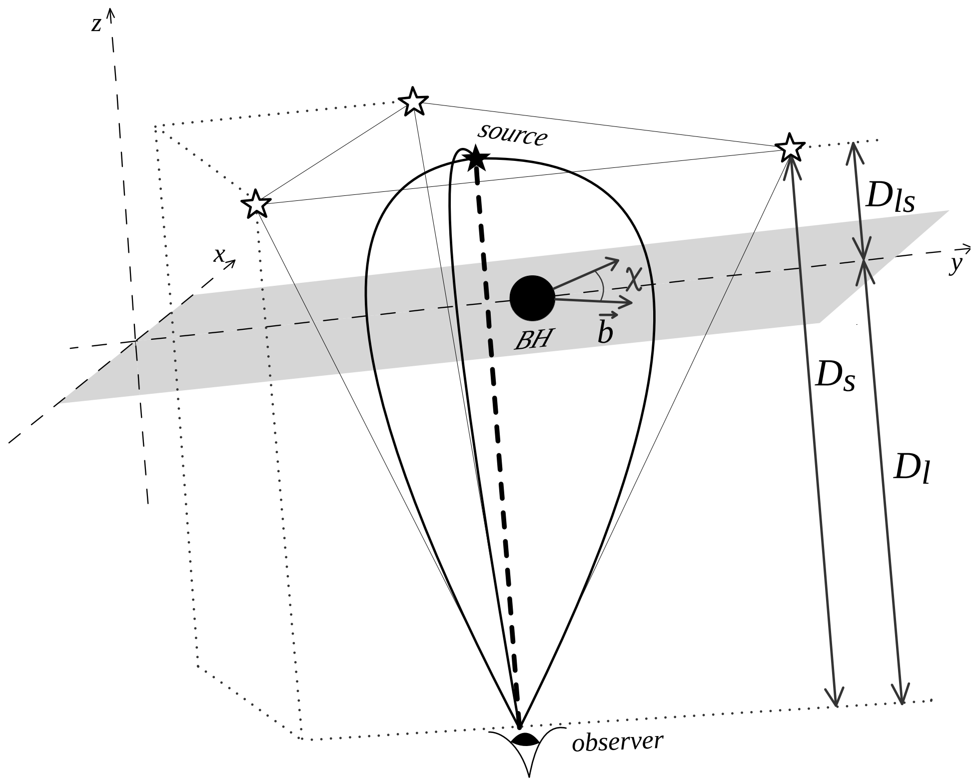

Figure 4.1: Schematic representation of the gravitating lensing system. The background source, which is indicated as black star is lensed by the central black hole. D_s is the distance between observer (below) and the source (star). D_{ls} is the distance from the lens (black hole) to the source. D_l is the distance between observer and lens. χ represents the inclination angle between the projection of the vector J to xy plane and vector b.

Next we are going to apply the obtained equation (4.24) for the deflection angle to calculate possible significant physical effects of dragging of inertial frames. For simplicity further in this subsection we will neglect the effect due to the azimuthal deflection of light and investigate the influence of the polar deflection of light on the microlensing effect. This result will strictly apply to the case of $\vec{b} \perp \vec{J}_r$, while in general case the simple picture presented below will be distorted by the azimuthal deflection.

The main equation of the gravitational lensing theory is the lens equation, which relates the angle β of the real object from the observer-lens axis, the angle θ of the appeared image of this object from the observer-lens axis and the deflection angle α (the angles are assumed to be small)

$$\theta D_s = \beta D_s + \alpha D_{ls} \ , \tag{4.26}$$

where D_s and D_{ls} are the distances from observer to the source and from the lens to the source correspondingly. Taking into account that in the small angles approximation $b \approx D_l\theta$, where D_l is the distance from the observer to the lens, one can write the lens equation for the case of rotating source in the following form:

$$\begin{aligned}\beta &= \theta - \frac{D_{ls}}{D_s}\hat{\alpha} = \theta - \frac{D_{ls}}{D_l D_s}\frac{2GM}{c^2}\left(1 + \frac{1}{1-\frac{\omega_0^2}{\omega^2}}\right)\frac{1}{\theta} \\ &- \frac{D_{ls}}{D_l^2 D_s} 2J_r \sin\chi \frac{G}{c^3}\frac{1}{\sqrt{1-\frac{\omega_0^2}{\omega^2}}}\frac{1}{\theta^2} \ .\end{aligned} \tag{4.27}$$

With the help of the substitution

$$\theta_E = \left(\frac{4GM}{c^2}\frac{D_{ls}}{D_l D_s}\right)^{1/2} \tag{4.28}$$

equation (4.27) becomes

$$\begin{aligned}\theta^3 - \beta\theta^2 &- \frac{1}{2}\theta_E^2\left(1 + \frac{1}{1-\frac{\omega_0^2}{\omega^2}}\right)\theta \\ &- \frac{1}{2}\frac{J_r}{MD_l c}\sin\chi\theta_E^2\frac{1}{\sqrt{1-\frac{\omega_0^2}{\omega^2}}} = 0 \ .\end{aligned} \tag{4.29}$$

Solutions of the lens equation give (in our case three) positions θ of the appeared images of the object due to the presence of the lens. θ_E is called the Einstein angle and sets the characteristic angular scale for gravitational lensing phenomena. For many cases (lensing by the stars and stellar mass objects) the Einstein angle is too small to be resolved with modern telescopes. However even the lensing by such small objects like a star can be detectable because it changes the appeared brightness of the star. This situation is called microlensing. The magnification of brightness of the star can be calculated through the formula

$$\mu_\Sigma = \frac{I_{tot}}{I_*} = \sum_k \left| \left(\frac{\theta_k}{\beta}\right) \left(\frac{d\theta_k}{d\beta}\right) \right| , k = 1, 2, ...s \ , \tag{4.30}$$

where s is the total amount of images. This function is always greater than unity and may be significant for small values of β. In this way gravitational lenses can be detected and used even when the individual images cannot be resolved.

Introducing new variable $\theta = x + \frac{\beta}{3}$ one can reduce equation (4.29) to the form

$$x^3 + px + q = 0 \ , \tag{4.31}$$

where

$$p = -\frac{\beta^2}{3} - \frac{1}{2}\theta_E^2 \left(1 + \frac{1}{1 - \frac{\omega_0^2}{\omega^2}}\right) \tag{4.32}$$

and

$$\begin{aligned} q = -2\frac{\beta^3}{27} - \frac{\beta}{6}\theta_E^2 \left(1 + \frac{1}{1 - \frac{\omega_0^2}{\omega^2}}\right) \\ - \frac{1}{2}\theta_E^2 \frac{J_r}{MD_l c} \sin\chi \frac{1}{\sqrt{1 - \frac{\omega_0^2}{\omega^2}}} \ . \end{aligned} \tag{4.33}$$

Equation (4.31) has three different real roots if the condition

$$\frac{q^2}{4} + \frac{p^3}{27} < 0 \tag{4.34}$$

satisfies, which takes place in our case. Our goal is to calculate $\mu_{\Sigma rot}/\mu_\Sigma$ for the case when $\beta \to 0$ and see how rotation affects the maximum value of the peak of magnification in the gravitational microlensing phenomena. Here $\mu_{\Sigma rot}$ is the magnification by the rotating and μ_Σ by the non-rotating gravitational lenses. The magnification in the case of the non-rotating lens surrounded by plasma was investigated in the earlier works and for $\beta \to 0$ is equal to

$$\mu_\Sigma \Big|_{\beta \to 0} \to \frac{1}{2} \frac{\sqrt{2\theta_E^2 \left(1 + \frac{1}{1 - \frac{\omega_0^2}{\omega^2}}\right)}}{\beta} \ . \tag{4.35}$$

Solution of equation (4.31) looks like

$$x = 2\sqrt[3]{r}\cos\frac{\phi + 2k\pi}{3} \ , \qquad (k = 0, 1, 2) \ , \tag{4.36}$$

where

$$r = \sqrt{-\frac{p^3}{27}} \ , \qquad \cos\phi = -\frac{q}{2r} \ . \tag{4.37}$$

The magnification for the case of slowly rotating gravitational lens surrounded by plasma can be obtained as

$$\begin{aligned}
\mu_{\Sigma rot} &= \sum_k \left| \frac{\theta_k}{\beta}\frac{d\theta_k}{d\beta} \right| = \sum_k \left| \frac{x_k + \beta/3}{\beta} \left(\frac{dx_k}{d\beta} + \frac{1}{3} \right) \right| \\
&= \sum_k \left| \frac{1}{3\beta} \left(2\sqrt[3]{r}\cos\frac{\phi + 2k\pi}{3} + \frac{\beta}{3} \right) \right. \\
&\times \left. \left[\frac{2r_\beta}{\sqrt[3]{r^2}}\cos\frac{\phi + 2k\pi}{3} - 2\sqrt[3]{r}\phi_\beta \sin\frac{\phi + 2k\pi}{3} + 1 \right] \right| ,
\end{aligned} \tag{4.38}$$

where the subscript β denotes the derivatives of the corresponding variables with respect to β. For the case when $\beta \to 0$

$$\begin{aligned}
\sqrt[3]{r} &\to \sqrt{\frac{1}{6}\theta_E^2 \left(1 + \frac{1}{1 - \frac{\omega_0^2}{\omega^2}} \right)} \ , \\
-\frac{q}{2r} &\to \frac{\sqrt{27}}{\sqrt{2}} \frac{1}{\theta_E} \frac{J_r}{M D_l c} \frac{\sin\chi}{\sqrt{1 - \frac{\omega_0^2}{\omega^2}}} \frac{1}{\sqrt{\left(1 + \frac{1}{1 - \frac{\omega_0^2}{\omega^2}} \right)^3}} \ , \\
r_\beta &\to 0 \ , \\
\phi_\beta &\to \frac{1}{\sqrt{1 - (q/2r)^2}} \frac{q_\beta}{2r} \ , \\
q_\beta &\to -\frac{1}{6}\theta_E^2 \left(1 + \frac{1}{1 - \frac{\omega_0^2}{\omega^2}} \right) \ .
\end{aligned} \tag{4.39}$$

Using equations (4.39) one can obtain for the ratio $\mu_{\Sigma rot}/\mu_\Sigma$ in the limit $\beta \to 0$ the following result

$$\begin{aligned}
\frac{\mu_{\Sigma rot}}{\mu_\Sigma} = \frac{1}{3\sqrt{3}} \sum_k & \left| \left[\sin\frac{2(\phi + 2k\pi)}{3} \frac{1}{\sqrt{1 - (q/2r)^2}} \right. \right. \\
& \left. \left. + 2\cos\frac{\phi + 2k\pi}{3} \right] \right| ,
\end{aligned} \tag{4.40}$$

which is equal to 1 in the case when $J_r = 0$ as it could be expected.

However, the effect of the dragging of inertial frames on the magnification appears to be insignificant as soon as we try to estimate it for the astrophysical situations. Assuming the lens to be a supermassive black hole with the mass $M = 10^{10}M_{\odot}$, $J_r/Mc \equiv a_r = 0.2M$, $D_l \sim D_s \sim D_{ls} \sim 10^{19}$ km (this corresponds to few Mpc, typical distance to the nearby galaxies), $\sin\chi = 1$ and $\omega_0/\omega = 0.5$, the value of $|q/2r|$ has the order of 10^{-6}. This brings us to a conclusion that for the realistic situations the rotation of the gravitational lens surrounded by a plasma makes no significant additional contribution to the magnification of the brightness of the source.

4.3.2 Faraday effect in a plasma surrounding slowly rotating lensing object

General relativity predicts the rotation of polarization plane of a light wave in vacuum in the curved spacetime as a result of parallel translation of the polarization vector along the null geodesic. This effect is known as gravitational Faraday-Rytov-Skrotskii rotation. Due to the presence of the so-called gravitomagnetic field in the spacetime with the nonvanishing nondiagonal components of the metric tensor, linearly polarized electromagnetic radiation propagating in a Kerr spacetime, Friedman-Robertson-Walker flat metric experiences a rotation of the polarization plane which is a very similar to the Faraday rotation of the polarization plane that occurs when the light during its propagation in the continuous medium is distorted by the presence of a magnetic field. Due to this reason in the presence of the magnetized plasma around intervening lenses such as rotating gravitating compact objects, the propagation of polarized radiation through plasma is accompanied by the rotation of the polarization plane caused by the Faraday effect.

In this subsection we aim to give the estimation of the angle of Faraday rotation of polarization plane for the radiation propagating in plasma in the background of compact object and external magnetic field.

The angle of rotation of the plane of polarization during propagation in a plasma is given by

$$\Delta\varphi = \frac{e^3}{2\pi m_e^2 c^4}\int_L B_\parallel(l) n_e(l)\lambda^2 dl \ , \tag{4.41}$$

where n_e is the electron number density, λ is the wavelength of the radiation as seen by the absorber medium, $B_\parallel$ is the line of sight component of the magnetic field and the integral is over the path length through the intervening absorbers. It should be noted that relativistic electrons of Lorentz factor γ contribute to n_e in approximate proportion to γ^{-2}.

From multi-wavelength observations of the polarization, it is found that a majority of sources have measured φ that vary over a wide range of wavelength such that $\Delta\varphi = \varphi(\lambda) - \varphi(0)$, where the intrinsic position angle $\varphi(0)$ is the zero-wavelength value. The constant RM is called the rotation measure and is a "polarized emission-weighted" mean of the Faraday depth.

The rotation measure, as measured by the observer at redshift of zero is given by

$$RM = \frac{\Delta\varphi}{\lambda_{obs}^2} = \frac{e^3}{2\pi m_e^2 c^4}\int B_\parallel(l) n_e(l)\left[\frac{\lambda(l)}{\lambda(obs)}\right]^2 dl. \tag{4.42}$$

For the Faraday Rotation produced by a deflector at redshift z, the rotation measure of the intervening galaxy with the average line of sight magnetic field component,

$$< B_\parallel >= \frac{\int n_e(z) B_\parallel(z) dl(z)}{\int n_e(z) dl(z)} \ , \tag{4.43}$$

and the electron column density, $N_e = \int n_e(z) dl(z)$ may be expressed as

$$RM \simeq 2.6\times 10^{13}\frac{< B_\parallel > N_e}{(1+z)^2}\text{rad m}^{-2} \ . \tag{4.44}$$

One can estimate RM for a plasma density in a vicinity of the lensing SMBH with mass $M = 10^{10} M_{\odot}$ of the order $N_e = 5 \times 10^4 \mathrm{cm}^{-3}$ and magnetic field background with strength $B_{\parallel} = 10^4$Gauss as

$$RM \simeq 1.3 \times 10^{22} (1+z)^{-2} \mathrm{rad/m}^2 \ . \tag{4.45}$$

Even though the Faraday Rotation may be caused by the source, the intervenor and the Milky Way, the difference in the rotation angle between the multiple images is practically due to the lens which is contained in Eq. (4.44). Consequently, the magnitude of the difference in rotation measures (RM) between images turns out to be a valuable probe for estimating the average line of sight component of magnetic field in the lenses.

Faraday rotation measure (RM) maps of the central parsecs of quasars and radio galaxies hosting relativistic jets also reveal that the medium on parsec scales surrounding AGNs could be significantly magnetized.

Let us estimate the value of the Faraday angle for the frequency of radiation $\nu = 3.27 \times 10^6$Hz, plasma density in the vicinity of the lensing SMBH with mass $M = 10^{10} M_{\odot}$ of the order of $N_e = 5 \times 10^4 \mathrm{cm}^{-3}$ and magnetic field background with strength $B_{\parallel} = 10^4$Gauss, at the distance $L = 1.48 \times 10^{15}$cm. Then an estimation of an Faraday angle takes form

$$\Delta\varphi = 1.62 \times 10^{15} \quad \mathrm{rad} \tag{4.46}$$

It has to be mentioned that estimates of magnetic fields for active galactic nuclei can be based on the observed polarization degrees. The distribution of magnetic field around black hole and polarization in accretion discs of AGN is studied in [255], as well as the dependence of the degree of polarization from the spin of the central black hole. The approximate analytical expressions for the polarization of the radiation from a magnetized disk around black hole can be found in [255].

4.4 Shadow of Reissner-Nordström–de-Sitter dyon black hole

We consider photon geodesics in the Reissner-Nordström – de-Sitter dyon metric. Critical impact parameters for photon geodesics separate capture and scattering regions and the parameters characterize shadow sizes (radii). In paper [120] critical impact parameters for the Reissner-Nordström black hole (including the Reissner-Nordström metric with a tidal charge) have been derived analytically while shadow sizes for the Schwarzschild – de Sitter (Köttler) metric have been found in papers [256, 257]. In the current section we obtain analytical expressions for the shadow radii of the Reissner-Nordström – de-Sitter black holes and discuss the critical values of relevant parameters, generalizing thus results discussed earlier in papers [120, 256, 257]. Assuming that such Reissner-Nordström – de-Sitter dyon black holes are located in the Galactic Center and the centres of other galaxies (including M87, for instance), one could use the results to analyse current and future observational data obtained with advanced observational facilities such as the Event Horizon Telescope.

At the first glance, the Reissner-Nordström – de-Sitter dyon black hole models look rather artificial for astrophysical black holes. However, there are, at least, five reasons to consider such a model and its applications for astrophysics. First, in the last years, the Reissner-Nordström black hole model was actively used to explain observed astrophysical phenomena, in particular for GRBs [258, 259, 260, 261], but there is a severe criticism of strong electric field paradigm [262] and due to these arguments perhaps an existence of stable astrophysical black holes with a significant electric charge does not look very probable. However, this argument is not relevant in the case of dyonic black holes with magnetic charges. Second, the Reissner-Nordström black hole solutions with a tidal charge arise in the multi-dimensional models, for instance in the Randall – Sundrum approach [263] (see a discussion of possible astrophysical consequences from the assumption about presence of a black hole with a tidal charge in [264, 129, 128, 265]). Importantly, a tidal charge corresponds to influence of an additional dimension, and it is formally equivalent to the electric charge squared, but the tidal charge may take both positive and negative values, and currently there are no severe constraints on the tidal charge value, contrary to the case of the electric charge. Moreover, it was suggested to apply the Reissner-Nordström black hole model with a tidal charge for the black hole at the Galactic Center, in particular to consider the gravitational lensing for such an object [128, 126, 266, 127]. Third, as shown in [267], the black holes with phantom fields could mimic the Reissner-Nordström black holes with an electric charge, and it was proposed to use this model instead of the Schwarzschild metric for the super-massive black hole at the Galactic Center. Fourth, the Reissner-Nordström – de-Sitter black hole metric arises in a natural way in the Horndeski gravity as shown in [268] where the authors also suggested to use this metric for astrophysical black holes, including the black hole at the Galactic Center. Fifth, from theoretical point of view, it would be interesting to have an analytical expression for the shadow size and the loss cone of the Reissner-Nordström – de-Sitter dyon black hole, because we could expect that in the future a wider class of alternative theories of gravity could predict a richer set of black hole models that could mimic the Reissner-Nordström black hole solution.

We consider spherically symmetric Reissner-Nordström – de-Sitter dyon (RNdSD) spacetime (one could find a review on searches of monopoles and dyons in [269] and references therein). In last years Reissner-Nordström – de-Sitter dyon black holes are considered as realistic objects, and different authors considered astrophysical processes, for instance, accretion, near such objects. The line element in the metric is given in the form [270]

$$ds^2 = -f(r)dt^2 + f(r)^{-1}dr^2 + r^2 d\theta^2 + r^2 \sin^2\theta d\phi^2, \tag{4.47}$$

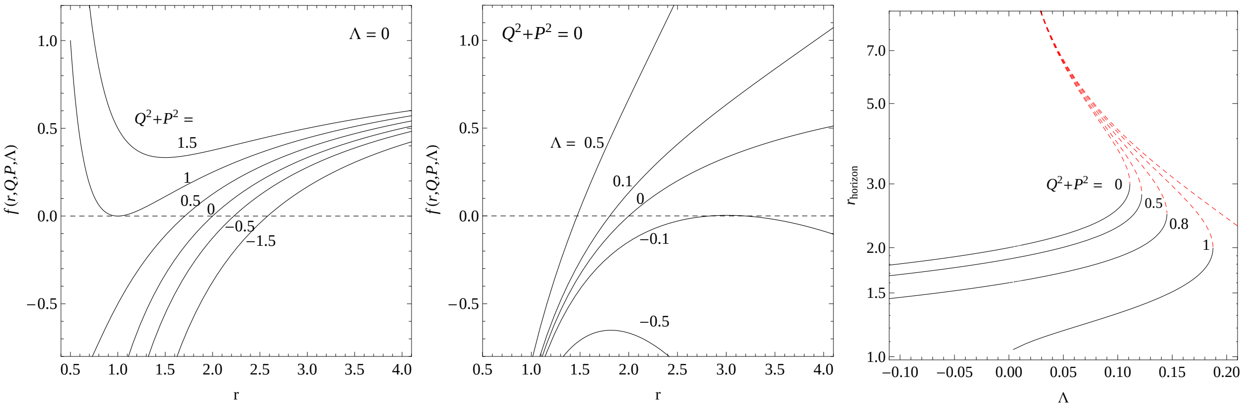

Figure 4.2: Left and middle plots show the lapse function $f(r, Q, P, \Lambda)$ for different values of parameters $Q^2 + P^2$ and Λ labelled by corresponding numbers. Without loss of generality the mass of compact object is taken to be unity. The points of intersections of curves with horizontal dashed lines correspond to the locations of event horizons and thus the existence of black holes. Right plot demonstrates the dependences of event horizons (solid black) and cosmological horizons (red dashed) on the parameters $Q^2 + P^2$ and Λ. For completeness, the negative values of $Q^2 + P^2$ reflect the case of the braneworld RNdSD spacetime geometry with negatively-valued tidal charges.

where the lapse function is defined as

$$f(r) = 1 - \frac{2M}{r} + \frac{Q^2 + P^2}{r^2} - \frac{1}{3}\Lambda r^2. \tag{4.48}$$

Here M is the mass of a central compact object, Q is the electric charge, P is the magnetic monopole charge, and Λ is the cosmological constant. The term dyon is used due to simultaneous existence of both electric and magnetic charges. The physical singularity is located at $r = 0$. The Reissner-Nordström – de-Sitter dyon black holes have three horizons which are defined by the positive real roots of $f(r) = 0$. These are the inner black hole horizon (or Cauchy horizon) at r_-, the event (outer black hole) horizon at r_+, and the cosmological horizon at r_c – there is $r_- < r_+ < r_c$. Behaviour of the lapse function $f(r, M, Q, P, \Lambda)$ is demonstrated in Fig.4.2. The RNdSD black holes can exist, if the condition $0 < Q^2 + P^2 < 9/8$ is satisfied, otherwise, RNdSD naked singularities occur where only the cosmological horizon survives.

The presence of a magnetic charge P generalizes Maxwell's equations in such a way that

$$F^{\mu\nu}{}_{;\nu} = 4\pi J^{\mu}_{Q}, \quad \tilde{F}^{\mu\nu}{}_{;\nu} = 4\pi J^{\mu}_{P}, \tag{4.49}$$

where J_Q and J_P are the electric and magnetic 4-current densities, $F_{\mu\nu} = A_{\nu,\mu} - A_{\mu,\nu}$ is the electromagnetic tensor and $\tilde{F}_{\mu\nu}$ its dual which has a form

$$\tilde{F}^{\mu\nu} = \frac{1}{2\sqrt{-g}}\epsilon^{\mu\nu\alpha\beta}F_{\alpha\beta}, \tag{4.50}$$

where $g = det|g_{\mu\nu}|$. Note that the electric and magnetic constants in the geometric units are taken to be equal to unity $\epsilon_0 = 1 = \mu_0$, as well as the constants $c = 1 = G$. The four-vector potential of the electromagnetic field of a dyonic compact object takes the form

$$A_{\mu} = \frac{Q}{r}\delta^{(t)}_{\mu} - P\cos\theta\ \delta^{(\phi)}_{\mu}, \tag{4.51}$$

which has two non-vanishing components, A_t and A_{ϕ}. The dual electromagnetic tensor $\tilde{F}_{\mu\nu} = \tilde{A}_{\nu,\mu} - \tilde{A}_{\mu,\nu}$ can be found using the four-potential (4.50) in the form

$$\tilde{A}_{\mu} = \frac{P}{r}\delta^{(t)}_{\mu} + Q\cos\theta\ \delta^{(\phi)}_{\mu}. \tag{4.52}$$

Let us estimate the maximal electric charge of the Reissner–Nordström black hole, given for $P = 0$ and $\Lambda = 0$. Characteristic length scale of the Reissner–Nordström charge $Q_{\rm G}$ can be compared with the Schwarzschild radius of a black hole due to the relation

$$\sqrt{\frac{Q_{\rm G}^2 G}{c^4}} = \frac{2GM}{c^2}. \tag{4.53}$$

This implies that the charge, whose gravitational effect is comparable with the spacetime curvature of the related black hole, must have magnitude

$$Q_{\rm G} = 2G^{1/2}M \approx 10^{30}\frac{M}{M_{\odot}}\ \mathrm{statC}. \tag{4.54}$$

For example, the value of the induced charge of a rotating black hole immersed into an external asymptotically uniform magnetic field aligned along the axis of rotation, generated due to the Faraday induction, namely the Wald charge $Q_{\rm W} = 2MaB \leq 2M^2B$ takes the value

$$Q_{\rm W} \leq 10^{18} \left(\frac{M}{M_\odot}\right)^2 \left(\frac{B}{10^8{\rm G}}\right) \ {\rm statC}, \tag{4.55}$$

which is obviously much less than the value of $Q_{\rm G}$ from (4.54). The properties of spherically symmetric black holes with the non-vanishing charge and the cosmological constant can be found, e.g., in [271]. The effect of the cosmological constant on the evolution of Magellanic Clouds in the gravitational field of the Galaxy is studied in [131].

4.4.1 Particle and photon motion in RNdSD spacetime

In this subsection we consider motion of massive particles and photons in the field of a spherically symmetric Reissner-Nordström–de-Sitter dyon black hole. For massive particles we study the most general case of particles demonstrating a simultaneous presence of an electric charge q and a magnetic monopole charge p, namely dyons. The dynamics of a dyon in a dyon field of a black hole is possible on a cone with the restriction $qP \neq pQ$. More details on the geodesic motion of dyons in the field of a Reissner-Nordström dyon black hole can be found in [256].

Due to the assumption of the symmetries of the background spacetime and generated electromagnetic fields, one can write the Hamiltonian for a particle with mass m, electric charge q, and magnetic monopole charge p, in the most general form

$$H = \frac{1}{2} g^{\alpha\beta}(\Pi_\alpha - qA_\alpha + p\tilde{A}_\alpha)(\Pi_\beta - qA_\beta + p\tilde{A}_\beta) + \frac{1}{2}\,\delta m^2, \tag{4.56}$$

where Π^μ is the generalized canonical four-momentum related to the kinetic four-momentum π^μ as

$$\Pi_\mu = \pi_\mu + qA_\mu - p\tilde{A}_\mu. \tag{4.57}$$

and $\delta = (0,\ 1)$. The case with $\delta = 1$ applies for massive particles, the case $\delta = 0$ applies to photons. For the kinetic four-momentum we can write

$$\pi_\mu = g_{\mu\nu} \frac{dx^\nu}{d\zeta} \tag{4.58}$$

where we introduced the affine parameter ζ along the geodesics, which is related to the test particle proper time τ by the relation $\zeta = \tau/m$. Note that the equations describing motion of neutral particles can be obtained by equalizing charge and magnetic monopole to zero, $q = p = 0$. For the photon motion, one has to put simultaneously $\delta = p = q = 0$.

The dynamics of particles and photons governed by the Hamiltonian (4.56) is given by the Hamilton equations

$$\frac{dx^\mu}{d\zeta} = \frac{\partial H}{\partial \Pi_\mu}, \qquad \frac{d\Pi_\mu}{d\zeta} = -\frac{\partial H}{\partial x^\mu}. \tag{4.59}$$

The background metric is static and axially symmetric, therefore, the metric admits two Killing vector fields $\xi^\alpha_{(t)}$ and $\xi^\alpha_{(\phi)}$ which satisfy the equation $\xi_{\alpha;\beta} + \xi_{\beta;\alpha} = 0$. The Killing vector fields are associated with two integrals of motion which are the energy E and the axial angular momentum L, and can be written in the form

$$E \;=\; -\xi^\alpha_{(t)} \Pi_\alpha = f(r) \frac{dt}{d\zeta} - \frac{qQ + pP}{r}, \tag{4.60}$$

$$L \;=\; \xi^\alpha_{(\phi)} \Pi_\alpha = r^2 \sin^2\theta \frac{d\phi}{d\zeta} - (qP - pQ) \cos\theta. \tag{4.61}$$

Equalizing the Hamiltonian (4.56) to zero, which is equivalent to imposing the normalization condition $\pi^\mu \pi_\mu = -\delta m^2$, and separating the term containing θ, we get the third integral of motion, or the separation constant, in the form

$$K = r^4 \left(\frac{d\theta}{d\zeta} \right)^2 + \frac{1}{\sin^2\theta} \left[L + (qP - pQ) \cos\theta \right]^2 . \tag{4.62}$$

Three integrals of the motion, E, L and K, allow us to find the full set of integrated equations of motion for both particles and photons. For the convenience, we can express some of the physical quantities in dimensionless form by the relations

$$\begin{aligned}\hat{r} &= \frac{r}{M}, \;\; \hat{t} = \frac{t}{M}, \;\; \hat{Q} = \frac{Q}{M}, \;\; \hat{P} = \frac{P}{M}, \;\; \hat{\zeta} = \frac{\zeta}{M} \\ \hat{L} &= \frac{L}{M}, \;\; \hat{K} = \frac{K}{M^2}, \;\; \hat{\Lambda} = \Lambda \; M^2.\end{aligned} \tag{4.63}$$

Neglecting further the hat symbols, we get the integrated equations of motion in the form:

$$\frac{dt}{d\zeta} = \frac{1}{f(r)}\left(E + \frac{qQ + pP}{r}\right), \tag{4.64}$$

$$\frac{d\phi}{d\zeta} = \frac{1}{r^2 \sin^2\theta}\left[L + (qP - pQ)\cos\theta\right], \tag{4.65}$$

$$r^4 \left(\frac{d\theta}{d\zeta}\right)^2 = K - \frac{1}{\sin^2\theta}[L + (qP - pQ)\cos\theta]^2, \tag{4.66}$$

$$r^4 \left(\frac{dr}{d\zeta}\right)^2 = R(r), \tag{4.67}$$

where the radial function reads

$$R(r) = (Er + qQ + pP)^2 r^2 - f(r)\left(\delta m^2 r^2 + K\right) r^2, \tag{4.68}$$

and $f(r)$ is the lapse function (4.48). The radial function $R(r)$ is taken in the particular form (4.68) in order to keep only the positive powers in r after expansion of $f(r)$ in the explicit form. Note that the equations for the θ and ϕ motion contain two terms of pairings of the electric charge of the particle q with the magnetic monopole charge of the black hole P, and the magnetic monopole charge of the particle p with the electric charge of the black hole Q. In two other equations of motion for t and r, the pairing occurs inversely, in the standard way, namely q is combined with Q, and p with P. This implies that the problem of the dyon dynamics in the field of the RNdSD black holes is axially symmetric, while the spacetime itself is spherically symmetric. The cross electro-magnetic interaction violates the spherical symmetry, and the trajectory of a dyon in the RNdSD black hole spacetime is concentrated on a cone. We shall study consequences of this violation in a future works.

Here, we concentrate on the motion of photons – they have $m = q = p = 0$ and for their motion the relevant equations keep the spherical symmetry of the spacetime geometry. For photons there is

$$E = -\xi^{\alpha}_{(t)}\Pi_{\alpha} = f(r)\frac{dt}{d\zeta}, \tag{4.69}$$

$$L = \xi^{\alpha}_{(\phi)}\Pi_{\alpha} = r^2 \sin^2\theta \frac{d\phi}{d\zeta}. \tag{4.70}$$

Since the metric (4.47) is spherically symmetric, a photon trajectory is flat and one can choose the central plane of the photon motion to be the equatorial plane at $\theta = \pi/2$ – then $\frac{d\theta}{d\zeta} = 0$, and $K = L^2$. The radial function governing the radial motion of photons reads

$$R(r) = E^2 r^4 - K f(r) r^2, \tag{4.71}$$

where $f(r)$ is the lapse function (4.48).

4.4.2 Capture cross section of photons

In this section we concentrate our attention on the motion of massless particles, and study the capture cross section of photons by RNdSD black hole. Later we demonstrate that the results related to the black hole shadow obtained in this way are in accord with those obtained in the standard method of the effective potential. In our study we assume that the black hole shadow is considered by a distant static observer that is located at the so called static radius where the gravitational attraction of the black hole is just balanced by the cosmic repulsion [256]. It is demonstrated in [271] that near the static radius the spacetime is nearly flat, if the cosmological constant is sufficiently small – such a condition is surely satisfied for any black hole in the Universe with the observationally restricted cosmological constant.

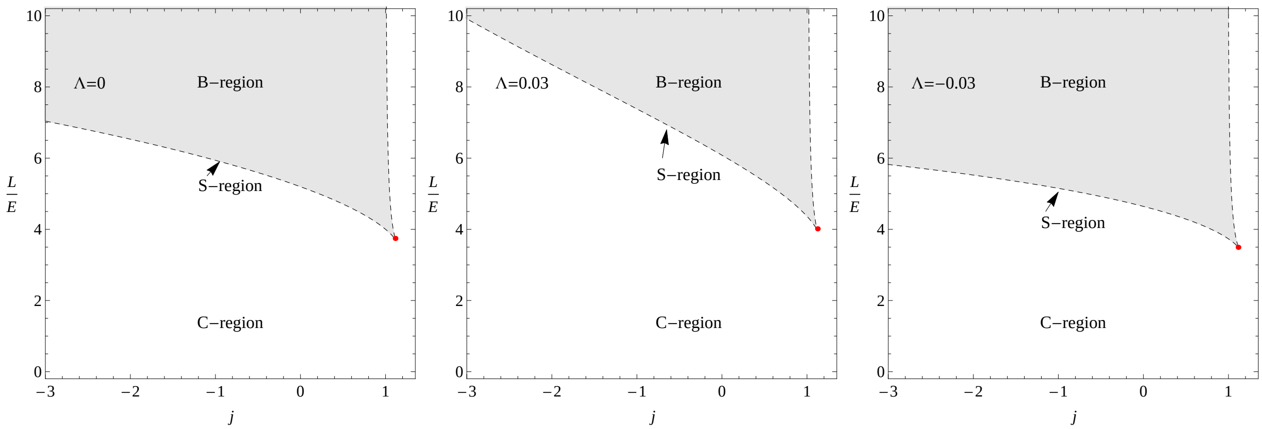

Figure 4.3: Capture region (C-region), scatter region (S-region) and boundary region (B-region) of photon in RNdSD spacetime in parameter space given by impact parameter L/E and charge parameter $j = Q^2 + P^2$ for different values of cosmological constant: $\Lambda = 0$ (left), $\Lambda = 0.03$ (middle) and $\Lambda = -0.03$ (right).

Applying thus the conditions $q = p = \delta = 0$ and using the motion constants E and K for photon in Eq.(4.68), one can write the radial function $R(r)$ in the following explicit form

$$R(r) = \left(E^2 + \frac{1}{3}\Lambda K\right) r^4 - Kr^2 + 2Kr - J^2 K, \tag{4.72}$$

where we introduced the notation $J^2 = Q^2 + P^2$ (we consider also the case when J^2 is negative, since this case corresponds to a RN black hole with a tidal charge which arises due to a presence of an additional dimension). Dividing both sides of (4.72) by the constant factor $(E^2 + \frac{1}{3}\Lambda K)$, one can rewrite the above equation in the form

$$\frac{R(r)}{E^2 + \frac{1}{3}K\Lambda} = r^4 - \frac{Kr^2}{E^2 + \frac{1}{3}K\Lambda} + \frac{2Kr}{E^2 + \frac{1}{3}K\Lambda} - \frac{KJ^2}{E^2 + \frac{1}{3}K\Lambda}. \tag{4.73}$$

Using the notation

$$\alpha = \frac{K}{E^2 + \frac{1}{3}K\Lambda}. \tag{4.74}$$

one can rewrite the equation (4.73) in the following form

$$\frac{\alpha}{K} R(r) = r^4 - \alpha r^2 + 2\alpha r - \alpha J^2. \tag{4.75}$$

The critical value of the impact parameter for a photon (which is defined as the ratio of angular momentum to the energy, L/E) to be captured by the RNdSD black hole depends on the multiplicity root condition of the polynomial $R(r)$. There is a capture region (C-region) which corresponds to impact parameters (or integrals of motion) where the corresponding polynomial has no root, there is a scatter region (S-region) which corresponds to impact parameters (or integrals of motion) where corresponding polynomial has a single root and there is a boundary region (B-region) which corresponds to impact parameters (or integrals of motion) where the corresponding polynomial has a double root. The S-region separates B and C regions and it is called shadow boundary. C, S and B regions are plotted in parametric space given by the impact parameter L/E and charge parameter $j = Q^2 + P^2$ in Fig. 4.3, for different values of Λ parameter. The shadow of the black hole is thus corresponding to the C-region where the photons are captured by the black hole. In the naked singularity case, there are no captured photons. The shadow in this case is different from that of a black hole, being a dark circumference, corresponding to photon orbit and the central dark point, corresponding to a singularity. In contrast to a black hole case, the region inside the circumference is not dark.

In order to calculate the multiplicity root, we use the method of Newton's equations that have the form

$$p_k - p_{k-1}s_1 + p_{k-2}s_2 + \cdots + (-1)^k k s_k = 0, \quad 1 \leq k \leq n \tag{4.76}$$

$$p_k - p_{k-1}s_1 + p_{k-2}s_2 + \cdots + (-1)^n p_{k-n}s_n = 0, \quad k > n \tag{4.77}$$

We introduce the following polynomial

$$\Delta_n(X_1, \cdots, X_n) = \prod_{1\leq i\leq j\leq n} (X_i - X_j) = 0, \tag{4.78}$$

which can be written as the Vandermonde determinant

$$\Delta_n(X_1, \cdots, X_n) = \begin{vmatrix} 1 & 1 & \cdots & 1 \\ X_1 & X_2 & \cdots & X_n \\ \cdots & \cdots & \cdots & \cdots \\ X_1^{n-1} & X_2^{n-1} & \cdots & X_n^{n-1} \end{vmatrix} \tag{4.79}$$

Applying the above given discriminant to the case of our study, we get

$$Dis(s_1, s_2, s_3, s_4) = \begin{vmatrix} 1 & 1 & 1 & 1 \\ X_1 & X_2 & X_3 & X_4 \\ X_1^2 & X_2^2 & X_3^2 & X_4^2 \\ X_1^3 & X_2^3 & X_3^3 & X_4^3 \end{vmatrix} = \begin{vmatrix} 4 & p_1 & p_2 & p_3 \\ p_1 & p_2 & p_3 & p_4 \\ p_2 & p_3 & p_4 & p_5 \\ p_3 & p_4 & p_5 & p_6 \end{vmatrix} \tag{4.80}$$

Using Newton's equations, we thus obtain:

$$\begin{aligned} p_1 &= 0, \\ p_2 &= -2s_2, \\ p_3 &= 3s_3, \\ p_4 &= 2(s_2^2 - 2s_4), \\ p_5 &= -5s_2s_3, \\ p_6 &= -2s_2^3 + 3s_3^2 + 6s_2s_4, \end{aligned}$$

where s_i is given by

$$\begin{aligned} s_1 &= 0, \\ s_2 &= -\alpha, \\ s_3 &= -2\alpha, \\ s_4 &= -\alpha J. \end{aligned}$$

Finally, one can calculate the determinant for given $R(r)$ in the form

$$\begin{vmatrix} 4 & 0 & 2\alpha & -6\alpha \\ 0 & 2\alpha & -6\alpha & 2(\alpha^2+2\alpha J^2) \\ 2\alpha & -6\alpha & 2(\alpha^2+2\alpha J^2) & -10\alpha^2 \\ -6\alpha & 2(\alpha^2+2\alpha J^2) & -10\alpha^2 & 12\alpha^2+2\alpha^3+6\alpha^2 J^2 \end{vmatrix} = \\ = 16\alpha^3\left[(1-J^2)\alpha^2-(8J^4-36J^2+27)\alpha-16J^6\right] \tag{4.81}$$

The polynomial $R(r)$ thus has a multiple root when

$$(1-J^2)\alpha^2-(8J^4-36J^2+27)\alpha-16J^6=0. \tag{4.82}$$

This equation coincides with Eq.(24) from [120], differing in the definitions of J and α. Substituting the explicit form of α given in (4.74), we solve the equation (4.82) with respect to the impact parameter $l=K/E^2$. The positive solution of the quadratic equation in terms of α determines the critical impact parameter of the capture cross section of photons by a RNdSD black hole that takes the form

$$l_{cr}=\frac{-24J^4+108J^2-3\sqrt{-\left(8J^2-9\right)^3}-81}{8J^4\Lambda-36J^2\Lambda+\sqrt{-\left(8J^2-9\right)^3}\Lambda+6J^2+27\Lambda-6}. \tag{4.83}$$

The square root of l_{cr} determines the radius of the shadow of RNdSD black hole, which is plotted in the middle plot of Fig.4.4 for selected values of the cosmological parameter Λ as function of the parameter j reflecting also the braneworld RNdS geometries. However, the expression (4.83) diverges when the cosmological constant coincides with the value

$$\Lambda_0=\frac{6\left(1-J^2\right)}{8J^4-36J^2+27+\sqrt{\left(9-8J^2\right)^3}}. \tag{4.84}$$

This implies that the shadow disappears when $\Lambda>\Lambda_0$. The region where the shadow can exist, $\Lambda<\Lambda_0$, in dependence on the parameter $j=J^2$, is demonstrated on the left plot of Fig.4.4. The presence of the root in the expression

(4.83) for l_{cr} gives the limit for the parameter J^2 allowing black holes that create a shadow. In other words, the shadows can exist only when $J^2 \leq 9/8$, which determines the critical value of J when the size of the shadow is minimal for given value of Λ. Of course, this means that there is no shadow possible for the naked singularity spacetimes. Solving the equation $\frac{\partial R}{\partial r}(r_{max}) = 0$, one can get the radius of the unstable photon orbit. From trigonometric formula for the roots of cubic equation, we obtain

$$r_{ph} = \sqrt{\frac{2l_{cr}}{3 + \Lambda l_{cr}}} \cos\frac{\theta}{3}, \tag{4.85}$$

where

$$\cos\theta = -3\sqrt{\frac{3 + \Lambda l_{cr}}{2l_{cr}}}. \tag{4.86}$$

An accurate simplification of the equation (4.85) shows that the Λ - dependence of the radius of the photon orbit vanishes, similarly to the simpler non-dyonic cases [271]. For $J = 0$, the photon orbit corresponds to $r_{ph} = 3$. For maximal value of $J^2 = 9/8$, the photon orbit is located at $r_{ph} = 1.5$. Decreasing the value of the parameter J^2, the radius of the photon circular orbit increases. The dependence of the photon orbit on the parameter $j = J^2$ is demonstrated in the right plot of Fig.4.4. One can see that in the regions of allowance, both the radius of the shadow and the radius of the photon circular orbit increase with decreasing value of the charge parameter j and fixed value of Λ, while they increase with increasing value of the cosmological constant Λ. Notice that while the cosmological constant is close to its limiting value when the horizons coincide, the static radius that is considered as site of the observer becomes located close to the coincident horizons – for details see [271].

4.4.3 Effective potential approach

It is useful and illustrative to compare the results obtained above, with those given by the standard analysis of the effective potential of the photon dynamics.

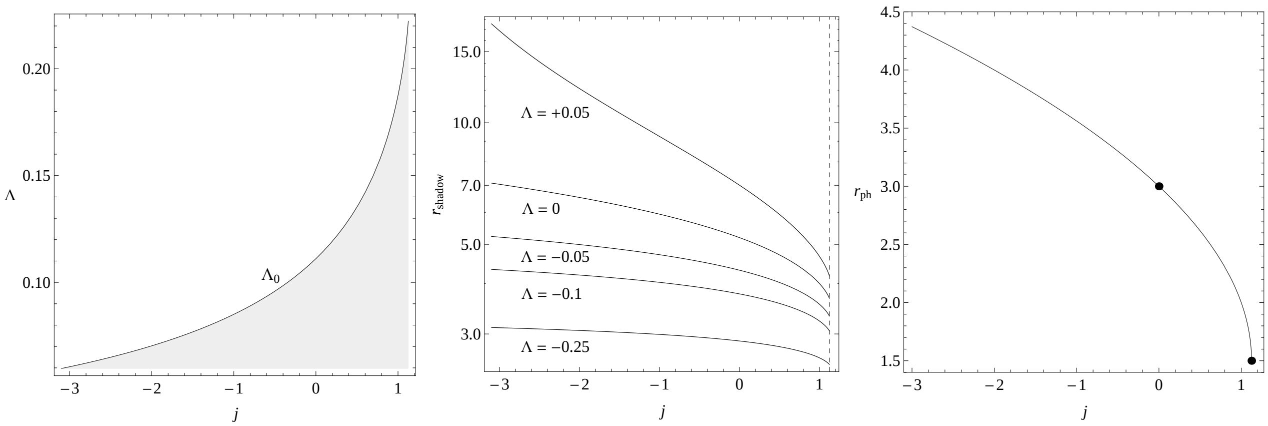

Figure 4.4: Left plot represents the dependence of the critical value of Λ_0 on the parameter $j = J^2$, for which the radius of a shadow diverges. The region where the shadow can exist $\Lambda < \Lambda_0$ is shaded. The plot in the middle represents the shadow radius in dependence on the parameter $j = J^2$ for different values of Λ. The critical value of $j = 9/8$ is dashed. Right plot demonstrates the dependence of a radius of photon orbit on the parameter j. The minimal value of the photon orbit ($r_{ph} = 1.5$ for $j = 9/8$) and the Schwarzschild limit ($r_{ph} = 3$ for $j = 0$) are marked by black points.

One can rewrite Eq.(4.67) for photon as follows

$$\left(\frac{dr}{d\tau}\right)^2 = E^2 - V_{\text{eff}}^2, \quad V_{\text{eff}}^2 = f(r, Q, P, \Lambda)\,\frac{K}{r^2}. \tag{4.87}$$

The motion is allowed where $E^2 \geq V_{\text{eff}}^2$. Introducing the impact parameter as the square of the ratio of the angular momentum to the energy $l \equiv K/E^2 = L^2/E^2$, one can rewrite the condition $E^2 \geq V_{\text{eff}}^2$ in the following form

$$l \leq l_R \equiv \frac{r^4}{r^2 - 2r + J^2 - \Lambda r^4/3} \tag{4.88}$$

The impact parameter $l = l_R$ determines the turning points of the radial motion of photons. The photon circular orbit is located at the stationary point of the effective potential, given by the root of the expression $dV_{\text{eff}}/dr = 0$. This implies that the photon orbit is located at

$$r_{ph} = \frac{1}{2}\left(3 + \sqrt{9 - 8J^2}\right). \tag{4.89}$$

Expression (4.85) coincides with expression (4.89) obtained earlier. Substituting (4.85) into (4.88), we get the expression for the critical impact parameter of the marginally captured photons in the form

$$l_{cr} = \frac{r_{ph}^4}{r_{ph}^2 - 2r_{ph} + J^2 - \Lambda r_{ph}^4/3}. \tag{4.90}$$

This expression is identical to (4.83) found above. Thus the square root of l_{cr} determines the radius of the shadow. The positiveness of the shadow radius restricts the possible values of the parameters J^2 and Λ. For cosmological constant this condition corresponds to $\Lambda < \Lambda_0$, with Λ_0 given by equation (4.84). One can conclude that both approaches lead to identical result.

4.5 Conclusions

Many different theoretical models have been proposed for the Galactic Center and different black hole models have a high priority among them.

We have studied the gravitational lensing in a plasma surrounding slowly rotating gravitational object and can summarize our main findings as the following.

1. The deflection angle of light by the slowly rotating gravitational source surrounded by plasma linearly depends on both the gravitational mass M and the angular momentum J of the gravitational lens. The ratio of term being responsible to angular momentum to the one induced by the total mass may reach 10^{-1} for the millisecond pulsars.

2. We have studied influence of rotation of gravitational lens to the magnification of brightness of the star in the case of microlensing and have shown that the rotation does not make noticeable contribution to the magnification.

3. The effect of the Faraday rotation of the polarization plane of a light wave propagating in plasma surrounding slowly rotating lensing object is considered. An estimation of the angle of the Faraday rotation and Rotation measure for the case of the rotating black hole surrounded by plasma is represented.

We have also determined the shadow of Reissner-Nordström–de-Sitter dyon black hole. Probably, assumptions about spherical symmetry and a presence of electric charge in the metric do not look realistic, however, a Reissner–Nordström metric could arise in a natural way in alternative theories of gravity like Reissner–Nordström solutions with a tidal charge in Randall–Sundrum model (such an approach is widely discussed in the literature). Moreover, the presence of a magnetic monopole charge seems to be an interesting possibility deserving a serious attention. Certainly, the Λ-term should be present in the model, however, if we adopt its value restricted by the cosmological models and recent observations, it should be very tiny to cause a significant impact. On the other hand, if we have a dark energy instead of the cosmological constant, one could propose ways to evaluate local dark energy for different cases, therefore, one could constrain the Λ-term from observations, as it was noted in [120] analysing impact of the Λ-term on the observational phenomena near the Galactic Center (similarly to the cases where an impact of the Λ-term has been analysed for the effects in the Solar system). Another possibility could be represented by the Λ-term implied possibly by the $f(R)$ gravity.

We obtained analytical expressions for the shadow sizes of the RNdSD black holes. The expressions may be used to constrain parameters of these black holes with current and future interferometric observations, for instance with the Event Horizon Telescope in the case if magnetic or tidal charge is significant. If a black hole indeed has a significant electric charge or/and a magnetic monopole charge, it could cause specific signatures in the accretion flow in contrast to a tidal charge. Since we considered a spherically symmetric metric, the shadow shape is circular, distribution of bright spots around shadows could violate the symmetry due to different reasons, for instance due to an asymmetry of an accretion flow.

Main results and conclusions

Below we list the main results and predictions of the dissertation work being of astrophysical relevance.

1. It has been shown that the black hole at the center of the Galaxy possesses stable unshielded electric charge with an upper limit of $Q_{\bullet} \lesssim 10^{15}\,\mathrm{C}$, which does not have an influence on the spacetime metric. A novel observational test of the charge based on the flattening and decrease of the surface brightness profile of the thermal bremsstrahlung inside the innermost 10^5 Schwarzschild radii has been proposed. According to Chandra X-ray data detecting a weak indication of the drop of the brightness profile at $R_{\mathrm{proj}} \lesssim 0.4''$, an observational upper limit on the charge of SgrA* has been obtained as $Q_{\mathrm{SgrA*}} \lesssim 3 \times 10^8\,\mathrm{C}$.

2. It has been shown that unscreened charge of a black hole can effectively mimic the spin parameter of the black hole up to 60% of its maximal value, which is reflected in considerable shift of the innermost stable circular orbits for charged particles. Thus, the models estimating the spin of a black hole may require reconsideration due to arising underdetermination in the measurements of the spin.

3. New, electromagnetic properties of bright flare components orbiting Sgr A*, detected by GRAVIY instrument in May-July 2018 have been found. In particular, it has been shown that a plasma surrounding SgrA* is relativistic

and magnetized, which leads to the charge separation in a plasma. The net charge number density of plasma surrounding Sgr A* is estimated by order $10^{-5}\mathrm{cm}^{-3}$, while the plasma number density is of order $10^{71}\mathrm{cm}^{-3}$.

4. A simple formula for the detection probability of a star crossing a sparse region of Galactic center, where the total number of bright stars is expected to fall below one has been derived. It has been shown that it is unlikely to detect a bright star in the innermost $R = 1500$ Schwarzschild radii from Sgr A*, although stellar fly-by at highly-eccentric orbit is possible.

5. The original ultra-efficient mechanism of acceleration of ultra-high-energy cosmic rays has been proposed, based on the energy extraction from rotating black holes. Applying the magnetic Penrose process to the radioactive decays and ionizations of ions it has been shown that protonвЂ™s energy can naturally exceed 10^{20}eV for supermassive black hole of $10^9 M_\odot$ and magnetic field of 10^4G. This gives constraints on UHECRs source parameters, such as mass, distance and magnetic field.

6. Applied to the Galactic center supermassive black hole Sgr A* the energy of escaping proton has been obtained by order $10^{15.5}$eV, which coincides with the knee of the cosmic ray energy spectra, where the flux of particles shows significant decrease. The sharpness of the knee energy spectra may indicate the existence of a single source at knee energy level. The results are confirmed numerically by the simulation of the ionization in the vicinity of rotating black hole immersed into external magnetic field. It was shown that the process is almost independent of the magnetic field configuration.

7. New effect of orbital widening in the vicinity of magnetized black holes has been found. Radiation reaction force can shift circular orbits of charged particles outwards from the black hole, which may occur in the case with

repulsive Lorentz, i.e. when $qLB > 0$, where q and L are charge and angular momentum of the particle and B is intensity of magnetic field. The effect operates in any magnetic field configuration sharing the symmetries of background spacetime. It has been shown that the protons are cooling in average 10^{10} times slower than electrons in identical conditions.

8. New analytical expressions for the shadow sizes of the RNdSD black holes have been derived. The expressions may be used to constrain parameters of these black holes with current and future interferometric observations, for instance with the Event Horizon Telescope in the case if magnetic or tidal charge is significant. The influence of a plasma on the gravitational lensing and Faraday rotation of the plane of polarization in case of highly nonuniform plasma surrounding compact object has been investigated.

Bibliography

[1] A. Tursunov and N. Dadhich, "Fifty years of energy extraction from rotating black hole: revisiting magnetic Penrose process," *Universe*, vol. 5, pp. 125–150, Apr. 2019.

[2] A. Tursunov, M. Kološ, Z. Stuchlík, and D. V. Gal'tsov, "Radiation Reaction of Charged Particles Orbiting a Magnetized Schwarzschild Black Hole," *ApJ*, vol. 861, p. 2, Jul. 2018.

[3] N. Dadhich, A. Tursunov, B. Ahmedov, and Z. Stuchlík, "The distinguishing signature of magnetic Penrose process," *MNRAS*, vol. 478, pp. L89–L94, Jul. 2018.

[4] M. Zajaček, A. Tursunov, A. Eckart, and S. Britzen, "On the charge of the Galactic centre black hole," *MNRAS*, vol. 480, pp. 4408–4423, Nov. 2018.

[5] A. A. Tursunov, M. KoloEг, and Z. StuchlГңk, "Orbital widening due to radiation reaction around a magnetized black hole," *Astronomische Nachrichten*, vol. 339, no. 5, pp. 341–346, 2018. [Online]. Available: https://onlinelibrary.wiley.com/doi/abs/10.1002/asna.201813502

[6] A. A. Tursunov and M. Kološ, "Constraints on Mass, Spin and Magnetic Field of Microquasar H 1743-322 from Observations of QPOs," *Physics of Atomic Nuclei*, vol. 81, pp. 279–282, Mar. 2018.

[7] M. Zajaček and A. A. Tursunov, "A stellar fly-by close to the Galactic center: Can we detect stars on highly relativistic orbits?" *Astronomische Nachrichten*, vol. 339, pp. 324–330, Jun. 2018.

[8] M. Kološ, A. Tursunov, and Z. Stuchlík, "Some astrophysical processes around magnetized black hole," *Contributions of the Astronomical Observatory Skalnate Pleso*, vol. 48, pp. 282–283, Jan. 2018.

[9] M. Zajaček and A. Tursunov, "Electric charge of black holes: Is it really always negligible?" *arXiv e-prints*, Apr. 2019.

[10] A. Eckart, A. Tursunov, M. Zajaček, M. Parsa, E. Hosseini, M. Subroweit, F. Peissker, C. Straubmeier, M. Horrobin, and V. Karas, "Mass, Distance, Spin, Charge, and Orientation of the super massive black hole SgrA," *Proceedings of Science*, Mar. 2019.

[11] M. Zajaček, A. Tursunov, A. Eckart, S. Britzen, E. Hackmann, V. Karas, Z. Stuchlík, B. Czerny, and J. A. Zensus, "Constraining the charge of the Galactic centre black hole," *arXiv e-prints*, Dec. 2018.

[12] B. Ahmedov, B. Turimov, Z. Stuchlík, and A. Tursunov, "Optical properties of magnetized black hole in plasma," *International Journal of Modern Physics: Conference Series*, vol. 49, Apr. 2019.

[13] A. Eckart, M. Zajaček, M. Valencia-S, M. Parsa, E. Hosseini, C. Straubmeier, M. Horrobin, M. Subroweit, and A. Tursunov, "Mass, Distance, Spin, Charge, and Orientation of the super massive black hole SgrA," *Proceedings of Science*, May 2019.

[14] R. A. Hulse, "The discovery of the binary pulsar," *Rev. Mod. Phys.*, vol. 66, pp. 699–710, Jul 1994. [Online]. Available: https://link.aps.org/doi/10.1103/RevModPhys.66.699

[15] Abbott, B. et. al, “Observation of gravitational waves from a binary black hole merger,” *Phys. Rev. Lett.*, vol. 116, p. 061102, Feb 2016. [Online]. Available: https://link.aps.org/doi/10.1103/PhysRevLett.116.061102

[16] A. Eckart, A. Hüttemann, C. Kiefer, S. Britzen, M. Zajaček, C. Lämmerzahl, M. Stöckler, M. Valencia-S, V. Karas, and M. García-Marín, “The Milky Way’s Supermassive Black Hole: How Good a Case Is It?” *Foundations of Physics*, vol. 47, pp. 553–624, May 2017.

[17] Gravity Collaboration, “Detection of the gravitational redshift in the orbit of the star S2 near the Galactic centre massive black hole,” *A&A*, vol. 615, p. L15, Jul. 2018.

[18] J. E. McClintock, R. Narayan, S. W. Davis, L. Gou, A. Kulkarni, J. A. Orosz, R. F. Penna, R. A. Remillard, and J. F. Steiner, “Measuring the spins of accreting black holes,” *Classical and Quantum Gravity*, vol. 28, p. 114009, Jun 2011.

[19] S. Babak, J. Gair, A. Sesana, E. Barausse, C. F. Sopuerta, C. P. L. Berry, E. Berti, P. Amaro-Seoane, A. Petiteau, and A. Klein, “Science with the space-based interferometer LISA. V. Extreme mass-ratio inspirals,” *Phys. Rev. D*, vol. 95, p. 103012, May 2017.

[20] R. M. Wald, “Black hole in a uniform magnetic field,” *Phys. Rev. D*, vol. 10, pp. 1680–1685, Sep. 1974.

[21] R. D. Blandford and R. L. Znajek, “Electromagnetic extraction of energy from Kerr black holes,” *MNRAS*, vol. 179, pp. 433–456, May 1977.

[22] E. R. Harrison, “Electrified black holes,” *Nature*, vol. 264, pp. 525–528, Dec. 1976.

[23] M. R. Morris, *Manifestations of the Galactic Center Magnetic Field*, 2015, p. 391.

[24] R. P. Eatough and et. al, "A strong magnetic field around the supermassive black hole at the centre of the Galaxy," *Nature*, vol. 501, pp. 391–394, Sep. 2013.

[25] Gravity Collaboration, "Detection of orbital motions near the last stable circular orbit of the massive black hole SgrA*," *A&A*, vol. 618, p. L10, Oct. 2018.

[26] D. V. Gal'Tsov and V. I. Petukhov, "Black hole in an external magnetic field," *Soviet Journal of Experimental and Theoretical Physics*, vol. 47, p. 419, Mar. 1978.

[27] M. Y. Piotrovich, Y. N. Gnedin, S. D. Buliga, T. M. Natsvlishvili, N. A. Silant'ev, and A. I. Nikitenko, "Magnetic Fields of Compact Objects in Close X-ray Binary Systems," in *Physics and Evolution of Magnetic and Related Stars*, ser. Astronomical Society of the Pacific Conference Series, Y. Y. Balega, I. I. Romanyuk, and D. O. Kudryavtsev, Eds., vol. 494, Apr. 2015, p. 114.

[28] R. M. Wald, *General relativity*, 1984.

[29] J. Bicak and V. Janis, "Magnetic fluxes across black holes," *MNRAS*, vol. 212, pp. 899–915, Feb. 1985.

[30] J. A. Petterson, "Magnetic field of a current loop around a Schwarzschild black hole," *Phys. Rev. D*, vol. 10, pp. 3166–3170, Nov. 1974.

[31] J. Levin, D. J. D'Orazio, and S. Garcia-Saenz, "Black hole pulsar," *Phys. Rev. D*, vol. 98, p. 123002, Dec. 2018.

[32] J. Bičák and T. Ledvinka, "Electromagnetic fields around black holes and Meissner effect," *Nuovo Cimento B Serie*, vol. 115, p. 739, Jul. 2000.

[33] K. S. Thorne, "Disk-Accretion onto a Black Hole. II. Evolution of the Hole," *ApJ*, vol. 191, pp. 507–520, Jul. 1974.

[34] R. Ruffini and J. R. Wilson, "Relativistic magnetohydrodynamical effects of plasma accreting into a black hole," *Phys. Rev. D*, vol. 12, pp. 2959–2962, Nov. 1975.

[35] S. S. Komissarov, "Blandford-Znajek Mechanism versus Penrose Process," *Journal of Korean Physical Society*, vol. 54, p. 2503, Jun. 2009.

[36] A. Tursunov, Z. Stuchlík, and M. Kološ, "Circular orbits and related quasi-harmonic oscillatory motion of charged particles around weakly magnetized rotating black holes," *Phys. Rev. D*, vol. 93, no. 8, p. 084012, Apr. 2016.

[37] B. Punsly, *Black hole gravitohydromagnetics*, 2001.

[38] V. S. Beskin, "REVIEWS OF TOPICAL PROBLEMS: Axisymmetric stationary flows in compact astrophysical objects," *Physics Uspekhi*, vol. 40, pp. 659–688, Jul. 1997.

[39] S. S. Komissarov, "Electrodynamics of black hole magnetospheres," *MNRAS*, vol. 350, pp. 427–448, May 2004.

[40] V. P. Frolov and A. A. Shoom, "Motion of charged particles near a weakly magnetized Schwarzschild black hole," *Phys. Rev. D*, vol. 82, no. 8, p. 084034, Oct. 2010.

[41] M. Kološ, Z. Stuchlík, and A. Tursunov, "Quasi-harmonic oscillatory motion of charged particles around a Schwarzschild black hole immersed in a uniform magnetic field," *Classical and Quantum Gravity*, vol. 32, no. 16, p. 165009, Aug. 2015.

[42] A. A. Sokolov, I. M. Ternov, A. N. Aliev, and D. V. Gal'tsov, "Synchrotron radiation in curved space-time," *Soviet Physics Journal*, vol. 26, pp. 36–40, Jan. 1983.

[43] A. A. Sokolov, D. V. Gal'tsov, and V. I. Petukhov, "Radiation emitted by relativistic particles moving in the vicinity of the Schwarzschild black hole, immersed in an external magnetic field," *Physics Letters A*, vol. 68, pp. 1–2, Sep. 1978.

[44] A. A. Shoom, "Synchrotron radiation from a weakly magnetized Schwarzschild black hole," *Phys. Rev. D*, vol. 92, no. 12, p. 124066, Dec. 2015.

[45] B. S. DeWitt and R. W. Brehme, "Radiation damping in a gravitational field," *Annals of Physics*, vol. 9, no. 2, pp. 220 – 259, 1960. [Online]. Available: http://www.sciencedirect.com/science/article/pii/0003491660900300

[46] J. Hobbs, "A vierbein formalism of radiation damping," *Annals of Physics*, vol. 47, no. 1, pp. 141 – 165, 1968. [Online]. Available: http://www.sciencedirect.com/science/article/pii/0003491668902315

[47] E. Poisson, "The Motion of Point Particles in Curved Spacetime," *Living Reviews in Relativity*, vol. 7, p. 6, May 2004.

[48] H. Spohn, "The critical manifold of the Lorentz-Dirac equation," *EPL (Europhysics Letters)*, vol. 50, pp. 287–292, 2000.

[49] L. D. Landau and E. M. Lifshitz, *The classical theory of fields*, 1975.

[50] A. G. Smith and C. M. Will, "Force on a static charge outside a Schwarzschild black hole," *Phys. Rev. D*, vol. 22, pp. 1276–1284, Sep. 1980.

[51] F. J. Zerilli, "Gravitational and electromagnetic radiation around black holes," *Nuovo Cimento B Serie*, vol. 115, p. 687, Jul. 2000.

[52] D. V. Gal'tsov, "Radiation reaction in various dimensions," *Phys. Rev. D*, vol. 66, no. 2, p. 025016, Jul. 2002.

[53] D. V. Gal'tsov and P. A. Spirin, "Radiation reaction reexamined: bound momentum and the Schott term," *Gravitation and Cosmology*, vol. 12, pp. 1–10, Mar. 2006.

[54] R. H. Price, J. W. Belcher, and D. A. Nichols, "Comparison of electromagnetic and gravitational radiation: What we can learn about each from the other," *American Journal of Physics*, vol. 81, pp. 575–584, Aug. 2013.

[55] L. Barack, *Gravitational Self-Force: Orbital Mechanics Beyond Geodesic Motion*, 2014, p. 147.

[56] S. V. Dhurandhar and N. Dadhich, "Energy-extraction processes from a Kerr black hole immersed in a magnetic field. I. Negative-energy states," *Phys. Rev. D*, vol. 29, pp. 2712–2720, Jun. 1984.

[57] ——, "Energy-extraction processes from a Kerr black hole immersed in a magnetic field. II. The formalism," *Phys. Rev. D*, vol. 30, pp. 1625–1631, Oct. 1984.

[58] S. Parthasarathy, S. M. Wagh, S. V. Dhurandhar, and N. Dadhich, "High efficiency of the Penrose process of energy extraction from rotating black holes immersed in electromagnetic fields," *ApJ*, vol. 307, pp. 38–46, Aug. 1986.

[59] R. Shiose, M. Kimura, and T. Chiba, "Motion of charged particles around a weakly magnetized rotating black hole," *Phys. Rev. D*, vol. 90, no. 12, p. 124016, 2014.

[60] M. Kološ, A. Tursunov, and Z. Stuchlík, "Possible signature of the magnetic fields related to quasi-periodic oscillations observed in microquasars," *EPJC*, vol. 77, p. 860, 2017.

[61] Y.-K. Lim, "Motion of charged particles around a magnetized/electrified black hole," *Phys. Rev. D*, vol. 91, no. 2, p. 024048, 2015.

[62] D. V. Gal'tsov and V. I. Petukhov, "Black hole in an external magnetic field," *Soviet Journal of Experimental and Theoretical Physics*, vol. 47, p. 419, Mar. 1978.

[63] A. N. Aliev and D. V. Gal'tsov, "REVIEWS OF TOPICAL PROBLEMS: "Magnetized" black holes," *Soviet Physics Uspekhi*, vol. 32, pp. 75–92, Jan. 1989.

[64] A. A. Abdujabbarov, B. J. Ahmedov, and V. G. Kagramanova, "Particle motion and electromagnetic fields of rotating compact gravitating objects with gravitomagnetic charge," *General Relativity and Gravitation*, vol. 40, pp. 2515–2532, Dec. 2008.

[65] A. Tursunov, M. Kološ, A. Abdujabbarov, B. Ahmedov, and Z. Stuchlík, "Acceleration of particles in spacetimes of black string," *Phys. Rev. D*, vol. 88, no. 12, p. 124001, 2013.

[66] A. M. Al Zahrani, V. P. Frolov, and A. A. Shoom, "Critical escape velocity for a charged particle moving around a weakly magnetized Schwarzschild black hole," *Phys. Rev. D*, vol. 87, no. 8, p. 084043, Apr. 2013.

[67] Z. Stuchlík, A. Kotrlová, and G. Török, "Multi-resonance orbital model of high-frequency quasi-periodic oscillations: possible high-precision determination of black hole and neutron star spin," *A&A*, vol. 552, p. A10, 2013.

[68] Z. Stuchlík and M. Kološ, "Acceleration of the charged particles due to chaotic scattering in the combined black hole gravitational field and asymptotically uniform magnetic field," *EPJC*, vol. 76, p. 32, Jan. 2016.

[69] A. Eckart, R. Schödel, and C. Straubmeier, *The black hole at the center of the Milky Way*, 2005.

[70] A. Eckart, A. Hüttemann, C. Kiefer, S. Britzen, M. Zajaček, C. Lämmerzahl, M. Stöckler, M. Valencia-S, V. Karas, and M. García-Marín, "The Milky Way's Supermassive Black Hole: How Good a Case Is It?" *Foundations of Physics*, vol. 47, pp. 553–624, May 2017.

[71] A. Eckart and R. Genzel, "Observations of stellar proper motions near the Galactic Centre," *Nature*, vol. 383, pp. 415–417, Oct. 1996.

[72] M. Zajaček and A. Tursunov, "A stellar fly-by close to the Galactic centre: Can we detect stars on highly-relativistic orbits?" *ArXiv e-prints*, Apr. 2018.

[73] A. Boehle, A. M. Ghez, R. Schödel, L. Meyer, S. Yelda, S. Albers, G. D. Martinez, E. E. Becklin, T. Do, J. R. Lu, K. Matthews, M. R. Morris, B. Sitarski, and G. Witzel, "An Improved Distance and Mass Estimate for Sgr A* from a Multistar Orbit Analysis," *ApJ*, vol. 830, p. 17, Oct. 2016.

[74] M. Parsa, A. Eckart, B. Shahzamanian, V. Karas, M. Zajaček, J. A. Zensus, and C. Straubmeier, "Investigating the Relativistic Motion of the Stars Near the Supermassive Black Hole in the Galactic Center," *ApJ*, vol. 845, p. 22, Aug. 2017.

[75] S. Gillessen, P. M. Plewa, F. Eisenhauer, R. Sari, I. Waisberg, M. Habibi, O. Pfuhl, E. George, J. Dexter, S. von Fellenberg, T. Ott, and R. Genzel,

"An Update on Monitoring Stellar Orbits in the Galactic Center," *ApJ*, vol. 837, p. 30, Mar. 2017.

[76] S. S. Doeleman and et al., "Event-horizon-scale structure in the supermassive black hole candidate at the Galactic Centre," *Nature*, vol. 455, pp. 78–80, Sep. 2008.

[77] M. J. Reid and A. Brunthaler, "The Proper Motion of Sagittarius A*. II. The Mass of Sagittarius A*," *ApJ*, vol. 616, pp. 872–884, Dec. 2004.

[78] T. Do, G. D. Martinez, S. Yelda, A. Ghez, J. Bullock, M. Kaplinghat, J. R. Lu, A. H. G. Peter, and K. Phifer, "Three-dimensional Stellar Kinematics at the Galactic Center: Measuring the Nuclear Star Cluster Spatial Density Profile, Black Hole Mass, and Distance," *ApJL*, vol. 779, p. L6, Dec. 2013.

[79] G. D. Karssen, M. Bursa, A. Eckart, M. Valencia-S, M. Dovčiak, V. Karas, and J. Horák, "Bright X-ray flares from Sgr A*," *MNRAS*, vol. 472, pp. 4422–4433, Dec. 2017.

[80] A. Eckart, R. Schödel, L. Meyer, S. Trippe, T. Ott, and R. Genzel, "Polarimetry of near-infrared flares from Sagittarius A*," *A&A*, vol. 455, pp. 1–10, Aug. 2006.

[81] L. Meyer, A. Eckart, R. Schödel, W. J. Duschl, K. Mužić, M. Dovčiak, and V. Karas, "Near-infrared polarimetry setting constraints on the orbiting spot model for Sgr A* flares," *A&A*, vol. 460, pp. 15–21, Dec. 2006.

[82] Y. Kato, M. Miyoshi, R. Takahashi, H. Negoro, and R. Matsumoto, "Measuring spin of a supermassive black hole at the Galactic centre - implications for a unique spin," *MNRAS*, vol. 403, pp. L74–L78, Mar. 2010.

[83] S. Ray, A. L. Espíndola, M. Malheiro, J. P. Lemos, and V. T. Zanchin, "Electrically charged compact stars and formation of charged black holes," *Phys. Rev. D*, vol. 68, no. 8, p. 084004, Oct. 2003.

[84] A. Eckart and et al., "Millimeter to X-ray flares from Sagittarius A*," *A&A*, vol. 537, p. A52, Jan. 2012.

[85] R. P. Eatough and et al., "A strong magnetic field around the supermassive black hole at the centre of the Galaxy," *Nature*, vol. 501, pp. 391–394, Sep. 2013.

[86] R. D. Blandford and R. L. Znajek, "Electromagnetic extraction of energy from Kerr black holes," *MNRAS*, vol. 179, pp. 433–456, May 1977.

[87] S. M. Wagh, S. V. Dhurandhar, and N. Dadhich, "Revival of the Penrose process for astrophysical applications," *ApJ*, vol. 290, pp. 12–14, Mar. 1985.

[88] G. W. Gibbons, "Vacuum polarization and the spontaneous loss of charge by black holes," *Communications in Mathematical Physics*, vol. 44, pp. 245–264, Oct. 1975.

[89] D. Pugliese, H. Quevedo, and R. Ruffini, "Motion of charged test particles in Reissner-Nordström spacetime," *Phys. Rev. D*, vol. 83, no. 10, p. 104052, May 2011.

[90] J. Kovář, P. Slaný, Z. Stuchlík, V. Karas, C. Cremaschini, and J. C. Miller, "Role of electric charge in shaping equilibrium configurations of fluid tori encircling black holes," *Phys. Rev. D*, vol. 84, no. 8, p. 084002, Oct. 2011.

[91] R. V. Shcherbakov and F. K. Baganoff, "Inflow-Outflow Model with Conduction and Self-consistent Feeding for Sgr A*," *ApJ*, vol. 716, pp. 504–509, Jun. 2010.

[92] Q. D. Wang and et al., "Dissecting X-ray-Emitting Gas Around the Center of Our Galaxy," *Science*, vol. 341, pp. 981–983, Aug. 2013.

[93] A. Różańska, P. Mróz, M. Mościbrodzka, M. Sobolewska, and T. P. Adhikari, "X-ray observations of the hot phase in Sagittarius A*," *A&A*, vol. 581, p. A64, Sep. 2015.

[94] A. Yalinewich, R. Sari, A. Generozov, N. C. Stone, and B. D. Metzger, "A generalized Bondi accretion model for the galactic centre," *MNRAS*, vol. 479, pp. 4778–4785, Oct. 2018.

[95] K. Ferrière, "Interstellar magnetic fields in the Galactic center region," *A&A*, vol. 505, pp. 1183–1198, Oct. 2009.

[96] H. Falcke and S. Markoff, "The jet model for Sgr A*: Radio and X-ray spectrum," *A&A*, vol. 362, pp. 113–118, Oct. 2000.

[97] M. Mościbrodzka, C. F. Gammie, J. C. Dolence, H. Shiokawa, and P. K. Leung, "Radiative Models of SGR A* from GRMHD Simulations," *ApJ*, vol. 706, pp. 497–507, Nov. 2009.

[98] J. Dexter, E. Agol, P. C. Fragile, and J. C. McKinney, "The Submillimeter Bump in Sgr A* from Relativistic MHD Simulations," *ApJ*, vol. 717, pp. 1092–1104, Jul. 2010.

[99] K. R. Lang, *Astrophysical formulae. A compendium for the physicist and astrophysicist (Berlin: Springer)*, 1978.

[100] F. K. Baganoff, Y. Maeda, M. Morris, M. W. Bautz, W. N. Brandt, W. Cui, J. P. Doty, E. D. Feigelson, G. P. Garmire, S. H. Pravdo, G. R. Ricker, and L. K. Townsley, "Chandra X-Ray Spectroscopic Imaging of Sagittarius A* and the Central Parsec of the Galaxy," *ApJ*, vol. 591, pp. 891–915, Jul. 2003.

[101] A. Różańska, B. Czerny, D. Kunneriath, T. P. Adhikari, V. Karas, and M. Mościbrodzka, "Conditions for thermal instability in the Galactic Centre mini-spiral region," *MNRAS*, vol. 445, pp. 4385–4394, Dec. 2014.

[102] L. Moser, Á. Sánchez-Monge, A. Eckart, M. A. Requena-Torres, M. García-Marin, D. Kunneriath, A. Zensus, S. Britzen, N. Sabha, B. Shahzamanian, A. Borkar, and S. Fischer, "Approaching hell's kitchen: Molecular daredevil clouds in the vicinity of Sagittarius A*," *A&A*, vol. 603, p. A68, Jul. 2017.

[103] A. Generozov, N. C. Stone, and B. D. Metzger, "Circumnuclear media of quiescent supermassive black holes," *MNRAS*, vol. 453, pp. 775–796, Oct. 2015.

[104] J.-P. Lasota, "Black Hole Accretion Discs," in *Astrophysics of Black Holes: From Fundamental Aspects to Latest Developments*, ser. Astrophysics and Space Science Library, C. Bambi, Ed., vol. 440, 2016, p. 1.

[105] F. Yuan and R. Narayan, "Hot Accretion Flows Around Black Holes," *ARA&A*, vol. 52, pp. 529–588, Aug. 2014.

[106] A. R. King, J. E. Pringle, and M. Livio, "Accretion disc viscosity: how big is alpha?" *MNRAS*, vol. 376, pp. 1740–1746, Apr. 2007.

[107] E. Mossoux and A. Eckart, "The X-ray footprint of the circumnuclear disc," *MNRAS*, vol. 474, pp. 3787–3807, Mar. 2018.

[108] D. Haggard, "Advances from Recent Multi-wavelength Campaigns on Sgr A*," in *The Multi-Messenger Astrophysics of the Galactic Centre*, ser. IAU Symposium, R. M. Crocker, S. N. Longmore, and G. V. Bicknell, Eds., vol. 322, Jan. 2017, pp. 1–10.

[109] L. Neslušan, "On the global electrostatic charge of stars," *A&A*, vol. 372, pp. 913–915, Jun. 2001.

[110] J. Bally and E. R. Harrison, "The electrically polarized universe," *ApJ*, vol. 220, p. 743, Mar. 1978.

[111] E. T. Newman, E. Couch, K. Chinnapared, A. Exton, A. Prakash, and R. Torrence, "Metric of a Rotating, Charged Mass," *Journal of Mathematical Physics*, vol. 6, pp. 918–919, Jun. 1965.

[112] C. W. Misner, K. S. Thorne, and J. A. Wheeler, *Gravitation (San Francisco: W.H. Freeman and Co., 1973)*, 1973.

[113] B. Wang, R.-K. Su, P. K. N. Yu, and E. C. M. Young, "Can a nonextremal Reissner-Nordström black hole become extremal by assimilating an infalling charged particle and shell?" *Phys. Rev. D*, vol. 57, pp. 5284–5286, Apr. 1998.

[114] R. Penrose, "Gravitational Collapse: the Role of General Relativity," *Nuovo Cimento Rivista Serie*, vol. 1, 1969.

[115] H. Kim, C. H. Lee, and H. K. Lee, "Nonvanishing magnetic flux through the slightly charged Kerr black hole," *Phys. Rev. D*, vol. 63, no. 6, p. 064037, Mar. 2001.

[116] D. P. Marrone, J. M. Moran, J.-H. Zhao, and R. Rao, "An Unambiguous Detection of Faraday Rotation in Sagittarius A*," *ApJL*, vol. 654, pp. L57–L60, Jan. 2007.

[117] K. Y. Lo, Z.-Q. Shen, J.-H. Zhao, and P. T. P. Ho, "Intrinsic Size of Sagittarius A*: 72 Schwarzschild Radii," *ApJL*, vol. 508, pp. L61–L64, Nov. 1998.

[118] T. P. Krichbaum, D. A. Graham, A. Witzel, A. Greve, J. E. Wink, M. Grewing, F. Colomer, P. de Vicente, J. Gomez-Gonzalez, A. Baudry, and J. A. Zensus, "VLBI observations of the galactic center source SGR A* at 86 GHz and 215 GHz," *A&A*, vol. 335, pp. L106–L110, Jul. 1998.

[119] H. Falcke, F. Melia, and E. Agol, "Viewing the Shadow of the Black Hole at the Galactic Center," *ApJL*, vol. 528, pp. L13–L16, Jan. 2000.

[120] A. F. Zakharov, "Constraints on a charge in the Reissner-Nordström metric for the black hole at the Galactic Center," *Phys. Rev. D*, vol. 90, no. 6, p. 062007, Sep. 2014.

[121] J. Dexter, J. C. McKinney, and E. Agol, "The size of the jet launching region in M87," *MNRAS*, vol. 421, pp. 1517–1528, Apr. 2012.

[122] M. Zamaninasab and et al., "Near infrared flares of Sagittarius A*. Importance of near infrared polarimetry," *A&A*, vol. 510, p. A3, Jan. 2010.

[123] L. Meyer, A. Eckart, R. Schödel, W. J. Duschl, K. Mužić, M. Dovčiak, and V. Karas, "Near-infrared polarimetry setting constraints on the orbiting spot model for Sgr A* flares," *A&A*, vol. 460, pp. 15–21, Dec. 2006.

[124] K. S. Thorne, "Disk-Accretion onto a Black Hole. II. Evolution of the Hole," *ApJ*, vol. 191, pp. 507–520, Jul. 1974.

[125] L. Randall and R. Sundrum, "Large Mass Hierarchy from a Small Extra Dimension," *Physical Review Letters*, vol. 83, pp. 3370–3373, Oct. 1999.

[126] A. Y. Bin-Nun, "Relativistic images in Randall-Sundrum II braneworld lensing," *Phys. Rev. D*, vol. 81, no. 12, p. 123011, Jun. 2010.

[127] ——, "Strong gravitational lensing by Sgr A*," *Classical and Quantum Gravity*, vol. 28, no. 11, p. 114003, Jun. 2011.

[128] Z. Stuchlík and A. Kotrlová, "Orbital resonances in discs around braneworld Kerr black holes," *General Relativity and Gravitation*, vol. 41, pp. 1305–1343, Jun. 2009.

[129] A. Kotrlová, Z. Stuchlík, and G. Török, "Quasiperiodic oscillations in a strong gravitational field around neutron stars testing braneworld models," *Classical and Quantum Gravity*, vol. 25, no. 22, p. 225016, Nov. 2008.

[130] R. Maartens, "Brane-World Gravity," *Living Reviews in Relativity*, vol. 7, p. 7, Jun. 2004.

[131] J. Schee and Z. Stuchlík, "Optical Phenomena in the Field of Braneworld Kerr Black Holes," *International Journal of Modern Physics D*, vol. 18, pp. 983–1024, 2009.

[132] V. L. Fish and et al., "1.3 mm Wavelength VLBI of Sagittarius A*: Detection of Time-variable Emission on Event Horizon Scales," *ApJL*, vol. 727, p. L36, Feb. 2011.

[133] L. Iorio, "Constraining the electric charges of some astronomical bodies in Reissner-Nordström spacetimes and generic r $^{-2}$-type power-law potentials from orbital motions," *General Relativity and Gravitation*, vol. 44, pp. 1753–1767, Jul. 2012.

[134] E. Chaliasos, "Perihelion Shift in the Reissner-Nordstroem Field," *Celestial Mechanics and Dynamical Astronomy*, vol. 79, pp. 135–144, Feb. 2001.

[135] R. Genzel, F. Eisenhauer, and S. Gillessen, "The Galactic Center massive black hole and nuclear star cluster," *Reviews of Modern Physics*, vol. 82, pp. 3121–3195, Oct. 2010.

[136] M. D. Johnson and et al., "Resolved magnetic-field structure and variability near the event horizon of Sagittarius A*," *Science*, vol. 350, pp. 1242–1245, Dec. 2015.

[137] B. C. Bromley, F. Melia, and S. Liu, "Polarimetric Imaging of the Massive Black Hole at the Galactic Center," *ApJL*, vol. 555, pp. L83–L86, Jul. 2001.

[138] J. Dexter, "A public code for general relativistic, polarised radiative transfer around spinning black holes," *MNRAS*, vol. 462, pp. 115–136, Oct 2016.

[139] R. Narayan, R. Mahadevan, J. E. Grindlay, R. G. Popham, and C. Gammie, "Advection-dominated accretion model of Sagittarius A*: evidence for a black hole at the Galactic center." *ApJ*, vol. 492, pp. 554–568, Jan. 1998.

[140] R. D. Blandford and M. C. Begelman, "On the fate of gas accreting at a low rate on to a black hole," *MNRAS*, vol. 303, pp. L1–L5, Feb 1999.

[141] S. M. Ressler, E. Quataert, and J. M. Stone, "Accretion of magnetized stellar winds in the Galactic centre: implications for Sgr A* and PSR J1745-2900," *MNRAS*, vol. 482, pp. L123–L128, Jan. 2019.

[142] F. Yuan, S. Markoff, and H. Falcke, "A Jet-ADAF model for Sgr A*," *A&A*, vol. 383, pp. 854–863, Mar. 2002.

[143] M. Mościbrodzka, H. Falcke, H. Shiokawa, and C. F. Gammie, "Observational appearance of inefficient accretion flows and jets in 3D GRMHD simulations: Application to Sagittarius A*," *A&A*, vol. 570, p. A7, Oct. 2014.

[144] C.-K. Chan, D. Psaltis, F. Özel, R. Narayan, and A. Saḑowski, "The Power of Imaging: Constraining the Plasma Properties of GRMHD Simulations using EHT Observations of Sgr A*," *ApJ*, vol. 799, p. 1, Jan. 2015.

[145] S. M. Ressler, A. Tchekhovskoy, E. Quataert, and C. F. Gammie, "The disc-jet symbiosis emerges: modelling the emission of Sagittarius A* with electron thermodynamics," *MNRAS*, vol. 467, pp. 3604–3619, May 2017.

[146] F. Yuan and R. Narayan, "Hot Accretion Flows Around Black Holes," *ARA&A*, vol. 52, pp. 529–588, Aug. 2014.

[147] H. Falcke, W. M. Goss, H. Matsuo, P. Teuben, J.-H. Zhao, and R. Zylka, "The Simultaneous Spectrum of Sagittarius A* from 20 Centimeters to 1

Millimeter and the Nature of the Millimeter Excess," *ApJ*, vol. 499, pp. 731–734, May 1998.

[148] G. C. Bower, S. Markoff, J. Dexter, M. A. Gurwell, J. M. Moran, A. Brunthaler, H. Falcke, P. C. Fragile, D. Maitra, D. Marrone, A. Peck, A. Rushton, and M. C. H. Wright, "Radio and Millimeter Monitoring of Sgr A*: Spectrum, Variability, and Constraints on the G2 Encounter," *ApJ*, vol. 802, p. 69, Mar. 2015.

[149] S. D. von Fellenberg, S. Gillessen, J. Graciá-Carpio, T. K. Fritz, J. Dexter, M. Bauböck, G. Ponti, F. Gao, M. Habibi, P. M. Plewa, O. Pfuhl, A. Jimenez-Rosales, I. Waisberg, F. Widmann, T. Ott, F. Eisenhauer, and R. Genzel, "A Detection of Sgr A* in the Far Infrared," *ApJ*, vol. 862, p. 129, Aug. 2018.

[150] F. K. Baganoff, M. W. Bautz, W. N. Brandt, G. Chartas, E. D. Feigelson, G. P. Garmire, Y. Maeda, M. Morris, G. R. Ricker, L. K. Townsley, and F. Walter, "Rapid X-ray flaring from the direction of the supermassive black hole at the Galactic Centre," *Nature*, vol. 413, pp. 45–48, Sep. 2001.

[151] R. Genzel, R. Schödel, T. Ott, A. Eckart, T. Alexander, F. Lacombe, D. Rouan, and B. Aschenbach, "Near-infrared flares from accreting gas around the supermassive black hole at the Galactic Centre," *Nature*, vol. 425, pp. 934–937, Oct 2003.

[152] A. M. Ghez, S. A. Wright, K. Matthews, D. Thompson, D. Le Mignant, A. Tanner, S. D. Hornstein, M. Morris, E. E. Becklin, and B. T. Soifer, "Variable Infrared Emission from the Supermassive Black Hole at the Center of the Milky Way," *ApJL*, vol. 601, pp. L159–L162, Feb. 2004.

[153] G. Witzel and et al., "Variability Timescale and Spectral Index of Sgr A* in the Near Infrared: Approximate Bayesian Computation Analysis of the Variability of the Closest Supermassive Black Hole," *ApJ*, vol. 863, p. 15, Aug. 2018.

[154] B. Shahzamanian and et al., "Polarized light from Sagittarius A* in the near-infrared K_s-band," *A&A*, vol. 576, p. A20, Apr. 2015.

[155] K. Zubovas, S. Nayakshin, and S. Markoff, "Sgr A* flares: tidal disruption of asteroids and planets?" *MNRAS*, vol. 421, pp. 1315–1324, Apr. 2012.

[156] F. Yuan, J. Lin, K. Wu, and L. C. Ho, "A magnetohydrodynamical model for the formation of episodic jets," *MNRAS*, vol. 395, pp. 2183–2188, Jun 2009.

[157] G. Witzel, A. Eckart, M. Bremer, M. Zamaninasab, B. Shahzamanian, M. Valencia-S., R. Schödel, V. Karas, R. Lenzen, N. Marchili, N. Sabha, M. Garcia-Marin, R. M. Buchholz, D. Kunneriath, and C. Straubmeier, "Source-intrinsic Near-infrared Properties of Sgr A*: Total Intensity Measurements," *ApJS*, vol. 203, p. 18, Dec. 2012.

[158] Y.-P. Li, F. Yuan, Q. Yuan, Q. D. Wang, P. F. Chen, J. Neilsen, T. Fang, S. Zhang, and J. Dexter, "Statistics of X-Ray Flares of Sagittarius A*: Evidence for Solar-like Self-organized Criticality Phenomena," *ApJ*, vol. 810, p. 19, Sep 2015.

[159] M. Subroweit, M. García-Marín, A. Eckart, A. Borkar, M. Valencia-S., G. Witzel, B. Shahzamanian, and C. Straubmeier, "Submillimeter and radio variability of Sagittarius A*. A statistical analysis," *A&A*, vol. 601, p. A80, May 2017.

[160] P. Goldreich and W. H. Julian, “Pulsar Electrodynamics,” *ApJ*, vol. 157, p. 869, Aug. 1969.

[161] T. W. Jones, S. L. O’dell, and W. A. Stein, “Physics of Compact Nonthermal Sources. II. Determination of Physical Parameters,” *ApJ*, vol. 192, pp. 261–278, Sep. 1974.

[162] F. Yuan, E. Quataert, and R. Narayan, “Nonthermal Electrons in Radiatively Inefficient Accretion Flow Models of Sagittarius A*,” *ApJ*, vol. 598, pp. 301–312, Nov 2003.

[163] R. Schödel, D. Merritt, and A. Eckart, “The nuclear star cluster of the Milky Way: proper motions and mass,” *A&A*, vol. 502, pp. 91–111, Jul. 2009.

[164] F. Eisenhauer and et al., “GRAVITY: Observing the Universe in Motion,” *The Messenger*, vol. 143, pp. 16–24, Mar. 2011.

[165] R. M. Buchholz, R. Schödel, and A. Eckart, “Composition of the galactic center star cluster. Population analysis from adaptive optics narrow band spectral energy distributions,” *A&A*, vol. 499, pp. 483–501, May 2009.

[166] W. J. Duschl, “On the inner edge of the circumnuclear disc in the Galaxy,” *MNRAS*, vol. 240, pp. 219–223, Sep. 1989.

[167] B. Vollmer and W. J. Duschl, “The Minispiral in the Galactic Center revisited,” *NewA*, vol. 4, pp. 581–590, Jan. 2000.

[168] L. Moser, Á. Sánchez-Monge, A. Eckart, M. A. Requena-Torres, M. García-Marin, D. Kunneriath, A. Zensus, S. Britzen, N. Sabha, B. Shahzamanian, A. Borkar, and S. Fischer, “Approaching hell’s kitchen: Molecular daredevil clouds in the vicinity of Sagittarius A*,” *A&A*, vol. 603, p. A68, Jul. 2017.

[169] M. Habibi and et al., "Twelve Years of Spectroscopic Monitoring in the Galactic Center: The Closest Look at S-stars near the Black Hole," *ApJ*, vol. 847, p. 120, Oct. 2017.

[170] L. Iorio, "Post-Keplerian effects on radial velocity in binary systems and the possibility of measuring General Relativity with the star S2 in 2018," *MNRAS*, vol. 472, pp. 2249–2262, Dec. 2017.

[171] C. Hopman and T. Alexander, "Resonant Relaxation near a Massive Black Hole: The Stellar Distribution and Gravitational Wave Sources," *ApJ*, vol. 645, pp. 1152–1163, Jul. 2006.

[172] P. Kroupa, "On the variation of the initial mass function," *MNRAS*, vol. 322, pp. 231–246, Apr. 2001.

[173] R. Schödel, R. Genzel, T. Ott, and A. Eckart, "The Galactic Center stellar cluster: The central arcsecond," *Astronomische Nachrichten Supplement*, vol. 324, pp. 535–541, Sep. 2003.

[174] T. Alexander, "Stellar processes near the massive black hole in the Galactic center [review article]," *Physics Reports* , vol. 419, pp. 65–142, Nov. 2005.

[175] N. Sabha and et al., "The S-star cluster at the center of the Milky Way. On the nature of diffuse NIR emission in the inner tenth of a parsec," *A&A*, vol. 545, p. A70, Sep. 2012.

[176] Pierre Auger Collaboration, "An Indication of Anisotropy in Arrival Directions of Ultra-high-energy Cosmic Rays through Comparison to the Flux Pattern of Extragalactic Gamma-Ray Sources," *ApJL*, vol. 853, p. L29, Feb. 2018.

[177] IceCube Collaboration, "Multimessenger observations of a flaring blazar coincident with high-energy neutrino IceCube-170922A," *Science*, vol. 361, p. eaat1378, Jul. 2018.

[178] ——, "Neutrino emission from the direction of the blazar TXS 0506+056 prior to the IceCube-170922A alert," *Science*, vol. 361, pp. 147–151, Jul. 2018.

[179] Pierre Auger Collaboration, "Observation of a large-scale anisotropy in the arrival directions of cosmic rays above 8×10^{18} eV," *Science*, vol. 357, pp. 1266–1270, Sep. 2017.

[180] K. Greisen, "End to the Cosmic-Ray Spectrum?" *Physical Review Letters*, vol. 16, pp. 748–750, Apr. 1966.

[181] G. T. Zatsepin and V. A. Kuz'min, "Upper Limit of the Spectrum of Cosmic Rays," *JETP Lett.*, vol. 4, p. 78, Aug. 1966.

[182] J. M. Bardeen, B. Carter, and S. W. Hawking, "The four laws of black hole mechanics," *Communications in Mathematical Physics*, vol. 31, pp. 161–170, Jun. 1973.

[183] T. Jacobson, "Thermodynamics of Spacetime: The Einstein Equation of State," *Physical Review Letters*, vol. 75, pp. 1260–1263, Aug. 1995.

[184] T. Padmanabhan, "Thermodynamical aspects of gravity: new insights," *Reports on Progress in Physics*, vol. 73, no. 4, p. 046901, Apr. 2010.

[185] D. Christodoulou and R. Ruffini, "Reversible Transformations of a Charged Black Hole," *Phys. Rev. D*, vol. 4, pp. 3552–3555, Dec. 1971.

[186] J. D. Bekenstein, "Extraction of Energy and Charge from a Black Hole," *Phys. Rev. D*, vol. 7, pp. 949–953, Feb. 1973.

[187] R. Penrose, "Gravitational Collapse: the Role of General Relativity," *Nuovo Cimento Rivista Serie*, vol. 1, 1969.

[188] J. M. Bardeen, W. H. Press, and S. A. Teukolsky, "Rotating Black Holes: Locally Nonrotating Frames, Energy Extraction, and Scalar Synchrotron Radiation," *ApJ*, vol. 178, pp. 347–370, Dec. 1972.

[189] R. M. Wald, "Energy Limits on the Penrose Process," *ApJ*, vol. 191, pp. 231–234, Jul. 1974.

[190] S. M. Wagh, S. V. Dhurandhar, and N. Dadhich, "Revival of the Penrose process for astrophysical applications," *ApJ*, vol. 290, pp. 12–14, Mar. 1985.

[191] M. Bhat, S. Dhurandhar, and N. Dadhich, "Energetics of the Kerr-Newman black hole by the Penrose process," *Journal of Astrophysics and Astronomy*, vol. 6, pp. 85–100, Jun. 1985.

[192] S. M. Wagh and N. Dadhich, "The energetics of black holes in electromagnetic fields by the penrose process," *Physics Reports* , vol. 183, pp. 137–192, Nov. 1989.

[193] R. Narayan, J. E. McClintock, and A. Tchekhovskoy, *Energy Extraction from Spinning Black Holes Via Relativistic Jets*, 2014, p. 523.

[194] A. Tchekhovskoy, R. Narayan, and J. C. McKinney, "Efficient generation of jets from magnetically arrested accretion on a rapidly spinning black hole," *MNRAS*, vol. 418, pp. L79–L83, Nov. 2011.

[195] R. K. Williams, "Collimated Escaping Vortical Polar e^-e^+ Jets Intrinsically Produced by Rotating Black Holes and Penrose Processes," *ApJ*, vol. 611, pp. 952–963, Aug. 2004.

[196] T. Piran, J. Shaham, and J. Katz, "High Efficiency of the Penrose Mechanism for Particle Collisions," *ApJL*, vol. 196, p. L107, Mar. 1975.

[197] T. Piran and J. Shaham, "Production of gamma-ray bursts near rapidly rotating accreting black holes," *ApJ*, vol. 214, pp. 268–299, May 1977.

[198] O. B. Zaslavskii, "Maximum efficiency of the collisional Penrose process," *Phys. Rev. D*, vol. 94, no. 6, p. 064048, Sep. 2016.

[199] E. Berti, R. Brito, and V. Cardoso, "Ultrahigh-Energy Debris from the Collisional Penrose Process," *Physical Review Letters*, vol. 114, no. 25, p. 251103, Jun. 2015.

[200] J. D. Schnittman, "The collisional penrose process," *General Relativity and Gravitation*, vol. 50, no. 6, p. 77, Jun 2018. [Online]. Available: https://doi.org/10.1007/s10714-018-2373-5

[201] E. Leiderschneider and T. Piran, "Maximal efficiency of the collisional Penrose process," *Phys. Rev. D*, vol. 93, p. 043015, Feb 2016.

[202] R. F. Penna, "Energy extraction from boosted black holes: Penrose process, jets, and the membrane at infinity," *Phys. Rev. D*, vol. 91, p. 084044, Apr 2015.

[203] M. Bañados, J. Silk, and S. M. West, "Kerr Black Holes as Particle Accelerators to Arbitrarily High Energy," *Physical Review Letters*, vol. 103, no. 11, p. 111102, Sep. 2009.

[204] V. P. Frolov, "Weakly magnetized black holes as particle accelerators," *Phys. Rev. D*, vol. 85, no. 2, p. 024020, Jan. 2012.

[205] A. Abdujabbarov, F. Atamurotov, N. Dadhich, B. Ahmedov, and Z. Stuchlík, "Energetics and optical properties of 6-dimensional rotating black hole in pure Gauss-Bonnet gravity," *EPJC*, vol. 75, p. 399, Aug. 2015.

[206] Z. Stuchlík, J. Schee, and A. Abdujabbarov, "Ultra-high-energy collisions of particles in the field of near-extreme Kehagias-Sfetsos naked singularities

and their appearance to distant observers," *Phys. Rev. D*, vol. 89, no. 10, p. 104048, May 2014.

[207] A. A. Abdujabbarov, A. A. Tursunov, B. J. Ahmedov, and A. Kuvatov, "Acceleration of particles by black hole with gravitomagnetic charge immersed in magnetic field," *Astroph. Space Sci.* , vol. 343, pp. 173–179, Jan. 2013.

[208] The Pierre Auger Collaboration, "The Pierre Auger Observatory: Contributions to the 35th International Cosmic Ray Conference (ICRC 2017)," *arXiv e-prints*, p. arXiv:1708.06592, Aug 2017.

[209] A. Aab *et al.*, "Combined fit of spectrum and composition data as measured by the Pierre Auger Observatory," *JCAP*, vol. 1704, no. 04, p. 038, 2017, [Erratum: JCAP1803,no.03,E02(2018)].

[210] R. U. Abbasi and et al., "Study of Ultra-High Energy Cosmic Ray composition using Telescope Array's Middle Drum detector and surface array in hybrid mode," *Astroparticle Physics*, vol. 64, pp. 49–62, Apr. 2015.

[211] ——, "Indications of Proton-Dominated Cosmic-Ray Composition above 1.6 EeV," *Physical Review Letters*, vol. 104, no. 16, p. 161101, Apr. 2010.

[212] ——, "Search for EeV protons of galactic origin," *Astroparticle Physics*, vol. 86, pp. 21–26, Jan. 2017.

[213] S. Ansoldi and et al., "The Blazar TXS 0506+056 Associated with a High-energy Neutrino: Insights into Extragalactic Jets and Cosmic-Ray Acceleration," *ApJ*, vol. 863, p. L10, Aug 2018.

[214] P. Bhattacharjee and G. Sigl, "Origin and propagation of extremely high-energy cosmic rays," *Phys. Rept.*, vol. 327, pp. 109–247, 2000.

[215] G. Rubtsov, P. Satunin, and S. Sibiryakov, "Constraints on violation of Lorentz invariance from atmospheric showers initiated by multi-TeV photons," *JCAP*, vol. 1705, p. 049, 2017.

[216] G. Domokos and S. Kovesi-Domokos, "Strongly interacting neutrinos and the highest energy cosmic rays," *Phys. Rev. Lett.*, vol. 82, pp. 1366–1369, 1999.

[217] R. D. Blandford, "Acceleration of Ultra High Energy Cosmic Rays," *Physica Scripta Volume T*, vol. 85, pp. 191–194, 2000.

[218] A. R. Bell, A. T. Araudo, J. H. Matthews, and K. M. Blundell, "Cosmic-ray acceleration by relativistic shocks: limits and estimates," *MNRAS*, vol. 473, pp. 2364–2371, Jan. 2018.

[219] R. S. Nemmen and A. Tchekhovskoy, "On the efficiency of jet production in radio galaxies," *MNRAS*, vol. 449, pp. 316–327, May 2015.

[220] A.-K. Baczko, R. Schulz, M. Kadler, E. Ros, M. Perucho, T. P. Krichbaum, M. Böck, M. Bremer, C. Grossberger, M. Lindqvist, A. P. Lobanov, K. Mannheim, I. Martí-Vidal, C. Müller, J. Wilms, and J. A. Zensus, "A highly magnetized twin-jet base pinpoints a supermassive black hole," *A&A*, vol. 593, p. A47, Sep. 2016.

[221] S. S. Doeleman and et al., "Jet-Launching Structure Resolved Near the Supermassive Black Hole in M87," *Science*, vol. 338, p. 355, Oct. 2012.

[222] M. Kino, F. Takahara, K. Hada, K. Akiyama, H. Nagai, and B. W. Sohn, "Magnetization Degree at the Jet Base of M87 Derived from the Event Horizon Telescope Data: Testing the Magnetically Driven Jet Paradigm," *ApJ*, vol. 803, p. 30, Apr. 2015.

[223] Z. Stuchlík and M. Kološ, "Acceleration of the charged particles due to chaotic scattering in the combined black hole gravitational field and asymptotically uniform magnetic field," *EPJC*, vol. 76, p. 32, Jan. 2016.

[224] J. C. McKinney, A. Tchekhovskoy, and R. D. Blandford, "Alignment of Magnetized Accretion Disks and Relativistic Jets with Spinning Black Holes," *Science*, vol. 339, p. 49, Jan. 2013.

[225] M. M. Reynoso, M. C. Medina, and G. E. Romero, "A lepto-hadronic model for high-energy emission from FR I radiogalaxies," *A&A*, vol. 531, p. A30, Jul 2011.

[226] R. Aloisio, "Acceleration and propagation of ultra high energy cosmic rays," *arXiv e-prints*, p. arXiv:1707.08471, Jul 2017.

[227] S. Koide, "Charge separation instability in an unmagnetized disk plasma around a Kerr black hole," *Phys. Rev. D*, vol. 83, p. 023003, Jan 2011.

[228] M. J. Reid, "Is There a Supermassive Black Hole at the Center of the Milky Way?" *International Journal of Modern Physics D*, vol. 18, pp. 889–910, 2009.

[229] F. Munyaneza and R. D. Viollier, "The Motion of Stars near the Galactic Center: A Comparison of the Black Hole and Fermion Ball Scenarios," *ApJ*, vol. 564, pp. 274–283, Jan. 2002.

[230] P. Jetzer, "Boson stars," *Physics Reports* , vol. 220, pp. 163–227, Nov. 1992.

[231] D. F. Torres, S. Capozziello, and G. Lambiase, "Supermassive boson star at the galactic center?" *Phys. Rev. D*, vol. 62, no. 10, p. 104012, Nov. 2000.

[232] F. De Paolis, G. Ingrosso, A. A. Nucita, D. Orlando, S. Capozziello, and G. Iovane, "Astrophysical constraints on a possible neutrino ball at the Galactic Center," *A&A*, vol. 376, pp. 853–860, Sep. 2001.

[233] F. H. Vincent, Z. Meliani, P. Grandclément, E. Gourgoulhon, and O. Straub, "Imaging a boson star at the Galactic center," *Classical and Quantum Gravity*, vol. 33, no. 10, p. 105015, May 2016.

[234] P. V. P. Cunha, C. A. R. Herdeiro, E. Radu, and H. F. Rúnarsson, "Shadows of Kerr Black Holes with Scalar Hair," *Physical Review Letters*, vol. 115, no. 21, p. 211102, Nov. 2015.

[235] P. V. P. Cunha, J. Grover, C. Herdeiro, E. Radu, H. Rúnarsson, and A. Wittig, "Chaotic lensing around boson stars and Kerr black holes with scalar hair," *Phys. Rev. D*, vol. 94, no. 10, p. 104023, Nov 2016.

[236] A. Zakharov, "The black hole at the Galactic Center: observations and models in a nutshell," in *Journal of Physics Conference Series*, ser. Journal of Physics Conference Series, vol. 934, Dec. 2017, p. 012037.

[237] A. F. Zakharov, "The black hole at the Galactic Center: Observations and models," *International Journal of Modern Physics D*, vol. 27, p. 1841009, 2018.

[238] A. M. Ghez, M. Morris, E. E. Becklin, A. Tanner, and T. Kremenek, "The accelerations of stars orbiting the Milky Way's central black hole," *Nature*, vol. 407, pp. 349–351, Sep. 2000.

[239] A. M. Ghez and et al., "The First Measurement of Spectral Lines in a Short-Period Star Bound to the Galaxy's Central Black Hole: A Paradox of Youth," *ApJL*, vol. 586, pp. L127–L131, Apr. 2003.

[240] A. M. Ghez, S. Salim, S. D. Hornstein, A. Tanner, J. R. Lu, M. Morris, E. E. Becklin, and G. Duchêne, "Stellar Orbits around the Galactic Center Black Hole," *ApJ*, vol. 620, pp. 744–757, Feb. 2005.

[241] N. N. Weinberg, M. Milosavljević, and A. M. Ghez, "Stellar Dynamics at the Galactic Center with an Extremely Large Telescope," *ApJ*, vol. 622, pp. 878–891, Apr. 2005.

[242] L. Meyer, A. M. Ghez, R. Schödel, S. Yelda, A. Boehle, J. R. Lu, T. Do, M. R. Morris, E. E. Becklin, and K. Matthews, "The Shortest-Known-Period Star Orbiting Our Galaxy's Supermassive Black Hole," *Science*, vol. 338, p. 84, Oct. 2012.

[243] M. R. Morris, L. Meyer, and A. M. Ghez, "Galactic center research: manifestations of the central black hole," *Research in Astronomy and Astrophysics*, vol. 12, pp. 995–1020, Aug. 2012.

[244] A. F. Zakharov, A. A. Nucita, F. de Paolis, and G. Ingrosso, "Apoastron shift constraints on dark matter distribution at the Galactic Center," *Phys. Rev. D*, vol. 76, no. 6, p. 062001, Sep. 2007.

[245] A. F. Zakharov, P. Jovanović, D. Borka, and V. Borka Jovanović, "Constraining the range of Yukawa gravity interaction from S2 star orbits II: bounds on graviton mass," *JCAP*, vol. 5, p. 045, May 2016.

[246] J. M. Bardeen, "Timelike and null geodesics in the Kerr metric." in *Black Holes (Les Astres Occlus)*, C. Dewitt and B. S. Dewitt, Eds., 1973, pp. 215–239.

[247] J.-P. Luminet, "Image of a spherical black hole with thin accretion disk," *A&A*, vol. 75, pp. 228–235, May 1979.

[248] O. James, E. von Tunzelmann, P. Franklin, and K. S. Thorne, "Visualizing Interstellar's Wormhole," *American Journal of Physics*, vol. 83, pp. 486–499, Jun. 2015.

[249] S. S. Doeleman, "Seeing the unseeable," *Nature Astronomy*, vol. 1, pp. 646–646, Oct. 2017.

[250] Event Horizon Telescope Collaboration, "First M87 Event Horizon Telescope Results. I. The Shadow of the Supermassive Black Hole," *ApJ*, vol. 875, no. 1, p. L1, Apr 2019.

[251] ——, "First M87 Event Horizon Telescope Results. IV. Imaging the Central Supermassive Black Hole," *ApJ*, vol. 875, no. 1, p. L4, Apr 2019.

[252] ——, "First M87 Event Horizon Telescope Results. VI. The Shadow and Mass of the Central Black Hole," *ApJ*, vol. 875, no. 1, p. L6, Apr 2019.

[253] J. L. Synge, *Relativity: The general theory*, 1960.

[254] L. Y. Arifov, *General theory of relativity and gravitation.*, 1983.

[255] N. A. Silant'ev, M. Y. Piotrovich, Y. N. Gnedin, and T. M. Natsvlishvili, "Magnetic fields of AGNs and standard accretion disk model: testing by optical polarimetry," *A&A*, vol. 507, pp. 171–182, Nov. 2009.

[256] Z. Stuchlik, "The motion of test particles in black-hole backgrounds with non-zero cosmological constant," *Bulletin of the Astronomical Institutes of Czechoslovakia*, vol. 34, pp. 129–149, Mar. 1983.

[257] A. F. Zakharov, "Are signatures of anti-de-Sitter black hole at the Galactic Center?" *arXiv e-prints*, p. arXiv:1407.2591, Jul 2014.

[258] G. Preparata, R. Ruffini, and S.-S. Xue, "The dyadosphere of black holes and gamma-ray bursts," *A&A*, vol. 338, pp. L87–L90, Oct. 1998.

[259] R. Ruffini, C. L. Bianco, S.-S. Xue, P. Chardonnet, F. Fraschetti, and V. Gurzadyan, "On the Instantaneous Spectrum of Gamma-Ray Bursts," *International Journal of Modern Physics D*, vol. 13, pp. 843–851, 2004.

[260] R. Ruffini, J. A. Rueda, M. Muccino, Y. Aimuratov, L. M. Becerra, C. L. Bianco, M. Kovacevic, R. Moradi, F. G. Oliveira, G. B. Pisani, and Y. Wang, "On the Classification of GRBs and Their Occurrence Rates," *ApJ*, vol. 832, p. 136, Dec. 2016.

[261] F. Tamburini, M. De Laurentis, L. Amati, and B. Thidé, "General relativistic electromagnetic and massive vector field effects with gamma-ray burst production," *Phys. Rev. D*, vol. 96, no. 10, p. 104003, Nov. 2017.

[262] D. N. Page, "Evidence against Macroscopic Astrophysical Dyadospheres," *ApJ*, vol. 653, pp. 1400–1409, Dec. 2006.

[263] N. Dadhich, R. Maartens, P. Papadopoulos, and V. Rezania, "Black holes on the brane," *Physics Letters B*, vol. 487, pp. 1–6, Aug. 2000.

[264] A. N. Aliev and A. E. Gümrükçüoğlu, "Charged rotating black holes on a 3-brane," *Phys. Rev. D*, vol. 71, no. 10, p. 104027, May 2005.

[265] H. Kucáková, P. Slaný, and Z. Stuchlík, "Toroidal configurations of perfect fluid in the Reissner-Nordström-(anti-)de Sitter spacetimes," *JCAP*, vol. 1, p. 033, Jan. 2011.

[266] A. Y. Bin-Nun, "Gravitational lensing of stars orbiting Sgr A* as a probe of the black hole metric in the Galactic center," *Phys. Rev. D*, vol. 82, no. 6, p. 064009, Sep. 2010.

[267] C. Ding, C. Liu, Y. Xiao, L. Jiang, and R.-G. Cai, "Strong gravitational lensing in a black-hole spacetime dominated by dark energy," *Phys. Rev. D*, vol. 88, no. 10, p. 104007, Nov. 2013.

[268] E. Babichev, C. Charmousis, and A. Lehébel, "Asymptotically flat black holes in Horndeski theory and beyond," *JCAP*, vol. 4, p. 027, Apr. 2017.

[269] L. Patrizii and M. Spurio, “Status of Searches for Magnetic Monopoles,” *Annual Review of Nuclear and Particle Science*, vol. 65, pp. 279–302, Oct. 2015.

[270] N. A. Sharp, “Geodesics in black hole space-times,” *General Relativity and Gravitation*, vol. 10, pp. 659–670, Jun. 1979.

[271] Z. Stuchlík and S. Hledík, “Some properties of the Schwarzschild-de Sitter and Schwarzschild-anti-de Sitter spacetimes,” *Phys. Rev. D*, vol. 60, no. 4, p. 044006, Aug. 1999.